# Active Micro-/Nano-Structures for Electromechanical Actuation

by

Jinchi Han

B.Eng. Electrical Engineering, Tsinghua University (2013)
M.S.E. Electrical Engineering, Tsinghua University (2015)
S.M. Electrical Engineering and Computer Science, Massachusetts Institute of Technology (2018)

Submitted to the Department of Electrical Engineering and Computer Science
in partial fulfillment of the requirements for the degree of
Doctor of Philosophy in Electrical Engineering and Computer Science
at the
MASSACHUSETTS INSTITUTE OF TECHNOLOGY
June 2021

© Massachusetts Institute of Technology 2021. All rights reserved.

Author . . . . . . . . . . . . . . . . . . . . . . . . . . . . . . . . . . . . . . . . . . . . . . . . . . . . . . . . . .
Department of Electrical Engineering and Computer Science
May 18, 2021

Certified by . . . . . . . . . . . . . . . . . . . . . . . . . . . . . . . . . . . . . . . . . . . . . . . . . . . . .
Vladimir Bulović
Professor of Electrical Engineering and Computer Science
Thesis Supervisor

Certified by . . . . . . . . . . . . . . . . . . . . . . . . . . . . . . . . . . . . . . . . . . . . . . . . . . . . .
Jeffrey H. Lang
Professor of Electrical Engineering and Computer Science
Thesis Supervisor

Accepted by . . . . . . . . . . . . . . . . . . . . . . . . . . . . . . . . . . . . . . . . . . . . . . . . . . . . .
Leslie A. Kolodziejski
Professor of Electrical Engineering and Computer Science
Chair, Department Committee on Graduate Students

# Active Micro-/Nano-Structures for Electromechanical Actuation

by

Jinchi Han

Submitted to the Department of Electrical Engineering and Computer Science
on May 18, 2021, in partial fulfillment of the
requirements for the degree of
Doctor of Philosophy in Electrical Engineering and Computer Science

## Abstract

The design and implementation of micro-/nano-structures as active components has become an increasingly popular scheme for the development of electronic devices and systems in pursuit of unprecedented device performance and unique system functionality. In particular, cooperative actuation of active structures assembled in parallel results in emerging concepts of electromechanical devices and systems with tunable characteristics enabled by exploiting all the degrees of design freedom available to the active components. Engineering such micro-/nano-structures requires precise and scalable fabrication with resolution down to the nanometer-scale, often beyond the capabilities of conventional processing techniques. Exploring these opportunities could contribute substantially to the understanding of fundamental physical phenomena and the upsurge of novel device structures and concepts, as well as pushing the frontier of nanoscale fabrication and metrology.

In this thesis, challenges and opportunities in engineering active micro-/nano-structures for electromechanical actuation are explored through two case studies, a tunneling nanoswitch and an acoustically-active surface, which aim to present paradigms for high-performance electromechanical devices and systems designed based on cooperating active micro-/nano-structures.

The tunneling nanoswitch utilizes molecules as active nanoscale springs. An ensemble of such molecular springs takes the form of a self-assembled molecular layer sandwiched between ultra-smooth bottom electrodes and an active top nanoparticle contact. This nanoswitch operates by electromechanical modulation of the current tunneling through the nanometer-scale molecular switch gap. This unique mechanism enables the device to demonstrate a low turn-on voltage (under 3 V) and a short delay (2 ns) simultaneously, which are among critical challenges facing nanoelectromechanical (NEM) switches. Significantly, the molecular layer and the top nanoparticle contact serve as two degrees of design freedom with which to independently tailor static and dynamic device characteristics, thereby enabling a path towards sub-1-V switching in the GHz regime for electromechanical logic.

The acoustically-active surface depends on widely distributed, microstructured

piezoelectric transducers as active components. One example of such an acoustic surface is a PVDF film embossed with active micro-domes in an array. Existence of these freestanding micro-domes actuating in parallel significantly enhances the acoustic performance and allows our acoustic surface to achieve a unit-area sensitivity of 0.2075 mPa/(V·cm$^2$), which well outperforms existing flexible loudspeakers. The acoustic response can be further improved by engineering the profile and dimensions of the micro-domes. In addition, coordinating actuation of the micro-domes based on adaptive amplitude and phase control could enable directional audible sound generation, currently unavailable based on standalone commercial loudspeakers. The outstanding acoustic performance, attractive features (wide-area, thin, flexible, low-cost and even transparent), and unique functionality make the acoustic surface promising for broad emerging application scenarios.

Creating high-performance active structures in these case studies has motivated our development of novel processing techniques, including scalable manipulation of nanomaterials and low-cost, high-precision micro-embossing of polymer thin films. The highly uniform, mechanically tunable molecular junctions and the wide-area, phased acoustic micro-transducer array provide promising platforms for scientific studies of fundamental physical phenomena and innovations in diverse electronic devices and systems.

Thesis Supervisor: Vladimir Bulović
Title: Professor of Electrical Engineering and Computer Science

Thesis Supervisor: Jeffrey H. Lang
Title: Professor of Electrical Engineering and Computer Science

# Acknowledgments

Time goes by so quickly, and it is hard to believe I have been staying at MIT for five years. I would never forget the excitement when I got the offer letter and started to imagine my journey at MIT. As this journey is about to come to an end, I look back on the days working towards my PhD degree and realize what I have gained along this challenging path is well beyond my imagination. It is hard to describe how grateful I am to my advisors, colleagues and friends. Their presence and support make this journey colorful, fruitful and filled with wonderful memories.

First and foremost, I would like to thank my advisors, Prof. Vladimir Bulović and Prof. Jeffrey H. Lang. They have always been patient with me, particularly at the beginning of my graduate study when I had limited background on my research topic. Throughout my entire PhD study, they are extremely supportive, providing great opportunities and sufficient freedom for me to learn and explore my research interests even beyond the scope of my thesis topic. Vladimir's broad horizon, deep understanding of science, cheerful character, creative thinking, leadership and entrepreneurship inspire me to pursue my interests and to develop into a great researcher and inventor like him. I am so honored and incredibly fortunate to be advised by Jeff over the past five years. I am deeply influenced by his broad horizon, in-depth perspective of technologies, great passion for teaching and advising, enthusiasm and rigorous attitude towards research. It has been a wonderful experience working with them, and I am thankful to the time and effort they have spent on teaching me and supporting my growth to be a better researcher.

I would also like to thank Prof. Farnaz Niroui. She served as my mentor in the first two years of my graduate study, teaching and training me on nanofabrication and metrology. She is always hardworking, passionate about research, and able to present her ideas and works in an elegant way. Her broad knowledge about nanoscale science and technology motivates me to keep learning and exploring like her.

I am very grateful to Prof. Jing Kong and Prof. Zoltán S. Spakovszky for their supports on my research. They have provided wonderful suggestions for me, and this

thesis work significantly benefits from their expertise and perspective. Prof. Kong is an expert on nanomaterials and also a great teacher with genuine interests in helping students to grow. It is my great pleasure to closely collaborate with her group. I am very honored to have Prof. Spakovszky in my thesis committee. It would be tougher for me to complete the acoustic part of my thesis without his expertise. The acoustic measurements would even be impossible without his help.

I was fortunate to join the Organic and Nanostructured Electronics Laboratory (ONELab) in my first year. The wonderful atmosphere and the close interactions with our lab members have made it easy to learn and do research here. I would like to thank Melany Sponseller, Ella Wassweiler, Roberto Brenes, Richard Swartwout, Annie Wang, Benjia Dak Dou, Apoorva Murarka for offering me help and giving me suggestions on my research over the past five years. I would like to express my special thanks to Mayuran Saravanapavanantham and Matthew Ruiyan Chua for their kind assistance whenever I need. I enjoy chatting with them late at night in their office on research, graduate study, career and random topics.

I would like to acknowledge the funding agencies, National Science Foundation (NSF) Center for Energy Efficient Electronics Science ($E^3S$) (Award ECCS-0939514) and Ford Motor Company (Ford-MIT Alliance Agreement January 2008, MIT0224), that supported my research. It was a great experience to be a member of $E^3S$ center for four years. I appreciate its financial support and all the opportunities it created for my research and professional development. I enjoy interacting with the faculty, staff, students and postdocs in the center and learning about diverse research fields. I am thankful to Ford Motor Company for its financial support, and I received numerous wonderful suggestions from the Ford team on my research. I want to thank Andre Van Schyndel, Thomas Chrapkiewicz, Scott Amman, Alan Norton for sharing their expertise in acoustics, which has greatly improved my thesis work.

I would like to acknowledge my collaborator Zachary P. Nelson and Jiaojian Shi. Working with them and participating in researches outside my own field broadened my horizon. I appreciate kind research staff in Microsystems Technology Laboratories (MTL), Materials Research Laboratories (MRL), Cypress Engineering Design Studio

(EDS) for their training and assistance that make my thesis work possible.

I was incredibly fortunate to make many friends at MIT, and my graduate life here wouldn't be so colorful and fruitful without the companionship of my friends. I would like to specially thank Jiahao Han and Zhantao Chen, who are my roommates over the past five years. It was such a pleasure to live with them, learn from them and encourage each other to walk through tough moments in graduate study. I also want to thank my friends Ang-Yu Lu, Pin-Chun Shen, Yuxuan Cosmi Lin, Yingnan Cui, Mingye Gao, Haozhe Wang, Jiangtao Wang, Mengyang Yuan, Qingyun Xie for their continuous supports and giving me great memories at MIT.

Finally, I would like to express my deepest love and gratitude to my family, and I dedicate this thesis to them. When I resigned from my job and decided to set off for a new adventure at an age of 25, they supported me without any reservation and encouraged me to chase my dream. Any success I have accomplished in my life so far would not be possible without their love, encouragement and unconditioned supports. I am deeply indebted to my wife Yujia. It was hard for us to be apart over these years, living in two countries. But she always cheered me up, supported me with no complaints and no regrets, and gave me courage that made me through all the tough days. I am so lucky to have her in my life.

I am grateful to all the challenges and setbacks I have encountered. They teach me to embrace failure and focus more on what I gained rather than lost along the journey. They keep reminding me of the deep and perpetual passion for research and innovation, which makes me choose this path and keep going.

# Contents

**1 Introduction** **27**

1.1 Active Micro-/Nano-Structures . . . . . . . . . . . . . . . . . . . . . . 27

1.2 Nanoelectromechanical Switches . . . . . . . . . . . . . . . . . . . . . . 28

1.2.1 Overview . . . . . . . . . . . . . . . . . . . . . . . . . . . . 28

1.2.2 Key Challenges . . . . . . . . . . . . . . . . . . . . . . . . . 30

1.2.3 Outlook . . . . . . . . . . . . . . . . . . . . . . . . . . . . . 35

1.3 Acoustically-Active Surfaces . . . . . . . . . . . . . . . . . . . . . . . . 37

1.3.1 Overview of Acoustic Transducers . . . . . . . . . . . . . . . . . 37

1.3.2 Prospects for Acoustically-Active Surfaces . . . . . . . . . . . . 39

1.3.3 Demand and Challenges . . . . . . . . . . . . . . . . . . . . . 44

1.3.4 Candidate Technologies for Acoustic Surfaces . . . . . . . . . . 46

1.3.5 Outlook . . . . . . . . . . . . . . . . . . . . . . . . . . . . . 49

1.4 Thesis Organization . . . . . . . . . . . . . . . . . . . . . . . . . . . . 51

**2 Theoretical Modeling of Tunneling Nanoelectromechanical Switch** **53**

2.1 Device Concept . . . . . . . . . . . . . . . . . . . . . . . . . . . . . . 53

2.2 Static Model . . . . . . . . . . . . . . . . . . . . . . . . . . . . . . . . 57

2.2.1 Electrostatic Force . . . . . . . . . . . . . . . . . . . . . . . . 57

2.2.2 Adhesive Force . . . . . . . . . . . . . . . . . . . . . . . . . . 60

2.2.3 Restoring Force . . . . . . . . . . . . . . . . . . . . . . . . . . 62

2.2.4 Force Balance . . . . . . . . . . . . . . . . . . . . . . . . . . . 63

2.3 Dynamic Model . . . . . . . . . . . . . . . . . . . . . . . . . . . . . . 65

2.4 Tunabilities of $I$-$V$ Characteristic . . . . . . . . . . . . . . . . . . . . 67

2.5 Tunabilities of Switching Speed . . . . . . . . . . . . . . . . . . . . . . 74

**3 Fabrication of Tunneling Nanoelectromechanical Switch 79**

3.1 Fabrication of a Two-Terminal Device . . . . . . . . . . . . . . . . . . . 79

3.2 Fabrication of a Multi-Terminal Device . . . . . . . . . . . . . . . . . . 87

3.3 Challenges and Outlook . . . . . . . . . . . . . . . . . . . . . . . . . . 93

**4 Performance of Tunneling Nanoelectromechanical Switch 95**

4.1 $I$-$V$ Characteristics of Nanoswitches Based on Poly(ethylene glycol)thiol Molecular Spacer and Gold Nanorod Active Electrode . . . . 95

4.2 Tuning $I$-$V$ Characteristics through Molecular Engineering . . . . . . 101

4.3 Dynamic Responses of Nanoswitches Based on Poly(ethylene glycol)thiol Molecular Spacer and Gold Nanorod Active Electrode . . . . 109

4.4 Tuning Switching Speed through Engineering the Nanoscale Active Electrode . . . . . . . . . . . . . . . . . . . . . . . . . . . . . . . 113

**5 Towards High-Performance Nanoelectromechanical Switches: Summary and Outlook 121**

5.1 Summary . . . . . . . . . . . . . . . . . . . . . . . . . . . . . . . . 121

5.2 Outlook . . . . . . . . . . . . . . . . . . . . . . . . . . . . . . . . . 124

5.2.1 Energy-Efficient NEM Switches . . . . . . . . . . . . . . . . . 124

5.2.2 Beyond Electromechanical Logic . . . . . . . . . . . . . . . . . 126

**6 Theoretical Modeling of Acoustically-Active Surface 129**

6.1 Device Concept . . . . . . . . . . . . . . . . . . . . . . . . . . . . . 129

6.2 Static Modeling . . . . . . . . . . . . . . . . . . . . . . . . . . . . . 131

6.2.1 Variables and General Assumptions . . . . . . . . . . . . . . . 131

6.2.2 Membrane Theory . . . . . . . . . . . . . . . . . . . . . . . . 133

6.2.3 Thin-Plate Theory . . . . . . . . . . . . . . . . . . . . . . . . 136

6.2.4 Sound Generation by an Acoustic Surface . . . . . . . . . . . 138

6.3 Dynamic Modeling . . . . . . . . . . . . . . . . . . . . . . . . . . . 140

6.4 Analysis of Dome Vibration Based on COMSOL Multiphysics Simulation and Theoretical Models . . . . . . . . . . . . . . . . . . . . . . . . 142
6.5 Performance of Acoustic Surface in Free Field . . . . . . . . . . . . . . 150

**7 Fabrication of Acoustically-Active Surface 157**
7.1 Overview of Fabrication Approaches . . . . . . . . . . . . . . . . . . . . 157
7.2 Micro-Embossing Process Based on Controlled Vacuum . . . . . . . . . 159
7.3 Self-Aligned Micro-Embossing Process . . . . . . . . . . . . . . . . . . 164

**8 Performance of Acoustically-Active Surface 169**
8.1 Acoustic Measurement Setup . . . . . . . . . . . . . . . . . . . . . . . . 169
8.2 Surface Velocities of Individual PVDF Micro-Domes . . . . . . . . . . . 174
8.3 Free-Field Acoustic Performance of Wide-Area Acoustic Surfaces . . . 183
8.3.1 Sensitivity . . . . . . . . . . . . . . . . . . . . . . . . . . . . . . 183
8.3.2 Frequency Response . . . . . . . . . . . . . . . . . . . . . . . . 187
8.3.3 Directivity . . . . . . . . . . . . . . . . . . . . . . . . . . . . . . 192

**9 Towards Multi-Functional Acoustically-Active Surfaces: Summary and Outlook 195**
9.1 Summary and Conclusion . . . . . . . . . . . . . . . . . . . . . . . . . 195
9.2 Outlook . . . . . . . . . . . . . . . . . . . . . . . . . . . . . . . . . . . 198
9.2.1 Enhancement of Sound Generation . . . . . . . . . . . . . . . . 198
9.2.2 Exploring Potentials of the Acoustic Surface . . . . . . . . . . . 200

**10 Engineering Electromechanical Devices and Systems: From Nanoscale to Macroscale 203**

# List of Figures

1-1 Schematic representation of a typical three-terminal NEM switch (a) in the OFF-state and (b) in the ON-state. . . . . . . . . . . . . . . . . 30

1-2 Application prospects of acoustically-active surface technology . . . . 40

1-3 Candidate technologies for acoustically-active surfaces, including (a) porous compressible film, (b) microcavity-based transducer array, (c) piezoelectric transducer array. . . . . . . . . . . . . . . . . . . . . . . 46

2-1 Tunneling current density as a function of junction width. The applied voltage and the barrier parameter are kept constant as 1 V and 0.57, respectively, in this example. . . . . . . . . . . . . . . . . . . . . . . . 55

2-2 Schematic respresentation of the (a) architecture and the operating mechanism ((b) OFF-state and (c) ON-state) of the tunneling NEM switch using molecular springs. . . . . . . . . . . . . . . . . . . . . . 56

2-3 Schematics of the three types of capacitors formed by the nanoparticles, the molecules and the bottom electrodes. (a) Parallel-plate capacitor that models devices with nanoplatelets. (b) Rod-plate capacitor that models devices with nanorods. (c) Cylinder-plate capacitor that models devices with nanotubes. . . . . . . . . . . . . . . . . . . . . . . . 57

2-4 Theoretical $I$-$V$ characteristics of an example device (solid curve) based on a stiff, thin molecular layer and an example device (dash-dotted curve) based on a soft, thick molecular layer, with corresponding Young's modulus $E_m$ and uncompressed molecular layer thickness $d_0$ marked in the figure. The dashed curves describe the pure tunneling $I$-$V$ characteristics at constant switch gaps. . . . . . . . . . . . . . . . 68

2-5 Dependence of the static behavior of a tunneling NEM switch on the thickness of uncompressed molecular layer $d_0$ at a constant Young's modulus $E_m = 15$ MPa. The ON-state switch gap after pull-in occurs is assumed as $g_{ON} = 0.5d_0$ to calculate the release voltage and release limit. Other simulation parameters are identical to those in Figure 2-4. 69

2-6 Dependence of the static device behavior on the drain voltage and the initial thickness of uncompressed molecular layer $d_0$ according to constant Young's moduli $E_m$ =10 MPa (a), 30 MPa (b), 50 MPa (c), respectively. The ON-state switch gap after pull-in occurs is assumed as $g_{ON} = 0.5d_0$ to calculate the release voltage and release limit. Other simulation parameters are identical to those in Figure 2-4. . . . . . . 71

2-7 Theoretical static behavior of nanoswitches based on nonlinear molecules. (a) Comparison between the surface adhesive force and the restoring force from compressed molecules with optimal 2nd-order, 4th-order, 6th-order polynomial Young's moduli as a function of compression $s$. (b) $I$-$V$ characteristics originating from the optimal nonlinear mechanics of molecules. . . . . . . . . . . . . . . . . . . . . . . . 73

2-8 Theoretical dynamic behavior of the nanoswitch. (a) Variation in the thickness of molecular layer and the tunneling current in response to an ideal 3 V pulse voltage at $t = 0$. (b) Variation in the device resistance and the voltage across a 1-M$\Omega$ resistor $R_s$ in series to the device. . . . 75

2-9 Dependence of the theoretical turn-on delay on the Young's modulus $E_m$ of the molecular spacer (a), the thickness of uncompressed molecular layer $d_0$ (b), and the area mass density of the nanoparticle $\rho$ (mass normalized by bottom surface area) (c), respectively, while the other variables are kept constant as marked in each figure. The theoretical turn-on delay corresponds to the time required to reach 1 $\mu$A drain current after applying a constant voltage. The maximum value and the minimum value of the colorbar in (c) correspond to gold and carbon nanoparticles, respectively, with the same geometry and dimensions. . 76

3-1 Nanofabrication process for a two-terminal tunneling nanoswitch. The process flow includes bottom electrodes patterning and transfer, self-assembly of molecular monolayer, and trapping of nanoparticle electrodes by DEP approach. . . . . . . . . . . . . . . . . . . . . . . . . 80

3-2 Atomic force microscopic (AFM) images of (a) evaporated gold bottom electrodes and (b) peeled gold bottom electrodes after pattern transfer. 82

3-3 Nanoscale infrared spectra of a sample with PEG-thiol molecular layers. The five screenshots indicate the positions for the measured spectra. 83

3-4 Scanning electron microscopic (SEM) images of trapped AuNR particles at different frequencies: (a) 10 kHz, (b) 100 kHz, and (c) 1 MHz. Concentrated nanoparticle suspension is dispensed onto the trapping electrodes. An identical trapping voltage of 1 $V_{p-p}$ is utilized at different frequencies. . . . . . . . . . . . . . . . . . . . . . . . . . . . . . 85

3-5 Trapping electrode array. (a) Picture of a trapping electrode array on a glass substrate. (b) Microscopic image of trapping electrodes with capacitors in series. (c) Close-up image of a pair of trapping electrodes. 86

3-6 SEM images of example devices based on diverse nanoparticle top electrodes, including (a) gold nanorod, (b) ribbon-shaped gold nanoplatelet, (c) hexagonal gold nanoplatelet, and (d) multi-walled carbon nanotube. . . . . . . . . . . . . . . . . . . . . . . . . . . 87

3-7 Schematic of a three-terminal tunneling nanoswitch (a) in the OFF-state and (b) in the ON-state. . . . . . . . . . . . . . . . . . . . . . . . 88

3-8 Nanofabrication process for a multi-terminal tunneling nanoswitch. The process flow includes sacrificial layer patterning, bottom electrodes patterning and transfer, sacrificial layer etching, self-assembly of molecular spacers, and trapping of the nanoparticle by DEP approach. . . . 89

3-9 Layouts of multi-terminal bottom electrodes. . . . . . . . . . . . . . . 90

3-10 AFM image of peeled multi-terminal bottom electrodes with height profile. . . . . . . . . . . . . . . . . . . . . . . . . . . . . . . . . . 91

3-11 SEM image of a fabricated multi-terminal tunneling nanoswitch. . . . 92

4-1 Experimental $I$-$V$ characteristics of example devices based on PEG-thiol spacers and an AuNR active electrode. The dashed curve provides a reference $I$-$V$ characteristic with respect to a constant molecular layer thickness extracted from low-voltage datapoints of D1. . . . . . 97

4-2 Statistics of device performance based on PEG-thiol molecular junctions and an AuNR active electrode. (a) Definition of the actuation voltage and the modulation in current for $I$-$V$ characteristics. (b) Distribution of device performance of AuNR nanoswitches. (c) Statistics of the actuation voltage. (d) Statistics of the modulation in current. . 98

4-3 $I$-$V$ characteristics of example devices based on PEG-thiol molecular spacers and an AuNR top electrode over cycles. (a) Experimental $I$-$V$ curves over cycles for a representative device, which fails due to stiction after 23 cycles. (b) Experimental $I$-$V$ curves over 1000 cycles of another representative device. The dashed curves provide reference tunneling $I$-$V$ characteristics according to constant molecular layer thicknesses which are extracted from low-voltage datapoints of the 1st cycle for both (a) and (b). (c) Extracted initial molecular layer thicknesses of the device in (a) over 23 cycles. (d) Extracted initial molecular layer thicknesses of the device in (b) over 1000 cycles. . . . 100

4-4 Devices with multiple Au nanoparticles. (a)-(c) SEM images of example devices with more than a single Au nanoparticle for the top electrode. (d) $I$-$V$ characteristics of the devices shown in (a)-(c). The compliance for the current is set as 1 $\mu$A. . . . . . . . . . . . . . . . . 102

4-5 Devices with Au nanoplatelet top electrodes. (a) A NEM switch with a ribbon-shaped Au nanoplatelet. (b) A NEM switch with a hexagonal Au nanoplatelet. (c) A NEM switch with a triangular Au nanoplatelet. (d) $I$-$V$ curves of the devices shown in (a)-(c). The compliance for current is set as 1 $\mu$A. . . . . . . . . . . . . . . . . . . . . . . . . 103

4-6 NMR Spectra of the synthesized molecules. (a) $^{1}$H NMR spectrum (400 MHz, $CDCl_3$) of tetradecyl 4-mercaptobenzoate. (b) $^{13}$C NMR spectrum (101 MHz, $CDCl_3$) of tetradecyl 4-mercaptobenzoate. (c) $^{1}$H NMR spectrum (400 MHz, $CDCl_3$) of 2-decyltetradecyl 4-mercaptobenzoate. (d) $^{13}$C NMR spectrum (101 MHz, $CDCl_3$) of 2-decyltetradecyl 4-mercaptobenzoate. . . . . . . . . . . . . . . . . . . . 104

4-7 GATR-FTIR spectra of DDT, TDMB, DTDMB, and PEG-thiol monolayers. The monolayers are self-assembled on 1 cm$^2$ thermally-evaporated gold surfaces. . . . . . . . . . . . . . . . . . . . . . . . . 106

4-8 Comparison of $I$-$V$ characteristics of devices with different molecular junctions. (a) 1-dodecanethiol (DDT). (b) tetradecyl 4-mercaptobenzoate (TDMB). (c) 2-decyltetradecyl 4-mercaptobenzoate (DTDMB). (d) Variation of the molecular layer thickness with the drain voltage for devices in (a)-(c). . . . . . . . . . . . . . . . . . . . 107

4-9 $I$-$V$ characteristics of devices with different molecules over 100 cycles. (a) 1-dodecanethiol (DDT). (b) Tetradecyl 4-mercaptobenzoate (TDMB). (c) 2-decyltetradecyl 4-mercaptobenzoate (DTDMB). The compliance for current is set as 100 nA. The dashed curve in each figure provides a no-modulation pure tunneling reference $I$-$V$ characteristic based on a constant spacer thickness extracted from low-voltage datapoints of the 10th cycle. . . . . . . . . . . . . . . . . . . . . . . 109

4-10 Schematic of the experimental setup that measures the device dynamic response. . . . . . . . . . . . . . . . . . . . . . . . . . . . . . . . . . 110
4-11 Dynamic responses from open-circuit and short-circuit control experiments. In both cases, the non-zero voltage signals across the sampling resistor $R_s$ for the first few nanoseconds after applying the pulse come from the measurement circuit and therefore the processed short-circuit $V_{Rs}$ waveform, which is free from device delay, can work as a reference to eliminate the electrical delay from the setup. . . . . . . . . . . . . 111
4-12 Dynamic response of an AuNR nanoswitch over multiple pulses. Decreasing turn-on delay suggests that the molecular layer thickness under zero drain voltage is reduced after each pulse. . . . . . . . . . . . 113
4-13 Experimental $I$-$V$ characteristics of MWCNT devices. The dashed curve provides reference pure tunneling $I$-$V$ characteristic according to a constant molecular layer thickness extracted from low-voltage datapoints of D1. . . . . . . . . . . . . . . . . . . . . . . . . . . . . . . . 115
4-14 Statistics of device performance based on PEG-thiol molecular junctions and a MWCNT active electrode. (a) Distribution of device performance of MWCNT nanoswitches. (b) Statistics of the actuation voltage. (c) Statistics of the modulation in current. . . . . . . . . . . 116
4-15 Dynamic responses of a nanoswitch before and after the MWCNT electrode was burned. (a) The SEM image of a nanoswitch with a MWCNT electrode likely burned by a high discharge current. (b) Comparison between dynamic responses of the nanoswitch before and after the electrode broke. . . . . . . . . . . . . . . . . . . . . . . . . . . . . . . . 117
4-16 Comparison between the turn-on delays of AuNR nanoswitches and those of MWCNT nanoswitches. (a) Dynamic responses of devices with 5 kDa PEG-thiol junctions and an AuNR electrode (1$\sim$2 $\mu$m in length and 80$\sim$100 nm in diameter). (b) Dynamic responses of devices with 5 kDa PEG-thiol junctions and a MWCNT electrode (1$\sim$2 $\mu$m in length and 100$\sim$150 nm in diameter). . . . . . . . . . . . . . . . . . . 118

6-1 Schematic illustrating the working mechanism of the acoustic surface based on vibration of piezoelectric micro-dome transducers in an array. 130

6-2 Schematic of a PVDF dome with definition of variables. . . . . . . . . 132

6-3 Comparison of simulated displacement distributions over two domes based on uniaxial and biaxial PVDF films. (a) 3D surface displacement distribution and (b) cross-section surface displacement distribution of a uniaxial PVDF dome ($d_{31}$ = 22 pC/N, $d_{32}$ = 0 pC/N). (c) 3D surface displacement distribution and (d) cross-section surface displacement distribution of a biaxial PVDF dome ($d_{31} = d_{32}$ = 12 pC/N). The drive voltage is 10 V, and the two domes have identical dimensions $R = 350$ $\mu$m, $H_0 = 35$ $\mu$m, and $h = 12$ $\mu$m. . . . . . . . . . . . . . . . 143

6-4 Theoretical and simulated dependence of deflection at the center of a PVDF dome on its height. Two dome sizes (a) $R = 1$ mm and (b) $R = 350$ $\mu$m are compared. . . . . . . . . . . . . . . . . . . . . . . . . 144

6-5 Theoretical and simulated dependence of deflection at the center of a PVDF dome on its radius. Results based on a constant aspect ratio (a) $H_0/R = 5\%$, (b) $H_0/R = 10\%$ and those based on a constant dome height (c) $H_0 = 15$ $\mu$m, (d) $H_0 = 35$ $\mu$m are compared. . . . . . . . . 145

6-6 Cross-section displacement distributions for large dome sizes. The simulation results of two PVDF domes based on (a) $R = 800$ $\mu$m, $H_0 = 80$ $\mu$m, $h = 12$ $\mu$m and (b) $R = 1$ mm, $H_0 = 100$ $\mu$m, $h = 12$ $\mu$m show flattened displacement distributions close to the dome center. . . . . . 146

6-7 Theoretical and simulated dependence of deflection at the center of a PVDF dome on the film thickness. Two dome heights (a) $H_0 = 15$ $\mu$m and (b) $H_0 = 35$ $\mu$m are compared. . . . . . . . . . . . . . . . . . . . . 147

6-8 Simulated dependence of the resonance frequency of a PVDF dome on its height. Two dome sizes $R = 1$ mm and $R = 350$ $\mu$m are compared. 149

6-9 Theoretical and simulated dependence of the resonance frequency of a PVDF dome on (a) the dome radius and (b) the film thickness. Two cases are simulated in (a) by keeping either a constant aspect ratio ($H_0/R = 5\%$, $H_0/R = 10\%$) or a constant dome height ($H_0 = 15$ $\mu$m, $H_0 = 35$ $\mu$m) during scaling of a PVDF dome. Two dome heights $H_0 = 15$ $\mu$m and $H_0 = 35$ $\mu$m are compared in (b). . . . . . . . . . . 150

6-10 On-axis SPL as a function of distance from the acoustic surface, at (a) 1 kHz, (b) 5 kHz and (c) 10 kHz, under a sinusoidal voltage of 10 V in amplitude. The red dashed line presents the monopole result (with perfect reflecting baffle) and the green dashed line marks a distance equal to the side length of the square acoustic surface ($L = 9$ cm). . . 152

6-11 On-axis SPL as a function of frequency, at (a) 1 cm (near-field) and (b) 30 cm (far-field) away from the acoustic surface, under a sinusoidal voltage of 10 V in amplitude. The red dashed line presents the frequency dependence ($p \propto f^2$) of a monopole radiator in free field. . . . 153

6-12 SPL directivity patterns at 30 cm from the acoustic surface with respect to frequencies of 1 kHz, 5 kHz, 10 kHz, 15 kHz, 17 kHz, 20 kHz. The SPL values for different observation points at each frequency are normalized by the peak SPL (0° angle) at the same frequency. . . . . 155

7-1 Fabrication of an acoustic surface with an array of PVDF domes based on the micro-embossing process. . . . . . . . . . . . . . . . . . . . . . . 160

7-2 Pictures of (a) a perforated Si mold prepared by microfabrication, (b) a setup for embossing domes on a PVDF film, and (c) a PVDF film with micro-domes in an array. . . . . . . . . . . . . . . . . . . . . . . . 161

7-3 Schematic of a flexible, robust acoustic surface with PVDF micro-domes protected by a perforated plastic film. . . . . . . . . . . . . . . . 163

7-4 Examples of flexible, transparent acoustic surfaces based on (a)Ag/ITO (5 nm/35 nm) electrodes and (b) ITO (50 nm) electrodes. . . . . . . 164

7-5 Pictures of (a) a PVDF dome misaligned with the through-holes on the top protective film, (b) a through-hole patterned by direct-write $CO_2$ laser rastering, (c) a through-hole patterned by mask-assisted laser rastering, and (d) a dome prepared by self-aligned micro-embossing with a perforated protective film on top. . . . . . . . . . . . . . . . . 165
7-6 Fabrication of an acoustic surface with an array of PVDF micro-domes based on self-aligned micro-embossing process. . . . . . . . . . . . . . 166
7-7 (a) Picture of a perforated PET thin film prepared by mask-assisted laser rastering. (b) Picture of an acoustic surface sample adhered to a glass substrate. (c) Microscopic image of PVDF domes in an array. (d) Microscopic image of PVDF domes under a higher magnification. 167

8-1 Schematic of the setup to measure surface velocities of PVDF domes. 170
8-2 (a) Schematic and (b) pictures of the acoustic measurement setup in an anechoic chamber. . . . . . . . . . . . . . . . . . . . . . . . . . . 171
8-3 Free-field correction curve for the B&K 4136 condenser microphone [141].174
8-4 (a) Statistics of surface velocities of PVDF domes on a freestanding acoustic surface. (b) Statistics of surface velocities of PVDF domes on an acoustic surface mounted on a glass substrate. . . . . . . . . . . 175
8-5 (a) Surface velocity mapping of a PVDF dome on a freestanding acoustic surface. (b) Surface velocity mapping of a PVDF dome on an acoustic surface mounted on a glass substrate. The surface velocity is measured under a 1 kHz, 10 V (amplitude) drive voltage in both (a) and (b). . . . . . . . . . . . . . . . . . . . . . . . . . . . . . . . . 176
8-6 Normalized experimental displacements along radial direction of the dome compared with theoretical normalized displacements given by the membrane model and the thin-plate model. . . . . . . . . . . . 177
8-7 Statistics of surface velocities of PVDF domes on three acoustic surface samples ((a) Sample S1, (b) Sample S2, (c) Sample S3) based on the same design variables ($R = 350$ $\mu$m, $h = 12$ $\mu$m, $H_0 =\sim 20$ $\mu$m). . . . 178

8-8 Statistics of surface velocities of PVDF domes on three acoustic surface samples based on different dome sizes, including (a) $R = 350$ $\mu$m, (b) $R = 275$ $\mu$m, (c) $R = 200$ $\mu$m. (d) Average experimental deflections of PVDF domes on the three samples compared to those theoretical and simulated deflections. The film thickness and the vacuum level utilized to emboss PVDF domes are identical for these samples. . . . . . . . . 179

8-9 Variation of the surface velocity with the drive voltage amplitude for PVDF domes with a radius of (a) $R = 350$ $\mu$m or (b) $R = 275$ $\mu$m. The theoretical and simulated responses between the dome surface velocity and the drive voltage are presented in each subfigure. . . . . . . . . . 180

8-10 Frequency responses of PVDF domes ($R = 350$ $\mu$m, $h = 12$ $\mu$m) driven by a voltage of 5 V in amplitude. . . . . . . . . . . . . . . . . . . . . . 181

8-11 Comparison between the experimental resonance frequencies and those predicted by theoretical model and COMSOL simulation, which shows their dependence on (a) the dome radius and (b) the film thickness. . 182

8-12 Sensitivities of fabricated acoustic surface samples at 30 cm away. Variation of (a) the acoustic pressure and (b) the SPL with the drive voltage (RMS) at 1 kHz. Variation of (c) the acoustic pressure and (d) the SPL with the drive voltage (RMS) at 5 kHz. Variation of (e) the acoustic pressure and (f) the SPL with the drive voltage (RMS) at 10 kHz. . . 185

8-13 Variation of the SPL with the drive voltage (RMS, 10 kHz) at 10 cm, 30 cm, 50 cm away. The theoretical SPL-voltage relations at these distances are also shown in the figure. . . . . . . . . . . . . . . . . . . . 188

8-14 Frequency responses of acoustic surface samples: (a) magnitude response; (b) phase response. Compensations for the attenuation from microphone protection grid (4 kHz$\sim$70 kHz) and for the drive voltage decay have been added to the magnitude response. Magnitude response at frequencies above 70 kHz (dashed curves) is uncompensated for microphone attenuation due to absence of correction data from the microphone manufacturer. . . . . . . . . . . . . . . . . . . . . . . . 189

8-15 Comparison between the surface velocity at the center of a dome and the surface velocity at void area in vicinity of the dome. . . . . . . . . 191

8-16 Radiation patterns of an acoustic surface at (a) 1 kHz, (b) 5 kHz, (c) 10 kHz, (d) 15 kHz, (e) 17 kHz, (f) 20 kHz. The SPL values at different angles for each frequency are normalized by the value measured at 0° angle for the same frequency. The theoretical directivity patterns are presented as dashed curves for comparison. . . . . . . . . . . . . . . . . 193

9-1 Pictures of a glass mug speaker enabled by a flexible, robust and transparent acoustic surface. . . . . . . . . . . . . . . . . . . . . . . . . . 201

9-2 Tuning the acoustic radiation pattern at 1 kHz, 1 m away based on (a) two pixels driven by voltages with the same amplitude but different phases, (b) three pixels driven by voltages with the same amplitude but different phases, and (c) three pixels driven by voltages with different amplitudes and phases. Each pixel is $10 \times 10$ cm$^2$ with an array of identical PVDF domes (vibrating in phase, 1 mm pitch). Normalized SPL is presented in the figure. . . . . . . . . . . . . . . . . . . . . . . . 202

10-1 Engineering electromechanical devices and systems through active component design at different scales. . . . . . . . . . . . . . . . . . . . 204

# List of Tables


5.1 Representative NEM switch techniques . . . . . . . . . . . . . . . . . 128

7.1 Properties of uniaxially-oriented PVDF films . . . . . . . . . . . . . . 163

8.1 Summary of dome dimensions of fabricated samples . . . . . . . . . . 183

8.2 Summary of the experimental results in terms of sensitivity, SPL-voltage slope and SPL at 25 V (RMS), 30 cm away . . . . . . . . . . 186

8.3 Normalized sensitivities of fabricated samples to the same design variables $R = 350$ $\mu$m, $H_0 = 17$ $\mu$m, $h = 12$ $\mu$m (unit: mPa/V) . . . . . . 186

8.4 Summary of SPL-frequency slope in different ranges (unit: dB/dec) . 190

9.1 Comparison with representative wide-area, flexible loudspeakers . . . 197

# Chapter 1

# Introduction

## 1.1 Active Micro-/Nano-Structures

Active structures in a device or system refer to the functional components that undergo changes in their structure, state and/or properties during their use, thereby rendering the device or system active in one or multiple ways. They could be a molecular structure in a chemical sensor [1], a metal-oxide-semiconductor structure in a modern processor [2], a nanoscale crystal in a light-emitting device [3], or a moving cantilever in an electromechanical switch [4], with physical dimensions ranging from one nanometer to a few millimeters. The ensemble of these active micro-/nano-structures decides or significantly contributes to the functionalities and the macroscopic characteristics of respective devices and systems.

Active micro-/nano-structures have played an increasingly significant role in the design of electromechanical devices, such as sensors [5], actuators [6], resonators [7], switches [4] and memories [8]. The advantages they bring exhibit at different scales. For micro-/nano-scale devices, employing molecules and nanomaterials as active nanostructures results in unique device concepts [9, 10] and unprecedented performance [11]. At a larger scale, adding active micro-/nano-structures with specific profiles to the surface of bulk materials may bring about additional tunabilities on the macroscopic properties [12] of conventional electromechanical devices; adaptive control on the actuation of active structures in an array may induce unique function-

ality to electromechanical systems [13].

This thesis seeks to demonstrate the merits of employing active micro-/nano-structures for electromechanical actuation in two representative scenarios. At the nanoscale, a tunneling electromechanical switch is developed using molecular springs and nanoparticle moving contact. These nanostructures induce tunabilities on the static and dynamic behavior of the switch, and thereby enable simultaneous low-voltage, high-speed switching, which used to be a longstanding challenge facing nanoelectromechanical (NEM) switches. For macroscale application, a wide-area acoustic surface is developed based on an array of piezoelectric micro-domes. It can be mounted on various objects and render them acoustically active due to unconstrained actuation of the active microstructures. Designing the profile and dimensions of the domes allows performance tuning for the acoustic surface. Moreover, additional functionality such as beam forming may be achieved when these microstructures are addressed as individual functional units and coordinated in certain ways.

## 1.2 Nanoelectromechanical Switches

### 1.2.1 Overview

For the past few decades, the continuous scaling of metal-oxide-semiconductor (MOS) field-effect transistors (FETs) has brought about significant performance gains and increased complexities to the integrated circuits and systems at a greatly reduced manufacturing cost. However, significant challenges including increased static leakage current, increased power dissipation, short channel effects, and so on are encountered as the critical dimensions of transistors kept shrinking [14]. Though new technologies including FinFET, metal gate/high-k dielectrics have been developed to mitigate the operating challenges of CMOS circuits [15], the OFF-state leakage current and the thermionic limit of 60 mV/dec subthreshold slope are fundamental issues that limit the energy-efficiency of nanoelectronic circuits based on complementary metal-oxide semiconductors (CMOS). This is driving interest in emerging beyond-CMOS

technologies [4, 16–21] that have the potential to overcome these fundamental limits.

NEM switches have received broad attention as a candidate energy-efficient beyond-CMOS technology for years. For a normally-off type conventional NEM switch (Figure 1-1), the electrodes are physically separated in the OFF-state. As a result, a NEM switch features near-zero OFF-state leakage and thereby negligible standby power consumption [4]. When a gate voltage is applied, an electrostatic force is induced on the active element to move it towards the stationary electrode. A gate voltage higher than a threshold value (namely the pull-in voltage) causes the attractive forces (including electrostatic force and van der Waals force) to suddenly overwhelm the restoring force from the deformed electrode, consequently making the active electrode into ohmic contact with the stationary electrode (i.e., ON-state). The transition between the ON-state and the OFF-state usually defines a several-orders-of-magnitude contrast in the drain current, and the abrupt switching behavior results in a low subthreshold swing for a NEM switch. These may allow the NEM switch to operate with a much lower voltage compared with CMOS devices and thus ultra-low dynamic power consumption in circuit [15]. In contrast to the normally-off type, a NEM switch can also be configured as the normally-on type, which has the source and drain electrodes initially in contact and relies on an applied gate voltage to pull them apart. A proper combination of these two types of NEM switches enables basic and complicated logic computation with a greatly reduced number of devices compared to conventional CMOS technology [22, 23]. Besides, the transition between the ON-state and the OFF-state depends on mechanical motion of the active electrode rather than the diffusion and drift of electrons and holes. Therefore, NEM switches are intrinsically less sensitive to temperature [24, 25] and various interference (e.g., high-dose radiation, microwaves and external electromagnetic fields) [26, 27], which makes them favorable for applications in harsh environments. These aforementioned fundamental merits make NEM switches promising energy-efficient logic devices to complement or substitute CMOS in the thriving Internet of Things (IOT) [15], where reducing energy consumption is one of the key challenges.

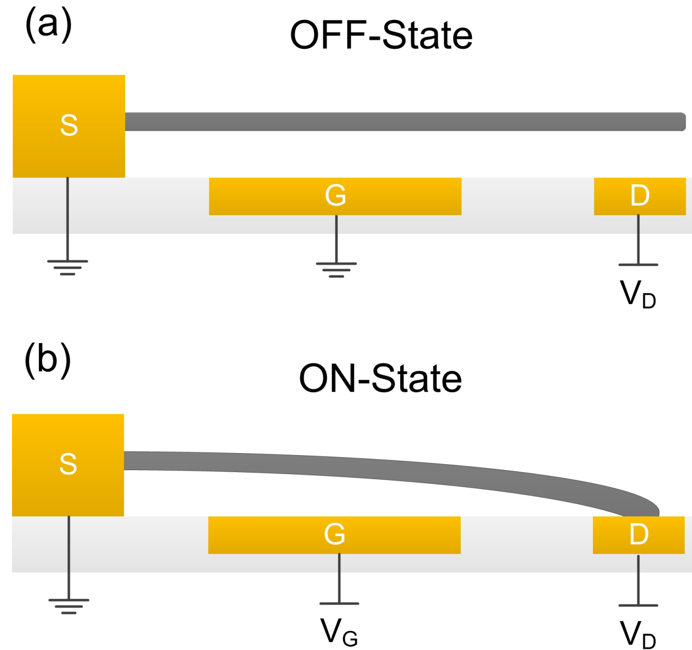


Figure 1-1: Schematic representation of a typical three-terminal NEM switch (a) in the OFF-state and (b) in the ON-state.

### 1.2.2 Key Challenges

The rapid advances of micro-/nano-fabrication techniques along with increasing diversity of materials available have enabled various designs of NEM switches, in terms of device architecture (e.g., cantilever architecture, relay architecture), electrode layout (e.g., vertical, lateral) and electrode material (e.g., metal, ceramic, nanomaterials). This has led to a wide distribution of device performance for NEM switches reported to date.

Similar to semiconductor devices, the actuation voltage and the switching delay are significant metrics to evaluate the performance of NEM switches. In addition, the device reliability is also a big concern, as NEM switches operate by deforming the active electrode to make frequent contact with the stationary electrode. Though NEM switches enjoy intrinsic advantages over semiconductor devices, there are a few key roadblocks facing NEM switches before they can fulfill their promise as a beyond-CMOS candidate technology for energy-efficient computing.

### High actuation voltage

In modern integrated circuits and systems, the power dissipation from charging and discharging parasitic capacitors in the circuit usually dominates the dynamic power consumption, which is proportional to the square of the actuation voltage. Therefore, the actuation voltage is critical to the dynamic power consumption. The minimum voltage to turn on a NEM switch is limited by its pull-in voltage (usually 5-50 V), when no DC bias is applied. The large actuation voltage and the resulting high dynamic power consumption greatly undermine the advantage of NEM switches over semiconductor devices in the OFF-state leakage. Reducing the pull-in voltage, therefore, has been the focus of researches in this field for decades.

The pull-in voltage corresponds to the drive voltage to achieve the critical switch gap, below which the nonlinear attractive forces (including the electrostatic force and surface adhesive force) suddenly overwhelm the linear restoring force from the deformed electrode. A smaller switch gap in the OFF-state leads to enhanced attractive forces as well as reduced displacement required for the active electrode to turn on, which thereby lowers the pull-in voltage. Electrostatic force microscopy enabled characterization of a nanoswitch based on a single-walled carbon nanotube (CNT) bundle, and a 2 V actuation voltage was demonstrated when the air gap was reduced to 6.5 nm [28]. In a lateral design, a multi-walled CNT acted as a mask for self-aligned patterning of the side electrodes, which led to a small switch gap and a 3.6 V pull-in voltage [29]. The smallest pull-in voltage (400 mV) reported so far for bias-free NEM switches was achieved by a so-called pipe clip structure [21]. The success was largely attributed to a fabricated 4-nm-thick air gap, a small contact and a large overlap area between the active electrode and the stationary electrode to induce a high electrostatic force.

Reducing the stiffness of the active electrode is also effective in lowering the pull-in voltage, through geometry tuning and/or material selection for the electrode. However, the decreased restoring force as a result of the more compliant moving contact may cause the NEM switch to be more susceptible to stiction failure. A U-shaped

NEM switch with 5 $\mu$m dual silicon (Si) nanowires was able to demonstrate an average pull-in voltage of 1.12 V but only survived 12 cycles [30]. A lateral NEM switch based on an ultrathin, long silicon carbide (SiC) nanowire active electrode as well as a small switch gap exhibited a minimum actuation voltage at 1 V level, but the subthreshold swing was large [31].

Although achieving a low pull-in voltage without sacrificing the device reliability still remains a challenge, introducing an auxiliary body electrode and applying a DC bias may allow NEM switches to operate under a small gate voltage, as an additional electrostatic force is induced by the DC bias to bring the active electrode close to the stationary electrode and reduces the switch gap. In this scenario, the minimum actuation voltage without observing any stiction failure under a proper DC bias is limited by the hysteresis of the $I$-$V$ characteristic. The hysteresis originates from the instability from the pull-in phenomenon, and NEM switches without the abrupt switching behavior usually exhibit little or no hysteresis [31–33]. In addition to reducing the switch gap and/or increasing the stiffness of moving electrode to achieve a lower hysteresis, a small contact area and an antistiction molecular coating on the electrodes can significantly lower the surface energy and thereby reduce the hysteresis. Sub-50 mV logic has been demonstrated by a NEM relay that features small dimple contacts, an antistiction coating on the surface of the electrodes, and a large body electrode to apply >10 V DC bias [34]. High uniformity in device performance is essential to ensure reliable switching at such a low voltage when an identical DC bias is applied to all NEM relays in an integrated circuit.

**Large switching delay**

The switching delay characterizes the computational capability of logic devices. Unlike semiconductor devices, NEM switches operate based on mechanical motion of active electrodes and therefore exhibit high switching delays (usually above 100 ns) [25, 35], which is a great weakness compared with semiconductors. In order to reduce the switching delay, a small switch gap is favorable, as the time needed to close and open the gap is short. Besides, a large gate area results in a large electrostatic

force that drives the moving component to switch on quickly; a stiff active electrode brings about a large restoring force and is thus favorable for fast switch-off. Reducing the mass of the active electrode is another effective way to achieve fast switching. In addition to these design considerations to tune the switching speed, operating the switch with an increased voltage leads to a higher acceleration and a shorter turn-on delay at a cost of unfavorably higher dynamic power consumption.

Nanomaterials have become increasingly popular to be employed as the active electrodes due to their small dimensions, light-weight feature and high stiffness. To date, NEM switches based on small gaps and nanomaterial-based active electrodes have been developed to achieve a fast switching speed. A turn-on delay of 10 ns was demonstrated by a NEM switch with a multi-walled CNT cantilever [36], when a ∼25 V drive voltage was applied. In another design that utilized a graphene cantilever, 25 ns was reported under a similar drive voltage [37]. These low turn-on delays suggest a 100 MHz operation regime for NEM switches employing nanomaterial-based active electrodes, which is much faster than classical NEM switches based on cantilever or relay architectures [24, 35]. The highest switching speed reported so far was achieved by a nanoswitch based on a suspended single-walled CNT [33]. A 2.8 ns delay was experimentally measured under a drive voltage as low as 5 V.

#### Poor device reliability

Poor reliability has been a longstanding challenge facing NEM switches. To make NEM switches a viable technology, prevalent failure modes must be studied, which will inform designs of NEM switches to greatly extend the lifecycles. In general, NEM switches of all kinds risk either structural failure or permanent stiction. In many cases, structural failure is caused by stress-induced fracture or fatigue [24, 31, 38, 39]. In other cases, surface wear, ablation, and even burn-out of electrodes can be attributed to transient or accumulative Joule heating induced by electrical discharge or high contact resistance [40]. Though the electrodes may survive structural damage, repetitive switching is likely to cause severe heat generation to weld the electrodes and thus leads to permanent stiction [30, 41]. At the nanoscale, poor heat dissipation

exacerbates these heating-induced issues. For non-memory nanoswitches, another prevalent cause for permanent stiction is the strong van der Waals interaction [33, 42] between electrodes in contact. When the van der Waals force is higher than the restoring force from the deformed electrode in the ON-state, the electrodes in contact cannot be separated even under zero voltage, and the NEM switch fails due to permanent stiction in this case. Though reducing contact area may lower the surface adhesive force and thus the probability of stiction failure, NEM switches based on nanoparticles such as CNTs are still susceptible to permanent stiction, and it has been revealed that stiction-free design window to maintain a low actuation voltage shrinks as the size of the NEM device scales down [43].

To avoid structural failure, metals with superior mechanical and thermal properties (e.g., tungsten) can be used as electrode materials [35], and protective coating with a thin oxide layer [40] or noble metals (e.g., platinum) [44] results in enhanced hardness, better heat and wear endurance as well as improved resistance to air exposure, corrosion and chemicals for the electrodes. To deal with concerns for permanent stiction, a stiff active component in a non-memory design is desired but could lead to a high actuation voltage. Besides, a NEM switch can be designed to work in non-contact mode [45] to eliminate the stiction issue. Another versatile approach to avoid stiction is through modifying the contact interface. This includes changing the materials [36, 46–48] or the roughness [49] of contact surfaces. Surface modifications by chemical approaches have also been explored [49]. Particularly, coating a monolayer of fluorinated molecules onto the surface of metal electrodes can effectively reduce the surface energy and avoid direct contact between metal electrodes [34].

### Scalable manufacturing

Nanoparticles and nanoparticle ensembles are attractive building blocks for designing NEM switches, as they enable ultra-small device pitches and bring about enhanced performance over their classical counterparts. However, circuit-level operation of nanomaterial-based NEM switches has not been demonstrated so far, primarily due to the absence of a universal and scalable manufacturing technique [4].

In general, the deposition of nanoparticles is constrained to just a few methods. Nano-manipulators [38, 46, 50] have been widely used to position individual nanoparticles, but such a method is not suitable for scalable manufacturing. Another straightforward approach is by randomly dispensing nanoparticles first and then finding individual nanoparticles for subsequent processing [29]. However, the demanding sorting process and the stochastic distribution of nanoparticles cause great challenges for circuit layout. Although the affinity between some nanoparticles and specific chemical terminations of pre-patterned molecular layers has been leveraged to achieve self-assembled nanoparticles after dispensing nanoparticle suspension [51], the yield for trapping individual nanoparticles on each spot was unclear. Another self-aligning approach is catalytic chemical vapor deposition (CVD). The pre-patterned catalysts on the substrate determine the position and orientation of synthesized nanoparticles. Though this method has enabled controlled deposition of individual CNTs [8,33,52], ensembles [48,53] or even arrays at the wafer-scale [54], it may not be suitable for nanoparticles that are not compatible with CVD process (such as many metallic nanoparticles). A more versatile approach to deposit nanoparticles is AC dielectrophoretic trapping [45, 55–58]. A high-frequency AC electric field induces a strong dielectrophoresis force that overcomes drag force and Brownian motion to trap nanoparticles onto the electrodes, given a proper contrast in the dielectric constant between the nanoparticle and the suspension liquid. Though high-yield scalable trapping has been demonstrated with long Si nanowires [58], the yield for trapping other kinds of nanoparticles with much reduced dimensions has not been reported. So far, a versatile and scalable method for nanoparticle deposition and assembly with a high yield receives broad interest and great demand, but still remains an open issue.

### 1.2.3 Outlook

Over the past two decades, great effort has been expended to address individual challenges for NEM switches. Ultra-low operating voltages and short turn-on delays were demonstrated separately based on high-performance nanomaterials and delicate device architectures; a NEM switch that simultaneously achieves a low operation volt-

age and a high-speed switching, however, is still absent. The simultaneous achievement of low-voltage and high-speed switching requires both reversible modulation of a nanometer-scale switch gap and an ultra-small, lightweight active component. To define a stable and reversible nanometer-scale switch gap, molecules can be incorporated into NEMS design as active nanostructures. Beyond working as a simple anti-stiction spacer, the self-assembled molecular monolayer is able to define a stable 1∼3 nm thick switch gap and each molecule could function as a nanoscale spring to allow reversible modulation of the gap. Additionally, nanoparticles make perfect candidates for miniaturized, lightweight active electrodes for NEM switches and thereby enable ultra-fast switching. Significantly, the coexisting molecules and nanoparticles in a device architecture may serve as two degrees of design freedom to independently tailor the static and dynamic characteristics of NEM switches. This further represents a universal strategy to achieve enhanced performance for diverse electromechanical devices and systems.

Assembling nanomaterials into functional devices requires nanometer-scale or even atomic precision in processing. Therefore, novel nanofabrication techniques that combine chemical synthesis, surface engineering, self-assembly and manipulation of nanomaterials are indispensible for precisely defining the active nanostructures. Particularly, development of these nanofabrication techniques in a versatile and scalable fashion has become more important than ever, given the growing diversity and amount of active nanostructures in the design of nanoelectronic devices nowadays. Advances in this field will greatly increase the throughput and thereby allow statistical learning of device behavior, optimization in the device performance, and large-scale device integration into circuits and systems.

## 1.3 Acoustically-Active Surfaces

### 1.3.1 Overview of Acoustic Transducers

Acoustic transducers are vibration-based electromechanical devices operating in the audio, ultrasound or infrasound frequency range that are able to convert between sound vibrational energy and electrical energy. According to the type of electroacoustic transduction, acoustic transducers are mainly categorized into speaker (emitting sound using electrical energy), microphone (receiving sound and turning it into measurable electrical signal) or ultrasonic transducers (transmitting ultrasound and receiving reflection).

Loudspeakers can be designed based on different mechanisms. The most prevalent types include electrodynamic speakers [59], piezoelectric speakers [60–62], electrostatic speakers [63], magnetostrictive speakers [64], etc. A dynamic speaker utilizes a moving coil driven by electromagnetic force to displace a diaphragm and generate sound. Such a speaker can produce high sound level with great accuracy within a certain frequency range. Two or more dynamic drivers are usually employed in the same commercial loudspeaker to evenly cover a wide audio frequency range. A piezoelectric speaker works based on converse piezoelectric effect. The applied electric field induces strain in a pre-polarized piezoelectric diaphragm and thereby causes it to deflect. These speakers are compact and cost-effective, but typically have an inferior low-frequency response compared to dynamic speakers. An electrostatic speaker uses a thin, charged metal membrane as the diaphragm, which is displaced by an electrostatic force induced by a high electric field. These speakers provide good linearity and low distortion, but the diaphragm excursion is limited due to structural constraints (i.e., small separation between the diaphragm and the stationary electrode for high electrostatic force). A magnetostrictive speaker produces sound by magnetic-field-induced vibration of magnetostrictive materials, and typically has large driving force, low distortion, and good robustness.

Among microphone technologies based on diverse mechanisms, condenser microphones (also known as capacitor microphones or electrostatic microphones) are the

most widely used type. A condenser microphone could be built based on a thin conductive film as diaphragm [65], which is deflected by incident sound. This causes a change in the capacitance formed between the diaphragm and the stationary plate. As the charge remains nearly constant within the timeframe of the capacitance change, the acoustic pressure incident on the microphone can be sensed by the alternating voltage signal across the capacitor. In another type of condenser microphone, the diaphragm is replaced by a polarized ferroelectric material and DC-bias is no longer required. However, the performance of these inexpensive electret-condenser microphones is not comparable with that of DC-polarized condenser microphones in terms of noise level and quality. A dynamic microphone has a similar structure to a dynamic loudspeaker. Vibration of the diaphragm induced by incident sound moves a coil in the magnetic field built by stationary permanent magnet and produces a varying voltage across the coil by electromagnetic induction. Similar to a dynamic loudspeaker, a dynamic microphone with a single diaphragm does not respond linearly to the entire audio frequency range. As a result, several diaphragms responsive to different frequencies are combined in a dynamic microphone. A piezoelectric microphone relies on a piezoelectric film or plate as the active component. Incident sound induces charge across the electrodes based on the piezoelectric effect, and the charge can be sensed after amplification and correlated to the acoustic pressure. These microphones usually have high impedance and are sensitive to handling noise.

Ultrasonic transducers typically refers to devices that are capable of both transmitting ultrasound and sensing the echo. According to this limit, ultrasonic transducers are mainly piezoelectric-type or condenser-type. When separate transmitters and receivers are allowed in specific scenarios, other types of transducers may also apply. For instance, magnetostrictive transducers can produce ultrasound as transmitters, but they are unable to sense the echo. Ultrasonic transducers provide highly accurate point-to-point distance measurement based on the time-of-flight between the transmitted ultrasound and the echo, assuming a known speed of sound in the medium. Moreover, an array of ultrasonic transducers can be employed for motion detection, and locating or imaging objects.

### 1.3.2 Prospects for Acoustically-Active Surfaces

The upsurge of IOT has created fast-growing demands and in the meantime more stringent requirements for acoustic transducers. Their applications are no longer constrained to simple sound generation and sensing, or distance measurement, but start to penetrate into scenarios such as industrial automation, artificial intelligence, robotics, smart homes, intelligent transportation, consumer electronics and biomedical engineering, where sound may act as an important medium for sensing and communication (Figure 1-2). Even in conventional scenarios, growing interests in free-field active noise cancelling and personal entertainment create demand for array of speakers and microphones coordinated with adaptive algorithms to realize beam forming and directional sound generation in the audio frequency range, which is beyond the reach of commercial loudspeakers or stereo audio systems at present. Therefore, multifunctional acoustic films that integrate arrays of diverse acoustic transducers may cater to the demand in the aforementioned scenarios. When these films are designed to be wide-area, transparent, paper-thin, flexible and robust, they can be mounted on the surfaces of various objects in an inconspicuous way and thereby render them acoustically active. The possibility of manufacturing these acoustic thin films in mass volume at low costs further adds to their popularity.

#### Active noise cancelling

Active noise cancelling is a method of reducing unwanted sound (noise) based on destructive interference through emitting a sound wave with the same amplitude but inverted phase to the noise. When the anti-noise speaker is positioned at/near the noise source, full-space noise reduction can be achieved but requires anti-noise sound with the same audio power level as the noise. A more energy-efficient approach is to reduce the noise locally, e.g., commerical noise-cancelling earbuds/headphones. Specifically, the noise signal is captured by microphone(s) located at the user's ear. An anti-noise signal is produced based on the adaptive algorithms [66,67], and further amplified to achieve desired attenuation at the user's ear. However, reducing ambient

noise in the free field is more complicated and expensive than in a small cavity (e.g., a user's ear) due to several reasons. First, the larger volume allows more frequency components to have nodes in the protected zone compared to in a small cavity, which increases the difficulty of reducing high-frequency noise. For instance, a 1 kHz noise may be perfectly cancelled at one spot but reinforced at ∼17 cm away along its direction of propagation. Second, multiple speakers with the same orientation may be insufficient to produce anti-noise sound to match the 3D noise pattern in the zone to be protected, especially when multiple frequency components are involved. Third, microphone(s) may not be available at spots of interest (users' ears), and the case could be even worse when the spots are not stationary (e.g., a moving person).

Wide-area, pixelated acoustic surfaces arranged along different orientations are more likely to realize noise cancellation in the free field, leveraging sufficient design freedom offered by the large amount of acoustic transducers deployed over a wide area. Specifically, the transducers may be divided into three groups to perform different roles, acting as ultrasonic transceivers to locate user's ears, or as microphones to detect sound at different spots in the surrounding area to reconstruct the noise at

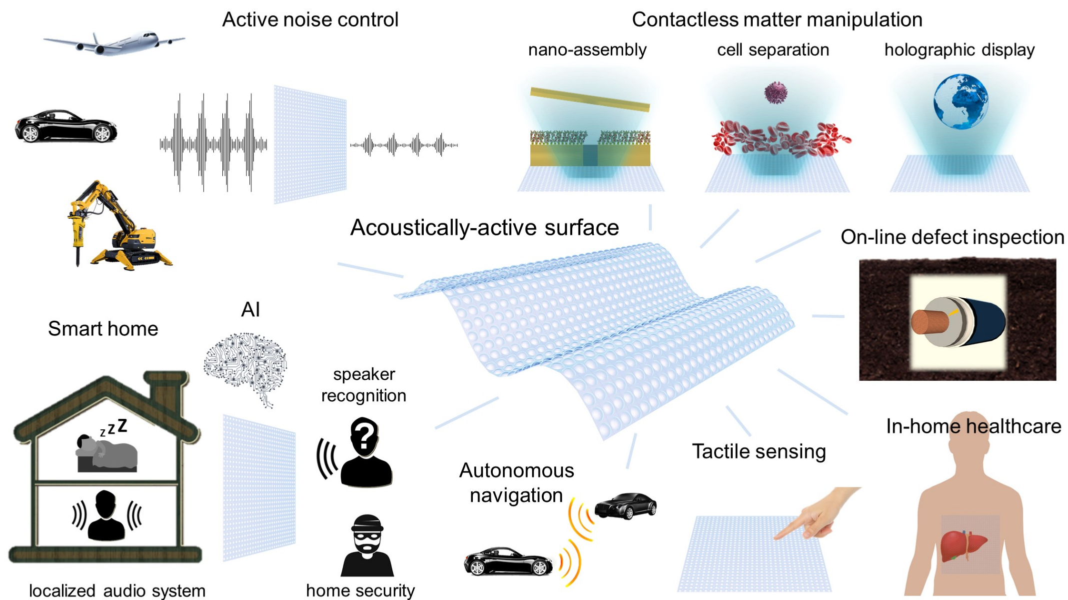


Figure 1-2: Application prospects of acoustically-active surface technology

the ears, or as loudspeakers to produce anti-noise sounds according to the adaptive cancellation algorithm. Such free-field active noise control has great prospects for both commercial and residential application scenarios. Reducing noise in aircraft and automobile cabins greatly improves the comfort of travelling. When acoustic surfaces are mounted on windows, curtains and/or walls in an apartment/office, noise from traffic and construction on the street, or renovation from neighbor apartments/offices can be well isolated, thereby creating a quiet environment for work, study and rest.

**Smart homes**

In a smart home scenario, various interconnected sensors and remotely-controllable appliances allow users to live with convenience, quality, security and cost-efficiency. A wide-area acoustic wallpaper with an acoustic transducer array could contribute to the concept of a smart home from multiple aspects, including entertainment, communication and home security.

Widely-deployed acoustic surfaces inherently create a surround-sound audio system in a cost-effective way. In addition, the large number of transducers can be grouped into blocks of loudspeakers through external electrical connections. When their dimensions are comparable or larger than the wavelength respective to the pitch of music, directionality of sound generation could enable personal entertainment without disturbing others. The same concept extends to other public scenarios such as offices, vehicles and aircrafts, etc. Microphones and loudspeakers from ubiquitous acoustic wallpapers also provide device-free communication among family members in different rooms and convenient voice control of smart appliances and robots virtually anywhere in a house. Acoustic surfaces mounted on the door and exterior of the house substantially contribute to the home security system. Visitors can be recognized as friends or strangers by comparing their voice patterns [68, 69] with the library in the home security system. The transducer arrays on the acoustic wallpapers installed on the exterior of the house are capable of detecting moving objects. The home security system further analyzes the data and alerts the owner instantly if there is a high security risk (e.g., detecting signs of an imminent break-in).

### Contactless matter manipulation

The transducers in an array on an acoustic surface are able to function as phased ultrasound emitters to generate acoustic radiation forces, which can be utilized to trap, levitate and position particles in various media [70–72]. The so-called "acoustic tweezers" provide unique characteristics including high trapping forces per unit power and abilities to manipulate various materials (e.g., biomolecules, cells, organic and inorganic nanomaterials) with dimensions ranging from sub-1-micrometer scale to centimeter scale [70, 73, 74].

The capability, versatility, and efficiency of this technique, enabled by wide-area, pixelated acoustic surfaces, give rise to broad application prospects. Nanoparticles in suspension can be selectively trapped and positioned independently to realize 3D assembly into diverse patterns [75], which provides a novel approach to build functional devices or systems using nanoscale blocks. This technique has also enabled an attractive platform in biomedical engineering for separation and manipulation of cells and particles, which have different densities and compression strengths, for life science research and diagnosis in medical clinics [73, 76]. The inherent capability of ultrasound to act through skin and tissue even allows noninvasive in-vivo treatments [77], which could be realized using a paper-thin pixelated acoustic surface adhered on skin. Additionally, acoustic radiation forces can be utilized to create microgravity environment for melting and solidifying materials confined only by surface tension [78]. This container-less processing is contaminant-free and permits solidification in undercooled melts, thereby resulting in unique microstructures and unusual properties. In addition, a wide-area acoustic surface could enable volumetric displays, where levitated voxels are moved by acoustic waves in high speed and form holographic images in 3D [13, 72].

### Autonomous navigation

Ultrasonic transceivers have been widely adopted for ranging based on time-of-flight or measuring velocity of target objects based on Doppler effect. Ultrasonic transducers,

as common proximity sensors, play an important role in current automobile driver-assistance systems (e.g., parking assist, adaptive cruising) and potentially in future autonomous driving as well [79]. A sound navigation and ranging (Sonar) system for automobile is cost-effective, independent on weather, and much more compact compared to alternative technologies based on radio waves (Radar) or light (Lidar). Particularly, acoustic surfaces with ultrasonic transducer arrays may bring about a few key advantages to the Sonar system. Paper-thin, transparent acoustic surfaces mounted on the exterior of vehicles cause the minimum appearance change. The great amount of ultrasonic transducers deployed over a wide area could provide high accuracy in 3D mapping of the surrounding environment as well as speed measurement of vehicles nearby. Moreover, part of the acoustic surfaces can be used to communicate with other autonomous vehicles (by emitting and receiving acoustic waves) in order to exchange cruise information, avoid collision due to non-consensus decisions, and alert others nearby when the vehicle is malfunctioning or uncontrollable. The acoustic surfaces with ultrasonic transducer arrays could also equip robots and underwater vehicles with Sonar skins for exploring unknown and unstructured environment [80].

**Tactile sensing**

Tactile sensing refers to measuring characteristics such as normal or shear forces, vibration, shape, texture, softness through physical contact [81]. Tactile sensors, based on their operating principles, can be categorized as capacitive sensors, piezoresistive sensors, piezoelectric sensors, inductive sensors, optical sensors, strain gauges, ultrasonic transceivers, multi-component sensors, and so on [81, 82]. Though tactile sensing has been an active research field for decades, none of the aforementioned techniques have gained prominence in industrial and commercial markets; array design and algorithms, spatial resolution, frequency response, cost, conformity, assembly and maintenance are among the key roadblocks to address before tactile sensing can fulfill its potential in disciplines of robotics, biomedical engineering, processing automation, and consumer electronics [81]. Acoustic surfaces with pixelated transducers intrinsically satisfy the demand for array design with a high spatial resolution and control

algorithms, and thereby may function as electronic skins for specific tasks (e.g., sensing vibration, force, shape, texture). In particular, acoustic surfaces designed based on piezoelectric polymers could offer additional merits including high sensitivity, good high-frequency response, large dynamic range, bio-compatibility, low-cost and good stability.

### 1.3.3 Demand and Challenges

Overall, an ideal acoustic surface should be wide-area, robust, thin and flexible, constructed with an array of active microstructures that can function individually or cooperatively for a multitude of applications. Tuning the design of these microstructures achieves task-centered performance; mixing active microstructures based on diverse designs leads to a multifunctional acoustic surface. These demands constitute the criteria to evaluate candidate technologies and also bring about challenges for the design and fabrication of acoustic surfaces.

#### Sensitivity

Sensitivity, as one of the most important metrics, characterizes the loudness of sound production under unit drive voltage (for a loudspeaker) or the output signal level under unit incident acoustic pressure (for a microphone). Commercial loudspeakers, for example, can produce above 100 dB SPL at a half meter way under 50 Hz−15 kHz with harmonic distortion $<10\%$. The average diaphragm displacement at low frequencies reaches the millimeter scale. In comparison, displacements of acoustic surfaces could be greatly restricted when they are adhered to walls, car or aircraft interiors. Therefore, freestanding active microstructures are essential in order to achieve large displacements for individual transducers and high sensitivity for the entire acoustic surface. We should also be aware that the acoustic surfaces do not have to outperform commercial speakers and microphones in terms of sensitivity, as their unique features make them an irreplaceable option for various scenarios where current commercial products do not apply.

### Robustness

Active microstructures fabricated on ultra-thin films typically bring about large displacement under unit excitation. However, such microstructures have poor mechanical strengths and may be damaged or destroyed by external mechanical impacts. Adding protective frameworks or layers could improve their physical integrity, but should not affect the displacement of the active microstructures and the overall properties of the acoustic surface (e.g., flexibility, transparency). For outdoor applications, the acoustic surface should be insensitive to temperature and work reliably under various weather conditions.

### Scalability

Wide-area deployment is one of the most critical features of the acoustic surface. Though high-performance acoustic transducers can be engineered with exotic materials and sophisticated micro-/nano-fabrication processes, they may not be suitable to scale up for wide-area applications due to fabrication challenges and cost. For the acoustic surface that targets mass adoption, engineering a huge amount of active structures over a wide area demands for high-precision, high-throughput, low-cost processing, which is usually beyond the capability of conventional microfabrication techniques. This could be achieved through a combination of scalable thin-film manufacturing (e.g., roll-to-roll method) and microfabrication techniques (suitable for machining molds).

### Pixelation

Most target applications for the acoustic surface rely on control of transducers in an array through modulation in amplitude and phase of the drive voltages. Two factors should be considered in order to achieve good pixelation. First, each acoustic transducer should be well isolated with minimum crosstalk between adjacent pixels. Second, acoustic transducers with the same design variables should exhibit identical properties (including sensitivity, linearity, directivity and frequency-dependence),

which also ensures good consistency in the performance of acoustic surfaces from different batches. These could greatly simplify the design of control algorithms for modulating the pixelated transducers in various application scenarios.

### 1.3.4 Candidate Technologies for Acoustic Surfaces

A candidate technology for the multi-funcional acoustic surface should be reversible, which means a transducer can work as a speaker or as a microphone, or even an ultrasonic transceiver according to needs. Among the technologies overviewed in Section 1.3.1, electrostatic, piezoelectric, and dynamic transducers are reversible. Of these, the first two types are more likely to be integrated onto wide-area, paper-thin acoustic surfaces. Here, three potential solutions based on electrostatic or piezoelectric transduction (Figure 1-3) are discussed and compared.

#### Porous compressible film

An active microstructure for this solution, presented in Figure 1-3 (a), comprises a porous dielectric thin film sandwiched between metal electrodes deposited on both sides. For a speaker application, the porous dielectric film is compressed by an electro-

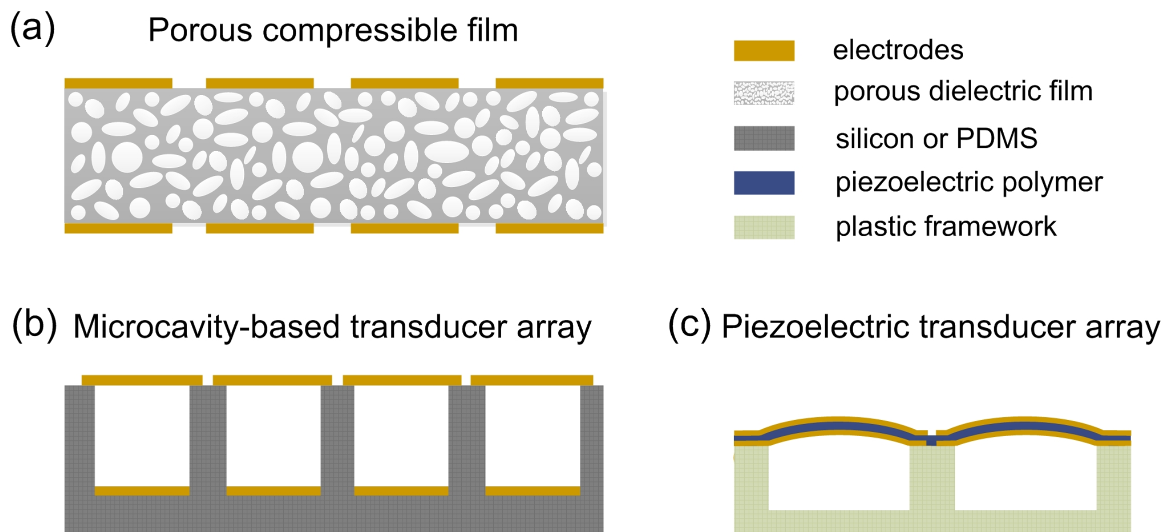


Figure 1-3: Candidate technologies for acoustically-active surfaces, including (a) porous compressible film, (b) microcavity-based transducer array, (c) piezoelectric transducer array.

static force induced by an applied voltage, which causes air displacement to generate sound; for a microphone application, a capacitance change is induced when the film is compressed by acoustic pressure, and correlated to the incident sound level.

Introducing pores into the material aims to greatly reduce the Young's modulus [83] and enhance the sensitivity of such a transducer. For instance, silica microshells can be fused together to form porous thin films. A Young's modulus as low as $\sim$1.5 GPa was achieved based on a porosity of 0.4 [84], as compared to $\sim$70 GPa for solid silica. In another example, porous compound based on polydimethylsiloxane (PDMS) and carbon black demonstrated a $\sim$50 kPa Young's modulus as compared to $\sim$8 MPa for solid compound [85]. Such a porous film can be easily prepared by mixing water soluble particles into an organic compound, which are dissolved afterwards by soaking the cured compound in water. The simple and scalable fabrication process constitutes a big advantage for this technology.

Despite the ultra-low Young's modulus, the thickness reduction of porous thin films and thereby the air displacement under unit excitation (drive voltage or acoustic pressure) are limited. For instance, the thickness change for a 1-$\mu$m-thick porous PDMS film at 10 V is estimated to be 0.1% or below. To compensate the low sensitivity, multiple layers of porous thin films can be stacked with electrode layers embedded in between to induce superposed air displacement at a cost of increased processing complexity. Another significant challenge lies in the pixel isolation based on such a continuous porous film, which may require additional processing (e.g., by laser scribing) to separate the pixels and minimize the crosstalk.

### Microcavity-based transducer array

The second solution utilizes active microstructures each comprising a thin metal membrane suspended on a microcavity (Figure 1-3 (b)). The sound production and sensing mechanisms are similar to those of the first solution, while the air displacement (for speaker application) or capacitance change (for microphone application) are caused by bending of the suspended membrane. A maximum deflection of 150 nm was achieved at the center of a 125-nm-thick circular gold membrane suspended on a 28-

$\mu$m-diameter, 400-nm-deep cavity, under a 15 V voltage applied across the membrane and the bottom electrode [86]. Such a deflection is equivalent to a 50 nm air displacement averaged over the circular membrane, which is over an order of magnitude larger than that based on a 1-$\mu$m-thick porous PDMS film under 15 V. Such microcavities can be patterned into an array on a flexible substrate such as PDMS [87]. The cavity size and depth as well as thickness of the membrane are important design variables for performance tuning and can be precisely defined through microfabrication.

This technology also has a few disadvantages. First, the maximum deflection of the membrane is constrained by the depth of the cavity. Increasing the depth is able to raise the limit, but a larger separation between the electrodes causes weakened electrostatic force, which is a prevalent tradeoff between the dynamic range and the sensitivity for electrostatic transducers. Second, when the air in a well-encapsulated cavity is compressed, the pressure difference inside and outside the cavity exerts a counteractive load on the membrane and impedes the deflection. Therefore, the cavity should be vented in some way to obtain balanced pressure, but adjacent cavities should be isolated to minimize the crosstalk. These considerations complicate the design and fabrication of microcavities. Third, scaling up this solution to produce wallpaper-size acoustic surfaces is challenging, as great difficulty is anticipated for transferring an ultra-thin metal membrane onto the microcavity array over a large area. The ultra-thin suspended membrane also casts doubt on the physical integrity of these devices.

**Piezoelectric transducer array**

When a piezoelectric acoustic transducer (Figure 1-3 (c)) performs as a microphone, polarization is induced by piezoelectric effect in response to incident acoustic pressure. The resulting charge accumulation or potential difference built on the electrodes of the transducer is amplified and sensed by peripheral circuits. For a speaker application, an applied voltage across the electrodes induces strain in the piezoelectric film. The strain results in vertical displacement when the piezoelectric film is either adhered to an inactive elastic layer (unimorph or bimorph structure) or designed into

a specific profile (e.g., spherical diaphragm). To date, piezoelectric ceramics such as lead zirconate titanate (PZT) have been widely utilized in ultrasonic transducers due to their outstanding piezoelectric responses. For application in the audio frequency range, a piezoelectric polymer such as polyvinylidene fluoride (PVDF) is more attractive due to its low stiffness, mass manufacturing at low cost and low-temperature processing, despite relatively low piezoelectric and dielectric constants compared to piezo-ceramics. When a PVDF film is molded to form a speaker with a spherical diaphragm, the dimensions and film thickness of the spherical diaphragm can be designed over a wide range, thereby leading to highly tunable sensitivity and dynamic range. Additionally, there is no fundamental constraint on the maximum displacement for these piezoelectric transducers. These constitute a big advantage over the other two candidate technologies. Moreover, the transparency, flexibility and compatibility with mass production at low cost inherent to piezoelectric polymers perfectly cater to the demands for the acoustic-surface technology.

Fabrication challenges should be addressed in order to fabriate high-performance piezoelectric transducer array. Freestanding piezoelectric microstructures are indispensible in design, since the vibration of a flat piezoelectric film can be greatly constrained when it is mounted onto a rigid surface (e.g., wall, car or aircraft interior). A good isolation between adjacent microstructures is essential when they are actuated in different phases or perform different roles (speaker, microphone, or ultrasonic transducers). Since the profile and dimensions are important tuning variables, high precision and good consistency are necessary for molding microstructures in a scalable fashion. In addition, the microstructures molded on an ultra-thin film should be well protected without affecting the sensitivity and other features (e.g., flexibility, transparency) of the acoustic surface.

### 1.3.5 Outlook

Challenges in the design and fabrication of a multifunctional acoustically-active surface must be overcome before its prospects can be fulfilled. Among the candidate technologies, the piezoelectric solution shows the most promise in consideration of the

sensitivity and the scalable, low-cost manufacturing. To date, piezoelectric polymers have been widely applied in microphones [88], loudspeakers [60–62] and ultrasonic transducers [89]. However, researches on wide-area acoustic devices are still limited. Eetta Saarimaki et al. developed a 15×15 cm$^2$ loudspeaker by bonding 8 layers of cyclo-olefin polymer, which demonstrated 10∼60 dB SPL (1∼10 kHz, 30 cm away) by applying a 80 V sinusoidal voltage [61]. A similar 12×12 cm$^2$ loudspeaker based on cyclo-olefin copolymer was developed by Wen-Ching Ko et al. and achieved 10∼80 dB SPL (100 Hz∼10 kHz, 1 m way) driven by a 70.7 V (RMS) voltage. In another work, a circular loudspeaker (25 mm in diameter) based on stacked fluoro-ethylene-propylene films achieved 10∼100 mPa (1∼10 kHz, 2 cm away, near field) driven by a 7.94 V (RMS) voltage [90], corresponding to 54∼74 dB SPL. However, these thin-film loudspeaker designs lack the potential for pixilation due to the absence of active microstructures. A wide-area acoustic surface simultaneously integrated with a microphone array, a speaker array, and an ultrasonic transducer array still remains unachieved.

Bulk piezoelectric polymers (PVDF or PVDF copolymers), piezoelectric composites and voided charged polymers are the most suitable options among candidate materials for the acoustic surface. For piezoelectric composites, single-crystal or ceramic piezoelectric nanoparticles can be embedded in polymers (e.g., PDMS) to achieve better flexibility [91, 92], and the reported piezoelectric constants for these composites are comparable to those of PVDF [92]. Voided charged polymers (also known as cellular electrets or cellular polymer) contain artificial dipoles (i.e., charged internal gas voids) and behave like piezoelectric bulk materials. Unlike bulk polymer or composite, the piezoelectric responses of voided charged polymers exhibit large frequency-dependence [93]. Quasi-static piezoelectric constants could reach up to 20000 pC/N (∼3 orders of magnitude higher than PVDF); though dynamic piezoelectric constants may decay with increasing frequency in the audio frequency range, they are still a few times higher than PVDF on average [94]. However, the piezoelectric constants heavily depend on the density and shape of the voids, and type and pressure of the gas inside the voids, which makes fabrication consistency a big

concern. Maintaining trapped charge over time is another challenge, particularly for high-temperature application. Therefore, a piezoelectric bulk polymer (e.g., PVDF) outperforms the other two types due to its good stability, consistent performance, easy and low-cost mass production. To fabricate a piezoelectric acoustic surface, an array of microstructures are molded into desired profile and dimensions over a wide-area PVDF film, and subsequently protected by an additional perforated plastic layer that is laminated to the PVDF film. The entire processing is compatible with roll-to-roll techniques, which allows high-throughput production of wide-area, flexible, robust, pixelated and even transparent acoustic surfaces.

## 1.4 Thesis Organization

As discussed, this thesis investigates a tunneling NEM switch and a wide-area acoustic surface as two cases to demonstrate the merits of active micro-/nano-structures for electromechanical actuation. Therefore, this thesis is divided into three parts:

**Part I: A Tunneling NEM Switch Using Molecular Springs and Nanoparticle Active Electrode**

Chapter 2 introduces the device concept and the theoretical modeling for device behavior. In this chapter, the critical roles of the molecules and the nanoparticle active electrode in tuning the static device behavior and the dynamic device behavior, respectively, are investigated.

Chapter 3 describes the nanofabrication of the tunneling NEM switch, including detailed steps for both a two-terminal architecture and a multi-terminal architecture. Challenges encountered during fabricating these NEM switches are reviewed and potential pathways to improve the yield and throughput are discussed.

Chapter 4 presents characterization of proof-of-concept two-terminal devices based on poly(ethylene glycol)thiol (PEG-thiol) molecules and gold nanorod electrodes, in terms of $I$-$V$ characteristic and turn-on speed. Further, the tunabilities afforded by the active nanostructures (molecule, nanoparticle) are demonstrated experimentally from the different $I$-$V$ characteristics and the turn-on speeds of devices employing

different molecular spacers and nanoparticle active electrodes.

Chapter 5 summarizes this part, describes future improvement of device performance, stability and fabrication, and discusses the potential of the proposed device architecture beyond energy-efficient logic application.

**Part II: An Acoustically-Active Surface Based on Piezoelectric Micro-Dome Array**

Chapter 6 introduces the device concept and establishes the theoretical modeling for actuation of a single piezoelectric dome, and sound generation of the entire acoustic surface. Theoretical modeling and simulation reveal tunabilities in acoustic performance afforded by designing the active microstructures.

Chapter 7 overviews conventional approaches for polymer processing, and describes our scalable fabrication method to create precise dome microstructures on a PVDF thin film through vacuum-induced micro-embossing. A self-aligned microembossing approach is further developed to obtain a robust acoustic surface with protected micro-domes.

Chapter 8 presents the characterization of individual piezoelectric micro-domes based on surface velocity measurement. A comprehensive study is conducted on the sound generation of the acoustic surface in terms of sensitivity, frequency response and directivity. The results also demonstrate sensitivity tuning from designing the active micro-domes.

Chapter 9 summarizes this part, reviews further improvement on microstructure design and fabrication, and presents an outlook on potentials of the acoustic surface that have not been covered in this thesis.

**Part III: Epilog**

Chapter 10 concludes this thesis with a brief discussion of the scheme of engineering high-performance electromechanical devices and systems based on active micro-/nano-structures, demonstrated by the two case studies in the thesis.

# Chapter 2

# Theoretical Modeling of Tunneling Nanoelectromechanical Switch

## 2.1 Device Concept

Molecules as active nanostructures can be assembled into an organic thin film over a specific area and sandwiched between a pair of electrodes to form a nanometer-scale molecular gap. A voltage applied across the electrodes induces an electrostatic force to compress the molecular layer. As a result, the tunneling current through the molecular junction increases exponentially in response to the reduction in the thickness of the molecular layer. When the voltage is removed, the compressed molecules act as nanoscale springs to provide strong restoring force to recover the molecular spacer to its initial thickness.

The dependence of the tunneling current on the junction width is given by the Simmons model [95]

$$
\begin{aligned}
I = \frac{q_e S_t}{4\pi^2 \hbar g_t^2} \Bigg\{ & \left(\Phi - \frac{q_e V_t}{2}\right) \exp\left[-\frac{2(2m_e)^{1/2}}{\hbar}\alpha_t \left(\Phi - \frac{q_e V_t}{2}\right)^{1/2} g_t\right] \\
& - \left(\Phi + \frac{q_e V_t}{2}\right) \exp\left[-\frac{2(2m_e)^{1/2}}{\hbar}\alpha_t \left(\Phi + \frac{q_e V_t}{2}\right)^{1/2} g_t\right] \Bigg\},
\end{aligned}
\tag{2.1}
$$

where $\hbar$, $q_e$ and $m_e$ are the reduced Planck's constant, the electron charge and the

electron mass, respectively; $S_t$ is the area of the gap; $g_t$ is the distance across the gap between the electrodes (i.e., tunneling width); $V_t$ is the applied voltage; $\Phi$ is the tunneling barrier height of the molecular layer; and $\alpha_t$ is a parameter that corresponds to the effect of the barrier shape and the electron effective mass.

A numerical example that simulates the alkylthiol molecules, which have been widely investigated in metal-molecule-metal motifs, is provided in Figure 2-1. The tunneling current density $J_t$ is calculated as a function of the gap $g_t$ for different barrier heights $\Phi$, while the barrier parameter $\alpha_t$ and the applied voltage $V_t$ are kept constant as 0.57 and 1 V, respectively. The result shows that a mere $\sim$1 nm modulation in the junction width leads to an over 5-orders-of-magnitude contrast in the tunneling current density for a barrier height $\Phi = 4$ eV, which is sufficient to define the ON-state and the OFF-state. Therefore, a novel tunneling NEM switch can be developed based on electromechanical modulation of the molecular junction. Since only 1 nm displacement is needed for switching, the voltage and time to achieve this tiny displacement (namely turn-on voltage and delay) can be a lot smaller compared to those conventional NEM switches based on large switch gaps. Moreover, a conductive nanoparticle can be employed as a miniaturized active electrode, which favors an even faster switching speed.

The device architecture for a two-terminal tunneling nanoswitch using molecular springs is presented in Figure 2-2 (a). The nanoswitch consists of a pair of ultra-smooth bottom electrodes, a floating conductive nanoparticle top electrode and self-assembled molecular spacers in between. The functions of the self-assembled molecular layer are four-folds. Beyond serving as a scaffolding nano-block to hold the device and set the tiny switch gap, the self-assembled molecular layer also functions as nanoscale springs to enable reversible compression and prevent stiction between electrodes by providing a strong restoring force under compression.

In the OFF-state (Figure 2-2 (b)), the molecular layer is designed thick enough to ensure negligible leakage. When a voltage is applied across the two bottom electrodes, the potential difference between the floating electrode and the bottom electrodes creates an electrostatic force to compress the molecular spacer, exponentially increases

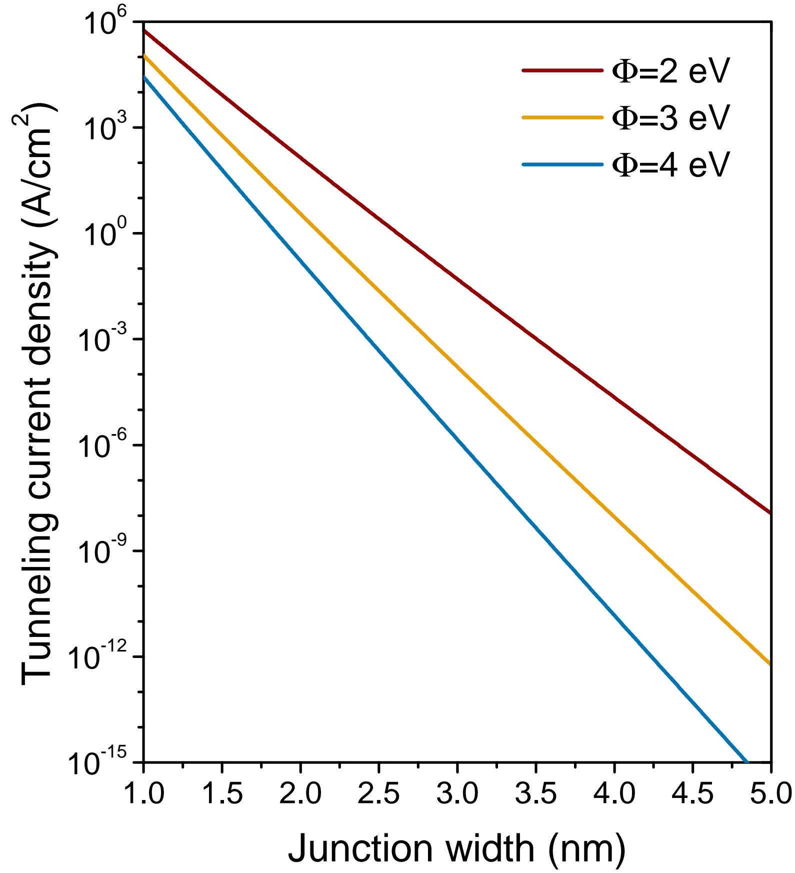


Figure 2-1: Tunneling current density as a function of junction width. The applied voltage and the barrier parameter are kept constant as 1 V and 0.57, respectively, in this example.

the tunneling current, and turns on the switch (Figure 2-2 (c)). Depending on the stiffness of the molecules, such a tunneling NEM switch can be designed with or without a pull-in phenomenon. When the voltage across the bottom electrodes is removed, the potentials of the floating electrode and the bottom electrodes are balanced and the restoring force from the compressed molecular spacer uplifts the nanoparticle and recovers the OFF-state.

Since the molecules and nanoparticles are key components of the tunneling nanoswitch, their properties can be leveraged to design the static and dynamic behav-

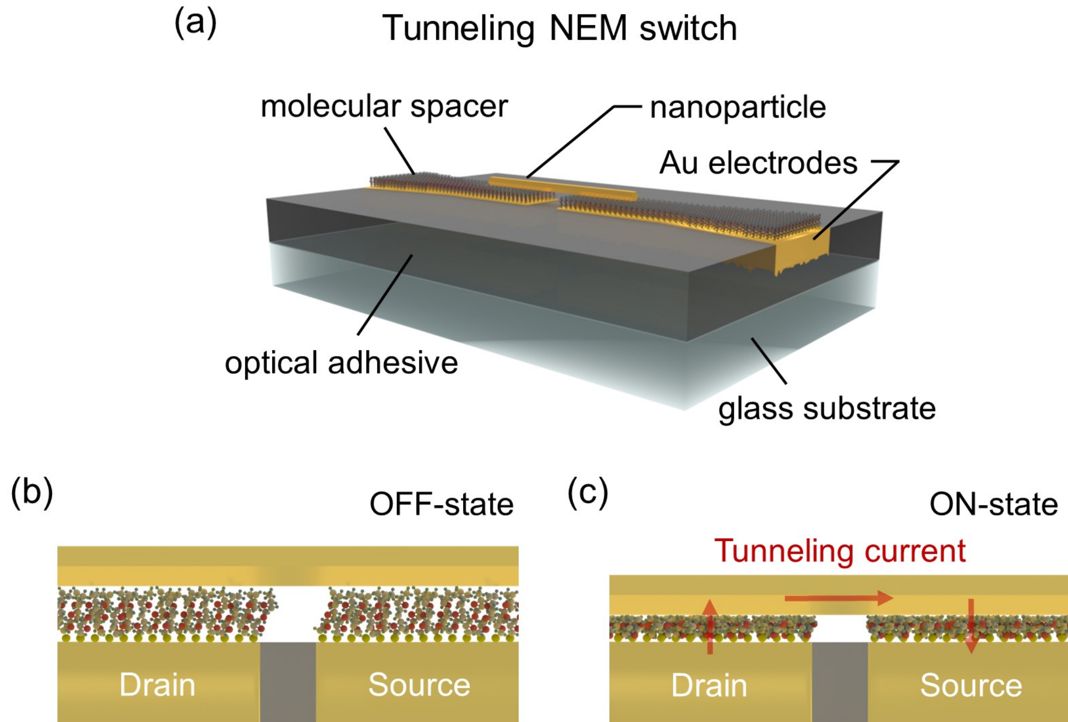


Figure 2-2: Schematic respresentation of the (a) architecture and the operating mechanism ((b) OFF-state and (c) ON-state) of the tunneling NEM switch using molecular springs.

ior of the nanoswitch. This chapter aims to develop models that describe the device behavior and its dependence on the properties of the molecules and the nanoparticles, which could inform designs of high-performance nanoswitch through engineering these nanoscale building blocks.

In this thesis, we focus mainly on a two-terminal architecture to study the device performance of this novel tunneling NEM switch and the tunabilities afforded by engineering the molecules and the nanoparticles as a result of the ease of fabrication. However, the device concept extends to multi-terminal NEM switches as well. Detailed nanofabrication processes for both two-terminal and multi-terminal architectures are discussed in Chapter 3.

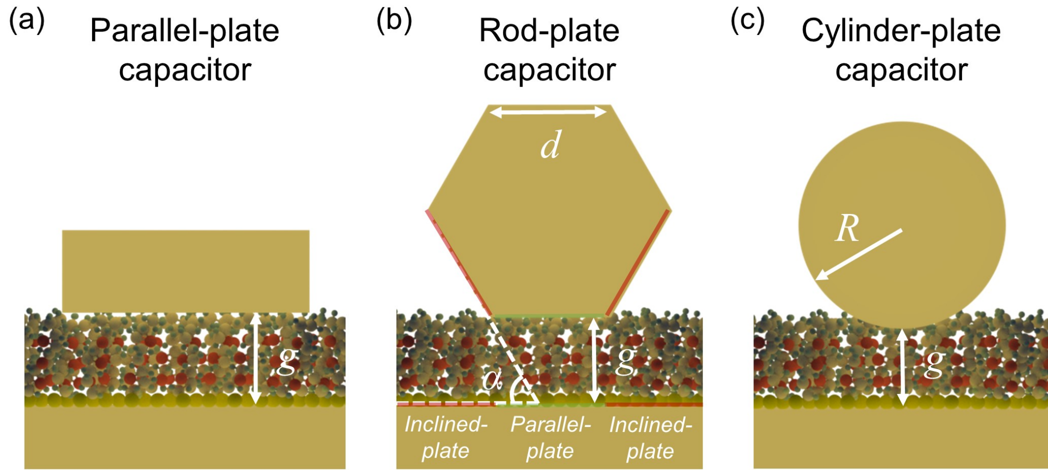


Figure 2-3: Schematics of the three types of capacitors formed by the nanoparticles, the molecules and the bottom electrodes. (a) Parallel-plate capacitor that models devices with nanoplatelets. (b) Rod-plate capacitor that models devices with nanorods. (c) Cylinder-plate capacitor that models devices with nanotubes.

## 2.2 Static Model

The modulation of the molecular layer thickness is critical to the device behavior. The variation of the spacer thickness is governed by balance of the electrostatic force induced by drain voltage, the adhesive force between surfaces of the nanoparticle and the bottom electrodes, and the repulsive force from compressed molecules.

### 2.2.1 Electrostatic Force

The electrostatic force depends on the geometry of the top and the bottom electrodes. When nanoparticles are employed for the floating top electrode, three types of capacitors are typically formed, as shown in Figure 2-3, including parallel-plate capacitor (graphene, metal nanoplatelets and nanoribbons), rod-plate capacitor (metal nanorods, Si nanowires), and cylinder-plate capacitor (CNTs).

The capacitance of a parallel-plate capacitor (Figure 2-3 (a)) is given by

$$C_{p-p}(g) = \frac{\epsilon_0 \epsilon_r S}{g}, \tag{2.2}$$

where $\epsilon_0$ is the vacuum permittivity, $\epsilon_r$ is the relative dielectric constant of the media (i.e., assembled molecular layer), $S$ is the overlap area of the parallel-plate capacitor, and $g$ is the gap between the plates (i.e., molecular layer thickness).

A rod-plate capacitor can be treated as two inclined-plate capacitors formed by the side walls of the rod and the bottom electrode in parallel with a parallel-plate capacitor formed by the bottom surface of the rod and the bottom electrode. Such treatment of rod-plate capacitor leads to its capacitance expressed as

$$C_{r-p}(g) = \frac{\epsilon_0 \epsilon_{r1} S}{g} + \frac{2\epsilon_0 \epsilon_{r2} L}{\alpha} \ln\left(\frac{g + d \sin\alpha}{g}\right), \tag{2.3}$$

where $L$ is the length of the rod, $\epsilon_{r1}$ is the relative dielectric constant of the media inside the parallel-plate capacitor, $\epsilon_{r2}$ is the averaged relative dielectric constant of the media ($1 < \epsilon_{r2} < \epsilon_{r1}$) inside the inclined-plate capacitors, and other geometric variables are defined in Figure 2-3 (b).

The capacitance of a cylinder-plate capacitor can be expressed by the typical wire-ground model [96] as

$$C_{c-p}(g) = \frac{2\pi \epsilon_0 \epsilon_r L}{\ln\left(\frac{R+g}{R} + \sqrt{(\frac{R+g}{R})^2 - 1}\right)}, \tag{2.4}$$

where $L$ is the length of the cylinder, $\epsilon_r$ is the relative dielectric constant of the media, and other geometric variables are defined in Figure 2-3 (c).

For any type of capacitor, the electrostatic force $F_e$ can be obtained by the derivative of the stored energy $E$ on the capacitor,

$$F_e(g) = -\frac{V^2}{2} \frac{\mathrm{d}C(g)}{\mathrm{d}g}, \tag{2.5}$$

where $C$ is the capacitance, $V$ is the voltage applied across the capacitor, $g$ is the gap between the electrodes of the capacitor. Considering that the dimensions of the nanoparticle used as the top electrode are much larger than the gap, we can make approximations for the electrostatic force.

For nanoswitches with a nanorod floating electrode (rod-plate capacitor), we consider typical pentagon ($\alpha = 72°$) or hexagon ($\alpha = 60°$) cross-section for the nanorod. Since side length of the nanorod (e.g., $d = 40 \sim 50$ nm) is much larger than the gap between electrodes (typical molecular layer thickness $g = 1 \sim 3$ nm), the electrostatic force induced on each of the two inclined plate capacitors is given by

$$F_{side}(g) = \frac{\epsilon_0 \epsilon_{r2} d L V^2 \sin\alpha}{2\alpha g(g + d\sin\alpha)}. \tag{2.6}$$

Since $d \sin\alpha$ is much larger than $g$, we have

$$F_{side}(g) \approx \frac{\epsilon_0 \epsilon_{r2} L V^2}{2\alpha g}. \tag{2.7}$$

Therefore, the overall electrostatic force becomes

$$F_e(g) = \frac{\epsilon_0 \epsilon_{r1} L d V^2}{2g^2}\left(1 + \frac{2\epsilon_{r2} g}{\epsilon_{r1} \alpha d}\right). \tag{2.8}$$

Considering $1 < \epsilon_{r2} < \epsilon_{r1}$, and $\alpha d/g \gg 1$ for typical nanoparticle dimensions,

$$F_e(g) \approx \frac{\epsilon_0 \epsilon_{r1} L d V^2}{2g^2}. \tag{2.9}$$

This approximation yields the same expression of electrostatic force for both nanorod particle and nanoplatelet particle.

For nanoswitches with a nanotube top electrode, the capacitance of cylinder-plate capacitor can be approximated by taking the 1st-order Taylor expansion of the denominator, when the radius of the nanotube, $R$, is much larger than the thickness of molecular layer, $g$, which yields

$$C_{c-p}(g) \approx \pi \epsilon_0 \epsilon_r L \sqrt{\frac{2R}{g}}. \tag{2.10}$$

The electrostatic force therefore becomes

$$F_e(g) \approx \frac{\pi \epsilon_0 \epsilon_r L V^2 \sqrt{2gR}}{4g^2}. \tag{2.11}$$

Comparing (2.9) and (2.11), the electrostatic forces experienced by nanorod and nanotube of the same diameter and length are different by a factor of $\pi\sqrt{g/(2R)}$. Considering an example that a gold nanorod and a multi-walled CNT both have a diameter of 100 nm, the electrostatic force induced on the CNT is approximately half of that on the gold nanorod, assuming that the molecular layer thicknesses for both devices are identical as 2∼3 nm. However, a nanotube particle like CNT is likely to sink a bit into the molecular spacer after trapping due to its curvature, resulting in a gap $g$ smaller than that for a nanoswitch with a nanorod particle which has single-crystal flat facet. Besides, the restoring force on a nanotube particle may be weaker compared to those on the nanoparticles with single-crystal flat facets, as molecules underneath the nanotubes are likely compressed and those near the edges of the nanotubes are likely pushed aside. These factors compensate for the smaller electrostatic drive force and therefore result in similar actuation voltages for nanoswitches based on nanotubes and nanorods with the same dimensions. For convenience, the electrostatic force expression for nanoplatelets is adopted in the static and dynamic models in this chapter.

### 2.2.2 Adhesive Force

The adhesive forces in general consist of Casimir force and van der Waals force. When the gap is smaller than 10% of the plasma wavelength of the metal, the van der Waals force dominates the adhesive forces [97]. For a tunneling switch with a 1∼3 nm thick molecular gap, it is reasonable to ignore the Casimir force, considering that the plasma wavelength of Au is 136 nm [97].

The van der Waals interaction energy between two metallic atoms is given by

$$w_{vdW}(r) = -\frac{C_L}{r^6}, \tag{2.12}$$

where $C_L$ is the coefficient in the particle-particle pair interaction, and $r$ is the separation between the two metallic atoms. The interaction energy between a single atom and a plate (plate 1) can be obtained through integration over the volume of the plate as

$$\mathrm{d}W_{vdW}(z) = -\frac{\pi\rho_1 S_1 C_L}{6z^3}, \tag{2.13}$$

where $z$ is the distance between the atom and the plate, and $\rho_1$, $S_1$ are the density of atoms and area of the plate 1, respectively. Therefore, the interaction energy between two metallic plates (plate 1 and plate 2) can be obtained by integrating the atom-plate interaction energy over the volume of plate 2, which is

$$W_{vdW}(g) = -\frac{\pi\rho_1\rho_2 S_1 S_2 C_L}{12g^2}, \tag{2.14}$$

where $g$ is the distance between the two plates (i.e., switch gap), and $\rho_2$, $S_2$ are the density of atoms and area of the plate 2, respectively. Therefore, the unit area interaction energy is given by

$$E_{vdW}(g) = -\frac{\pi\rho_1\rho_2 C_L}{12g^2}. \tag{2.15}$$

The derivative of this interaction energy results in unit area van der Waals force

$$f_{vdW}(g) = \frac{\pi\rho_1\rho_2 C_L}{6g^3}. \tag{2.16}$$

As a result, the adhesive force for the tunneling nanoswitch is approximated as

$$F_a(g) = \frac{A_H S_t}{6\pi g^3}, \tag{2.17}$$

where $S_t$ is the overlap area between electrodes (same as area of the molecular junction), and $A_H = \pi^2\rho_1\rho_2 C_L$ is the Hamaker constant that characterizes the van der Waals interaction between electrodes.

### 2.2.3 Restoring Force

Since molecules perform as nanoscale springs under compression, the restoring force on the nanoparticle electrode depends on the Young's modulus of the molecular layer. Under a linear molecule assumption, the Young's modulus is constant regardless of the compression. As a result, the restoring force is linear to the compression, given by

$$F_r(g) = \frac{E_m S_t}{d_0}(d_0 - g), \tag{2.18}$$

where $S_t$ is the overlap area between electrodes, and $E_m$, $d_0$, $g$ are the Young's modulus, the initial thickness (uncompressed state), the thickness under an applied drain voltage (compressed state) of the molecular layer, respectively.

However, such a linear-molecule assumption fails when the compression is above a threshold, and the molecules start to behave nonlinearly. The threshold compression depends on the molecular composition, order, and chain length, etc. For instance, 1-hexadecanethiol molecules exhibit an elastic response until over 25% compression [98], while the threshold compression for PEG-thiol macromolecules can be over 40% and increases with the chain length [99].

In our tunneling nanoswitch architecture, the electrodes are never in direct contact, which means the molecular layer is the only source to provide restoring force for maintaining force balance of the nanoparticle active electrode. Particularly for a nanoswitch designed with a pull-in phenomenon, the attractive forces (electrostatic force (2.9) and surface adhesive force (2.17)) that are nonlinearly dependent on the gap cannot be balanced with a linearly increasing restoring force in the ON-state. Therefore, nonlinear mechanics of the molecular layers in the ON-state are indispensable. To model the nonlinear elastic behavior of the molecular layer, a Young's modulus $E_m(g)$ that varies with compression should replace the constant $E_m$ in (2.18). Each kind of molecule has specific nonlinear elasticity. In most cases, the nonlinear Young's modulus can be expanded in Taylor series and thus approximated by a polynomial of

compression, given by

$$E_m(g) = \sum_{i=0}^{N} E_m^{(i)}(\frac{d_0 - g}{d_0})^i, \tag{2.19}$$

where $E_m^{(i)}$ is the coefficient for the $i$th-order polynomial term, and $N$ is the highest order. A higher $N$ represents increasing nonlinearity in the mechanics of the molecular layer.

### 2.2.4 Force Balance

The governing equation that describes the balance between the attractive forces (electrostatic force, adhesive force) and the restoring force for a tunneling nanoswitch in Figure 2-2 is

$$\begin{aligned} \frac{1}{2}\frac{\epsilon_0\epsilon_{rm}S_D}{g^2}(V_D - V_F)^2 + \frac{1}{2}\frac{\epsilon_0\epsilon_{rm}S_S}{g^2}(V_S - V_F)^2 + \frac{A_H(S_D + S_S)}{6\pi g^3} \\ - \frac{E_m(S_D + S_S)}{d_0}(d_0 - g) = 0, \end{aligned} \tag{2.20}$$

where: $\epsilon_0$ is the vacuum permittivity; $\epsilon_{rm}$, $E_m$, $d_0$, $g$ are the relative dielectric constant, the Young's modulus, the initial thickness (uncompressed state), the thickness under an applied drain voltage $V_D$ (compressed state) of the molecular layer, respectively; $S_S$, $S_D$ are the area of the molecular junctions on the source electrode and the drain electrode, respectively; $A_H$ is the Hamaker constant; and $V_D$, $V_S$, $V_F$ are the voltage potentials of the drain, the source, and the floating top electrode (i.e., nanoparticle), respectively.

Upon applying a drain voltage $V_D$, the charging currents through the two molecular junctions are identical. Here, the same potential $V_F$ is assumed along the entire floating nanoparticle, which is

$$V_F = \frac{C_D}{C_D + C_S}V_D + \frac{C_S}{C_D + C_S}V_S, \tag{2.21}$$

where $C_S$, $C_D$ are the capacitance of the molecular junction at the source electrode and that at the drain electrode, respectively. For a specific drain voltage $V_D$, the

molecular spacer thickness $g$ can be calculated by (2.20) given the parameters of molecules and electrode materials as well as dimensions of the molecular junctions. The tunneling current at drain voltage $V_D$ is further obtained using the Simmons model (2.1) with barrier parameters of the molecular junctions.

In a simplified case, we considered two identical junctions on the source electrode and the drain electrode, which results in $V_F = V_D/2$ when the source electrode is grounded. The force balance equation reduces to

$$\frac{1}{8}\frac{\epsilon_0\epsilon_{rm}}{g^2}V_D^2 + \frac{A_H}{6\pi g^3} - \frac{E_m}{d_0}(d_0 - g) = 0. \tag{2.22}$$

The theoretical $I$-$V$ characteristic of the tunneling nanoswitch can therefore be calculated within a specific range of drain voltage $V_D$. When the tunneling nanoswitch is designed with a pull-in phenomenon and free from stiction failure in the ON-state, the pull-in voltage $V_{pi}$ as well as the critical gap $g_{pi}$ can be calculated by solving

$$\frac{1}{8}\frac{\epsilon_0\epsilon_{rm}}{g_{pi}^2}V_{pi}^2 + \frac{A_H}{6\pi g_{pi}^3} - \frac{E_m}{d_0}(d_0 - g_{pi}) = 0, \tag{2.23}$$

$$-\frac{1}{4}\frac{\epsilon_0\epsilon_{rm}}{g_{pi}^3}V_{pi}^2 - \frac{A_H}{2\pi g_{pi}^4} + \frac{E_m}{d_0} = 0, \tag{2.24}$$

where the second equation describes the balance of derivatives of forces at the critical molecular spacer thickness. Assuming that the spacer thickness is $g_{ON}$ in the static ON-state, the release voltage $V_r$ can be calculated from

$$\frac{1}{8}\frac{\epsilon_0\epsilon_{rm}}{g_{ON}^2}V_r^2 + \frac{A_H}{6\pi g_{ON}^3} - \frac{E_m}{d_0}(d_0 - g_{ON}) = 0. \tag{2.25}$$

The hysteresis of the $I$-$V$ characteristic is therefore $V_h = V_{pi} - V_r$. It should be pointed out that not all nanoswitches exhibit pull-in phenomenon. Nanoswitches based on soft and thick molecular spacers may have the right instability to work in a pull-in mode, while those based on stiff molecular spacers typically show no pull-in. Besides, it is possible that one junction collapses during fabrication [100] and the potential of the nanoparticle is clamped either to the ground or to the drain voltage,

which can still be analyzed in a similar way by assigning either $V_F = 0$, $S_S = 0$ or $V_F = V_D$, $S_D = 0$ in (2.20). The static model is useful for studying the dependence of device $I$-$V$ characteristics on the mechanics of molecules by varying the Young's modulus $E_m$ and the initial thickness $d_0$ of the molecular layer.

## 2.3 Dynamic Model

In general, the speed of an electromechanical switch is constrained by the large mechanical delay due to motion of the active electrode. Specifically for the nanoswitches based on metal-molecule-metal junctions, the mechanical delay comes from nanometer-scale displacement of the nanoparticle, which is the same as the thickness change of the molecular layer between the ON-state and the OFF-state. In the OFF-state, the thickness of the molecular layer is smaller than the uncompressed thickness $d_0$ due to the existence of the adhesive force. The OFF-state spacer thickness $g_{OFF}$ can be calculated by assigning $V_D = V_F = 0$ in the force balance (2.20), i.e.,

$$\frac{A_H}{6\pi g_{OFF}^3} - \frac{E_m}{d_0}(d_0 - g_{OFF}) = 0. \tag{2.26}$$

The ON-state spacer thickness $g_{ON}$ is determined by the desired ON-state current $I_{ON}$ (or resistance) at a given drain voltage $V_D$ using the Simmons model by assigning $I = I_{ON}$, $V_t = V_D/2$ and $S_t = S_D = S_S$ in (2.1) (assuming two identical junctions at the source electrode and the drain electrode), which gives

$$\begin{aligned} I_{ON} = \frac{q_e S_D}{4\pi^2 \hbar g_{ON}^2} \Bigg\{ & \left(\Phi - \frac{q_e V_D}{4}\right) \exp\left[-\frac{2(2m_e)^{1/2}}{\hbar}\alpha_t \left(\Phi - \frac{q_e V_D}{4}\right)^{1/2} g_{ON}\right] \\ & - \left(\Phi + \frac{q_e V_D}{4}\right) \exp\left[-\frac{2(2m_e)^{1/2}}{\hbar}\alpha_t \left(\Phi + \frac{q_e V_D}{4}\right)^{1/2} g_{ON}\right] \Bigg\}, \end{aligned} \tag{2.27}$$

The differential equation that describes the movement of the nanoparticle during

transition between the OFF-state and ON-state is expressed by

$$
\begin{aligned}
-m\frac{\mathrm{d}^2 g(t)}{\mathrm{d}t^2} = & \frac{1}{2}\frac{\epsilon_0\epsilon_{rm}S_D}{g(t)^2}(V_D - V_F)^2 + \frac{1}{2}\frac{\epsilon_0\epsilon_{rm}S_S}{g(t)^2}(V_S - V_F)^2 \\
& + \frac{A_H(S_D + S_S)}{6\pi g(t)^3} - \frac{E_m(S_D + S_S)}{d_0}(d_0 - g(t)),
\end{aligned} \tag{2.28}
$$

where $g(t)$ is the time-dependent molecular layer thickness, and $m$ is the mass of the active nanoparticle electrode. In the simplified case assuming two identical tunneling junctions, when a drain voltage $V_D$ is applied to turn on the nanoswitch (source electrode grounded) at $t = 0$, the moment when the tunneling current reaches desired ON-state value (i.e., nanoswitch turns on) is calculated by solving

$$
\begin{aligned}
-\sigma\frac{\mathrm{d}^2 g(t)}{\mathrm{d}t^2} &= \frac{1}{8}\frac{\epsilon_0\epsilon_{rm}}{g(t)^2}V_D^2 + \frac{A_H}{6\pi g(t)^3} - \frac{E_m}{d_0}(d_0 - g(t)), \\
\text{s.t. } & g(t=0) = g_{OFF}, g(t = t_{ON}) = g_{ON},
\end{aligned} \tag{2.29}
$$

where $t_{ON}$ is the turn-on delay, $\sigma = m/(S_S + S_D)$ is the mass of the floating electrode normalized by the junction area. This normalized mass can be different from the area mass density $\rho$ of the nanoparticle (i.e., mass over bottom surface area) when the gap between the two bottom electrodes is not negligible compared to the length of nanoparticle. When the drain voltage $V_D$ is removed at $t = t_0$, the time needed in order that the spacer thickness increases back to OFF-state value $g_{OFF}$ corresponds to the turn-off delay $t_{OFF}$, which can be calculated by

$$
\begin{aligned}
\sigma\frac{\mathrm{d}^2 g(t)}{\mathrm{d}t^2} &= -\frac{A_H}{6\pi g(t)^3} + \frac{E_m}{d_0}(d_0 - g(t)), \\
\text{s.t. } & g(t = t_0) = g_{ON}, g(t = t_0 + t_{OFF}) = g_{OFF}.
\end{aligned} \tag{2.30}
$$

Similar to the static $I$-$V$ characteristic, the switching delay is also dependent on the Young's modulus and initial thickness of the molecular layer. Besides, an additional dependence of the delay on the inertia term can be observed from the model. In this Chapter, the dependence of the switching delay on the area mass density $\rho$ of the nanoparticle instead of the normalized mass $\sigma$ is studied, since $\rho$

is intrinsic to the nanoparticle and does not depend on the layout of the bottom electrodes.

## 2.4 Tunabilities of $I$-$V$ Characteristic

Two numerical examples are studied first in order to demonstrate the effect of molecules on the $I$-$V$ characteristic of the tunneling nanoswitch. Linear molecules are assumed in both examples. The first example simulates a nanoswitch based on a soft and thick molecular spacer. The Young's modulus and the initial thickness of the molecular spacer are assigned as $E_m = 15$ MPa and $d_0 = 3$ nm, respectively. It is assumed that an abrupt stiffening happens when the molecules are compressed by 60% in thickness. Two identical molecular junctions, each with an area of $50 \times 500$ nm$^2$, are assumed. The active electrode is a gold nanorod with a length of 1.5 $\mu$m and a diameter of 100 nm. Constant barrier parameters including barrier height $\Phi = 3.5$ eV and parameter $\alpha_t = 0.57$ are taken from alkylthiol molecules [101]. We use the relative dielectric constant of alkylthiol molecules [102] $\epsilon_{rm} = 2.1$ and Hamaker constant $A_H \approx 3 \times 10^{-19}$ J for Au-Au attraction [97]. The theoretical $I$-$V$ characteristic under a drain voltage from 0 V to 3 V is shown as the dash-dotted curve in Figure 2-4. The second example simulates a nanoswitch with a stiff and thin molecular spacer, which has a Young's modulus $E_m = 100$ MPa and an initial thickness $d_0 = 2$ nm. Other parameters and variables are assigned the same as the first example. The theoretical $I$-$V$ characteristic under a drain voltage from 0 V to 3 V is presented by the solid curve in Figure 2-4.

Significant difference in the $I$-$V$ characteristic can be observed from comparing the two examples in Figure 2-4. In the first example, the device $I$-$V$ characteristic based on a soft and thick molecular spacer exhibits a negligible OFF-state leakage current and an abrupt switching behavior (namely pull-in phenomenon) at 2.3 V. The molecular layer thickness at each point corresponding to specific drain voltage and tunneling current is represented by the color in the background. The modulation in the thickness of the molecular layer can be clearly observed by the change in the

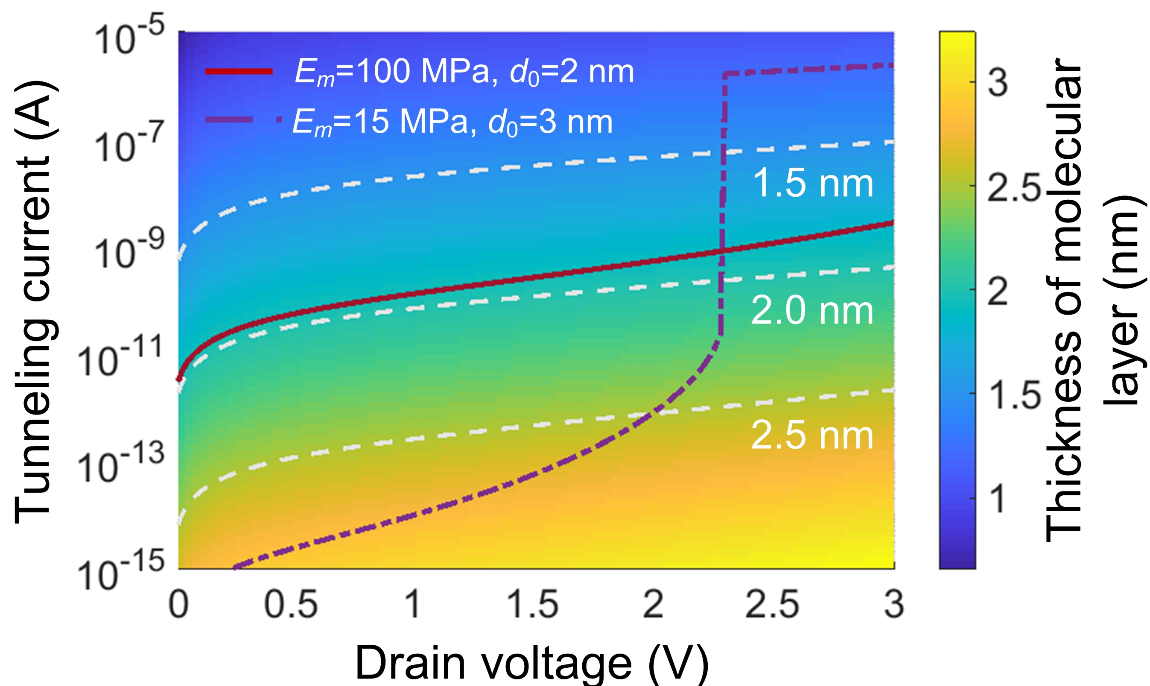


Figure 2-4: Theoretical $I$-$V$ characteristics of an example device (solid curve) based on a stiff, thin molecular layer and an example device (dash-dotted curve) based on a soft, thick molecular layer, with corresponding Young's modulus $E_m$ and uncompressed molecular layer thickness $d_0$ marked in the figure. The dashed curves describe the pure tunneling $I$-$V$ characteristics at constant switch gaps.

background color as the $I$-$V$ curve is traversed, which agrees with the compliant feature of the molecular spacer assigned in this example. In the second example, the theoretical $I$-$V$ characteristic does not exhibit a pull-in phenomenon. The leakage current is high in the OFF-state, resulting from a thin molecular layer. The $I$-$V$ characteristic is similar to that of pure tunneling at a constant 2 nm gap, and the thickness of the stiff molecular layer does not have a noticeable change. The contrast in the theoretical $I$-$V$ characteristics in the two examples suggests a great impact from the properties of the molecular spacer.

To make a high-performance nanoswitch, a thick and soft molecular spacer is desired in order to achieve a negligible OFF-state leakage as well as a large modulation in the tunneling current at a low actuation voltage. These two numerical cases represent soft, thick molecular spacer formed by macromolecules like PEG-thiol and stiff, thin molecular spacer formed by small molecules like alkylthiols. Experimental re-

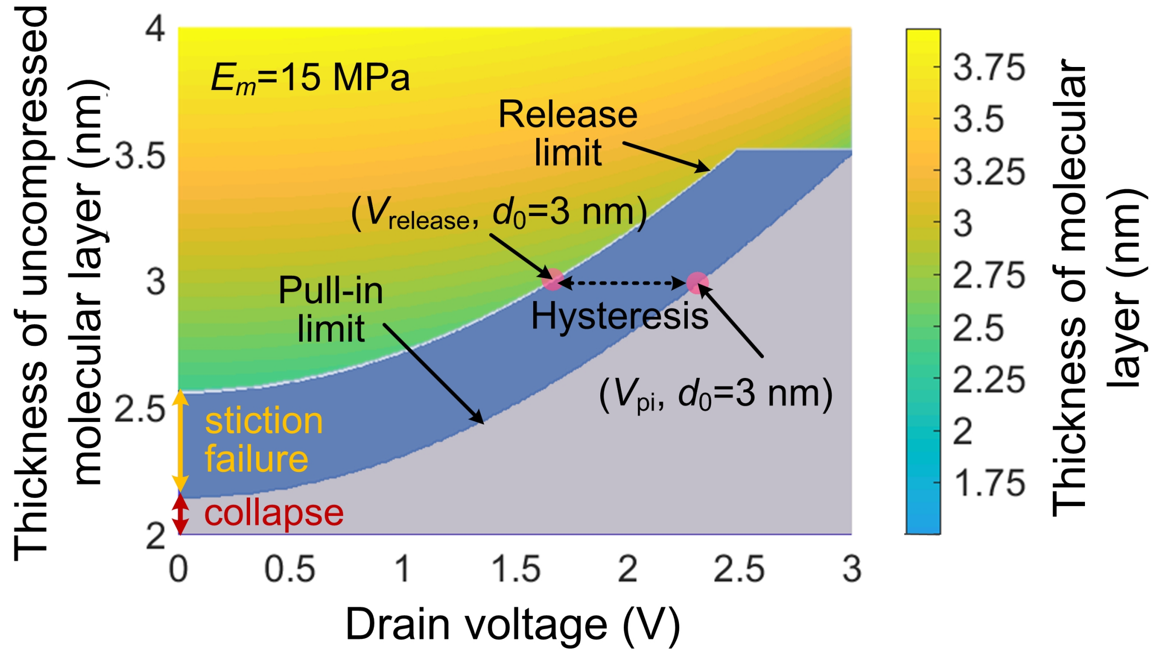


Figure 2-5: Dependence of the static behavior of a tunneling NEM switch on the thickness of uncompressed molecular layer $d_0$ at a constant Young's modulus $E_m = 15$ MPa. The ON-state switch gap after pull-in occurs is assumed as $g_{ON} = 0.5d_0$ to calculate the release voltage and release limit. Other simulation parameters are identical to those in Figure 2-4.

sults from nanoswitches fabricated based on these model molecules will be presented in Chapter 4.

To further study the dependence of the $I$-$V$ characteristic on the initial thickness of the molecular layer, a constant Young's modulus $E_m = 15$ MPa is assigned, while the initial thickness of the molecular layer in uncompressed state is changed from 2 nm to 4 nm. For a certain initial thickness, the molecular layer thickness under a 0∼3 V drain voltage (compressed state) can be calculated using the static model, and the results regarding 2∼4 nm initial thicknesses are presented as a colormap in Figure 2-5. The pull-in voltages and release voltages corresponding to different $d_0$ form two boundaries that represent the pull-in limit and the release limit, respectively. For an initial thickness $d_0$ between 3.5 nm and 4 nm, the pull-in limit does not extend into this region, meaning that the pull-in voltage is higher than 3 V. As a result, nanoswitches based on such thick molecular spacers do not exhibit pull-in and hysteresis in their $I$-

$V$ characteristics below 3 V. In comparison, a nanoswitch based on a slightly thinner molecular spacer ($d_0 = 2.5 \sim 3.5$ nm) exhibits both a pull-in phenomenon and a hysteresis. The hysteresis is given by the horizontal distance between the pull-in limit and release limit that corresponds to a specific initial thickness $d_0$. The simulation also indicates that the pull-in voltage increases with a thicker molecular layer, while the hysteresis gradually decreases. Further reduction in the initial thickness $d_0$ to 2.2∼2.5 nm results in a region completely below the release limit. The corresponding nanoswitches are able to turn on with a pull-in phenomenon in the first cycle, but unable to open after removing the drain voltage due to strong van der Waals force in the ON-state. This is when the permanent stiction failure happens, which is common for nanoswitches based on soft but thin molecular spacers. An excessively thin molecular layer ($d_0 < 2.2$ nm) corresponds to a region even below the pull-in limit. In this case, the molecular spacer collapses due to strong van der Waals force right after fabrication, and the nanoswitch shows an ohmic $I$-$V$ characteristic as a result.

The Young's modulus of the molecular layer also plays a significant role on the device behavior. When the Young's modulus are assigned as $E_m$ =10 MPa, 30 MPa, 50 MPa, simulations with varying initial spacer thickness, like Figure 2-5, have been conducted and compared in Figure 2-6. For a soft molecular layer (e.g., $E_m = 10$ MPa), a large initial thickness is essential to avoid stiction failure. The design region for nanoswitches operating in a pull-in mode under 3 V is also larger than those with stiffer molecular layers. On the other hand, an increase in the stiffness of the molecular layer results in less probability of device stiction failure. For a constant initial spacer thickness $d_0$, a stiffer molecular layer leads to a reduced compression and a higher pull-in voltage. For a stiff molecular layer ($E_m = 50$ MPa), no device stiction failure exists for a spacer thicker than 2 nm. Nevertheless, the design region for pull-in operating mode under 3 V almost vanishes, and little modulation is observed at 3 V for most initial thicknesses due to the high stiffness of the molecular spacer. The simulation results in Figure 2-6 show that a soft and thick molecular spacer is favorable and preferred in the design of our tunneling nanoswitch, in order to achieve

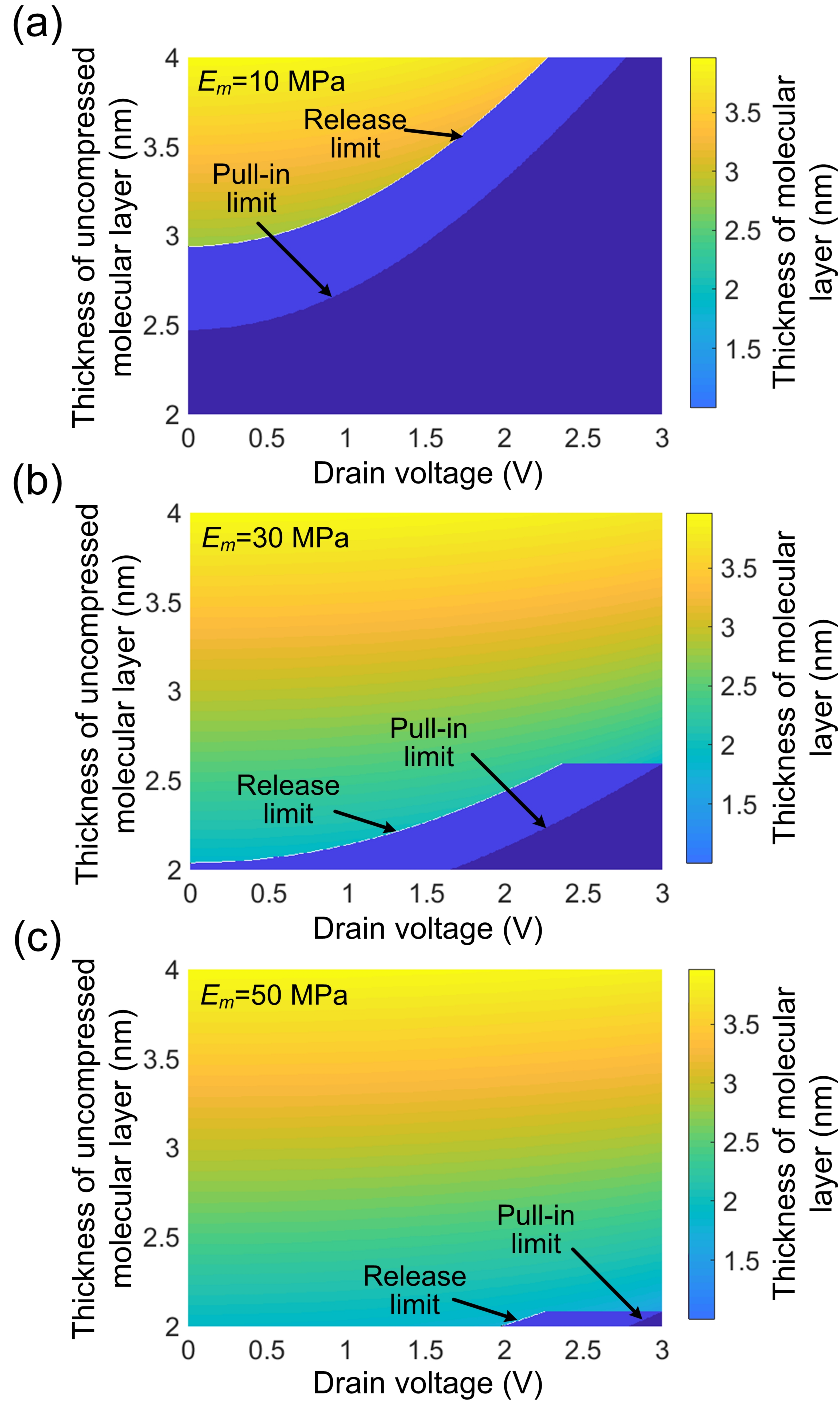


Figure 2-6: Dependence of the static device behavior on the drain voltage and the initial thickness of uncompressed molecular layer $d_0$ according to constant Young's moduli $E_m$ =10 MPa (a), 30 MPa (b), 50 MPa (c), respectively. The ON-state switch gap after pull-in occurs is assumed as $g_{ON} = 0.5d_0$ to calculate the release voltage and release limit. Other simulation parameters are identical to those in Figure 2-4.

a negligible OFF-state leakage, a large on-off current ratio and an abrupt switching at a low actuation voltage. Significantly, our theoretical study suggests that the device $I$-$V$ characteristic can be tuned by engineering the Young's modulus $E_m$ and intial thickness $d_0$ of the molecular spacer.

The simulations above are established based on a linear-molecule assumption. For most molecules under a large compression, nonlinear mechanics are unavoidable and also significant to maintain force balance in the ON-state. Moreover, nonlinear mechanical properties of the molecules may play a key role in reducing the actuation voltage.

To conduct a study on the effect of nonlinear molecules, we describe the nonlinear Young's modulus by (2.19), which is dependent on the compression $s = (d_0 - g)/d_0$, because any nonlinearity of the Young's modulus can be approximated by a polynomial with a proper $N$. A higher $N$ allows higher-order terms in the expression of $E_m$, and therefore represents an increase in nonlinearity. An extreme but interesting case is that when the elastic restoring force from the nonlinear molecules perfectly matches the nonlinear surface adhesive force at any spacer thickness, an arbitrarily small voltage is enough to turn the switch on. As a result, an effective way to achieve low operation voltage of the nanoswitch is by optimizing the nonlinear Young's modulus in order to match the restoring force with the adhesive force. However, the optimization problem is subject to a few constraints below to make the as-designed nanoswitches with nonlinear molecules physically feasible.

1. Young's modulus $E_m$ monotonically increases with compression $s$;

2. Repulsive force should always be able to overcome the adhesive force within the assigned compression range bounded by OFF-state and ON-state compressions, i.e., $[s_{OFF}, s_{ON}]$. This constraint ensures that the nanoswitch is free from stiction failure during operation;

3. The repulsive force in the ON-state balances the adhesive force and the electrostatic force with the turn-on voltage applied. This constraint ensures that an equilibrium point exists in the ON-state even for nanoswitches operating in pull-in mode.

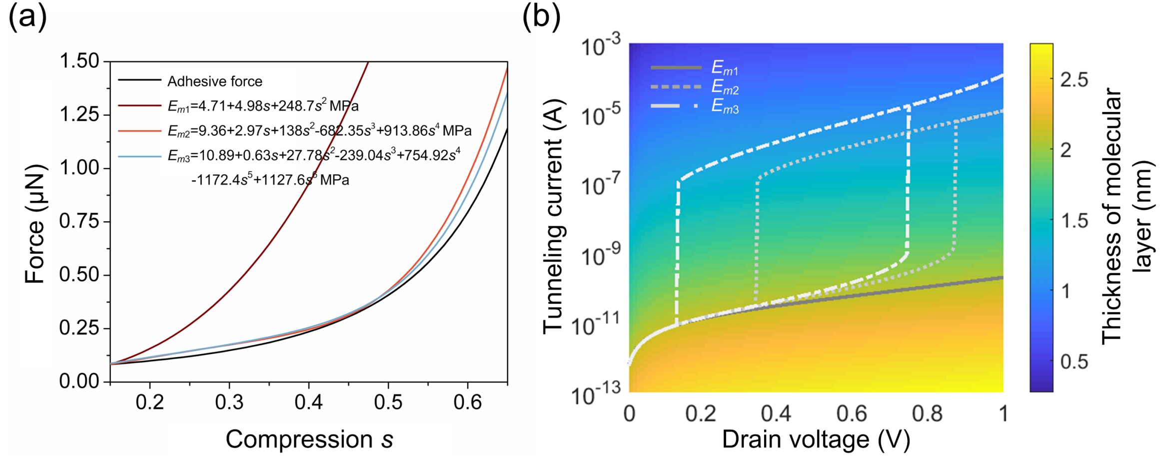


Figure 2-7: Theoretical static behavior of nanoswitches based on nonlinear molecules. (a) Comparison between the surface adhesive force and the restoring force from compressed molecules with optimal 2nd-order, 4th-order, 6th-order polynomial Young's moduli as a function of compression $s$. (b) $I$-$V$ characteristics originating from the optimal nonlinear mechanics of molecules.

A numerical example is simulated by assigning an initial molecular layer thickness $d_0 = 2.5$ nm. Other parameters for the molecules and electrodes are consistent with those in the two examples in Figure 2-4, i.e., junction area $S_S = S_D = 50 \times 500$ nm$^2$, particle length $L = 1.5$ $\mu$m, barrier height $\Phi = 3.5$ eV, barrier parameter $\alpha_t = 0.57$, relative dielectric constant of molecules $\epsilon_{rm} = 2.1$ and Hamaker constant $A_H \approx 3 \times 10^{-19}$ J. In this example, we set the maximum thickness modulation amount to be 40% ($s_{OFF} = 15\%$ and $s_{ON} = 55\%$). Three cases $N = 2$, $N = 4$, $N = 6$ are simulated regarding different nonliearities of the molecules. The optimal Young's moduli and the corresponding repulsive forces are compared with the adhesive force in Figure 2-7 (a), while the corresponding $I$-$V$ curves are presented in Figure 2-7 (b).

The result shows that optimal molecules ($N = 4, 6$) perform linearly at small compression and nonlinearly at large compression, which is in line with typical mechanical properties of molecules [98, 99]. Under the linear-molecule assumption, previous study (Figure 2-6 (a)) indicates that a nanoswitch based on such a thin and compliant molecular layer ($d_0 = 2.5$ nm, $E_m = 10$ MPa) is likely to fail due to stiction, while stiff molecule layers (Figure 2-6 (b) and (c)) bring about little compression and high actuation voltage. The theoretical results in this example, however, show reversible

switching behavior even when the molecules are initially compliant (e.g., $\sim 11$ MPa in the OFF-state where $s_{OFF} = 15\%$). Unlike the linear-molecule case, stable ON-state can be observed in the $I$-$V$ curves even after pull-in occurs. It should also be noticed that in the vicinity of pull-in, the current increase is suppressed by the increased stiffness of molecules compared with the theoretical $I$-$V$ curve (Figure 2-4) based on linear-molecule assumption. It is noteworthy that the drain voltage needed to achieve certain on-off current ratio is reduced with increased nonlinearity of molecules, and that sub-1-V actuation voltage is possible when molecules can be designed with certain nonlinear behavior. Moreover, the results again demonstrate the significance of the mechanics of molecules to the device performance and further suggest that ultra-low voltage switching can be realized potentially through designing molecules with specific nonlinear mechanics based on molecular engineering approaches.

## 2.5 Tunabilities of Switching Speed

To study the dynamic variation of the switch gap (i.e., molecular layer thickness) and the tunneling current under a constant drain voltage, a numerical example is simulated using the established dynamic model. Linear molecules are assumed. The parameters in the example are identical to those used in the previous numerical examples simulating statics, i.e., $E_m = 15$ MPa, $d_0 = 3$ nm, $S_S = S_D = 50 \times 500$ nm$^2$, $\epsilon_{rm} = 2.1$, $A_H = 3 \times 10^{-19}$ J. In addition, the mass of the nanoparticle $m = 1.8823 \times 10^{-13}$ g is evaluated from dimensions of typical gold nanorods (length $L = 1.5$ $\mu$m, diameter $D = 100$ nm) we use for device fabrication. The OFF-state gap $g_{OFF}$ and the ON-state gap $g_{ON}$ can be calculated using (2.26) and (2.27), respectively.

When a resistor is connected in series with the nanoswitch to sample the tunneling current, the waveform of the voltage across the sampling resistor can be used to estimate the moment when the nanoswitch turns on. This enables an approach to experimentally measure the turn-on delay of the switch. To verify the effectiveness of this measurement approach, the variation of voltage across a 1-M$\Omega$ sampling resistor is simulated, and we choose 1 $\mu$A for the ON-state current $I_{ON}$. An ideal pulse

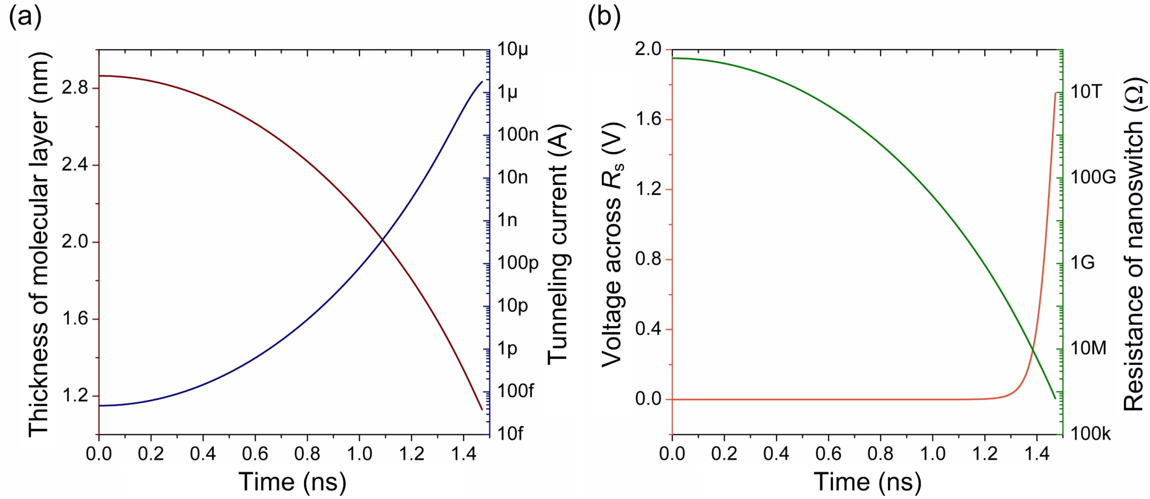


Figure 2-8: Theoretical dynamic behavior of the nanoswitch. (a) Variation in the thickness of molecular layer and the tunneling current in response to an ideal 3 V pulse voltage at $t = 0$. (b) Variation in the device resistance and the voltage across a 1-MΩ resistor $R_s$ in series to the device.

voltage with an amplitude of 3 V is applied across the switch and the resistor at $t = 0$. The theoretical time-dependent spacer thickness and tunneling current are presented in Figure 2-8 (a). Based on linear-molecule assumption, the nanoparticle keeps accelerating in the process of moving towards the bottom electrodes. The tunneling current increases exponentially as a result of reduction in the switch gap. The nanoswitch turns on at $t = 1.437$ ns assuming an ON-state with a 1-$\mu$A tunneling current. Such a turn-on delay may be smaller than the actual delay, considering that molecules become nonlinear at large compression and that nanoparticle experiences a higher repulsive force as the switch gap approaches $g_{ON}$.

The time-dependent resistance of the nanoswitch and the theoretical voltage across the sampling resistor are presented in Figure 2-8 (b). Thanks to the exponential increase of the tunneling current, the voltage across the sampling resistor exhibits a sharp rise edge with an onset at $t = 1.344$ ns. When the onset of the rise edge is treated as the moment of turning ON, the error for such an estimate of the turn-on delay is only 6.5%, suggesting the effectiveness of this approach for experimental measurement of the switching speed.

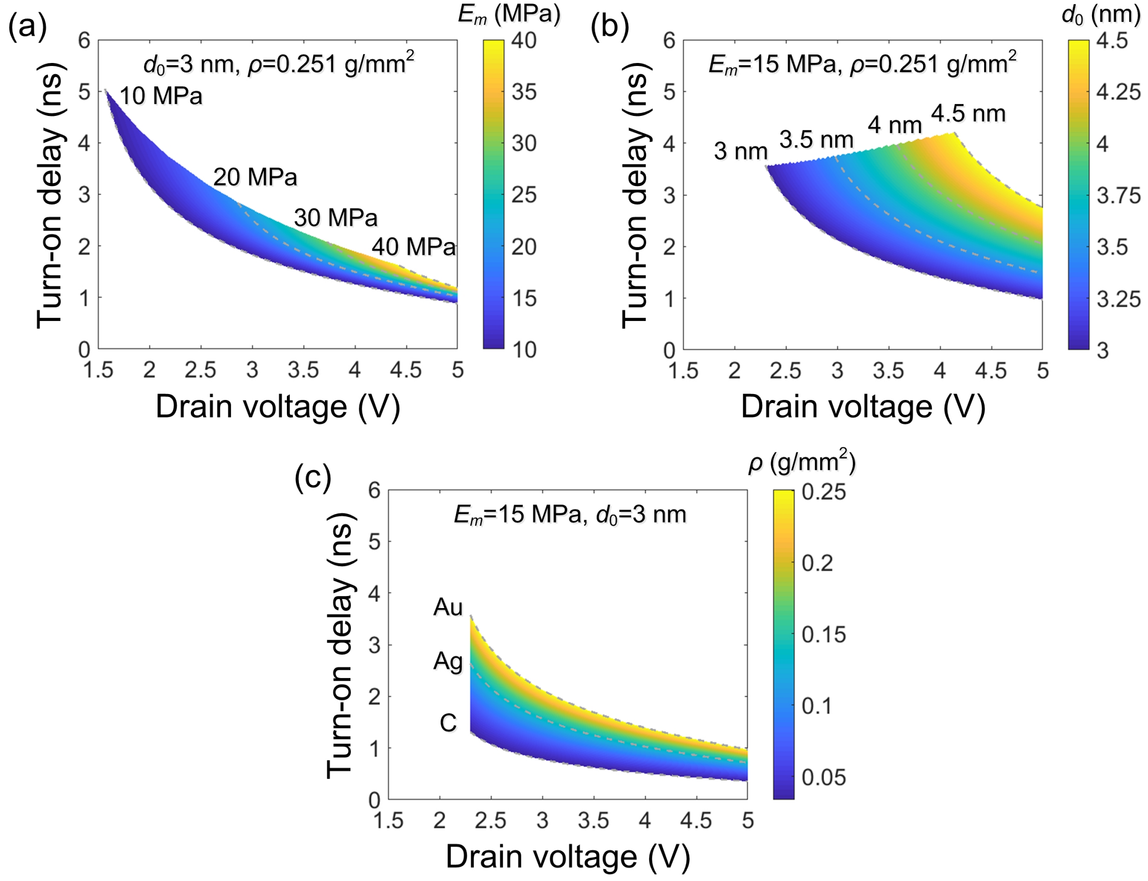


Figure 2-9: Dependence of the theoretical turn-on delay on the Young's modulus $E_m$ of the molecular spacer (a), the thickness of uncompressed molecular layer $d_0$ (b), and the area mass density of the nanoparticle $\rho$ (mass normalized by bottom surface area) (c), respectively, while the other variables are kept constant as marked in each figure. The theoretical turn-on delay corresponds to the time required to reach 1 $\mu$A drain current after applying a constant voltage. The maximum value and the minimum value of the colorbar in (c) correspond to gold and carbon nanoparticles, respectively, with the same geometry and dimensions.

Similar to the $I$-$V$ characteristic, the switching speed of the nanoswitch is closely linked with stiffness and thickness of the molecular layer as well. The dependencies of the turn-on delay on the Young's modulus $E_m$ and the initial thickness $d_0$ of the molecular layer are simulated separately and presented in Figure 2-9 (a) and (b), respectively. A gold nanorod with a length $L = 1.5$ $\mu$m and a diameter $D = 100$ nm is employed as the moving electrode. Other parameters include $S_S = S_D = 50 \times 500$ nm$^2$, $\epsilon_{rm} = 2.1$, $A_H = 3 \times 10^{-19}$ J.

In Figure 2-9 (a), we assign a constant thickness of the uncompressed molecular

layer $d_0 = 3$ nm, while changing its Young's modulus (under linear-molecule assumption) from 10 MPa to 40 MPa. Since the pull-in voltage is dependent on the Young's modulus, an applied voltage below the pull-in voltage cannot fully close the nanoswitch and does not lead to a theoretical turn-on delay. Therefore, the simulation is conducted by applying a constant drain voltage that is assigned between the pull-in voltage and 5 V with respect to each Young's modulus. The results show a nanoswitch with a stiffer molecular layer needs longer time to turn on, as the acceleration of the moving contact is smaller than those based on more compliant molecules under the same drive voltage.

In Figure 2-9 (b), we assign a constant Young's modulus $E_m = 15$ MPa, while varying the initial thickness $d_0$ of uncompressed molecular layer from 3 nm to 4.5 nm. The dependence of the pull-in voltage on $d_0$ is also taken into consideration while assigning the range of the drive voltage for different thicknesses. The results show that a thicker molecular layer brings about a larger turn-on delay, as the moving electrode needs to travel a longer distance to reach the desired ON-state switch gap. The theoretical values of turn-on delay in both Figure 2-9 (a) and (b) are below 5 ns in the entire simulation range and approach 1 ns at a 5 V drive voltage.

Unlike the $I$-$V$ characteristic, the switching speed is dependent on the inertia of the moving electrode as well. In theory, a nanoswitch employing a lighter nanoparticle electrode should exhibit a smaller switching delay compared to those based on heavier electrodes. To study such a dependence, nanoparticle electrodes are assumed with the same geometry (hexagonal cross-section, good for nanorods and approximately applies to nanotubes) but different area mass densities (i.e., mass over bottom surface area). The area mass density is more suitable to be presented in the result than the volume mass density, considering the attractive and repulsive forces are proportional to the junction area. We assign Young's modulus $E_m = 15$ MPa, initial thickness $d_0 = 3$ nm, while other parameters are identical to those utilized in Figure 2-9 (a) and (b). In this example, the layout of bottom electrodes is similar to our fabricated samples, but the gap between the bottom electrodes (500 nm) is comparable to the length of nanoparticle electrode. As a result, the mass normalized by junction area

$\sigma$ is different from the area mass density $\rho$, as discussed while deriving the dynamic model. We choose to present the area mass density in the result (Figure 2-9 (c)).

Since the pull-in voltage is independent on the mass of the nanoparticle, the drive voltage is varied in the same range (2.3 V$\sim$5 V) for different area mass densities. The results corresponding to gold, silver and carbon nanoparticles have been marked by the dashed curves in Figure 2-9 (c). The comparison indicates that a lightweight nanoparticle like CNT results in a faster speed than heavy nanoparticles like silver and gold nanorods/nanowires. The theoretical turn-on delay for a nanoswitch using CNT electrode can reach sub-1-ns level at 2.5 V, which is a significant improvement in speed over existing NEM switches and suggests a GHz-regime for our nanoswitches. Such a switching delay can be further reduced potentially by employing nanoparticles with smaller diameters (i.e., a reduced area mass density). More importantly, the mass of the nanoparticle offers an additional tunability on the switching speed without interfering with tuning $I$-$V$ characteristic through the mechanics of molecules.

# Chapter 3

# Fabrication of Tunneling Nanoelectromechanical Switch

## 3.1 Fabrication of a Two-Terminal Device

The nanofabrication process for a two-terminal tunneling nanoswitch is developed following a bottom-up paradigm, shown in Figure 3-1. First, gold bottom electrodes are patterned and deposited on a silicon or silicon oxide substrate, following a standard lift-off process involving electron-beam lithography and thermal evaporation. The substrate surface is then functionalized with fluorinated molecules to induce an anti-stiction property. Optical adhesive is dispensed on the substrate, and a glass receiving substrate is placed on top. After curing the adhesive, the sample stack is cleaved by a razor blade. The gold bottom electrodes are transferred onto the glass receiving substrate in this way. Such a template-stripping process enables ultra-smooth bottom electrodes, which are critical to fabricating uniform nanometer-scale molecular junctions. The peeled sample is subsequently immersed in a solution of thiol-terminated molecules to assemble the molecular spacer onto the bottom electrodes. In the last step, a droplet of a nanoparticle suspension is dispensed on the sample and high-frequency electric field is applied to position nanoparticles across the source and the drain bottom electrodes, which is known as the dielectrophoresis (DEP) approach. The details for each fabrication step are discussed as follows.

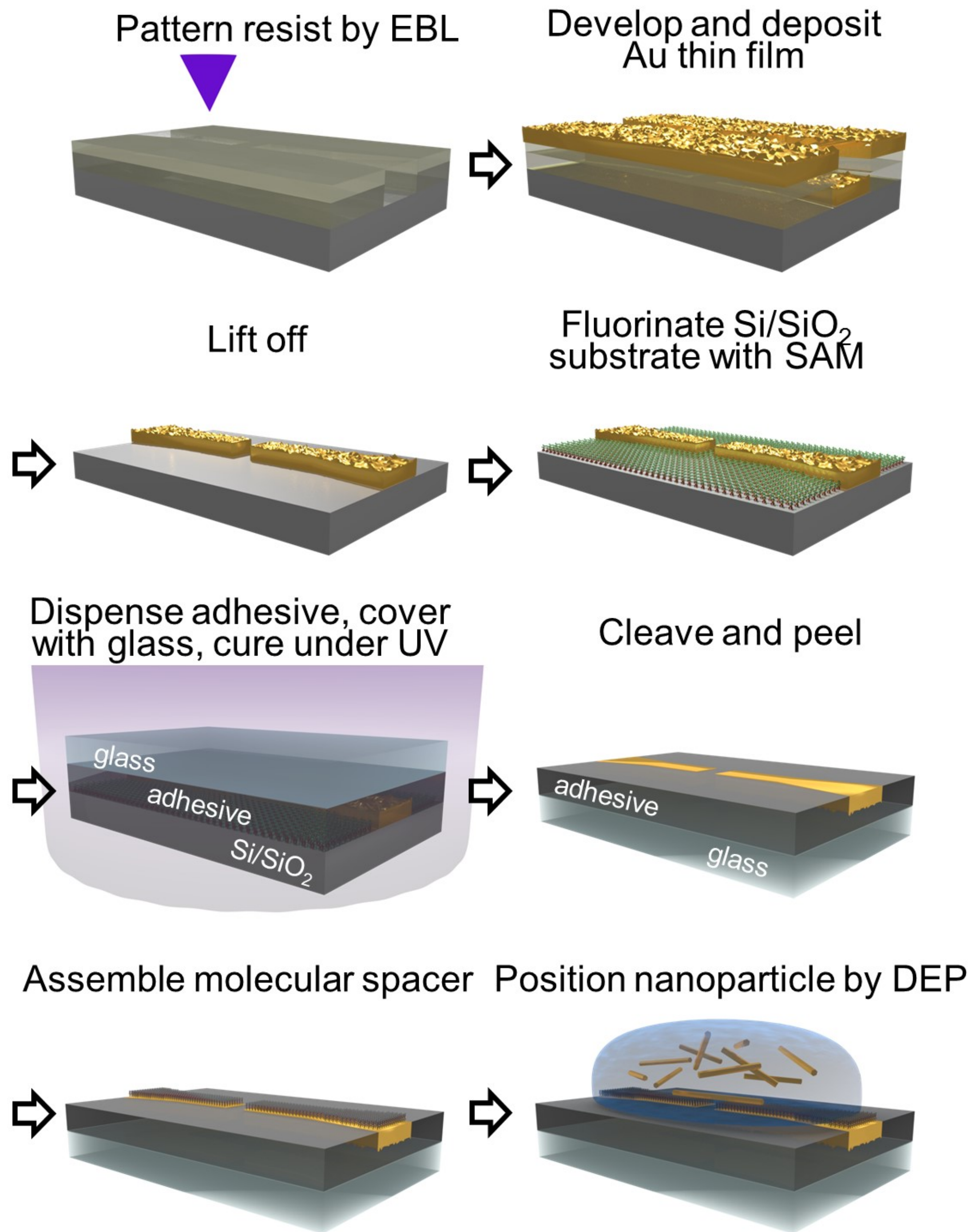


Figure 3-1: Nanofabrication process for a two-terminal tunneling nanoswitch. The process flow includes bottom electrodes patterning and transfer, self-assembly of molecular monolayer, and trapping of nanoparticle electrodes by DEP approach.

### Patterning bottom electrodes

Bilayer resist with copolymer MMA(8.5)MAA EL9 underneath PMMA950 A4 is utilized for patterning bottom electrodes. In order to achieve ultrasmooth surfaces, gold bottom electrodes will be stripped from the substrate in subsequent steps, and adhesion layer should not be adopted. Therefore, a bilayer resist improves the yield of fabricating gold bottom electrodes (low adhesion to the substrate), as it forms an undercut after development and results in an easy lift-off. Copolymer MMA(8.5)MAA EL9 is first spincoated onto a Si substrate with a native or thermal oxide layer at 2500 rpm for 45 s, annealed at 180 °C for 2 min. PMMA950 A4 resist is subsequently spincoated on top, following the same procedure. The bilayer resist is patterned using Elionix FS-125, exposed with an area dose of 1400$\sim$1500 $\mu$C/cm$^2$. After exposure, the sample is developed in MIBK/IPA=1:3 solution for 90 s. Then an 80-nm Au thin film is thermally evaporated onto the sample, followed by a standard lift-off process in acetone. After lift-off, the sample is rinsed in IPA for twice and dried with nitrogen flow.

### Template-stripping bottom electrodes

The surface roughness of as-evaporated bottom electrodes (Figure 3-2 (a)) can cause degraded and shorted molecular junctions, which results in significant device nonuniformity and failure. In order to reduce surface roughness and create uniform molecular junctions, a template-stripping process has been developed. When the evaporated bottom electrodes are peeled by adhesive and transferred onto a receiving substrate, the surface initially in contact with the Si/$SiO_2$ substrate is thereby exposed, and its smoothness is limited only by the roughness of the polished substrate. The as-obtained ultrasmooth bottom electrodes (Figure 3-2 (b)) enable assembly of molecular layers uniform in thickness over the entire area, with the help of a nanoparticle top electrode with atomically-smooth single crystal facets. To induce an antistiction property on the substrate surface, the sample is fluorinated by vapor-phase 1H,1H,2H,2H-Perfluorodecyltriethoxysilane in a desiccator under 30 min continuous

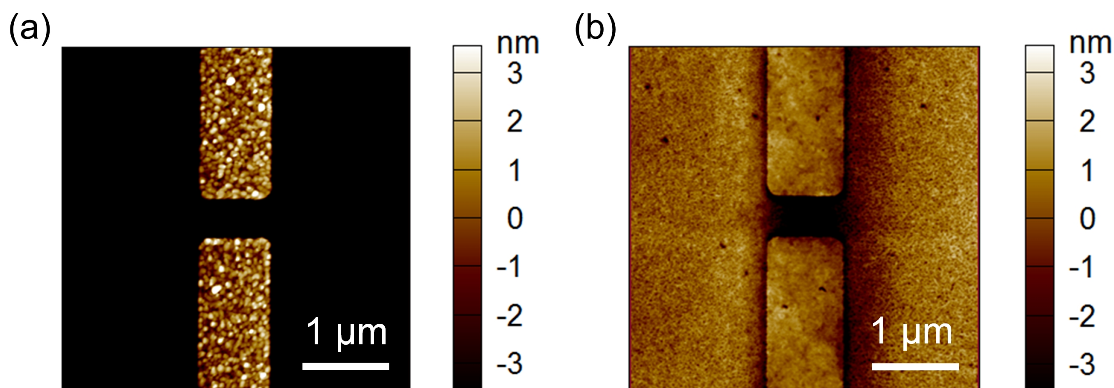


Figure 3-2: Atomic force microscopic (AFM) images of (a) evaporated gold bottom electrodes and (b) peeled gold bottom electrodes after pattern transfer.

vacuum and 30 min isolation. NOA 61 optical adhesive (Norland Products, Inc.) is then dispensed on the edge of the sample after fluorination. A piece of glass substrate is placed on top of the sample, and the sample stack is put in a desiccator under vacuum for 30 min to obtain a uniform adhesive layer between the sample and the glass. Then the sample stack is exposed under UV (from a 100 W lamp, 30 min) to cure the adhesive. A thin razor blade is used to cleave the laminated sample, and the gold bottom electrodes are thereby transferred onto the receiving glass substrate.

**Self-assembly of molecular monolayers**

The surfaces of gold electrodes are cleaned before assembling molecules on top. Rinsing the sample in ethanol for a few times and/or a 15 s gentle oxygen-plasma treatment help remove any contaminants that may attach to the gold surfaces and result in poorly assembled molecular layers. To prepare the solution of thiol-terminated molecules, 200 proof ethanol is typically used for alkyl- and aryl-thiol molecules. For PEG-thiol with a large molecular weight, either pure deionized (DI) water or an ethanol-DI water mixture (5% DI water by volume) is utilized as solvent. The small amount of deionized water added into the ethanol helps dissolve these macromolecules. The sample is immersed in the as-prepared 5 mM solution of desired molecules for 24 h, before rinsed with ethanol for twice to remove residual molecules

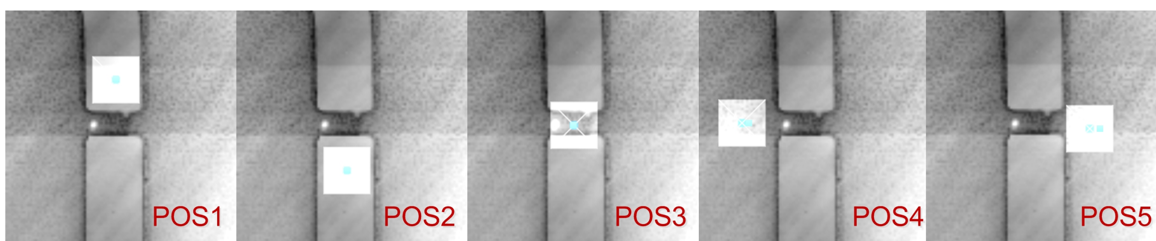


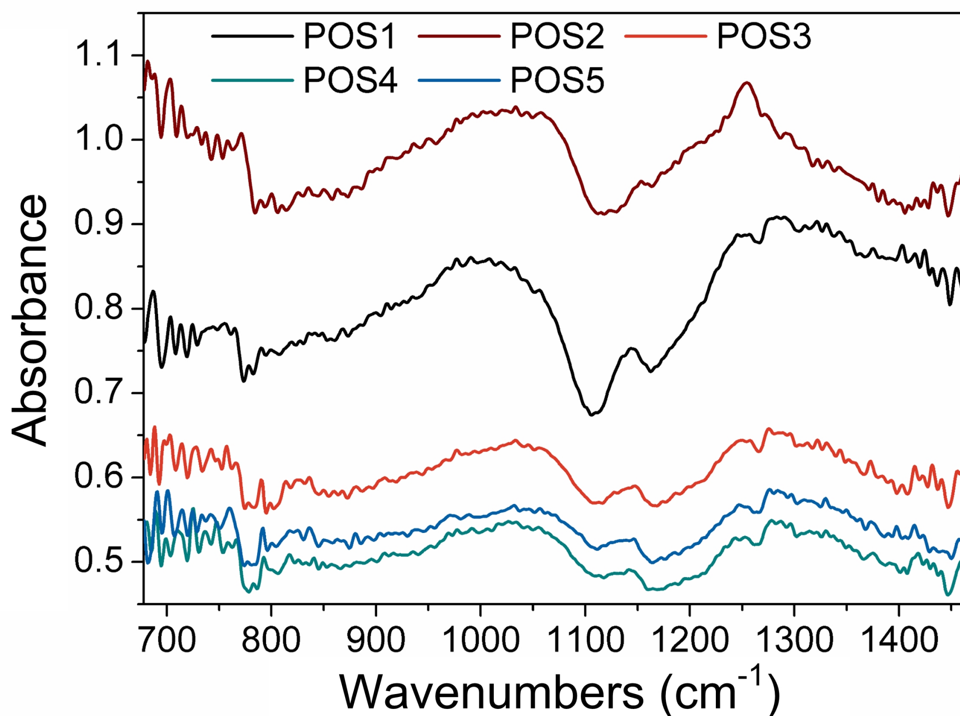


Figure 3-3: Nanoscale infrared spectra of a sample with PEG-thiol molecular layers. The five screenshots indicate the positions for the measured spectra.

and dried with nitrogen flow. As an example, the bottom electrodes after assembly of 5 kDa PEG-thiol have been characterized by nanoscale infrared spectroscopy, shown in Figure 3-3. The absorbance on the bottom electrodes (site 1, 2) agrees with the absorbance of PEG-thiol molecules but differs from those on the optical adhesive (site 3, 4, 5).

**Positioning nanoparticle electrode by DEP**

The most common nanoparticles we use to fabricate the nanoswitches are gold nanorod/nanowire (AuNR) and multi-walled carbon nanotubes (MWCNT). Com-

mercial suspensions of the AuNR particles in DI water and MWCNT particles in DI water are available from Nanopartz, Inc. and NanoLab Inc., respectively. The dimensions of the AuNRs we use are 1∼2 $\mu$m in length, 80∼100 nm in diameter, while the dimensions of the MWCNTs are 1∼2 $\mu$m in length, 100∼150 nm in diameter. The concentrations of the nanoparticle suspensions are $6 \times 10^8$ AuNRs/mL and $1\times10^7$ MWCNTs/mL. The custom MWCNT suspension is surfactant-free. The AuNRs have surfactants of cetrimonium bromide (CTAB), and an additional washing step is necessary to remove the surfactants on the nanoparticle. 100 $\mu$L suspension is diluted with 300 $\mu$L DI water and then centrifuged at 2000 rpm for 15 min. The supernatant is carefully removed, and the settled nanoparticles are re-suspended in 100 $\mu$L DI water with gentle sonication. The concentration of AuNR suspension after the washing process is lower than that of the original suspension. 100 $\mu$L suspension in DI water with surfactant-free nanoparticles (AuNR suspension after washing, or original custom MWCNT suspension) is then mixed with 100 $\mu$L ethanol and ready for use.

To position nanoparticles onto the bottom electrodes with molecular spacers, the DEP approach is adopted. Specifically, a high-frequency voltage is applied across the bottom electrodes and thereby induces drive forces on nanoparticles nearby. The drive force overcomes the Brownian motion and the drag from solvent to trap a nanoparticle onto the electrodes. The trapping process is a result from the interplay among the DEP force, the hydrodynamic drag force and the thermodynamic force that characterizes the Brownian motion. The most significant DEP force for a cylinder-shaped nanoparticle [55] is given by

$$\mathbf{F}_{DEP} = \frac{\pi r^2 l}{2} \frac{\epsilon_l^*(\epsilon_p^* - \epsilon_l^*)}{\epsilon_l^* + (\epsilon_p^* - \epsilon_l^*)L_{//}} \nabla|\mathbf{E}|^2, \tag{3.1}$$

where: $r$, $l$ are the radius and length of the nanoparticle; $\epsilon_p^*$, $\epsilon_l^*$ are the frequency-dependent complex dielectric constants of the nanoparticle and the suspension liquid, respectively; $\mathbf{E}$ is the electric field around the bottom electrodes; $L_{//}$ is the depolarization factor $L_{//} \approx 4r^2/l^2[\ln(l/r) - 1]$.

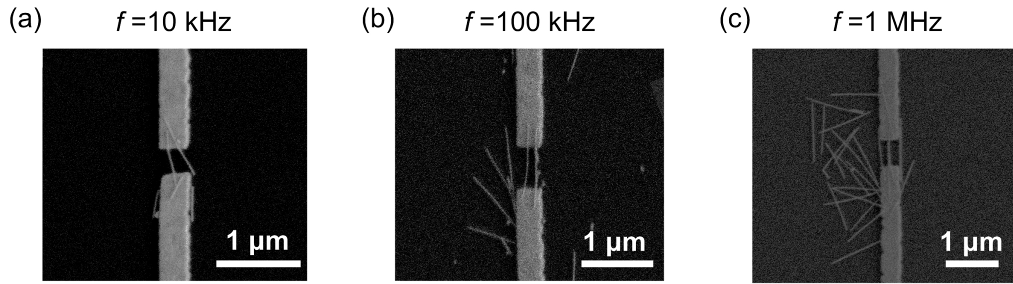


Figure 3-4: Scanning electron microscopic (SEM) images of trapped AuNR particles at different frequencies: (a) 10 kHz, (b) 100 kHz, and (c) 1 MHz. Concentrated nanoparticle suspension is dispensed onto the trapping electrodes. An identical trapping voltage of 1 $V_{p-p}$ is utilized at different frequencies.

From the expression of DEP force, we observe dependence on the contrast between the complex dielectric constant of nanoparticle and that of the suspension liquid. Besides, the dependencies of DEP force on the electric field gradient, the frequency of the field and the dimensions of nanoparticles offer several conditions to optimize towards a high yield for the trapping process. The electric field distribution can be tuned through the design of electrode layout [103, 104] in order to achieve an improved yield. Changing the amplitude and frequency of the field is also effective to tune the trapping. For instance, Figure 3-4 shows that an increased frequency may bring a higher DEP force under the same voltage (1 $V_{p-p}$), thus leading to more AuNR particles aligning around the electrodes. Other parameters useful for tuning the trapping process include suspension concentration, temperature and time [55,105].

After nanoparticles are trapped onto the electrodes, van der Waals force and DEP force maintain the nanoparticle in position; however, the van der Waals force for trapped nanoparticle is still weak before the sample dries. As a result, the nanoparticle can be washed away by hydrodynamic drag force from excessive flow rate, which has been intentionally used to reduce the number of trapped nanoparticles [58]. Besides, the strong capillary force from the receding edge of the suspension droplet as the sample is drying can also dislocate or wash away the trapped nanoparticles, which is the reason for adding ethanol into the suspension. The voltage is also ap-

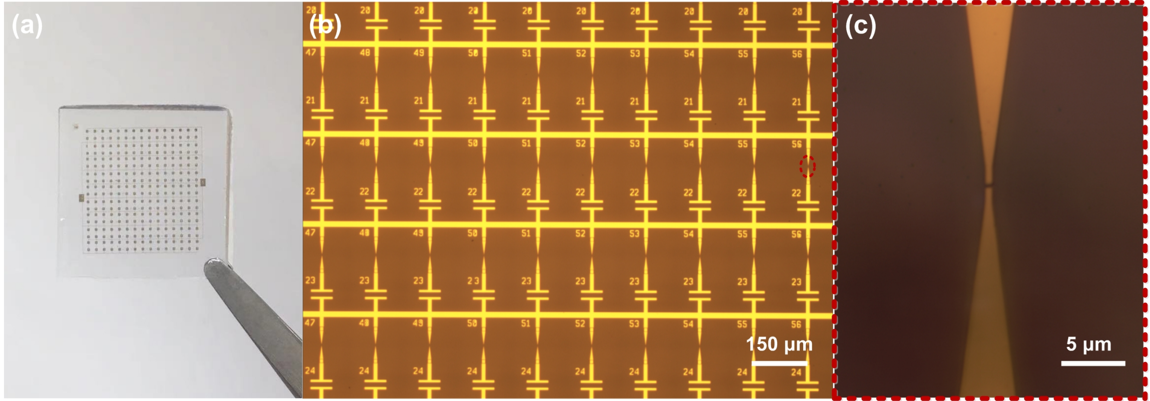


Figure 3-5: Trapping electrode array. (a) Picture of a trapping electrode array on a glass substrate. (b) Microscopic image of trapping electrodes with capacitors in series. (c) Close-up image of a pair of trapping electrodes.

plied throughout the drying process to keep the trapped nanoparticle in position. In our fabrication process, a 10-$\mu$L prepared nanoparticle suspension is dispensed onto the substrate and a 1-MHz, 3-$V_{p-p}$ sinusoidal voltage is applied across the bottom electrodes for 2 min to trap the nanoparticles.

In order to increase the yield of devices with a single nanoparticle, the suspension is diluted for a low concentration of nanoparticles. In addition, we have designed a self-limiting trapping process with the help of an on-chip capacitor (Figure 3-5) in series with the bottom electrodes. The capacitance is designed to be much larger than that formed by the pair of bottom electrodes, while much smaller than that of the tunneling nanoswitch after a single nanoparticle is trapped. As a result, majority of the source voltage is applied across the bottom electrodes before a nanoparticle is trapped; after a nanoparticle lands on the bottom electrodes, majority of the voltage is taken away by the designed capacitor, which thereby prevents trapping more nanoparticles onto the electrodes. When such branches are connected in parallel (Figure 3-5), the self-limiting trapping process in each branch does not affect those in other branches. Therefore, scalable fabrication of the tunneling nanoswitch is enabled by the developed self-limiting process, and such a method may extend to high-throughput manufacturing of various nanoscale devices built by direct assembly of nanoparticles.

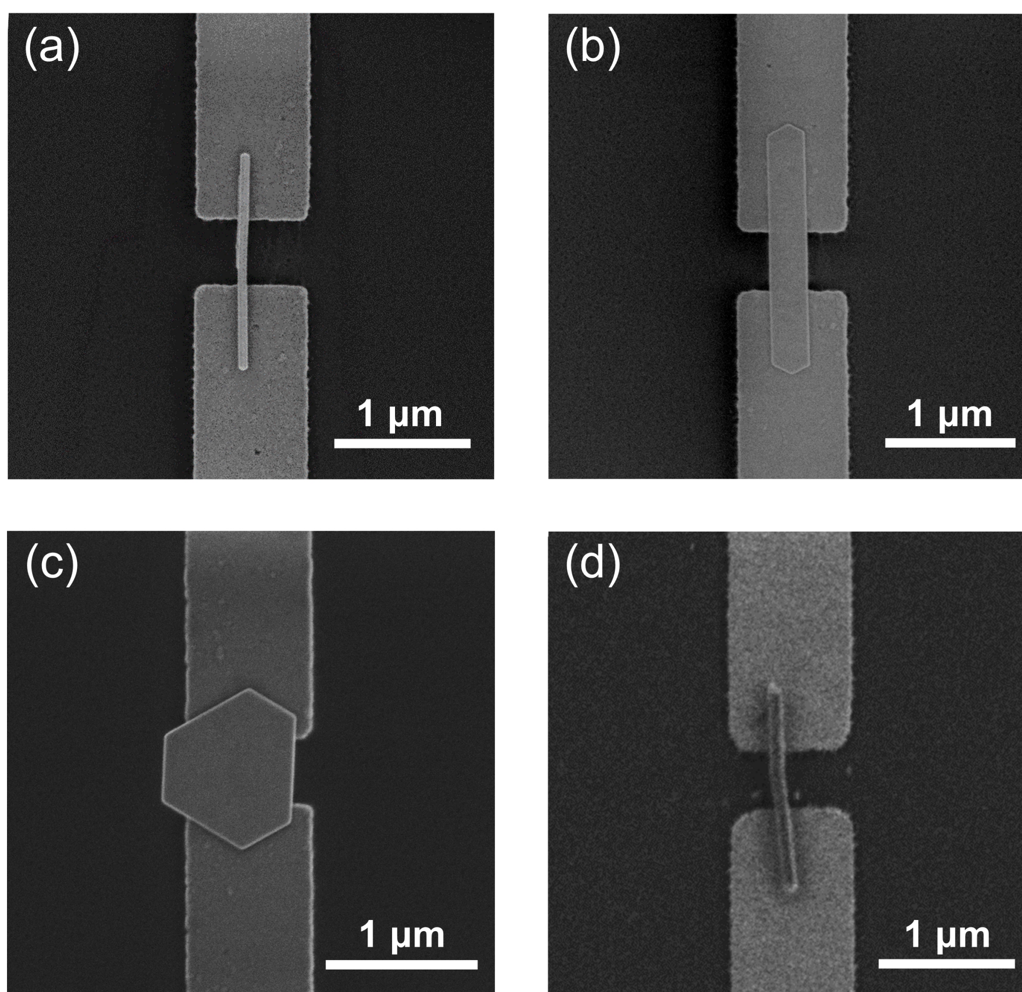


Figure 3-6: SEM images of example devices based on diverse nanoparticle top electrodes, including (a) gold nanorod, (b) ribbon-shaped gold nanoplatelet, (c) hexagonal gold nanoplatelet, and (d) multi-walled carbon nanotube.

Figure 3-6 presents some example devices we have fabricated based on diverse nanoparticle electrodes, including AuNR, Au nanoplatelet, and MWCNT.

## 3.2 Fabrication of a Multi-Terminal Device

The device concept and nanofabrication process of the two-terminal tunneling nanoswitch may extend to multi-terminal architectures. Figure 3-7 shows the

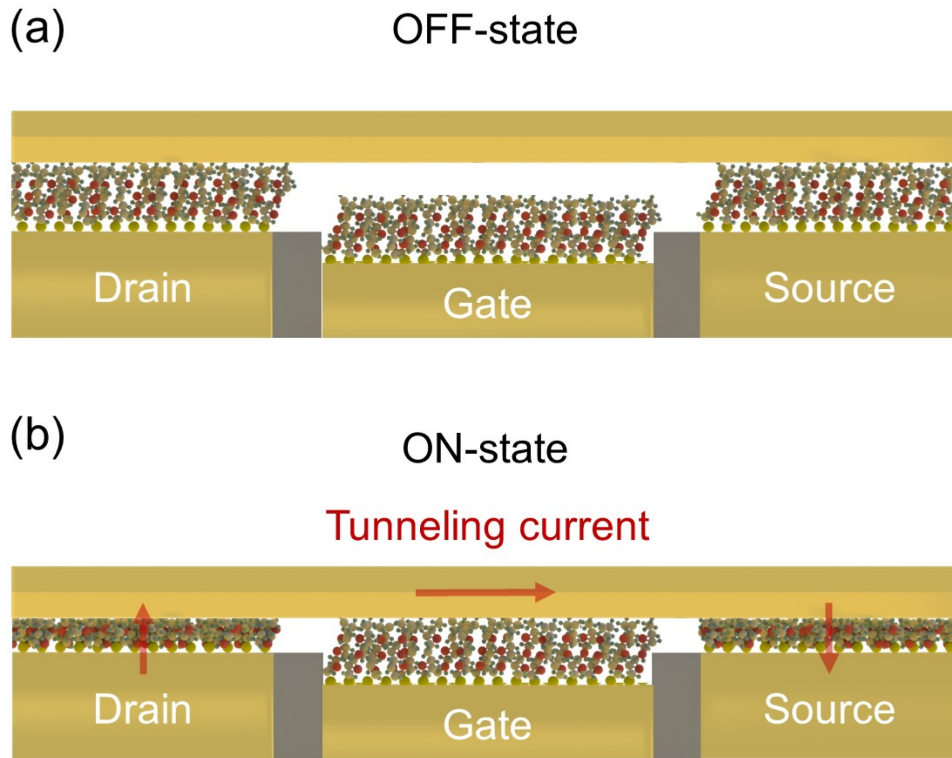


Figure 3-7: Schematic of a three-terminal tunneling nanoswitch (a) in the OFF-state and (b) in the ON-state.

schematic of a three-terminal nanoswitch. The only difference from a two-terminal architecture is the addition of a gate electrode. The gate-induced electrostatic force can potentially reduce the actuation voltage. However, the gate electrode has to be lower than the source electrode and the drain electrode so that the gate leakage in the ON-state is negligible. To avoid sacrificing gate-induced electrostatic force too much, a recess by only a few nanometers is preferred, which brings great challenge to the fabrication of bottom electrodes. Therefore, we have modified the nanofabrication process for two-terminal devices, and utilized two-dimensional materials as a sacrificial layer to define a proper gate recess during bottom-electrode patterning. The process flow for making a multi-terminal tunneling nanoswitch (four-terminal architecture as an example) is presented in Figure 3-8.

A monolayer of graphene is grown by chemical vapor deposition (CVD) and transferred onto a Si/$SiO_2$ (usually 300-nm-thick $SiO_2$) substrate. Alignment marks are

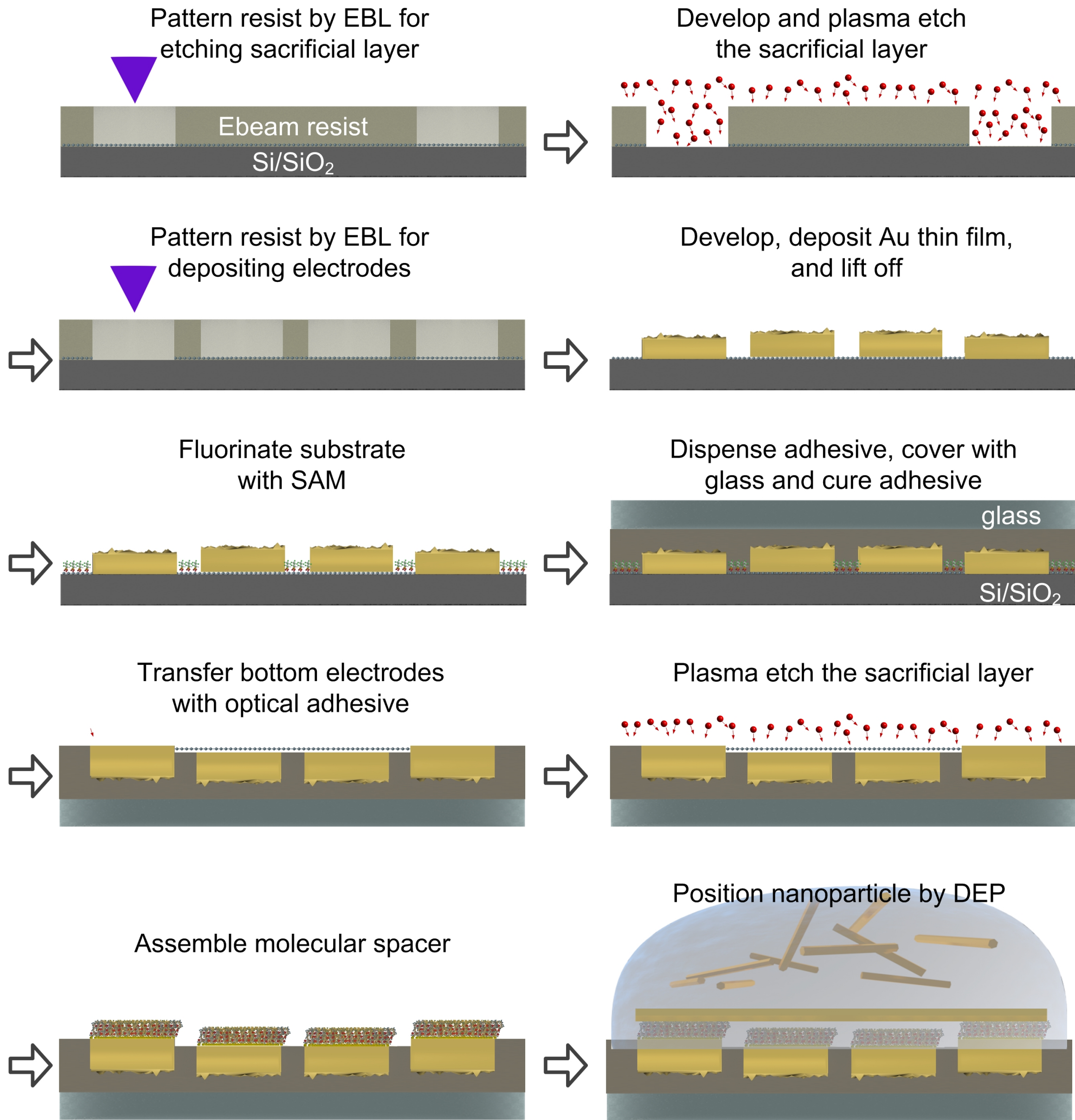


Figure 3-8: Nanofabrication process for a multi-terminal tunneling nanoswitch. The process flow includes sacrificial layer patterning, bottom electrodes patterning and transfer, sacrificial layer etching, self-assembly of molecular spacers, and trapping of the nanoparticle by DEP approach.

patterned first, following a standard lift-off process involving lithography, development and thermal evaporation, to assist with alignment in subsequent lithography steps. In the next electron-beam lithography, the exposed regions are reserved for source and drain electrodes. After development in MIBK:IPA=1:3 solution, the graphene in those regions are subsequently removed by 30 s oxygen plasma etch-

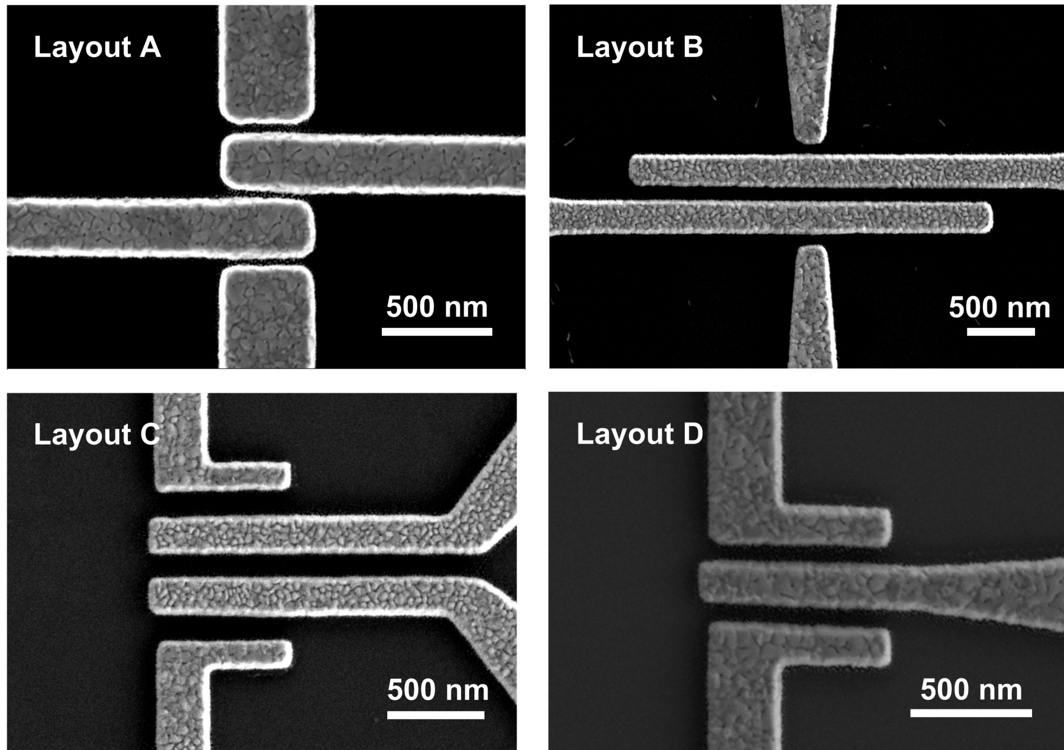


Figure 3-9: Layouts of multi-terminal bottom electrodes.

ing. The resist is stripped by acetone, and bilayer resist is coated on the substrate with etched graphene for next lithrography step. The source and drain bottom electrodes are patterned and deposited on no-graphene region, while the gate electrodes are patterned and deposited on graphene in the same step. A few layouts for bottom electrodes are shown in Figure 3-9.

Though the graphene sacrificial layer can induce antistiction property for the substrate surface, the sample is still fluorinated in the same way as fabricating two-terminal devices, in case of locally incomplete graphene layer and stiction at sample edges. Optical adhesive is then dispensed on the edge of the sample, and a receiving glass substrate is placed on top of the sample. The sample stack is put in a desiccator under vacuum for 30 min to obtain a uniform adhesive layer, and then exposed under a 100 W UV lamp for 30 min to cure the adhesive. An ultra-thin razor blade is used to cleave the laminated sample, and the gold bottom electrodes are thereby transferred onto the receiving glass substrate. The graphene layer may also be peeled in this

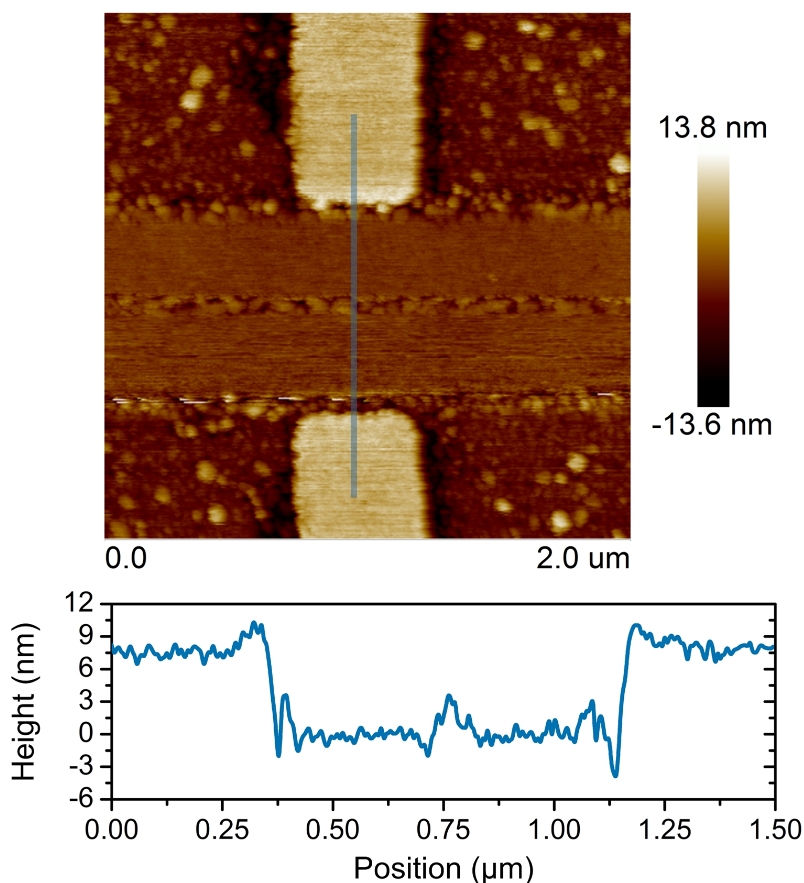


Figure 3-10: AFM image of peeled multi-terminal bottom electrodes with height profile.

process. Large graphene sheets could short the bottom electrodes, and small flakes adhered to the gate electrodes could result in significant gate leakage. To remove the graphene residual, the peeled sample is treated in oxygen plasma for 45 s and then rinsed in ethanol for twice. The gold surfaces remain intact during this process while the surface of optical adhesive may turn rougher.

An AFM image of example template-stripped multi-terminal bottom electrodes is presented in Figure 3-10. The polished $Si/SiO_2$ substrate and the atomically-smooth graphene monolayer help define ultrasmooth surfaces of source/drain electrodes and gate electrodes, respectively. A $\sim$8 nm recess of the gate electrodes is also enabled by the selectively-etched sacrificial graphene layer. The sample is then immersed in a 5 mM solution of desired thiol-terminated molecules for 24 h to assemble the molecular spacer onto the bottom electrodes. In the last step, a 10-$\mu$L droplet of a nanoparticle

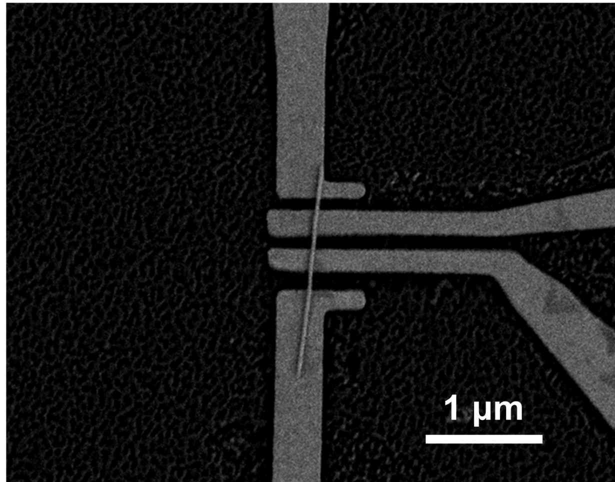


Figure 3-11: SEM image of a fabricated multi-terminal tunneling nanoswitch.

suspension is dispensed on the sample, and a 1-MHz, 3-$V_{p-p}$ voltage is applied across the source electrode and the drain electrode (while leaving gate electrodes floating) to position nanoparticles. The self-limiting scalable trapping process, introduced for two-terminal device fabrication, applies to fabricating multi-terminal devices as well. An example of fabricated multi-terminal tunneling nanoswitch is presented in Figure 3-11.

A multi-terminal nanoswitch operates based on the same mechanism as two-terminal devices, i.e., by electromechanical modulation of the molecular junctions. The tunabilities of device behavior based on the molecular layer and the nanoparticle electrode are also identical to both two-terminal and multi-terminal architectures. However, fabricating a multi-terminal nanoswitch is a lot more challenging, with a low yield observed. Therefore, two-terminal device architecture is the focus for experimental study of device performance and demonstration of tunabilities afforded by engineering the molecules and the nanoparticle electrodes, as the result of ease of fabrication.

## 3.3 Challenges and Outlook

The concept of the tunneling nanoswitch is established by electromechanical modulation of the molecular junctions. Our developed fabrication process enables uniform molecular layers and thereby enhanced device performance. The scalable self-limiting approach we develop for manipulating nanoparticles greatly improves the throughput of device fabrication. However, the yield for fabricating nanoswitches with single-nanoparticle electrode still needs improvement. A nanoswitch with a bundle of nanoparticles as the top electrode is more susceptible to stiction failure. Mixture of devices with a single nanoparticle and devices with a bundle of nanoparticles may lead to nonuniform device performance (not favorable for circuit building and operation). The existence of multiple nanoparticles is greatly attributed to the quality of the nanoparticle suspension. After the surfactants are removed, the nanoparticles agglomerate quickly and the formed aggregates are subsequently positioned onto the electrodes by DEP. A low concentration of the nanoparticles may reduce the probability of agglomeration, but more electrodes can end up with no nanoparticle trapped, as fewer nanoparticles exist in the suspension. Therefore optimization on the concentration as well as other trapping conditions is imperative. Another potential solution is trapping nanoparticles in flowing diluted suspension based on the developed self-limiting process. The flowing suspension increases the presence of nanoparticles close to each pair of bottom electrodes and only vacant electrodes create strong electric field to trap a nanoparticle, owing to the on-chip capacitors. Besides, tuning the flow rate may also help, as a proper drag force can be induced to wash away redundant trapped nanoparticles. Further study will be conducted to demonstrate this improved trapping technique.

Additional challenges exist for fabrication of multi-terminal devices in particular. The template-stripping process for the multi-terminal bottom electrodes is found to be more vulnerable to triboelectric damage, and a solution to overcome this issue has been developed [106]. Besides, the trapping process for multi-terminal device-field distribution, which greatly reduces the yield for trapping a single nanoparticle.

Simulation of the electric-field distribution and the resulting DEP force may inform optimized design for the layout of multi-terminal bottom electrodes.

# Chapter 4

# Performance of Tunneling Nanoelectromechanical Switch

## 4.1 $I$-$V$ Characteristics of Nanoswitches Based on Poly(ethylene glycol)thiol Molecular Spacer and Gold Nanorod Active Electrode

Theoretical study on the $I$-$V$ characteristic of the tunneling nanoswitch suggests that a soft and thick molecular spacer is preferred in order to achieve a negligible OFF-state leakage, a large on-off ratio and an abrupt switching at a low turn-on voltage. For proof-of-concept purpose, 5 kDa PEG-thiol is selected as the model molecule to fabricate the nanoswitches, because PEG-thiol is well known to form a soft and thick molecular layer. Besides, 1∼2 $\mu$m long, 80∼100 nm thick AuNR particles are employed as the active top electrodes.

The $I$-$V$ characteristics of fabricated devices are measured in ambient environment by a probe station with an Agilent B1500 semiconductor parameter analyzer. A double sweep is conducted with 200 points in total sampled within the voltage range of interest. To reduce damage to the nanoparticle and the molecular junctions caused by joule heating and discharge current during measurement, a 1-$\mu$A compliance is

set for $I$-$V$ sweep. The $I$-$V$ characteristics of example devices based on an AuNR electrode and PEG-thiol spacers from different batches are shown in Figure 4-1. The dashed curve presents a pure tunneling $I$-$V$ characteristic assuming a constant gap extracted from low-voltage datapoints of device D1, using the Simmons model and parameters $\Phi = 3.5$ eV, $\alpha_t = 0.57$. The barrier parameters are taken from alkylthiol molecules due to the absence of parameters for PEG-thiol in literature. At low voltages, the $I$-$V$ characteristics of these example devices exhibit tunneling behavior with small compressions in the molecular layers, as compared with the reference curve of pure tunneling. Pull-in phenomena are observed at sub-3-V drain voltages for these devices. The abrupt switching brings about an over 5-orders-of-magnitude on-off current ratio and a subthreshold slope as low as 30 mV/dec. The experimental results from these example devices prove the superiority of the tunneling nanoswitch, arising from the nanometer-scale modulation of the molecular spacer.

PEG-thiol molecules with large molecular weights are also known to form brush-like islands, attributed to the dense attachment of these randomly coiling polymeric macromolecules [107]. It may cause nonuniform initial thicknesses and Young's moduli of the assembled molecular spacers among devices. Therefore, a distribution of device performance is expected. A statistical study has been conducted on the device performance of nanoswitches based on 5 kDa PEG-thiol spacers and an AuNR active electrode. 130 devices are fabricated, and the actuation voltage $V_{on}$ and the modulation in current are measured as the metrics to evaluate performance for each device. As shown in Figure 4-2 (a), the actuation voltage corresponds to the drain voltage at which the drain current, $I_{D(actual)}$, reaches 1 $\mu$A for each device. The 1 $\mu$A is not only the compliance we set but also the state where we assume a nanoswitch turns on. The modulation in current characterizes how much change in current arises from compression in the molecular layer. To obtain the modulation in current, the initial molecular layer thickness $d_0$ is extracted from the low voltage datapoints of each device using the Simmons model assuming the same barrier parameters, $\Phi = 3.5$ eV, $\alpha_t = 0.57$. Then the theoretical tunneling current, $I_{D(uncompressed)}$, assuming no modulation in molecular layer thickness (i.e., constant $g = d_0$) at the same actuation

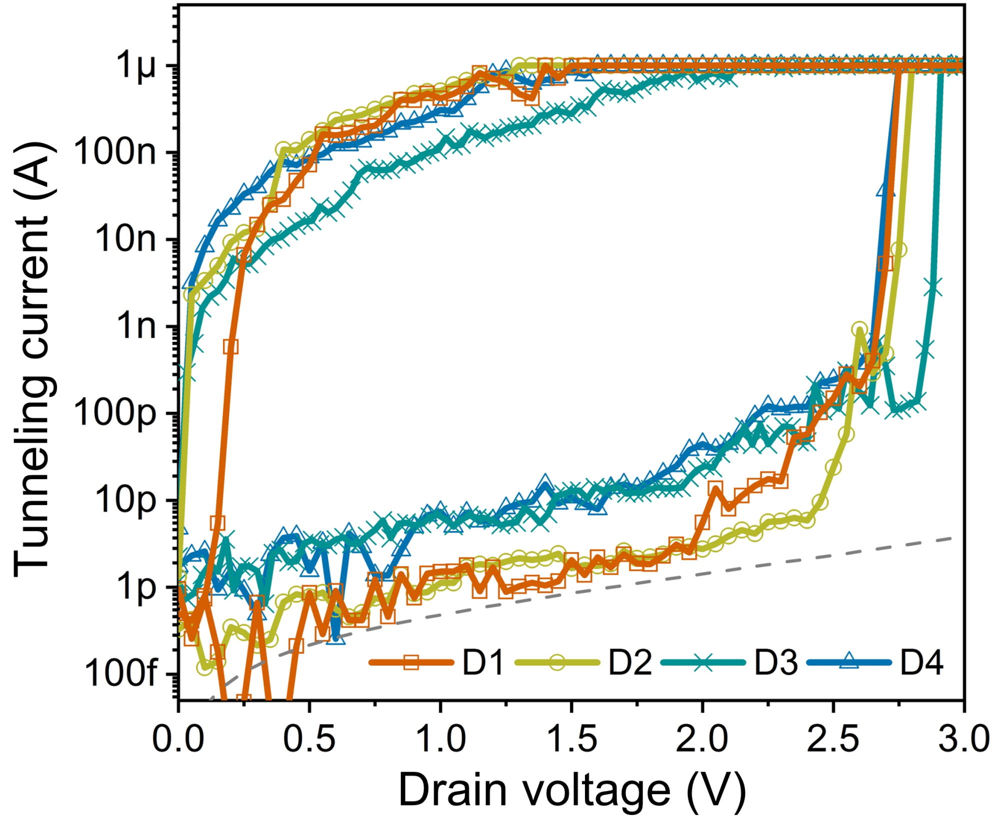


Figure 4-1: Experimental $I$-$V$ characteristics of example devices based on PEG-thiol spacers and an AuNR active electrode. The dashed curve provides a reference $I$-$V$ characteristic with respect to a constant molecular layer thickness extracted from low-voltage datapoints of D1.

voltage $V_{on}$ is calculated by the Simmons model. The modulation in current is therefore given by $I_{D(actual)}/I_{D(uncompressed)}$. It should be pointed out that the as-defined modulation in current is independent on the junction area and mainly determined by the thickness and the elastic properties of the molecular layer, which depend on the type of the molecule and the quality of self-assembled molecular layer. The device performance (actuation voltage, modulation in current) of the fabricated 130 devices form a random distribution (Figure 4-2 (b)). It agrees with the expectation that the molecular spacers assembled from 5 kDa PEG-thiol molecules are nonuniform in the initial thickness and the Young's modulus among devices. The statistics in Figure

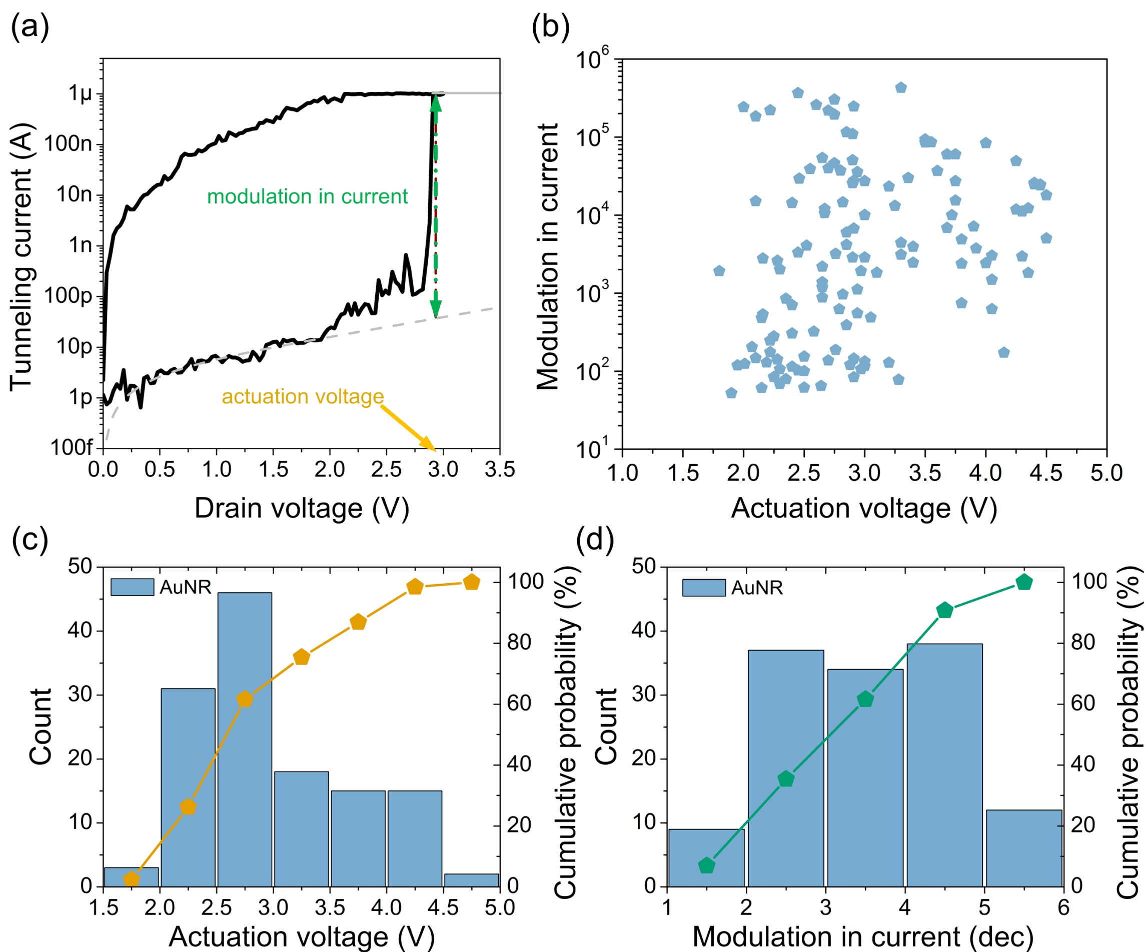


Figure 4-2: Statistics of device performance based on PEG-thiol molecular junctions and an AuNR active electrode. (a) Definition of the actuation voltage and the modulation in current for $I$-$V$ characteristics. (b) Distribution of device performance of AuNR nanoswitches. (c) Statistics of the actuation voltage. (d) Statistics of the modulation in current.

4-2 (c) and (d) indicate that 59.2% AuNR devices have actuation voltages between 2 V and 3 V and that 64.6% AuNR devices exhibit over three-orders-of-magnitude modulation in current beyond a pure tunneling behavior (i.e., >5 orders of magnitude on-off current ratio). The statistical results further evidence the superior performance of our tunneling nanoswitch over conventional NEM switches.

In order to study the device stability, we have conducted cycling measurement for the fabricated nanoswitches based on an AuNR active electrodes and PEG-thiol spacers. During continuous testing for over 100 cycles, a 100-nA compliance is selected

to further reduce heat generation from repetitive switching. The $I$-$V$ characteristics of two example devices over multiple operating cycles are shown in Figure 4-3. In the first example, the nanoswitch continuously operates with a pull-in phenomenon until it fails due to stiction after 23 cycles. Over these operating cycles, the pull-in voltage gradually decreases, while the currents at low voltages increase, resulting in decreasing modulation in current. We extract the molecular layer thickness at the beginning of each cycle using the low voltage datapoints and the Simmons model with parameters $S_S = S_D = 50 \times 500$ nm$^2$, $\Phi = 3.5$ eV, $\alpha_t = 0.57$. A gradual reduction in the initial molecular layer thickness can be observed in Figure 4-3 (c). Such a decreasing initial thickness leads to an increasing leakage and a decreasing pull-in voltage (Figure 2-5) in theory, when the Young's modulus does not increase significantly. This coincides well with the experimental results in Figure 4-3 (a).

There may be several explanations for why the molecular spacer is not able to recover to its initial thickness after each cycle. The most likely reason is the large compression in the molecular spacer after pull-in. To estimate the compression in the ON-state, we can assume the junction area of this nanoswitch to be the typical values $S_S = S_D = 0.5 \times 0.05$ $\mu$m$^2$ for convenience. The junction area may influence calculation of the absolute gap value but does not affect the calculation of compression as the area term cancels out. Barrier parameters from alkylthiols are still employed. For a nanoswitch whose tunneling current reaches 1 $\mu$A compliance at around 2.7 V, the molecular layer thickness in the ON-state is calculated to be 1.26 nm. Considering the OFF-state molecular layer thickness is 2.3$\sim$2.4 nm for the first few cycles, the corresponding compression from the OFF-state to the ON-state is over 45%. Such a large compression can possibly result in structural rearrangement that damages the self-assembled monolayer (SAM) [98], especially considering that the amorphous SAM assembled by the PEG-thiol with a large molecular weight is typically not densely packed. However, such reconfiguration does not necessarily cause immediate degradation and stiction. The device in Figure 4-3 (b) is able to cycle hundreds of times with acceptable performance ($>$3 orders on-off ratio at 1.5 V). Unlike the device in Figure 4-3 (a), the abrupt switching behavior in the $I$-$V$ characteristic of the first

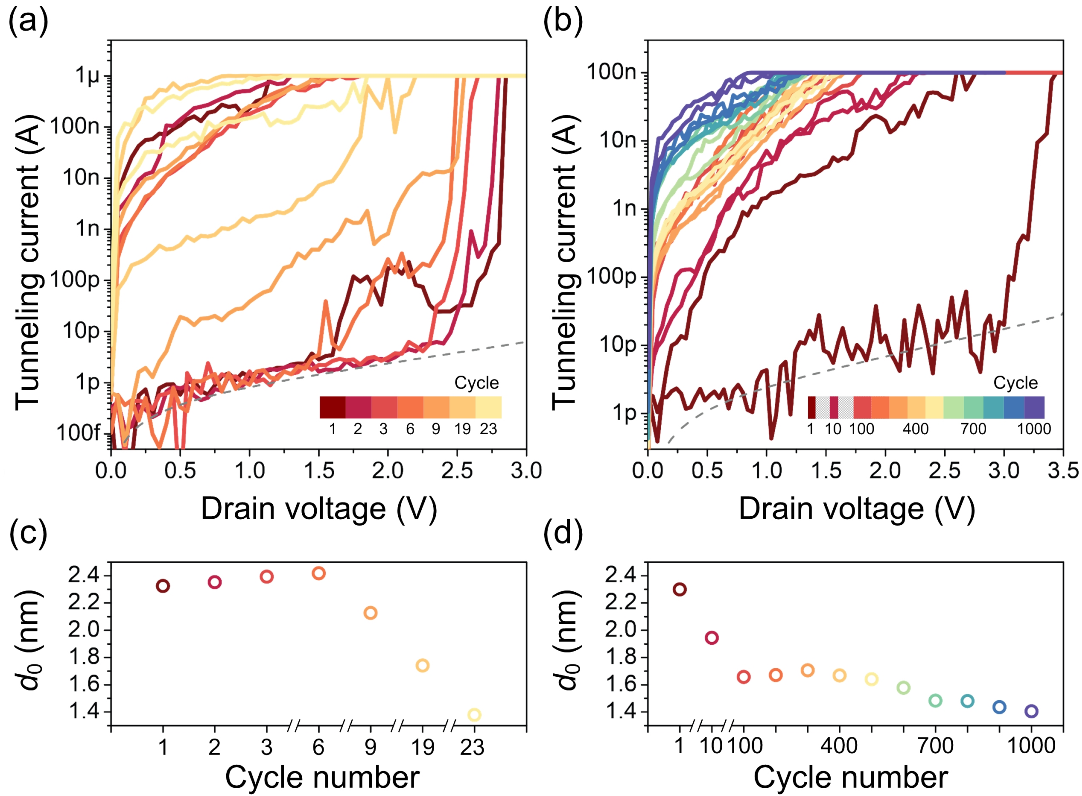


Figure 4-3: $I$-$V$ characteristics of example devices based on PEG-thiol molecular spacers and an AuNR top electrode over cycles. (a) Experimental $I$-$V$ curves over cycles for a representative device, which fails due to stiction after 23 cycles. (b) Experimental $I$-$V$ curves over 1000 cycles of another representative device. The dashed curves provide reference tunneling $I$-$V$ characteristics according to constant molecular layer thicknesses which are extracted from low-voltage datapoints of the 1st cycle for both (a) and (b). (c) Extracted initial molecular layer thicknesses of the device in (a) over 23 cycles. (d) Extracted initial molecular layer thicknesses of the device in (b) over 1000 cycles.

cycle disappears in subsequent cycles, and the nanoswitch then operates without pull-in and hysteresis. Besides, the initial molecular spacer thickness is gradually reduced in the first 100 cycles, and then remains almost constant for over 500 cycles before further degradation occurs.

The differences compared with the device in Figure 4-3 (a), in terms of absent pull-in and hysteresis, and stabilized initial spacer thickness after 100th cycle, are likely attributed to the change in the Young's modulus. Recall the theoretical study (Figure 2-6) on the effect of Young's modulus of the molecular spacer. An increase

in the Young's modulus allows absence of pull-in and hysteresis at a reduced initial molecular layer thickness, as the pull-in limit moves downward in Figure 2-6. After large compressions in the first few cycles, the structural reconfiguration may result in a thinner but stiffer SAM. The more densely packed SAM is more robust to compression, and the pull-in as well as hysteresis disappears in the $I$-$V$ characteristic, as a result of the increased Young's modulus. Though the speculated structural rearrangement of SAM under a large compression can explain the experimental results in Figure 4-3 (a) and (b), other possibilities such as electromigration and joule heating may also be contributing factors to the device degradation over cycles. Further understanding of the degradation mechanisms will inform designs for more stable device performance.

For AuNR-based nanoswitches, a single AuNR particle is preferred for the active electrode. It should be pointed out that devices with a bundle of nanoparticles as the active electrode exhibit similar $I$-$V$ characteristics (Figure 4-4) as those with a single nanoparticle as the active electrode; however, nanoswitches with multiple nanoparticles are less uniform in performance and more susceptible to stiction failure. Besides AuNR particles, Au nanoplatelets can be utilized as the active electrode as well. The $I$-$V$ characteristics of example devices are presented in Figure 4-5.

## 4.2 Tuning $I$-$V$ Characteristics through Molecular Engineering

Our theoretical studies suggest the significant role of mechanics of molecules to the static device behavior of the nanoswitches. Engineering the thickness and the Young's modulus of the self-assembled molecular layer may allow us to tune the $I$-$V$ characteristic of the nanoswitch. In order to demonstrate this tunability, we replace the PEG-thiol molecules with alkyl- and aryl-thiol molecules to form the molecular junctions of the nanoswitches. These types of molecules with alkane chains have been extensively investigated in the metal-molecule-metal motif [101,102,108,109]. Well-characterized barrier parameters for these molecules have been reported in literature [101], and they

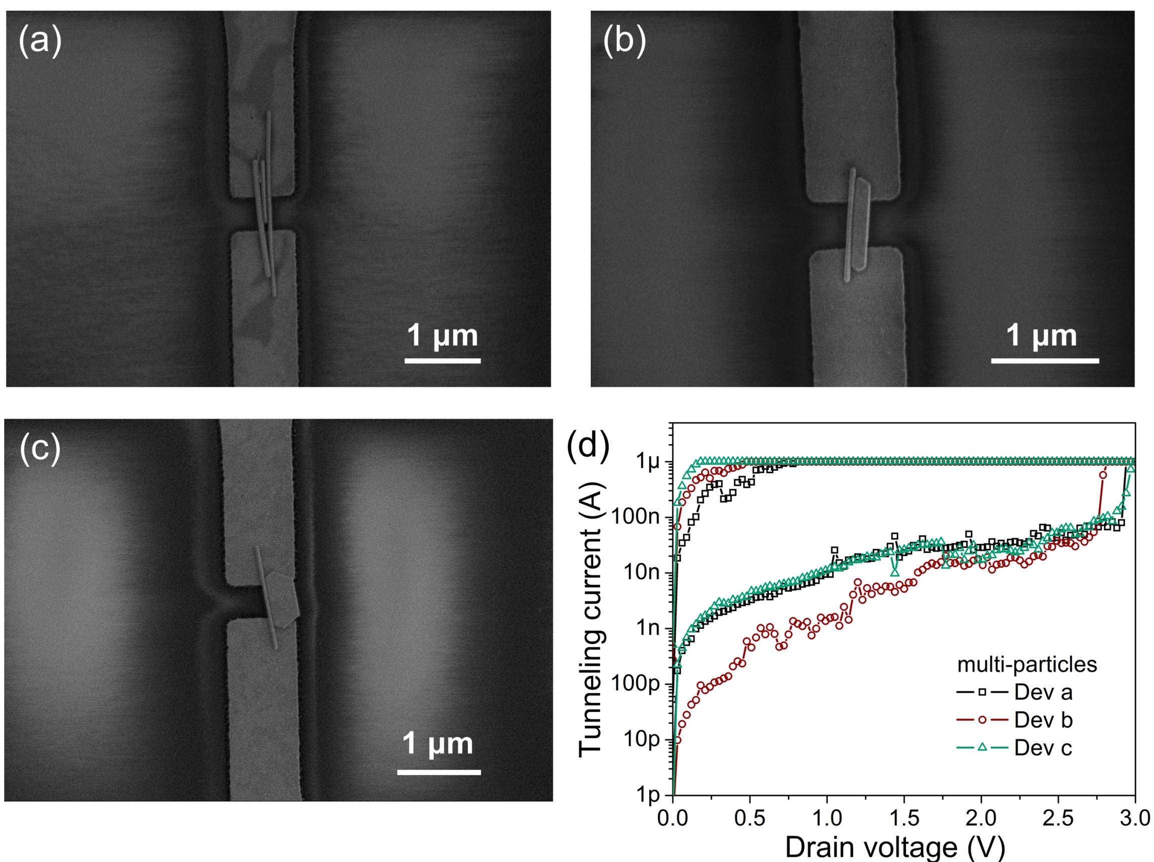


Figure 4-4: Devices with multiple Au nanoparticles. (a)-(c) SEM images of example devices with more than a single Au nanoparticle for the top electrode. (d) $I$-$V$ characteristics of the devices shown in (a)-(c). The compliance for the current is set as 1 $\mu$A.

are known to form well-packed, ordered monolayers [109], which allow us to extract the molecular layer thickness with better accuracy. In addition, the resulting SAMs are typically stiff, and no pull-in phenomena are expected in the $I$-$V$ characteristics of nanoswitches based on these molecules. The initial thickness and the Young's modulus of the molecular layer therefore directly influence the OFF-sate leakage (i.e., currents at low voltages) and the slope of the $I$-$V$ characteristic, respectively. Three molecules are utilized as the junction spacers including 1-dodecanethiol (DDT) and two specially designed arylthiol molecules (NMR spectra shown in Figure 4-6), tetradecyl 4-mercaptobenzoate (TDMB) and 2-decyltetradecyl 4-mercaptobenzoate (DTDMB). The DDT is commercially available from Sigma Aldrich, Inc. The TDMB and DTDMB are synthesized, via the acid-catalyzed esterification of 4-mercaptobenzoic acid

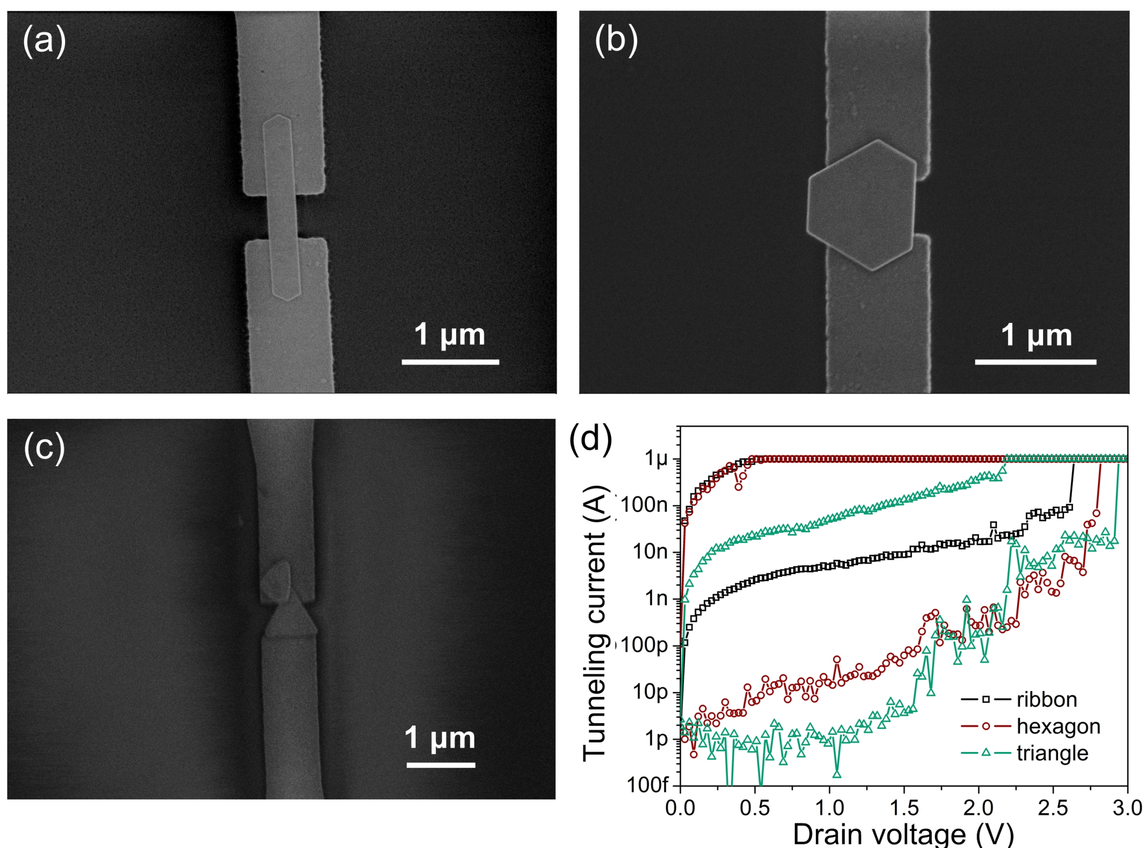


Figure 4-5: Devices with Au nanoplatelet top electrodes. (a) A NEM switch with a ribbon-shaped Au nanoplatelet. (b) A NEM switch with a hexagonal Au nanoplatelet. (c) A NEM switch with a triangular Au nanoplatelet. (d) $I$-$V$ curves of the devices shown in (a)-(c). The compliance for current is set as 1 $\mu$A.

with either 1-tetradecanol (for TDMB) or 2-decyl-1-tetradecanol (for DTDMB). The two arylthiol molecules are designed based on the considerations as follows.

Arylthiol headgroups anchoring long n-alkyl chains form SAMs with packing densities comparable to n-alkylthiol SAMs on gold surfaces [110, 111]. Additionally, the rate of thermal desorption of SAMs with arylthiol headgroups and long n-alkyl chains was found to be lower than for a comparable n-alkylthiol SAM, which suggests improved thermal stability due to the presence of anchoring arylthiol headgroups [112]. Other methods for improving SAM stability include adsorbates which chelate the gold surface [113], cross-linking of the monolayer [114, 115], and the incorporation of aromatic groups [116, 117].

Careful selection of the small molecules may allow us to tune the Young's modu-

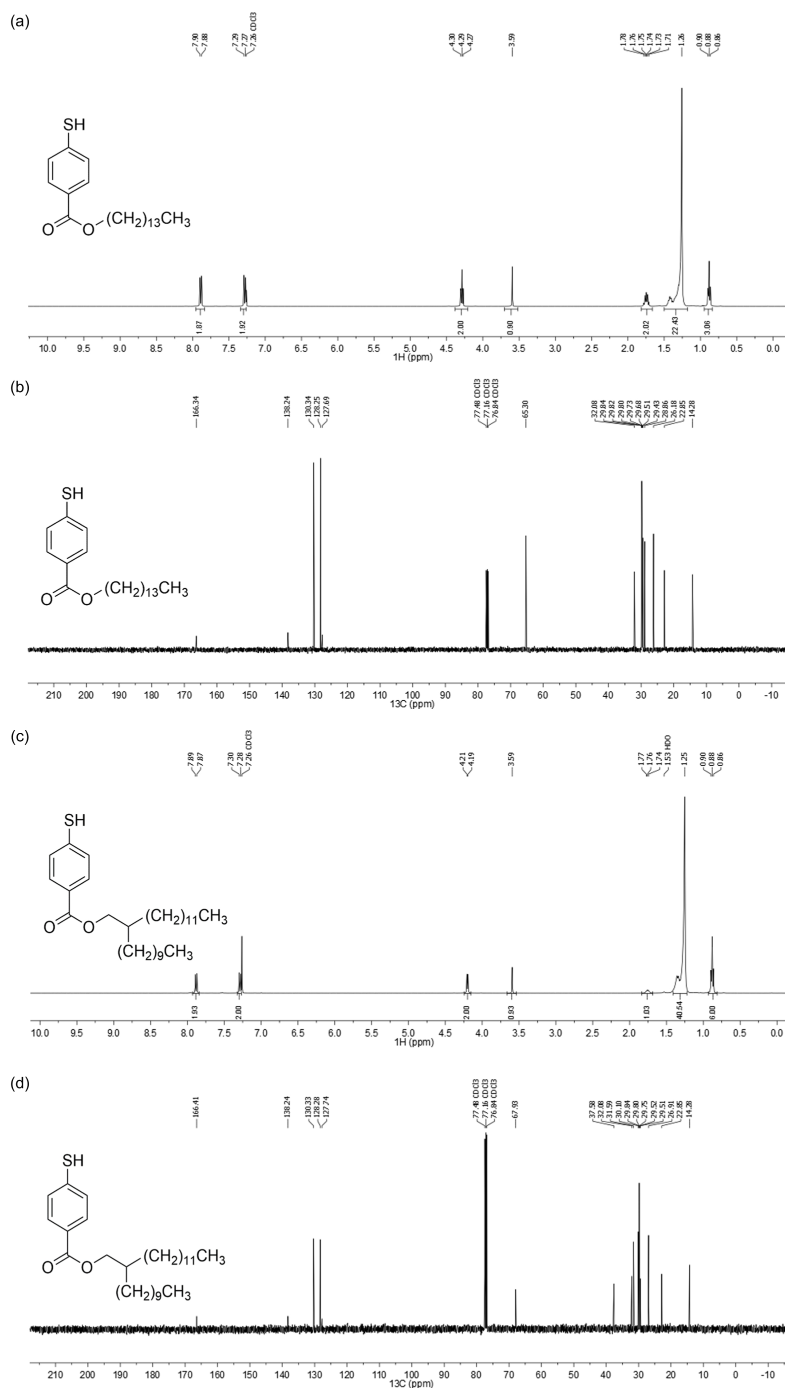


Figure 4-6: NMR Spectra of the synthesized molecules. (a) $^{1}H$ NMR spectrum (400 MHz, $CDCl_3$) of tetradecyl 4-mercaptobenzoate. (b) $^{13}C$ NMR spectrum (101 MHz, $CDCl_3$) of tetradecyl 4-mercaptobenzoate. (c) $^{1}H$ NMR spectrum (400 MHz, $CDCl_3$) of 2-decyltetradecyl 4-mercaptobenzoate. (d) $^{13}C$ NMR spectrum (101 MHz, $CDCl_3$) of 2-decyltetradecyl 4-mercaptobenzoate.

lus of the molecular layer and thereby optimize the device performance. The Young's moduli of several classes of SAMs have been estimated via AFM, including for alkanethiol (0.86 to 8.0 GPa) [118–120] and PEG-thiol (0.2 to 5 MPa) [99, 107]. These studies establish the dependence of compressibility of SAMs on many factors of molecular composition, including head group [121] and tail group identity [120], as well as spacer chain identity [122] and length [118, 119]. Notably, a study on the mechanical properties of alkanethiols of varying chain length demonstrated that the decrease in Young's modulus if short-chain alkylthiols corresponds with a decrease in the conformational order of the SAM [118]. Well packed, crystalline-like SAMs are stiffer than poorly-packed, more amorphous SAMs of similar composition. This conclusion may be utilized to design molecular layers with intermediate stiffness.

One molecular motif that has been shown to decrease the degree of conformational order of SAMs is branching, in which a single headgroup anchors two or more alkyl chains [113, 123]. Examples of branching resulting in lowered conformational order relative to simple n-alkylthiols may be found for a variety of headgroups, including alkylthiol [124] and alkoxyphenylethanethiol [125]. Therefore, branching is introduced in the molecular structure of 2-decyltetradecyl 4-mercaptobenzoate (DTDMB), which is hypothesized to form poorly-packed, more amorphous SAMs with lower Young's moduli. To spectroscopically probe the conformational order of the three molecules, grazing-angle ATR FTIR spectra of monolayers of DDT, TDMB and DTDMB on thermally-evaporated gold surfaces are obtained in the region of 3000-2800 $cm^{-1}$ (Figure 4-7) using a Thermo Fisher FTIR 6700 FTIR spectrometer with a liquid-nitrogen cooled MCT/A detector and a Harrick grazing angle ATR (GATR) accessory. For unbranched DDT and TDMB, the $\nu_a(CH_2)$ vibrational mode appears strongly near 2918 $cm^{-1}$, which indicates a high degree of conformational order. For the branched DTDMB, however, the $\nu_a(CH_2)$ vibrational mode is difficult to resolve, which is consistent with a lower degree of conformational order.

DDT, which forms a highly-ordered monolayer, should result in SAMs with the highest stiffness among the three molecules with alkane chains. The SAMs formed by DTDMB, which has larger arylthiol headgroups as well as branching, should have

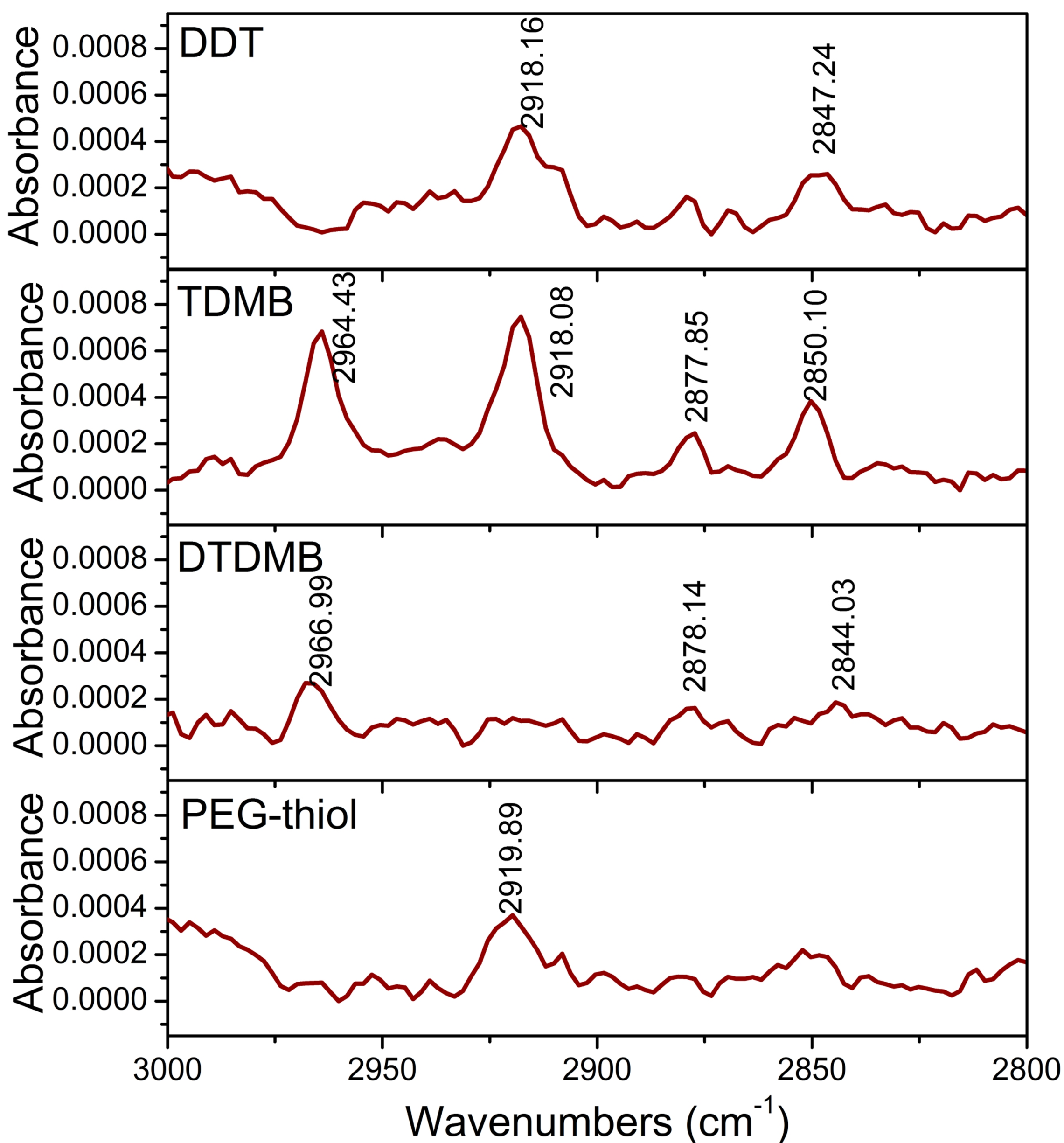


Figure 4-7: GATR-FTIR spectra of DDT, TDMB, DTDMB, and PEG-thiol monolayers. The monolayers are self-assembled on 1 $cm^2$ thermally-evaporated gold surfaces.

the lowest intermolecular order and exhibit the lowest effective Young's modulus. Besides, the molecular layer thickness and therefore OFF-state leakage can be affected by factors such as chain length and molecular tilt angle. The arylthiol headgroups add to the chain length and may result in slightly thicker SAMs than those formed

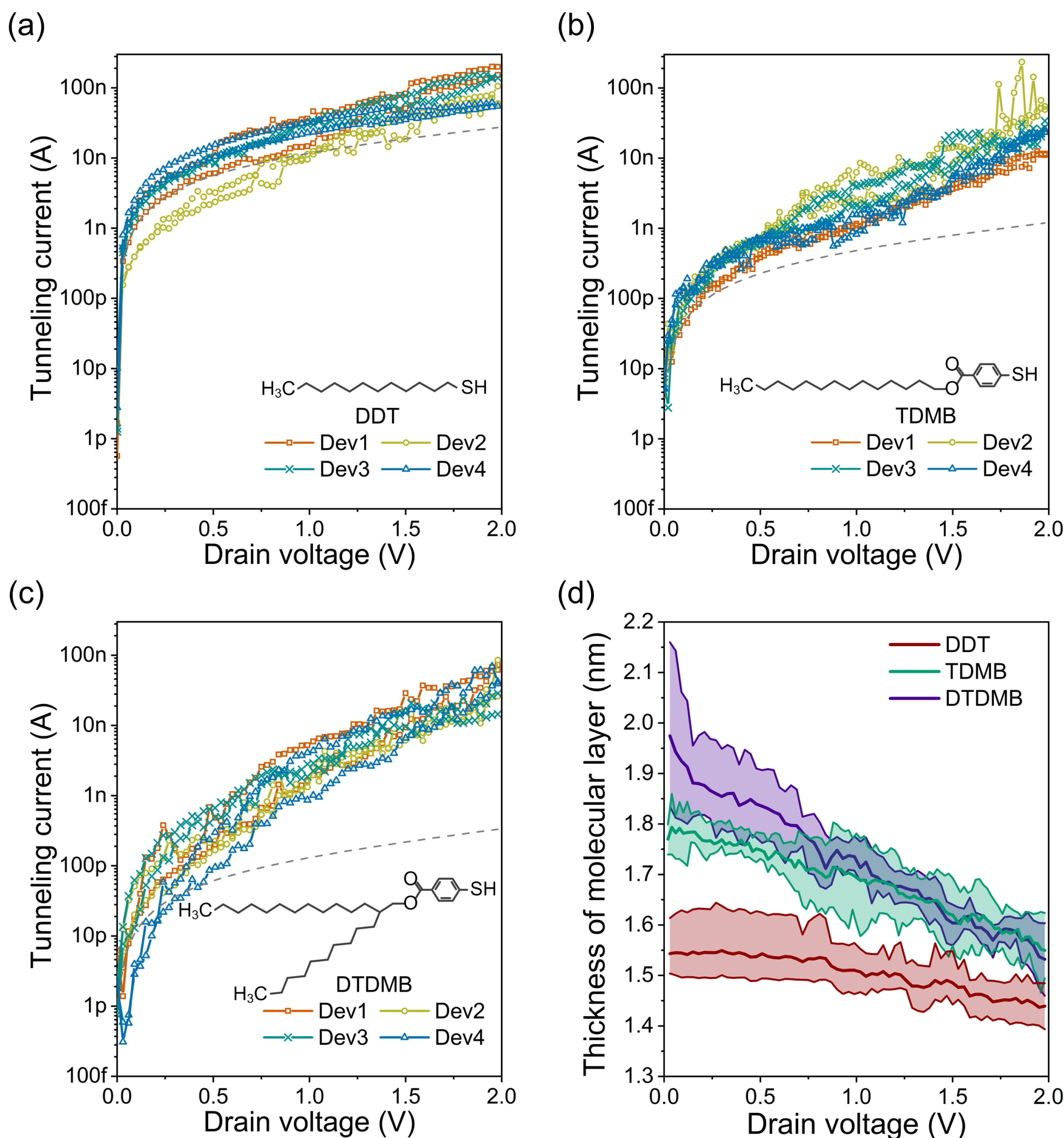


Figure 4-8: Comparison of $I$-$V$ characteristics of devices with different molecular junctions. (a) 1-dodecanethiol (DDT). (b) tetradecyl 4-mercaptobenzoate (TDMB). (c) 2-decyltetradecyl 4-mercaptobenzoate (DTDMB). (d) Variation of the molecular layer thickness with the drain voltage for devices in (a)-(c).

by DDT. The poorly packed, more amorphous SAMs formed by DTDMB may have a smaller molecular tilt angle and therefore larger thicknesses than those formed by TDMB.

The $I$-$V$ characteristics of nanoswitches fabricated with DDT, TDMB and DT-

DMB have been compared in Figure 4-8. Indeed, the performance of our devices exhibit a behavioral trend closely linked to the predicted molecular properties. The dashed curve in each subfigure describes a pure tunneling $I$-$V$ characteristic assuming a constant molecular layer thickness, which is extracted from the low-voltage data-points of Dev1. Devices based on DTDMB exhibit the highest modulation in current, while the $I$-$V$ characteristics from devices based on DDT follow the pure-tunneling reference curve closely. With regard to the OFF-state leakage, we consider the tunneling current at ∼0.1 V. The leakage current of TDMB-based devices is larger than that of DTDMB-based devices by ∼8 times on average, but smaller than that of DDT-based devices by over 1.5 orders of magnitude. We further extract the molecular layer thicknesses from these experimental $I$-$V$ characteristics. Two identical junctions, each with an area of $50\times500$ nm$^2$, are assumed and the parameters for alkyl- and aryl-thiols used in the Simmons model are $\Phi = 3.5$ eV and $\alpha_t = 0.57$. We observe from Figure 4-8 (d) that DTDMB results in the thickest and the most compliant molecular spacers among the three, while DDT forms the thinnest and stiffest molecular spacers. These experimental results align well with the predicted properties of the three molecules.

Further, the nanoswitches based on DDT, TDMB and DTDMB are measured over 100 cycles. The behavioral trends for the three molecules over 100 cycles are consistent with those in Figure 4-9, which further verifies the relative mechanical properties of SAMs formed by DDT, TDMB and DTDMB. Besides, the cycling $I$-$V$ characteristics of devices based on DDT, TDMB and DTDMB seem more stable than those of PEG-based devices, which again suggests the correlation between device stability and mechanics of molecules. Overall, the close link between the mechanical properties of the molecular spacers and the respective $I$-$V$ characteristics from our experimental results demonstrates that static device performance of the tunneling nanoswitch can be tuned through molecular engineering.

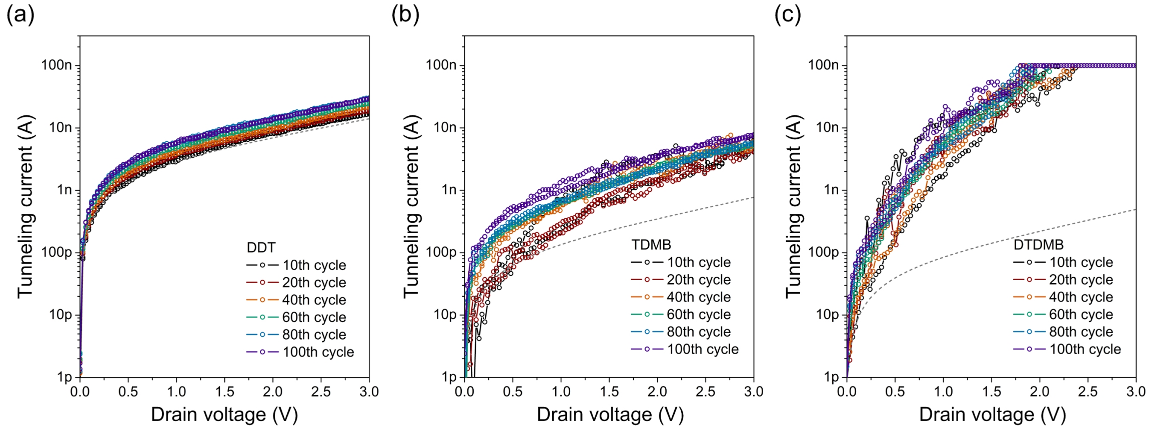


Figure 4-9: $I$-$V$ characteristics of devices with different molecules over 100 cycles. (a) 1-dodecanethiol (DDT). (b) Tetradecyl 4-mercaptobenzoate (TDMB). (c) 2-decyltetradecyl 4-mercaptobenzoate (DTDMB). The compliance for current is set as 100 nA. The dashed curve in each figure provides a no-modulation pure tunneling reference $I$-$V$ characteristic based on a constant spacer thickness extracted from low-voltage datapoints of the 10th cycle.

## 4.3 Dynamic Responses of Nanoswitches Based on Poly(ethylene glycol)thiol Molecular Spacer and Gold Nanorod Active Electrode

High switching speed is another predicted feature of our developed tunneling nanoswitches, thanks to the small (∼1 nm) mechanical modulation required to transition between their OFF-state and ON-state. To demonstrate this advantage, the turn-on delays of devices based on an AuNR active electrode and PEG-thiol spacers are measured by experiments.

The setup for measurement of the turn-on delay is shown in Figure 4-10. A SIGLENT SDG5000 function generator produces a 2-$\mu$s wide pulse signal with a 6-ns rise time. A pulse amplitude of 6 V is selected to ensure that the nanoswitches remain reliably closed in the ON-state and that the RC delays of the nanoswitches are negligible. Two passive 10× voltage probes (8 pF capacitance), connected to a Tektronix TDS3054C oscilloscope, are used to measure the waveforms of the pulse signal and the voltage across a 1-MΩ resistor, which samples the current through the

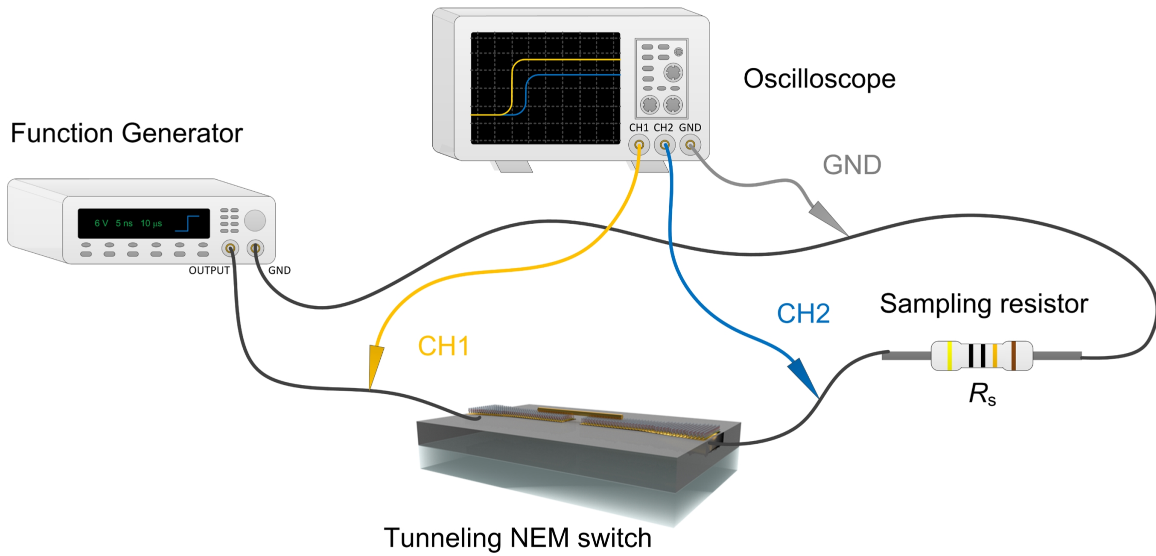


Figure 4-10: Schematic of the experimental setup that measures the device dynamic response.

nanoswitch. The exponential dependence of the tunneling current on the thickness of molecular spacer creates an abrupt switching with a several-orders-of-magnitude on-off current ratio. As a result, the voltage across the 1-MΩ sampling resistor ($V_{Rs}$) in series with the nanoswitch shows a noticeable increase only after the nanoswitch turns on. The onset of the $V_{Rs}$ waveform can thus provide a good estimate for the moment when the nanoswitch turns on, which has been theoretically proved (Figure 2-8).

In the actual measurement setup, the parasitic inductance, capacitance of cables and impedance mismatch of the measurement circuit could cause electrical delay that does not stem from the nanoswitch itself. Therefore, the response of $V_{Rs}$ for the first few nanoseconds is likely caused by the measurement circuit rather than the actual behavior of the nanoswitch. The capacitance of the nanoswitch with typical dimensions shown in Figure 3-6 (a) is estimated to be below 1 fF, which is over 3-orders-of-magnitude smaller than the capacitance in the measurement circuit. As a result, the electrical delay caused by charging the capacitance of the nanoswitch is negligible. To exclude the influence from the measurement circuit, an open-circuit control experiment is first conducted, and the transient waveforms of the pulse signal (i.e., $V_s$(OC)) and the voltage across $R_s$ (i.e., $V_{Rs}$(OC)) are shown in Figure 4-11.

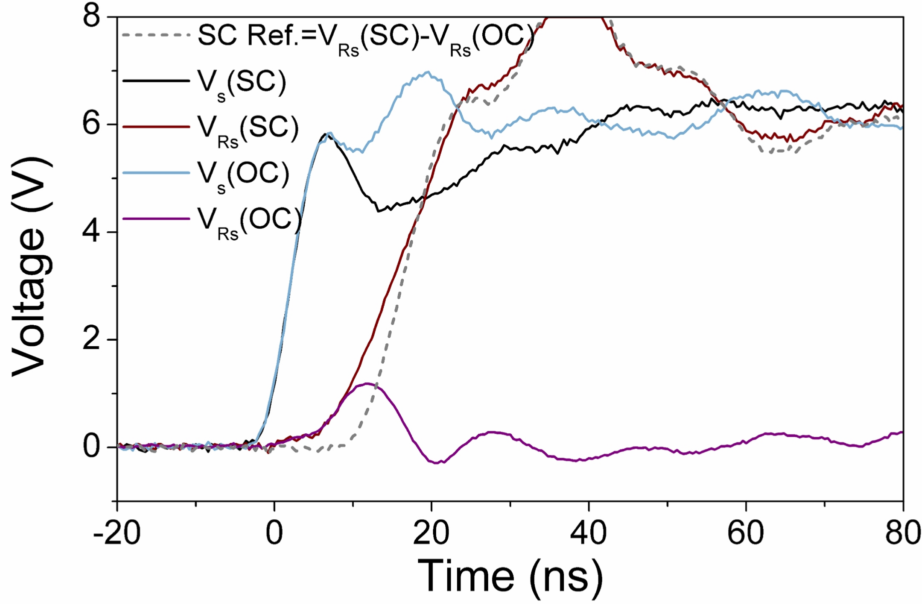


Figure 4-11: Dynamic responses from open-circuit and short-circuit control experiments. In both cases, the non-zero voltage signals across the sampling resistor $R_s$ for the first few nanoseconds after applying the pulse come from the measurement circuit and therefore the processed short-circuit $V_{Rs}$ waveform, which is free from device delay, can work as a reference to eliminate the electrical delay from the setup.

When a nanoswitch is measured, the transient voltage across the sampling resistor $R_s$ is same as that in the open-circuit control experiment ($V_{Rs}$(OC) waveform in Figure 4-11), if the nanoswitch is in the OFF-state. After the nanoswitch turns on, a conducting path through the nanoswitch and $R_s$ is added into the measurement circuit topology. As a result, the time constant of the measurement circuit is changed and the $V_{Rs}$ waveform starts to deviate from the open-circuit response. In order to find the exact split point (i.e., the moment when the switch turns on), the open-circuit $V_{Rs}$ waveform is subtracted from the $V_{Rs}$ waveform with a nanoswitch connected in circuit. Though the as-processed waveform itself does not possess a clear physical meaning, the onset of its rising edge can indicate the moment at which the nanoswitch turns on.

Such waveform processing, however, cannot exclude the electrical delay from the measurement circuit. In order to obtain a more accurate estimate of the turn-on delay

caused by the nanoswitch, another short-circuit control experiment is conducted by directly shorting the pins that probe the nanoswitch ($R_s$ is connected directly to the pulse generator in this case). The transient $V_{Rs}$ waveform (i.e., $V_{Rs}$(SC)) is shown in Figure 4-11. After subtracting the $V_{Rs}$ waveform obtained from open-circuit control experiment, we observe that the onset of processed $V_{Rs}$ rising edge (SC Ref.) obtained in short-circuit experiment corresponds to $t_0 = 8.8$ ns. Since the nanoswitch is not connected in circuit, such a delay only includes the electrical delay from the measurement circuit. The as-processed $V_{Rs}$ waveform therefore provides a reference to help exclude the electrical delay from the measurement circuit. In another word, the turn-on delay from a nanoswitch can be estimated by the difference in time between the onset of $V_{Rs}$ rising edge ($t_{on}$) measured with the nanoswitch in circuit and that of short-circuit reference waveform ($t_0 = 8.8$ ns).

The dynamic response of an example device based on PEG-thiol spacers and an AuNR active electrode over multiple cycles is presented in Figure 4-12, which includes waveforms of the pulse signal (dashed curves), the short-circuit reference edge (short dashed curve) and the voltage across sampling resistor $R_s$ (solid curves). In the first cycle, the onset of $V_{Rs}$ rising edge corresponds to $t = 14.8$ ns, which leads to a turn-on delay of 6 ns. Such a short turn-on delay verifies that our tunneling nanoswitch well outperforms conventional MEM/NEM switches [25, 35] based on relay architectures in terms of switching speed. This delay is even better than those from NEM switches based on lightweight nanoparticle (e.g., MWCNT, graphene) active electrodes [36,37]. It is interesting to observe that the turn-on delay gradually decreases in the subsequent cycles from 6 ns to 3.2 ns. Considering the dependence of the turn-on delay on the properties of molecular spacer, the decreasing turn-on delay we observe is likely caused by the same reason for the device degradation observed in cycling $I$-$V$ characteristics (Figure 4-3), i.e., irreversible compression in the molecular spacer. Specifically, when the device is switched on by an applied pulse voltage, the large compression may result in structural reconfiguration in the molecular layer, whose thickness is unable to recover to its initial value. The repetitive switching results in a thinner and thinner molecular spacer after each cycle, and the time required to switch on the device is

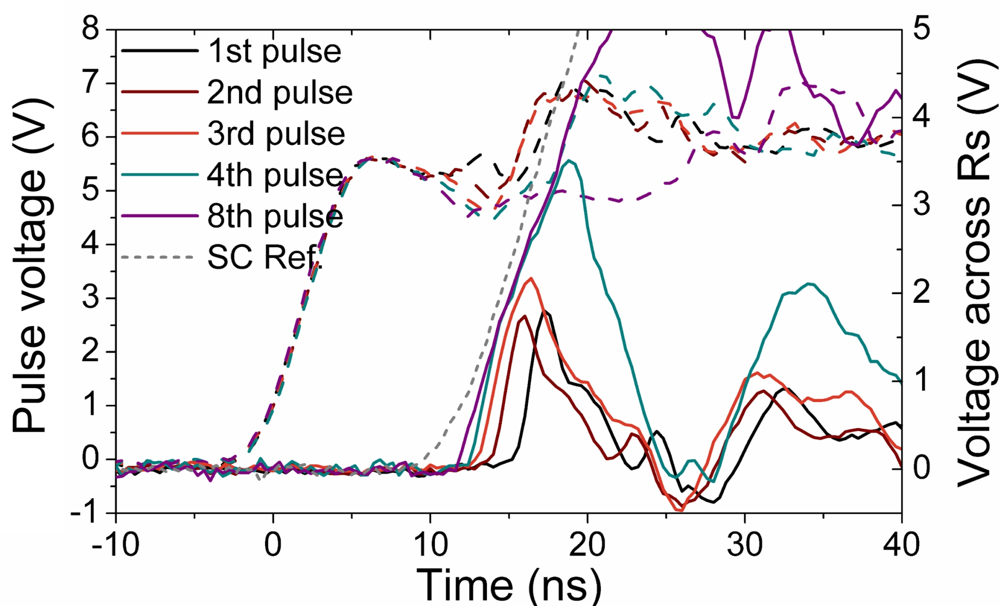


Figure 4-12: Dynamic response of an AuNR nanoswitch over multiple pulses. Decreasing turn-on delay suggests that the molecular layer thickness under zero drain voltage is reduced after each pulse.

therefore gradually decreasing. We also notice that the $V_{Rs}$ value after the nanoswitch turns on is increasing after each cycle, suggesting that the molecular layer in the ON-state gets thinner as well. These results collectively provide extra evidence (from the aspect of device dynamic response) for our speculation that large compression may cause structural change and thus irreversible reduction in the initial thickness of the PEG-thiol spacer.

## 4.4 Tuning Switching Speed through Engineering the Nanoscale Active Electrode

Similar to the $I$-$V$ characteristics, the device dynamics are dependent on the Young's modulus and the initial thickness of the molecular spacer as well. Unlike the $I$-$V$ characteristics, the device dynamics have strong dependence on the inertia of the active electrode, which thereby offers a tunability on the switching speed by changing

the mass of active electrode without affecting the $I$-$V$ characteristic in theory.

To demonstrate this tunability, we fabricate devices based on the same PEG-thiol molecular spacers but different nanoparticle active electrodes of similar dimensions, i.e., either AuNR (1∼2 $\mu$m long, 80∼100 nm thick) or MWCNT (1∼2 $\mu$m long, 100∼150 nm thick). $I$-$V$ characteristics and dynamic responses for these two type of nanoswitches are compared.

The $I$-$V$ characteristics of example MWCNT devices from different batches are shown in Figure 4-13, which resemble those of AuNR devices (Figure 4-1). The MWCNT devices exhibit similar pull-in voltages as AuNR devices. Tunneling behavior with some modulation in current caused by compression in the molecular layer is observed for both AuNR devices and MWCNT devices, as compared to constant-gap tunneling behavior (dashed line). There are some differences between their $I$-$V$ characteristics as well. The leakage current of MWCNT devices on average is slightly higher than that of AuNR devices, which is caused by the different geometries of the two nanoparticles. A MWCNT is more likely to sink into the molecular spacer after trapping due to its curvature, resulting in a smaller tunnel gap in the OFF-state than that of a nanoswitch with an AuNR electrode which has single-crystal flat facets. Besides, steeper slopes of the $I$-$V$ curves and more modulation in current before pull-in occurs are observed for MWCNT devices, which can be explained by the different geometries as well. For a MWCNT device, the molecules underneath the particle are likely compressed, while those near the edges of the MWCNT are likely pushed aside due to the curvature of MWCNT. As a result, the restoring force on the MWCNT may be weaker compared to those on nanoparticles with single-crystal flat facets, and more compression can be expected for MWCNT devices than AuNR devices under the same voltage (lower than $V_{pi}$).

We further conduct a statistical study on the performance of MWCNT devices using the same metrics as we did on AuNR devices. Figure 4-14 (a) shows the distribution in performance, which overlaps well with that of AuNR devices (Figure 4-2). The distribution is also believed to be caused by the nonuniform stiffness and initial thickness of the molecular spacers among devices, considering that the same

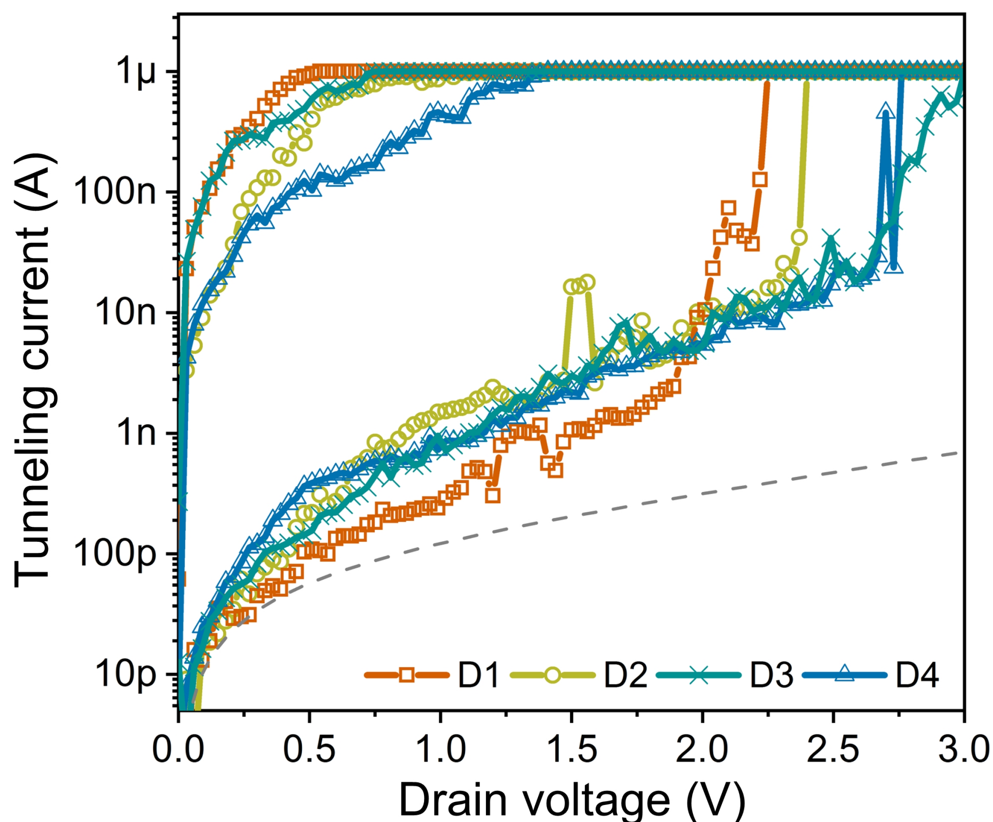


Figure 4-13: Experimental $I$-$V$ characteristics of MWCNT devices. The dashed curve provides reference pure tunneling $I$-$V$ characteristic according to a constant molecular layer thickness extracted from low-voltage datapoints of D1.

5 kDa PEG-thiol molecules are employed for both types of devices. The statistics suggest that 48.7% MWCNT devices have actuation voltages between 2 V and 3 V, and 46.0% MWCNT devices exhibit over three-orders-of-magnitude ON-state modulation in current (i.e., >5 orders of magnitude on-off current ratio). Overall, the $I$-$V$ characteristics of MWCNT nanoswitches are parallel with those of the nanoswtiches fabricated using similar-size AuNR particles.

The turn-on delays of the MWCNT devices are measured using the same approach, setup and conditions as those for AuNR devices. It should be pointed out that the dynamic measurement is destructive and the nanoparticle can burn out even after applying a single pulse due to the high discharge current. But comparing the dynamic

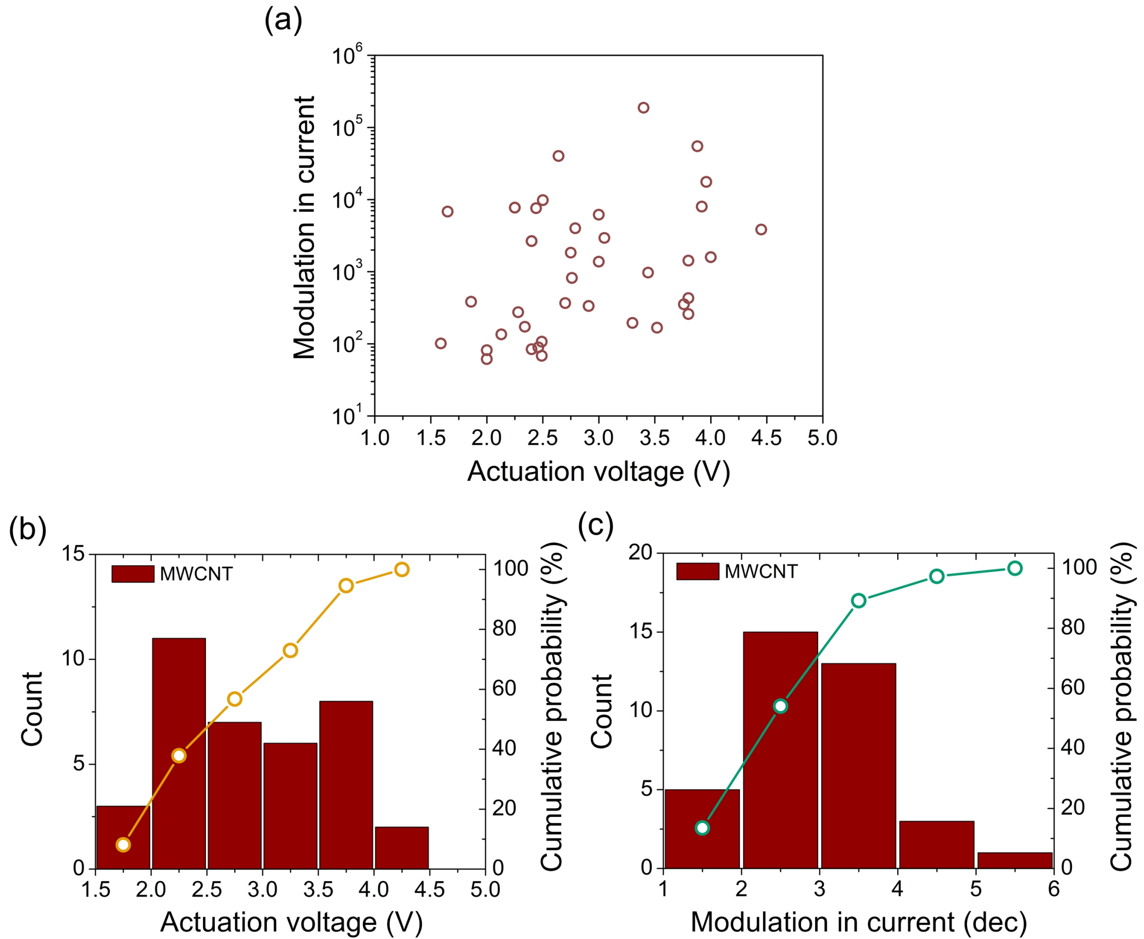


Figure 4-14: Statistics of device performance based on PEG-thiol molecular junctions and a MWCNT active electrode. (a) Distribution of device performance of MWCNT nanoswitches. (b) Statistics of the actuation voltage. (c) Statistics of the modulation in current.

responses before and after the nanoparticle electrode burns out leads to interesting findings. For instance, the SEM image in Figure 4-15 (a) shows a broken MWCNT electrode, which was likely burned by high discharge current after applying the first pulse. The $V_{Rs}$ waveforms in the first two cycles are presented in Figure 4-15 (b), which present the device dynamic responses before and after the MWCNT electrode broke. The $V_{Rs}$ signal deviated from that in the open-circuit control experiment (reflected by non-zero processed $V_{Rs}$ waveform) only before the MWCNT was burned (first cycle), while the processed $V_{Rs}$ waveform remained zero after the MWCNT was burned (second cycle). It further validates that the waveform split is caused by the

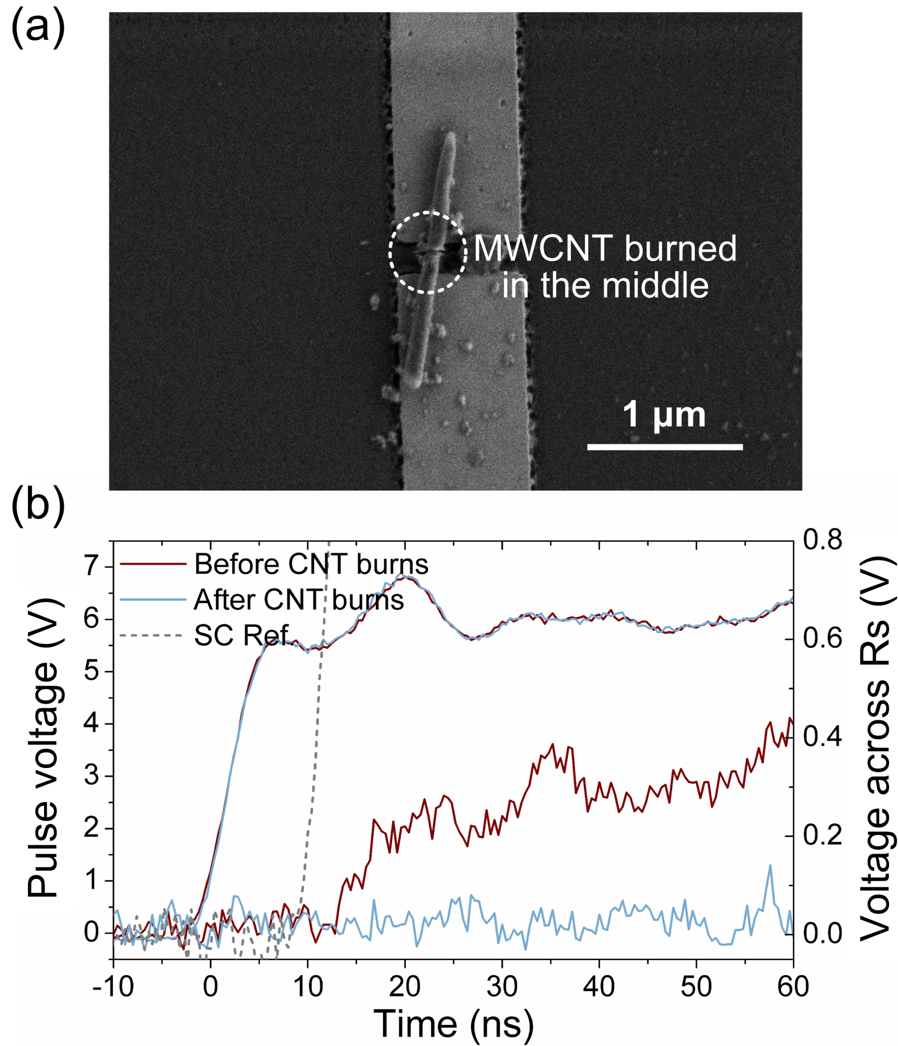


Figure 4-15: Dynamic responses of a nanoswitch before and after the MWCNT electrode was burned. (a) The SEM image of a nanoswitch with a MWCNT electrode likely burned by a high discharge current. (b) Comparison between dynamic responses of the nanoswitch before and after the electrode broke.

switching behavior of the device and that the rising edge of the processed waveform can be used to determine the moment at which a nanoswitch turns on, which supports our measurement approach for the turn-on delay.

The dynamic responses of AuNR devices and MWCNT devices are compared in Figure 4-16. The short-circuit reference waveforms in Figure 4-16 (a) and (b) are identical. Different $V_{Rs}$ values in the ON-state are observed, owing to difference in conductivity between AuNR particles and MWCNT particles. The AuNR devices

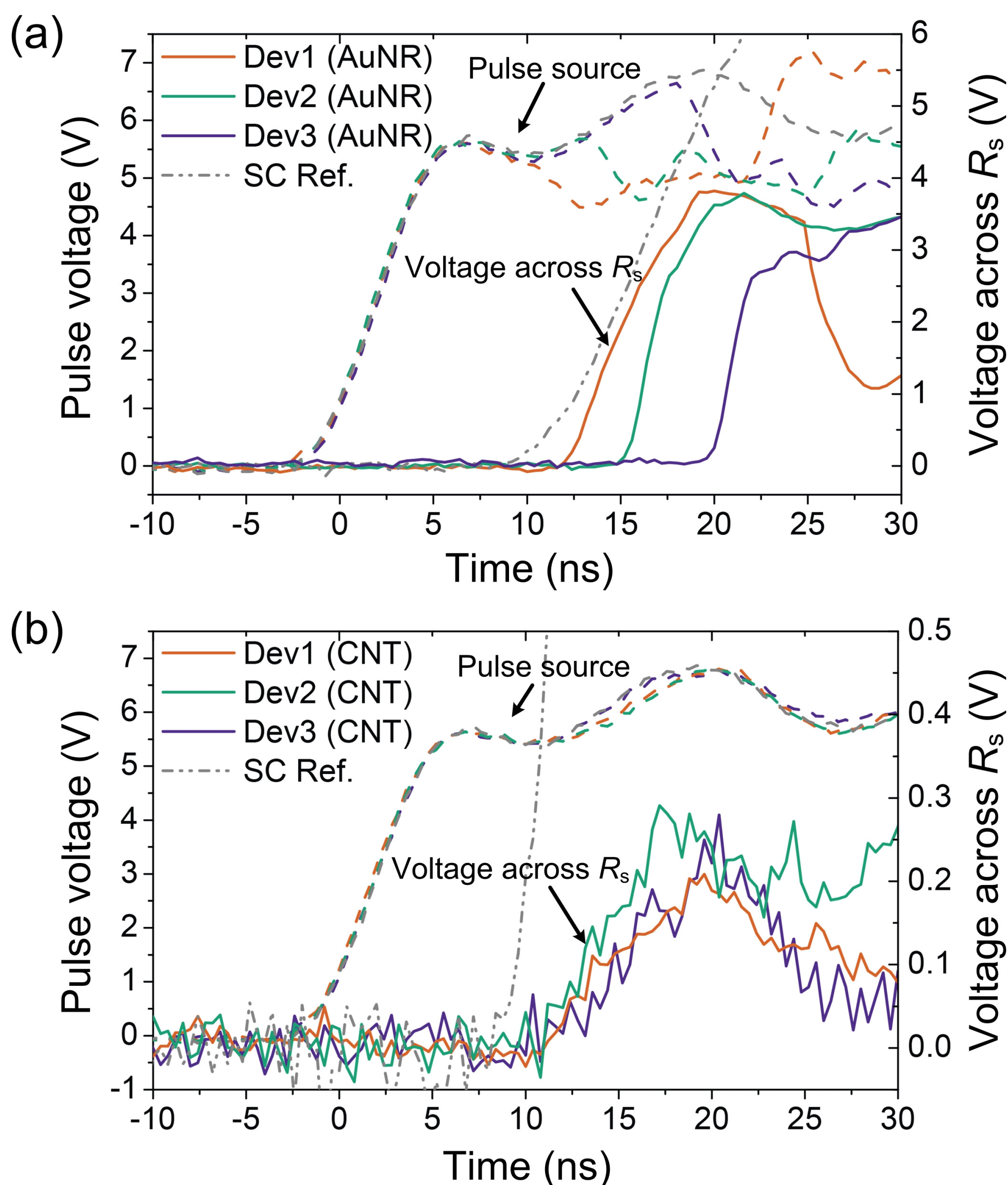


Figure 4-16: Comparison between the turn-on delays of AuNR nanoswitches and those of MWCNT nanoswitches. (a) Dynamic responses of devices with 5 kDa PEG-thiol junctions and an AuNR electrode (1∼2 $\mu$m in length and 80∼100 nm in diameter). (b) Dynamic responses of devices with 5 kDa PEG-thiol junctions and a MWCNT electrode (1∼2 $\mu$m in length and 100∼150 nm in diameter).

switch on at $t_{on}$ =12.4 ns, 15.2 ns, 18.8 ns, corresponding to a minimum turn-on delay of 3.6 ns. In comparison, the MWCNT devices turn on at $t_{on}$ =10.8 ns, 11.2 ns,

12.8 ns, resulting in a reduced minimum turn-on delay of 2 ns. Such a turn-on delay is even lower than the minimum value ever reported, which is from a single-walled CNT switch actuated at a comparable voltage [33]. The switching speed can be further improved by reducing the dimensions of MWCNT particles or applying other lighter miniaturized moving contact. More significantly, observation of the reduced delay using MWCNTs versus AuNRs demonstrates that the dynamics of these nanoswitches can be engineered by judicious top contact selection, without affecting the device static behavior. Therefore, the molecules and the nanoparticle electrode constitute two degrees of design freedom for the nanoswitch, enabling independent tuning on the $I$-$V$ characteristic and the switching speed.

# Chapter 5

# Towards High-Performance Nanoelectromechanical Switches: Summary and Outlook

## 5.1 Summary

NEM switches are a candidate technology for beyond-CMOS energy-efficient computing. The abrupt switching behavior, near-zero leakage current and robust performance in harsh environment make them particularly favorable and attractive for applications with energy-consumption concerns such as the internet of things. However, high actuation voltages and slow speeds are significant hurdles to overcome before NEM switches can fulfill their promise. The simultaneous achievement of a low turn-on voltage and a high speed requires both reversible modulation of a nanometer-scale switch gap and an ultra-small, lightweight active component for the moving contact. These bring significant challenges to the design and fabrication of NEM switches, which usually results in a device performance compromise. Introducing active nanostructures as functional components to replace classical counterparts has been treated as a viable pathway to overcome longstanding challenges facing nanoelectronics. Molecules and nanoparticles, as attractive active nanostructures, have become increasingly pop-

ular for building electromechanical devices and systems in pursuit of unique device concepts and enhanced performance. Specifically for NEM switches, a self-assembled molecular spacer could create a stable nanometer-scale switch gap, and a nanoparticle could act as a lightweight, miniaturized moving contact, which perfectly cater to the demands for achieving high-performance NEM switches.

A novel tunneling nanoswitch has been developed in this thesis using molecules as nanoscale springs and nanoparticles as active electrodes. The molecular springs assembled between the bottom electrodes and the top nanoparticle electrode provide a strong restoring force under compression, thereby creating a stable and reversible nanometer-scale tunnel gap. This enables our devices to switch by electrostatically tuning the nanogap and thereby exponentially modulating the current tunneling through the molecular junction. Thanks to the unique mechanism, a mere $\sim$1 nm change in the molecular layer thickness is sufficient to switch our device, which allows simultaneous low-voltage, high-speed switching. The nanoparticle electrode, as another active nanostructure in design, defines an ultra-small device pitch and significantly reduces the switching delay.

Theoretical modeling and simulation have revealed strong dependence of the device performance on the properties of these active nanostructures. Specifically, the stiffness and the initial thickness of the molecular spacers create a design space to configure the static device behavior in terms of actuation voltage and modulation in current. Diverse $I$-$V$ characteristics in terms of existence of a pull-in phenomenon, leakage current and actuation voltage are predicted based on different combinations of the stiffness and the initial thickness of the molecular layer. This suggests a possibility of tuning the $I$-$V$ characteristic of this device through molecular engineering approach. Molecular springs designed with specific nonlinearities are predicted to bring the actuation voltage down to hundreds of millivolts. The inertia of the active nanoparticle electrode is critical to device dynamics but irrelevant to statics. Numerical simulation verifies the possibility of tuning the turn-on delay through changing area mass density of the moving contact without affecting the $I$-$V$ characteristic. Therefore, the switching speed can be engineered by judicious selection of

the moving contact from the vast library of nanomaterials available, and switching in the GHz-regime is viable by employing a miniaturized, lightweight nanoparticle active electrode (e.g. CNTs, Si nanowires). More significantly, the molecules and the nanoparticle moving contact offer two independent degrees of freedom to design static and dynamic device performance and thus enable simultaneous achievement of a low actuation voltage and a high switching speed.

A universal platform has been developed to assemble high-performance devices based on diverse molecules and nanoparticles following a bottom-up approach. The device concept of the tunneling nanoswitch is established on modulation of nanometer-thick molecular junction; however, the surface roughness resulting from conventional deposition techniques typically leads to device failure or degradation. Our platform enables fabricating uniform molecular junctions sandwiched between atomically-smooth surfaces, provided by the active nanoparticle and the template-stripped bottom electrodes. Moreover, a scalable, self-limiting approach has been designed for assembly of nanoparticle electrodes, thus enabling high-throughput fabrication and statistical study on the characteristics of our devices.

A soft and thick molecular spacer offers a negligible OFF-state leakage, a large on-off current ratio, an abrupt switching at low voltage with a steep subthreshold slope. PEG-thiols as model molecules have been utilized to fabricate proof-of-concept devices. Statistical study shows majority of our nanoswitches demonstrate sub-3-V actuation voltages and $>$5 orders-of-magnitude on-off current ratios. The subthreshold swings and turn-on delays of our example AuNR devices are as low as 30 mV/dec and 3.6 ns, respectively. The superior properties over classical NEM switches arise from the unique switching mechanism that requires only $\sim$1 nm modulation of a nanometer-scale gap. Further, we have fabricated nanoswitches based on three different molecules with alkane chains that are expected to have different stiffness due to their molecular compositions and conformational orders of the resulting SAMs. Comparison in terms of leakage and slope of the $I$-$V$ characteristics based on these molecules aligns well with their predicted stiffness and thicknesses. The close link between the properties of the molecular spacers and the $I$-$V$ characteristics demon-

strates tunability on the device static behavior afforded by engineering the molecules. MWCNT and AuNR particles of similar dimensions are employed as the "light" and "heavy" active electrodes for devices based on PEG-thiol spacers, respectively. Similar actuation voltages and modulation in current are observed from the resulting devices. A turn-on delay as low as 2 ns has been achieved with the MWCNT active electrode. Reduced turn-on delay using MWCNT versus AuNR demonstrates that the switching speed of our nanoswitches can be tuned by engineering the moving contact.

The performance of our tunneling nanoswitch is compared to other representative NEM switches in Table 5.1. Simultaneous low actuation voltage and short turn-on delay achieved by our devices, which outperform classical NEM switches, arise from the unique mechanism allowed by the key active nanostructures (molecules and nanoparticles) and the independent tunabilities they induce on the static and dynamic device behavior. This offers a good example that demonstrates the significant role of active structures in enhancing device performance and surmounting operating challenges at the nanoscale.

## 5.2 Outlook

### 5.2.1 Energy-Efficient NEM Switches

Though superior performance over conventional NEM switches has already been demonstrated, our current design, in particular the selection of molecules and nanoparticles, is far from optimal. PEG-thiol molecules are employed to assemble a soft and thick molecular spacer. The minimum actuation voltage to achieve an over 5 orders-of-magnitude on-off ratio is around 2 V. However, the actuation voltage in theory can be reduced down to a few hundred millivolts, when the mechanics of molecules lead to a restoring force matching well with the adhesive force. Such a gap can be bridged through molecular engineering and thin-film engineering approaches. Specifically, desired mechanics may be attainable through designing the molecular composition and tuning the conformational order of SAMs. Adding electroactive

compounds that change shape and/or conductivity in response to electrical potential change and charge injection can assist with the switching process and thereby reduce the actuation voltage. Nonlinear mechanics are also available by combining molecules with different stiffness. For instance, soft and stiff molecular spacers can be assembled on the nanoparticle and the bottom electrodes, respectively. The resulting combined thin film may behave compliant under small compression and stiff under large compression. This renders the restoring force with higher nonlinearity to match well with the adhesive force and the design space without stiction failure can also be expanded in this way.

Device uniformity and stability can potentially be improved by engineering the molecules as well. Nonuniform performance among devices are unfavorable for circuit design. The randomly coiling polymeric PEG-thiols are known to form brushlike islands and therefore bring nonuniform stiffness and thickness of the SAMs over a wide area. It is imperative to find or design alternative molecules, assisted with an optimized self-assembly process, to achieve uniform SAMs with desired properties over a wide area and thereby reduce device-to-device variation. Device degradation is observed in terms of increased leakage and reduced modulation in current over repetitive switching. Further understanding is required to reveal the failing mechanism, which may be attributed to compression-induced structural damage, electromigration, heating-induced degradation, etc. It is also noticed that majority of PEG-based devices survive less than 100 cycles, while many alkane-based devices can operate over 1000 cycles without stiction failure and exhibit more consistent $I$-$V$ characteristics. Therefore, designing molecular composition and configuration of SAMs may lead to improved robustness to structural damage by large compressions.

Though this thesis focuses mainly on two-terminal architecture for proof-of-concept and demonstration purpose, multi-terminal devices are more practical for realizing logic gates and designing integrated circuits. A scalable nanofabrication process for multi-terminal devices has been devised; however, the yield is greatly constrained by the dielectrophoresis step. The yield can be improved potentially through modified trapping process and/or optimized trapping conditions, including

concentration and liquid media of the suspension, flow rate, layout of the bottom electrodes, frequency and amplitude of the electric field, temperature and time. Other approaches that allow scalable manipulation of nanoparticles potentially with a high yield are also worth exploring.

### 5.2.2 Beyond Electromechanical Logic

The multi-functionality of these NEM devices extends the potential applications beyond energy-efficient logic. The stable and electrostatically-tunable nanogap filled with molecular springs makes a versatile architecture that allows development of various nanoelectronic devices, nanomechanical devices, plasmonic devices and nanophotonic devices. In particular, when the molecular composition is designed with specific compounds, the mechanical properties of the molecular spacer could be modified by certain environmental stimuli (e.g., moister, temperature, chemicals, light), thereby allowing our device architecture to be utilized as a universal platform for developing diverse environmental sensors.

The highly-uniform molecular junctions sandwiched between atomically-smooth electrodes create a sensitive and repeatable metrology platform for studies of fundamental physical phenomena. For instance, the electronic transport properties through molecules can be better characterized based on ensemble average using a large-area junction with angstrom-level variations in thickness enabled by this nanoscale metrology platform. Besides, the measurement of Young's modulus of SAMs heavily relies on indentation or stretching of molecules using AFM tips. The molecules could be bent during their interactions with the tip, which may result in a gap between the measured and the real Young's moduli. Fabricating a SAM sandwiched between atomically-smooth nanostructures and displacing the top nanostructure either mechanically or electrostatically effectively avoids the issue caused by the AFM tip morphology and is believed to result in more accurate measurements through ensemble average. Other potential applications of this nanoscale platform include studies of light-matter interaction, exciton dynamics measurements, Kazimir force measurements, etc.

The mechanism of exponentially modulating electrical conductance of such molecular junctions applies to other NEM devices, and novel device concepts of sensors, actuators, oscillators, switches, and memory devices may emerge based on repeatable nanoscale mechanical actuation of molecular springs. More generally, the demonstrated modular design with two or more active nanostructures provides independent degrees of design freedom and represents a versatile strategy to enhance performance, overcome operating challenges, and induce additional functionalities for devices in the field of nanoelectronics, nanomechanics, thermoelectrics, nanophotonics and nanomagnetics.

Table 5.1: Representative NEM switch techniques

| design | layout | active-area dimensions ($\mu$m) | switch gap (nm) | min actuation voltage (V) | min turn-on delay (ns) | max on-off ratio | SS (mV/dec) | lifecycle |
|---|---|---|---|---|---|---|---|---|
| this work | 2T | 1∼2 ($L$), 0.1 ($W$) | 2∼3 | 2.5 | 2 (@6 V) | $10^6$ | 30 | up to $10^3$ |
| pipe clip relay [21] | 2T | 1.4 ($L$), 0.3 ($W$), 0.04 ($T$) | 4 | 0.4 | 62.5 (@1 V, theory) | $10^5$ | 10 | 20 (shown) |
| MWCNT linear bearing [56] | 2T | 0.22 ($L$) | 6∼15 | 0.8 | NR | NR | ∼800 | 3 (shown) |
| $WN_x$ lateral cantilever [126] | 3T | 20 ($L$), 0.5 ($W$), 0.09 ($T$) | 150 | 0.8 | NR | $10^4$ | ∼200 | 2 (shown) |
| relay with SiC nanowire [31] | 3T | 8 ($L$), 0.08 ($D$) | 27 | 1 | 50∼1000 (theory) | $10^2$ | ∼600 | $< 100$ |
| dual-Si nanowire beam [30] | 2T | 7 ($L$), 4 ($W$) | 145 | 1.8 | NR | $10^4$ | 4 | 12 |
| SWCMT relay [33] | 2T | 0.13 ($L$) | 20 | 2 | 2.8 (@5 V) | $10^4$ | ∼400 | 3 (shown) |
| MWCNT relay [29] | 3T | 0.8 ($L$), 0.1 ($W$) | 40∼60 | 3.6 | NR | $10^4$ | ∼70 | 3 (shown) |
| vertical CNT triode [127] | 3T | NR | 30 | 4.5 | NR | $10^5$ | ∼20 | NR |
| MWCNT cantilever [45] | 3T | 2∼3 ($L$), 0.05 ($D$) | 180 | 5 | NR | NR | ∼1500 | 2 (shown) |
| graphene relay [47] | 3T | 1.5 ($L$), 0.8 ($W$) | 80 | 6 | NR | $10^5$ | 10.4 | 12 |
| SiC lateral cantilever [24] | 3T | 8 ($L$), 0.35 ($W$) | 150 | 6 | <1000 (@6 V) | NR | NR | $2.1 \times 10^{10}$ |
| graphene cantilever [37] | 2T,3T | 1∼2 ($L$), 2∼4 ($W$) | 300 | 6 | 25 (@20 V) | NR | ∼1500 | NR |
| SiGe relay with body electrode [35] | 4T | 70∼80 ($L$), 70∼80 ($W$) | 60 | 6 (<2 with bias) | 100 (@$V_G$ = 6 V, $V_B$ = −7.6 V) | $10^7$ | 3 | $10^6$ |
| Pt-coated p-Si lateral cantilever [44] | 5T | 23.6 ($L$), 3 ($W$) | 500 | 8 | 500∼1000 | $10^6$ | <10 | $10^8$ |
| TiN cantilever [40] | 2T | 0.3 ($L$), 0.2 ($W$), 0.035 ($T$) | 15 | 13 | NR | $10^5$ | 3 | 500 |
| SiGe relay with body electrode [25] | 4T | ∼80 ($L$), ∼80 ($W$) | 60 | 17 (0.1 with bias) | 190 (@19 V) | $10^7$ | 3 | $10^6$ |
| Ge/Si nanowire relay [42] | 3T | 1.32 ($L$), 0.025 ($D$) | 35 | 18 | NR | $10^3$ | 6 | 130 |
| MWCNT cantilever (C), relay (R) [36] | 2T | 1∼3 ($L$) | NR | 23.4 (C) 42 (R) | 10 (@25 V) 12 (@42 V) | $10^3$ | NR | $10^6$ (C) $10^5$ (R) |
| CNT ensemble cantilever [54] | 3T | 3.6 ($L$), 0.17 ($W$), 0.5 ($T$) | NR | 50 | ∼70 (theory) | $10^7$ | NR | 23 |

Acronyms: subthreshold swing (SS), not reported (NR), length ($L$), width ($W$), thickness ($T$), diameter ($D$)

# Chapter 6

# Theoretical Modeling of Acoustically-Active Surface

## 6.1 Device Concept

An acoustic surface based on an array of active micro-dome transducers is presented in Figure 6-1. These domes are freestanding and able to vibrate without constraint after the acoustic surface is mounted onto a rigid object. When a dome is excited by an AC voltage applied across its electrodes, the strain in the piezoelectric film induced by converse piezoelectric effect causes the dome to expand and contract periodically (Figure 6-1), thereby displacing air around it to generate sound. These microscale active structures can be separately addressed and actuated either individually or co-operatively by adapting the connections of electrode terminals as needed. Each dome transducer is also able to function as a microphone. Specifically, the acoustic pressure from incident sound causes strain inside the piezoelectric film and further charge accumulation on the electrodes, which can be measured by peripheral circuits and correlated to the incident acoustic pressure. However, this thesis mainly focuses on the actuation of these piezoelectric domes. A comprehensive study on the capability of the acoustic surface for sound generation is conducted both theoretically and experimentally.

In this thesis, PVDF is utilized as the piezoelectric material to make the acoustic

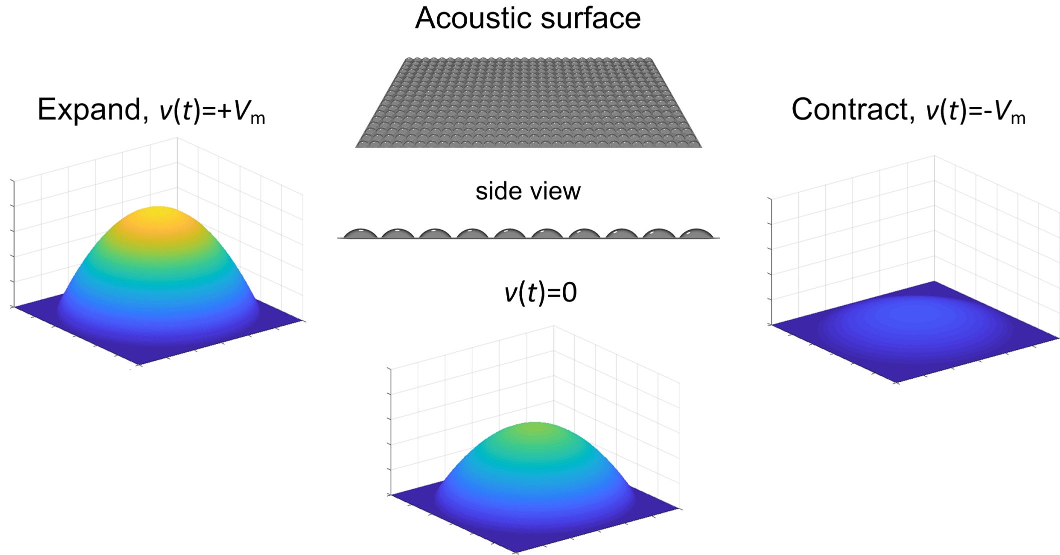


Figure 6-1: Schematic illustrating the working mechanism of the acoustic surface based on vibration of piezoelectric micro-dome transducers in an array.

surface. Therefore, parameters of PVDF films are applied in the theoretical analyses and simulation in this chapter. For fabrication of an acoustic surface sample, a protective layer made with a flexible plastic thin film is laminated to the top surface of the PVDF film with micro-dome array, in order to improve the robustness of the domes to external force and impact. The protective layer is perforated and the through-holes perfectly align with the domes. In this way, vibration of the domes should not be affected by the inactive protective layer, which is thus not considered in theoretical modeling and simulation.

After the acoustic surface is mounted on an object, the domes are isolated and their edges as well as the area between adjacent domes (void area) are assumed perfectly clamped (i.e., no displacement). An encapsulated cavity is also formed at the back of each dome. To avoid counteracting load on a vibrating dome induced by pressure change in these small cavities, another perforated plastic layer (same as the protective layer) is laminated to the back side of the PVDF film with micro-dome array. The through-hole that aligns with each dome substantially increases the cavity volume and minimizes the pressure change inside the cavity when the dome vibrates.

Therefore, the counteracting load is not considered in modeling and simulation.

The sound generation by an acoustic surface relies on the vibration of piezoelectric domes. When the domes are actuated well below their resonance frequencies, performance of the entire acoustic surface can be studied by modeling the displacement of individual domes in a quasi-static state. One approach is to treat the dome as a shallow spherical shell that is subject to a fixed boundary condition. Though analytical models for the bending of such a spherical shell under point load or uniform load over a small circular area are available [128], the piezoelectric response results in load over the entire dome, which makes the problem difficult to solve analytically. Alternatively, the well-known membrane theory and thin-plate theory can be applied to derive approximate but simple solutions to describe the dome deformation in the static state. These simplified models are useful to qualitatively study the dependence of dome vibration on the design variables, and even able to provide reasonably good estimates for the dome displacements under certain conditions. In general, a circular film with clamped boundary conditions and a radius/thickness ratio above 100 behaves like a circular membrane; for a smaller radius/thickness ratio (between 8 and 80), its deformation resembles bending of a rigid thin plate [129]. A shallow dome can be modeled in a similar way as a circular film.

In this chapter, simplified models are established based on membrane theory and thin-plate theory, which are further used to study the effects of design variables. For comparison purposes, PVDF domes are also simulated using finite element analysis software (COMSOL multiphysics), which provides more accurate predictions of their deformation and displacement.

## 6.2 Static Modeling

### 6.2.1 Variables and General Assumptions

The variables associated with the dimensions of a PVDF dome are defined in Figure 6-2, including dome radius $R$, dome height $H_0$, film thickness $h$, curvature of the

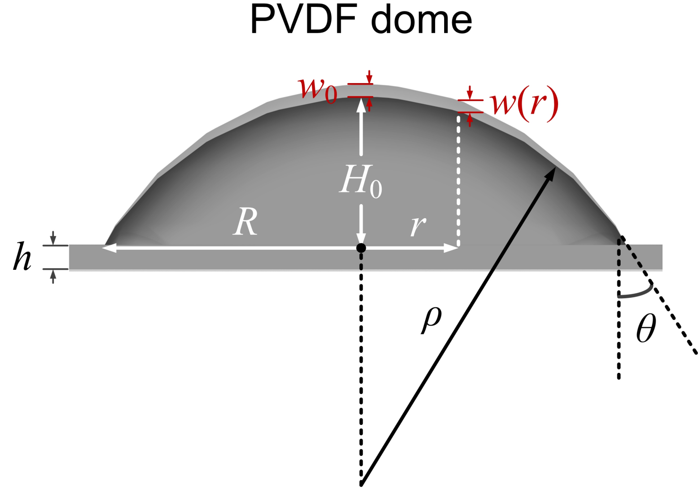


Figure 6-2: Schematic of a PVDF dome with definition of variables.

dome $\rho$, deflection at the dome center $w_0$, deflection at a projected radial distance of $r$ from the center $w(r)$, and angle $\theta$ between the $z$-axis and the tangential direction at the dome edge. The Young's modulus and the Poisson's ratio of the piezoelectric film are $E_Y$ and $\nu$, respectively.

The relation between strain and stress is governed by the piezoelectric constitutive equation, expressed as

$$\epsilon_i = s_{ij}^E \sigma_j + d_{ik} E_k, \tag{6.1}$$

where: $\epsilon_i$, $\sigma_j$ are the strain and the stress, respectively; $s_{ij}^E$ is the elastic compliance tensor under constant electric field; $d_{ik}$ is the piezoelectric constant; and $E_k$ is the electric field strength.

In order to simplify modeling, assumptions are made as follows.

1) The dome is shallow and the horizontal components of electric field are ignored.

2) The elastic and in-plane piezoelectric properties of the film are assumed to be isotropic and not affected by the thin electrodes deposited on both sides.

3) The middle plane of the film does not undergo any deformation, and the shear strains associated with the thickness-direction (along $z$-axis) are thus neglected, i.e., $\epsilon_{xz} = 0$, $\epsilon_{yz} = 0$.

4) The film thickness is uniform over the entire dome and does not change under an applied voltage. The normal strain $\epsilon_{zz}$ in the thickness direction is ignored,

which results in a negligible normal stress component $\sigma_{zz}$ as compared to other stress components.

5) The frequency of the excitation that induces dome deformation is far smaller than the intrinsic frequency of the dome, and the dome is in a quasi-static state.

According to the assumptions above, the components associated with $z$-axis are ignored and the expansion of the piezoelectric constitutive equation in matrix form becomes

$$\begin{bmatrix} \epsilon_{xx} \\ \epsilon_{yy} \\ \epsilon_{xy} \end{bmatrix} = \begin{bmatrix} \frac{1}{E_Y} & -\frac{\nu}{E_Y} & 0 \\ -\frac{\nu}{E_Y} & \frac{1}{E_Y} & 0 \\ 0 & 0 & \frac{2(1+\nu)}{E_Y} \end{bmatrix} \begin{bmatrix} \sigma_{xx} \\ \sigma_{yy} \\ \sigma_{xy} \end{bmatrix} + \begin{bmatrix} 0 & 0 & d_{31} \\ 0 & 0 & d_{32} \\ 0 & 0 & 0 \end{bmatrix} \begin{bmatrix} 0 \\ 0 \\ E_z \end{bmatrix}, \tag{6.2}$$

where the entries in compliance tensor matrix are expressed by the Young's modulus $E_Y$ and the Poisson's ratio $\nu$, and horizontal components of the electric field are ignored, i.e., $E_x = E_y = 0$.

### 6.2.2 Membrane Theory

When the film thickness is sufficiently small compared to the dome radius, the dome behaves like a membrane with clamped edge and the bending effect is insignificant. We follow the approach by R. Abram [130] to derive the membrane theory that describes the deformation and displacement of a PVDF dome excited by an applied voltage in quasi-static state. The dome is assumed to form part of a spherical surface. Under an applied voltage, perturbation to the dome profile is small, and the diaphragm always takes a spherical shape with uniform and isotropic surface tension and strain. According to the isotropic assumptions, we have

$$\epsilon_{xx} = \epsilon_{yy} = \epsilon, \tag{6.3}$$

$$\sigma_{xx} = \sigma_{yy} = \sigma = T/h, \tag{6.4}$$

where the subscripts of stress and strain are dropped, and $T$ is the surface tension. Therefore, the piezoelectric constitutive equations can be simplified as

$$\epsilon = \frac{1-\nu}{E_Y h} T + d_{3ave} E_t, \tag{6.5}$$

where $E_t$ is the electric field strength along the thickness direction, and the average piezoelectric constant $d_{3ave} = d_{31} = d_{32}$ (for biaxial piezoelectric material) or $d_{3ave} = d_{31}/2$ (for uniaxial piezoelectric material). Since the dome is assumed to always form part of the spherical surface, the strain can be calculated by the change in film area, which gives

$$\epsilon = \frac{\delta A}{2A}, \tag{6.6}$$

where $A$ is the dome area and $\delta A$ is the area change. For a spherical diaphragm, the strain is approximated as

$$\epsilon \approx \frac{x^2}{2(R^2 + H_0^2)} - \frac{H_0^2}{2(R^2 + H_0^2)}, \tag{6.7}$$

where $H_0$ and $x$ ($x = H_0 + w_0$) are the dome height under no excitation, and the dome height perturbed by the converse piezoelectric effect and a static pressure $P$ on the dome, respectively. The relation between the tension $T$ and the static pressure $P$ on the dome can be deduced by the force balance on the boundary,

$$\pi R^2 P = 2\pi R T \cos\theta, \tag{6.8}$$

where $\theta$ is the angle between the tension orientation at the dome edge and the $z$-axis (Figure 6-2), given by $\cos\theta = R/\rho$. For a spherical diaphragm, the curvature of the dome $\rho$ can be expressed by the perturbed dome height $x$ as

$$\rho = \frac{x}{2} + \frac{R^2}{2x}. \tag{6.9}$$

The tension $T$ therefore becomes

$$T = \frac{P}{4}(x + \frac{R^2}{x}). \tag{6.10}$$

Substituting (6.10) into (6.5), the perturbed dome height $x$ can be obtained by solving

$$x^3 - \frac{(1-\nu)P(R^2+H_0^2)}{2E_Y h}x^2 - [H_0^2 + 2d_{3ave}E_t(R^2+H_0^2)]x - \frac{(1-\nu)PR^2(R^2+H_0^2)}{2E_Y h} = 0. \tag{6.11}$$

When no static pressure is applied ($P = 0$), the dome height under a voltage $V$ across the electrodes is given by

$$x(V) = \sqrt{\frac{2d_{3ave}V(R^2+H_0^2)}{h} + H_0^2}. \tag{6.12}$$

The peak value of the deflection $w_0$ at the dome center under a periodic voltage with an amplitude of $V_m$ is

$$w_0 = \frac{1}{2}(\sqrt{\frac{2d_{3ave}V_m(R^2+H_0^2)}{h} + H_0^2} - \sqrt{-\frac{2d_{3ave}V_m(R^2+H_0^2)}{h} + H_0^2}). \tag{6.13}$$

To calculate the displaced volume of air, an expression for the dome profile $x_r(r)$ is necessary. $x_r(r)$ for a spherical diaphragm is given by

$$x_r(r) = x - \rho + \sqrt{\rho^2 - r^2}, \tag{6.14}$$

which represents the perturbed height at a projected radial distance $r$ from the dome center. The curvature $\rho$ of the spherical diaphragm with respect to a dome height $x$ is given by (6.9). The volume of the dome is therefore calculated as

$$V_{bc} = \frac{\pi x^2}{3}(3\rho - x), \tag{6.15}$$

where $x$, $\rho$ both depend on the drive voltage amplitude $V_m$. The displaced volume of

air is therefore given by

$$\triangle V_{bc} = |V_{bc}(V_m) - V_{bc}(-V_m)|. \tag{6.16}$$

We can further calculate the average displacement with respect to the projected area of the dome as

$$\overline{w} = \frac{\triangle V_{bc}}{\pi R^2}. \tag{6.17}$$

For a shallow dome that always takes a spherical profile, further approximations can be made to evaluate the average displacement. Substituting (6.9) into (6.14) and considering $R^2/x \gg R > r$, $R^2/x \gg w$, $x = H_0 + w_0$, $x_r(r) = H(r) + w(r)$ ($H(r)$ is the unperturbed height), the deflection $w(r)$ at position $r$ is therefore

$$w(r) \approx w_0[1 - (\frac{r}{R})^2], \tag{6.18}$$

which results in an average deflection $\overline{w} = w_0/2$.

The approximate solution above provided by the membrane theory only applies when the film is thin compared to the dome radius and bending is insignificant.

### 6.2.3 Thin-Plate Theory

For domes with a large film thickness ($8 < R/h < 80$), the bending becomes important, particularly when the deflection is small compared to the thickness ($w_0/h < 0.2$). A shallow dome in this case behaves like a rigid circular thin plate [129]. The solution to symmetrical bending of a circular thin plate subject to clamped boundary conditions [128] gives the departure from the original curvature as

$$w(r) = w_0[1 - (\frac{r}{R})^2]^2. \tag{6.19}$$

When the deflection is small compared to the thickness of the plate and the strain

of the middle plane can be neglected, the deflection at the thin-plate center is

$$w_0 = \frac{PR^4}{64D}, \tag{6.20}$$

where $P$ is the uniform load applied on the thin plate, and $D$ is the bending stiffness given by

$$D = \frac{E_Y h^3}{12(1-\nu^2)}. \tag{6.21}$$

When the deflection is large, an energy method from S. Timoshenko [128] provides an approximate solution of the large deflection at the center of the thin plate $w_m$ by

$$\frac{w_m}{h} + 0.488(\frac{w_m}{h})^3 = \frac{PR^4}{64Dh}. \tag{6.22}$$

Though the dome profile is formed during fabrication of the acoustic surface and able to maintain under zero pressure, we can still treat the dome as a thin plate with a large deformation and assume the initial dome height $H_0$ is induced by an imaginary pressure $P_i$, which enables us to apply the thin-plate theory as

$$\frac{H_0}{h} + 0.488(\frac{H_0}{h})^3 = \frac{P_i R^4}{64Dh}. \tag{6.23}$$

The actual deflection at the dome center $w_0$ induced by the converse piezoelectric effect is much smaller compared to $H_0$. In order to obtain a simple analytical solution for $w_0$, we translate the piezoelectric response into an equivalent uniform load on the dome [131], which is

$$P_V = \frac{2d_{3ave} V E_Y}{\rho(1-\nu)}, \tag{6.24}$$

where the average piezoelectric constant $d_{3ave} = d_{31} = d_{32}$ for a biaxial piezoelectric film and $d_{3ave} = d_{31}/2$ for a uniaxial piezoelectric film. Therefore, $w_0$ can be treated as an incremental deflection caused by a perturbation load $P_V$. (6.22) can be linearized at $H_0$, which gives

$$w_0 = P_V \left.\frac{\mathrm{d}w_m}{\mathrm{d}P}\right|_{P=P_i}, \tag{6.25}$$

where

$$\left.\frac{\mathrm{d}w_m}{\mathrm{d}P}\right|_{P=P_i} = \frac{R^4 h^2}{64D(h^2 + 1.464H_0^2)}. \tag{6.26}$$

The deflection caused by piezoelectric response averaged over the projected area of the dome assuming the profile in (6.19) is therefore $\overline{w} = w_0/3$.

It should be noticed that the simplified thin-plate model creates an imaginary pressure to induce the initial dome height. The resulting deflection $w_0$ is typically smaller than the actual value, as it is easier to displace a dome with film slackness (resulting in the actual $w_0$) compared to displacing a thin plate already deformed under a large load (calculated $w_0$ in this simplified model). Therefore, the approximate solution based on the thin-plate theory is more accurate for shallow domes, i.e., when the dome height is comparable to or smaller than the film thickness.

### 6.2.4 Sound Generation by an Acoustic Surface

To further evaluate the sound generation by an acoustic surface, the air displacement caused by vibration of the piezoelectric micro-dome transducers in an array must be translated into the acoustic pressure and the sound pressure level (SPL). Here, we only consider the free-field response and additional assumptions are made as follows.

1) The thickness of the acoustic surface is small compared to the acoustic wavelength in the frequency range of interest.

2) The vibration of the dome is unimpeded by air damping and other forces, and the static model applies to evaluate the dome displacement in dynamic state, when the frequency of excitation is well below the resonance frequency.

3) The acoustic surface is mounted on a large rigid baffle (perfect reflecting) and the overall motion of the piezoelectric film is ignored.

We use Rayleigh integral, which is a simplified form of the Kirchhoff-Helmholtz integral, to calculate the acoustic pressure and the SPL produced by the acoustic surface in free field. The acoustic pressure $p(\mathbf{r_d})$ at a point located at $\mathbf{r_d}$ is

$$p(\mathbf{r_d}, k, V_m) = \frac{i\rho c k}{4\pi} \iint_S v(\mathbf{r'_d}, V_m) \frac{e^{ik|\mathbf{r_d} - \mathbf{r'_d}|}}{|\mathbf{r_d} - \mathbf{r'_d}|} \mathrm{d}S, \tag{6.27}$$

where: $\mathbf{r_d}$ is the vector from the designated origin to the observation point; $\mathbf{r'_d}$ is the vector from the origin to the location of d$S$ on the acoustic surface; $v(\mathbf{r'_d})$ is the velocity at $\mathbf{r'_d}$ normal to the plane of the acoustic surface ($z$-axis); $\rho$ is the density of air; $k$ is the wavenumber; $c$ is the sound speed; and $V_m$ is the amplitude of drive voltage.

For the far-field response, when the distance from the observation point to the acoustic surface is much larger than the size of the acoustic surface, $|\mathbf{r_d} - \mathbf{r'_d}|$ can be approximated to be the constant $r_d$. As a result, the Rayleigh integral is reduced to

$$p(r_d, k, V_m) = \frac{i\rho ckv(V_m)A}{2\pi}\frac{e^{ikr_d}}{r_d}, \tag{6.28}$$

where $v$ is the surface velocity averaged over all the domes, and $A$ is the active area of the acoustic surface. When the velocity is replaced by derivative of the displacement, the acoustic pressure becomes

$$p(r_d, \omega, V_m) = \frac{i\rho\omega^2\overline{w}(V_m)A}{2\pi r_d}e^{ikr_d}, \tag{6.29}$$

where the wavenumber is substituted using $k = \omega/c$, $\omega$ is the angular frequency and $\overline{w}$ is the displacement averaged over all the domes. Then the RMS value of the acoustic pressure is

$$p(r_d, f, V_m) = \frac{\sqrt{2}\pi\rho f^2\overline{w}(V_m)A_m(1 - R_v)}{r_d}, \tag{6.30}$$

where $f$ is the sound frequency, $A_m$ is the area of the acoustic surface, and $R_v$ is the percentage of void area on the acoustic surface. Therefore, the SPL is further given by

$$SPL(r_d, f, V_m) = 20log_{10}|\frac{p(r_d, f, V_m)}{p_0}|, \tag{6.31}$$

where $p_0 = 20\ \mu$Pa is the reference sound pressure. SPL is a function of distance $r_d$, sound frequency $f$, and amplitude of drive voltage $V_m$. It is also dependent on material properties, dome dimensions as well as active area of the acoustic surface. Since the acoustic pressure is proportional to the drive voltage, the sensitivity of an

acoustic surface is defined as

$$S(r_d, f) = \sqrt{2}\frac{\mathrm{d}p(r_d, f, V_m)}{\mathrm{d}V_m}. \tag{6.32}$$

## 6.3 Dynamic Modeling

The bandwidth of an acoustic surface, which is primarily determined by the resonance frequencies of the piezoelectric domes on it, is another important metric to consider. A dynamic model is introduced in this section to study how the design variables of the domes may influence their resonance frequencies. Here, we treat the shallow dome as a flat thin film for simplification, and follow the modeling approach developed by H. Suzuki [132]. A general dynamic model for a circular thin film includes both the bending stiffness $D$ and the tension term $T$ in the governing equation for transverse free vibration, which is

$$D\nabla^4 w - T\nabla^2 w + \sigma\frac{\mathrm{d}^2 w}{\mathrm{d}t^2} = 0, \tag{6.33}$$

where $w$ is the transverse displacement (deflection) and $\sigma$ is the area mass density of the film. Assuming harmonic vibration with an amplitude of $W$, the differential equation reduces to

$$(D\nabla^4 - T\nabla^2 - \sigma\omega^2)W = 0, \tag{6.34}$$

which is further transformed as

$$(\nabla^2 - k_1^2)(\nabla^2 + k_2^2)W = 0, \tag{6.35}$$

where

$$k_1^2 = \frac{T + \sqrt{T^2 + 4D\sigma\omega^2}}{2D}, \tag{6.36}$$

$$k_2^2 = \frac{-T + \sqrt{T^2 + 4D\sigma\omega^2}}{2D}. \tag{6.37}$$

The relation between the two wavenumbers $k_1$ and $k_2$ is

$$(k_1 R)^2 = (k_2 R)^2 + \frac{TR^2}{D}, \tag{6.38}$$

which is dimensionless due to the introduction of dome radius $R$. The intrinsic frequency is therefore obtained as

$$w_r = k_2 R \sqrt{\frac{D}{\sigma} k_2^2 + \frac{T}{\sigma}}, \tag{6.39}$$

and the general solution of the amplitude is

$$W_m(r, \theta) = [A J_m(k_2 r) + B I_m(k_1 r)] \cos m\theta, \tag{6.40}$$

where $J_m$, $I_m$ are the $m$th-order cylindrical Bessel function with coefficient $A$, modified $m$th-order cylindrical Bessel function with coefficient $B$, respectively. Considering clamped boundary conditions

$$\begin{aligned} W_m(R, \theta) &= 0, \\ \left.\frac{\mathrm{d}W_m(r, \theta)}{\mathrm{d}r}\right|_{r=R} &= 0, \end{aligned} \tag{6.41}$$

the $k_1 R$ and $k_2$R are therefore the solutions to

$$\begin{vmatrix} J_m(k_2 R) & I_m(k_1 R) \\ (k_2 R) J_m'(k_2 R) & (k_1 R) I_m'(k_1 R) \end{vmatrix} = 0 \tag{6.42}$$

After replacing $k_1 R$ with $k_2 R$ using (6.38), the eigenvalue $k_2 R$ can be solved by the equation above and the intrinsic frequency is therefore given by

$$\omega_r^{(mn)} = \frac{(k_2^{(mn)} R)}{R} \sqrt{\frac{D}{\sigma R^2} (k_2^{(mn)} R)^2 + \frac{T}{\sigma}}, \tag{6.43}$$

where $m$, $n$ denote the number of nodal circles and the number of nodal lines, respectively, that define the vibration mode. For two extreme cases, i.e., ideal thin plate ($T = 0$) and ideal membrane ($D = 0$), the intrinsic frequency is reduced to

$$\omega_{r-tp}^{(mn)} = \frac{(k_2^{(mn)} R)^2}{R^2} \sqrt{\frac{D}{\sigma}}, \tag{6.44}$$

$$\omega_{r-mem}^{(mn)} = \frac{(k_2^{(mn)}R)}{R}\sqrt{\frac{T}{\sigma}}. \tag{6.45}$$

## 6.4 Analysis of Dome Vibration Based on COMSOL Multiphysics Simulation and Theoretical Models

COMSOL Multiphysics is a cross-platform finite element analysis software that is able to simulate piezoelectric transducers. The static and dynamic responses of a piezoelectric micro-dome transducer can be analyzed by creating the geometry and assigning the piezoelectric material, boundary conditions as well as an excitation. Here, we mainly focus on the quasi-static displacement and the resonance frequency, which determine the sensitivity and the bandwidth of an acoustic surface, respectively.

The first example simulates and compares the displacement from the starting shape of a dome based on a uniaxial PVDF film to that of a dome based on a biaxial PVDF film. The simulation variables associated with dome dimensions are similar to our fabricated samples (in Chapter 7 and Chapter 8), i.e., $R = 350$ $\mu$m, $H_0 = 35$ $\mu$m, $h = 12$ $\mu$m. The piezoelectric constants for the uniaxial PVDF film are assigned as $d_{31} = 22$ pC/N, $d_{32} = 0$ pC/N, while those for the biaxial PVDF film are assigned as $d_{31} = d_{32} = 12$ pC/N. The surface displacement distributions over the two domes under a voltage of 10 V are presented in Figure 6-3.

From the displacement distribution in the cross-section image, we observe that the deformation of the dome resembles the bending of a circular thin plate for both cases, which can be explained by the small radius/thickness ratio ($\sim$29) of the domes. Besides, the displacement at the center of the uniaxial PVDF dome and that at the center of the biaxial PVDF dome are 44 nm and 48 nm, respectively. Considering the assigned piezoelectric constants for uniaxial and biaxial PVDF films, the overall dome displacement can be treated as the superposition of the displacement caused by the $d_{31}$ piezoelectric response and that by the $d_{32}$ piezoelectric response.

The dome dimensions are significant design variables that can be easily tuned during fabrication. The dependence of dome displacement on these variables is stud-

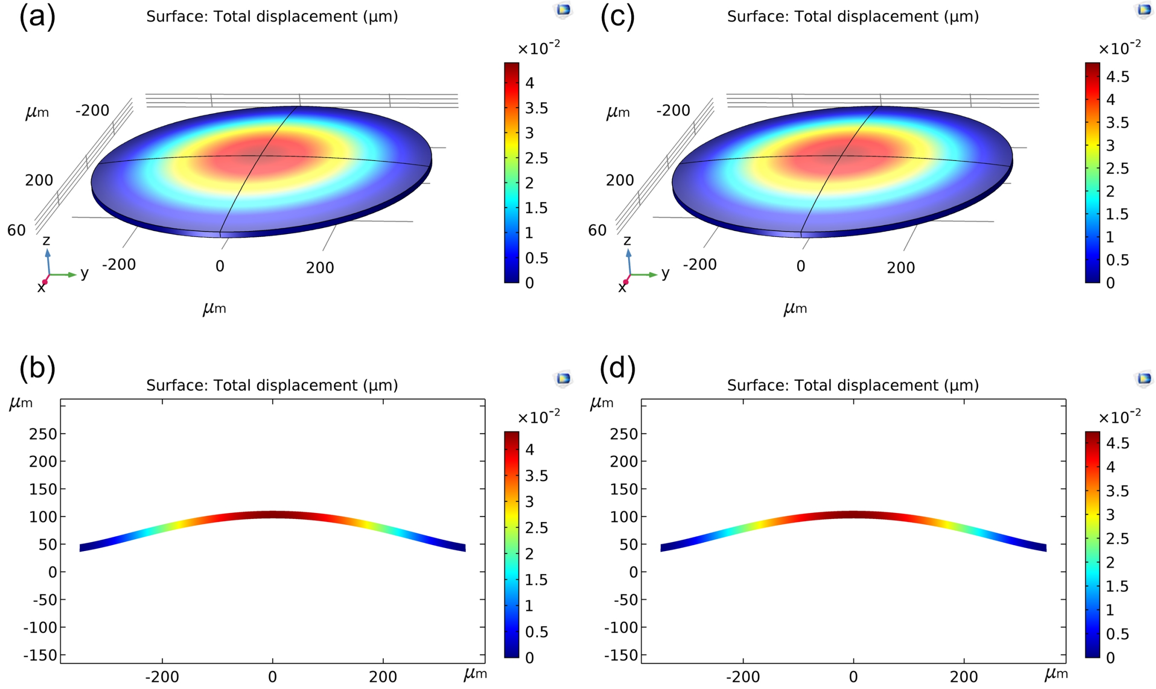


Figure 6-3: Comparison of simulated displacement distributions over two domes based on uniaxial and biaxial PVDF films. (a) 3D surface displacement distribution and (b) cross-section surface displacement distribution of a uniaxial PVDF dome ($d_{31} = 22$ pC/N, $d_{32} = 0$ pC/N). (c) 3D surface displacement distribution and (d) cross-section surface displacement distribution of a biaxial PVDF dome ($d_{31} = d_{32} = 12$ pC/N). The drive voltage is 10 V, and the two domes have identical dimensions $R = 350$ $\mu$m, $H_0 = 35$ $\mu$m, and $h = 12$ $\mu$m.

ied using COMSOL simulation as well as the simplified membrane and thin-plate analytical models. The influence of the dome height $H_0$ is simulated for both a large PVDF dome ($R = 1$ mm) and a small PVDF dome ($R = 350$ $\mu$m) with the same film thickness $h = 12$ $\mu$m, while other parameters are constant as $d_{31} = 22$ pC/N (uniaxial), $E_Y = 2.6$ GPa, $\nu = 0.38$, $V_m = 10$ V. The results are shown in Figure 6-4. When the dome height is small, the dome is similar to a flat film and bending dominates the dome deformation. Both the thin-plate model and the COMSOL simulation predict that the deflection increases with the dome height $H_0$. This indicates that pre-bending the circular film within a certain range can facilitate its deformation under excitation. However, the optimal dome height given by the thin-plate model is different from that based on the COMSOL simulation, likely due to treating the dome height as induced by an imaginary pressure (rather than a zero-strain initial

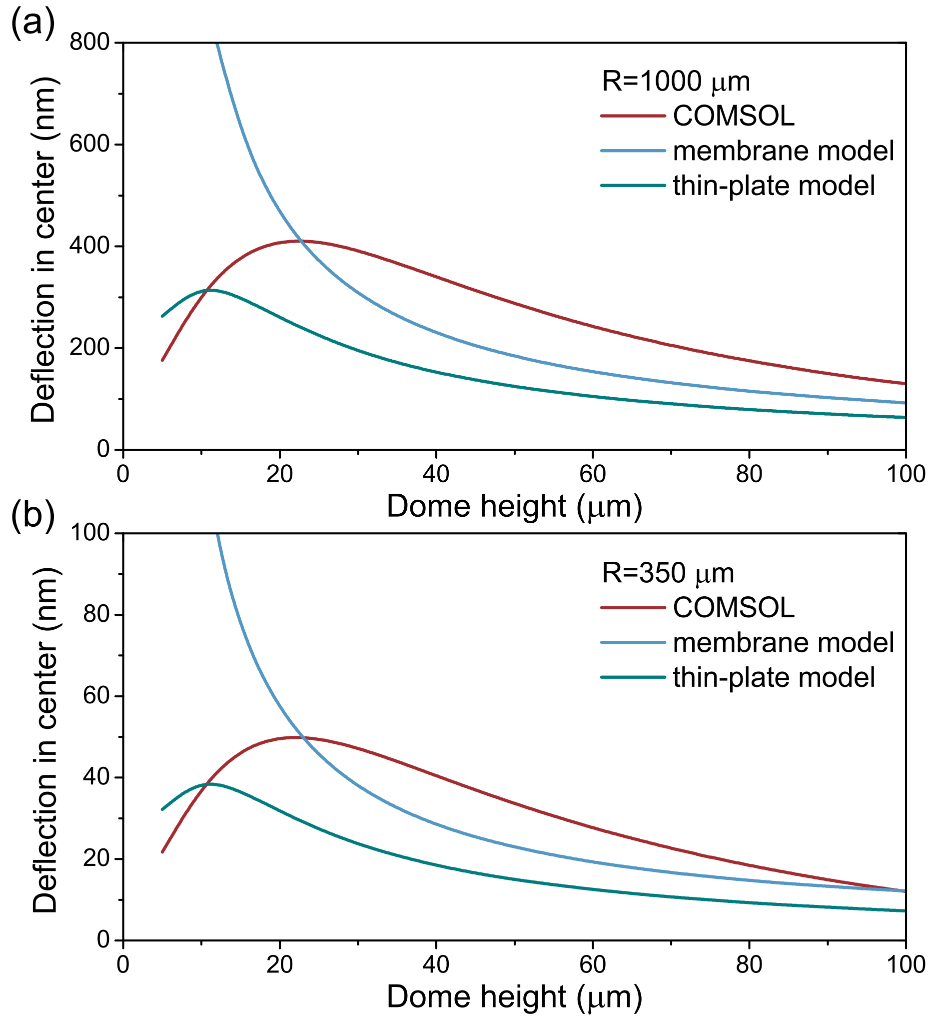


Figure 6-4: Theoretical and simulated dependence of deflection at the center of a PVDF dome on its height. Two dome sizes (a) $R = 1$ mm and (b) $R = 350$ $\mu$m are compared.

shape) for simplification. This may also explain why the deflection decays faster based on thin-plate theory as the dome height further increases, compared to the trend shown in simulation results. The membrane theory only considers stretching effect and therefore predicts monotonically decaying deflection with the dome height, which results in both a wrong trend and much larger error particularly for small dome heights.

The dependence of the deflection at the dome center on the radius $R$ is studied by keeping either a constant aspect ratio ($H_0/R = 5\%$, $H_0/R = 10\%$) or a constant

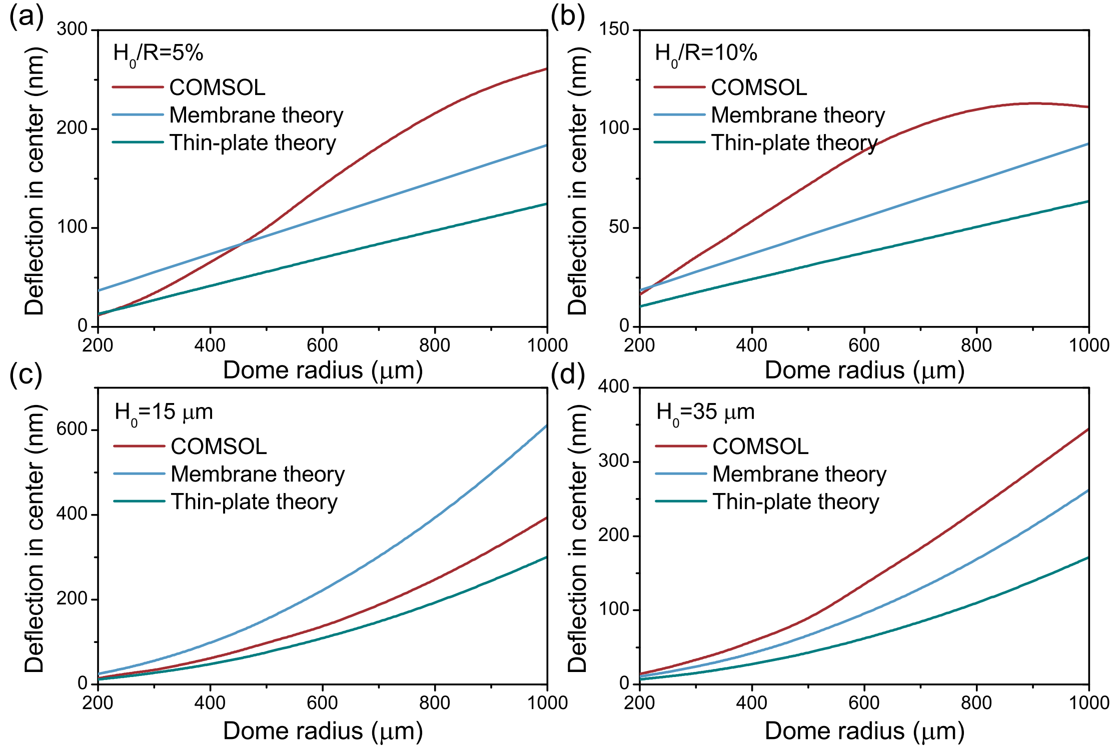


Figure 6-5: Theoretical and simulated dependence of deflection at the center of a PVDF dome on its radius. Results based on a constant aspect ratio (a) $H_0/R = 5\%$, (b) $H_0/R = 10\%$ and those based on a constant dome height (c) $H_0 = 15$ $\mu$m, (d) $H_0 = 35$ $\mu$m are compared.

dome height ($H_0 = 15$ $\mu$m, $H_0 = 35$ $\mu$m). The results calculated by theoretical models and those simulated by COMSOL are compared in Figure 6-5. Other parameters are kept constant as $h = 12$ $\mu$m, $d_{31} = 22$ pC/N (uniaxial), $E_Y = 2.6$ GPa, $\nu = 0.38$, $V_m = 10$ V. For the simulation results associated with a constant aspect ratio, the deflection increases linearly with the dome size when the radius is below 700 $\mu$m. However, as the dome radius further increases, limited rigidity of the film results in a gradually flattened displacement distribution close to the dome center, as observed in Figure 6-6 (compared to Figure 6-3 (b)). However, the two simplified analytical models always assume identical dome profile and displacement distribution for domes of different sizes. The corresponding results thus still hold the linear deflection-radius correlation above 700 $\mu$m in radius. For a constant dome height ($H_0 = 15$ $\mu$m, or $H_0 = 35$ $\mu$m), the increase in the radius makes the dome "shallower" and easier to deform, which thereby results in a superlinear correlation between the deflection and

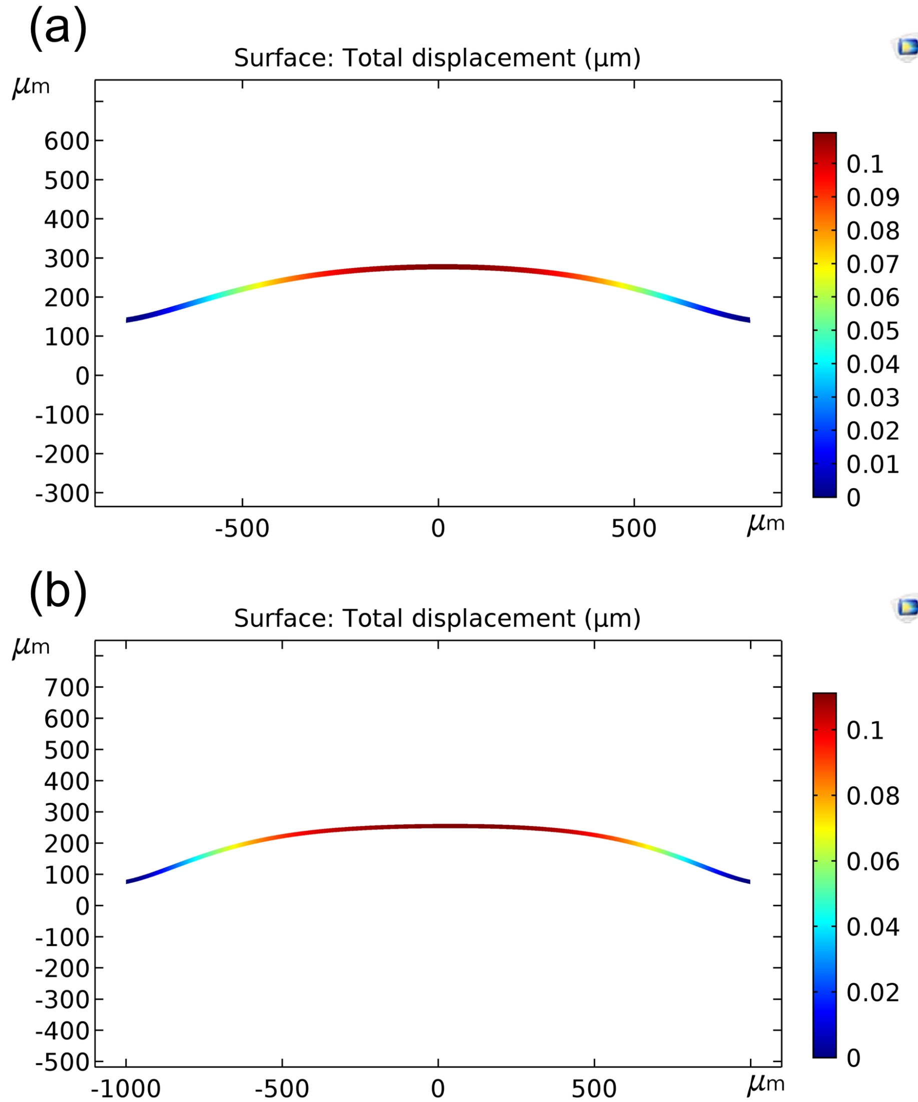


Figure 6-6: Cross-section displacement distributions for large dome sizes. The simulation results of two PVDF domes based on (a) $R = 800\ \mu$m, $H_0 = 80\ \mu$m, $h = 12\ \mu$m and (b) $R = 1$ mm, $H_0 = 100\ \mu$m, $h = 12\ \mu$m show flattened displacement distributions close to the dome center.

the dome radius.

The dependence of deflection at the dome center on the film thickness is studied by keeping constant dome radius $R = 350\ \mu$m and height ($H_0 = 15\ \mu$m, or $H_0 = 35\ \mu$m), while other simulation parameters are $d_{31} = 22$ pC/N (uniaxial), $E_Y = 2.6$ GPa, $\nu = 0.38$, $V_m = 10$ V. Figure 6-7 shows the significant impact of film thickness on the deflection. For a thinner film, the enhanced electric field and the reduced bending stiffness both contribute to a larger deflection.

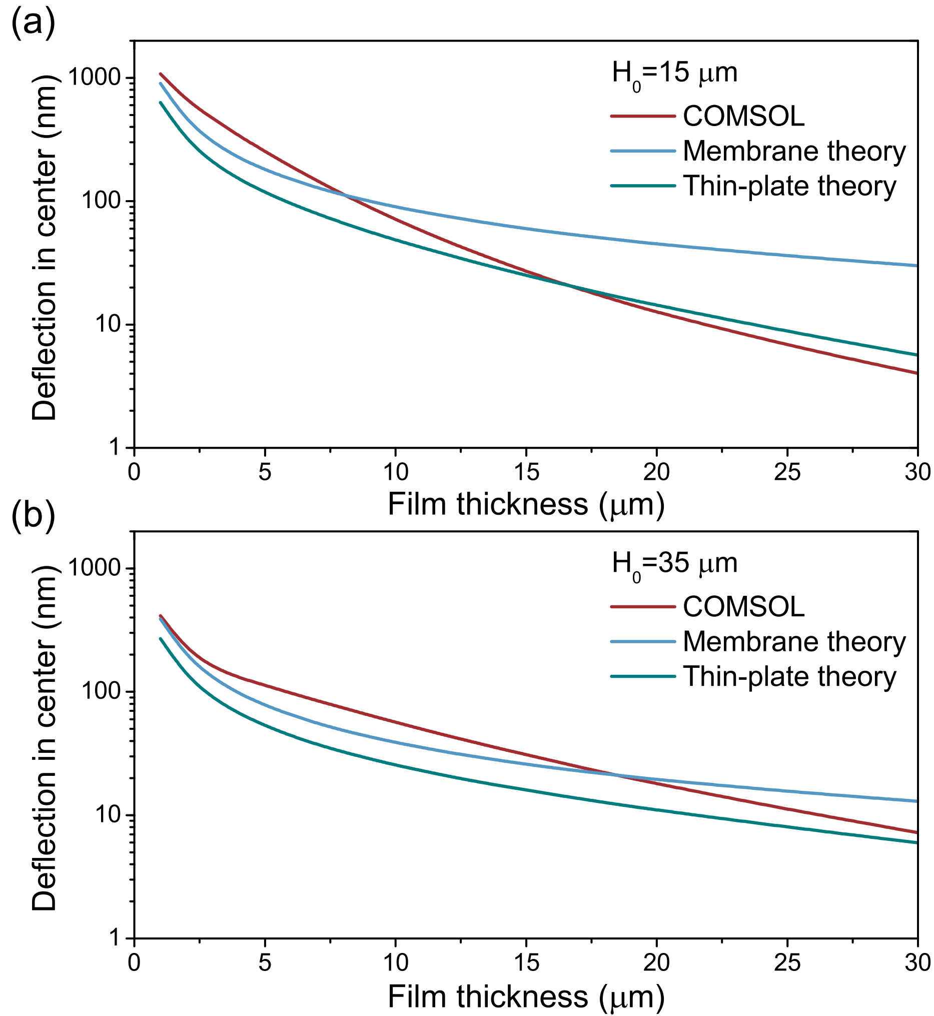


Figure 6-7: Theoretical and simulated dependence of deflection at the center of a PVDF dome on the film thickness. Two dome heights (a) $H_0 = 15$ $\mu$m and (b) $H_0 = 35$ $\mu$m are compared.

Figure 6-7 (a) and (b) both show the same trend that the deflection obtained by COMSOL simulation is close to the result calculated by the thin-plate model given a thick film, and gradually approaches the result based on the membrane model as the film thickness decreases. This agrees well with the fact that a PVDF dome behaves like a thin plate given a large film thickness (small $R/h$ ratio), or like a membrane given a small film thickness (large $R/h$ ratio).

Overall, the COMSOL simulation is believed to provide a more accurate prediction of the displacement than the simplified analytical models, and will be used to compare

with the experimental results in Chapter 8. Though the absolute displacement values calculated based on the membrane model and the thin-plate model do not always match well with the COMSOL results, these simplified analytical models provide useful tools to qualitatively study the correlation between the displacement and the design variables like dome dimensions and thereby to guide the design of PVDF domes towards optimized performance of the acoustic surface. In summary of the results in Figures 6-4, 6-5 and 6-7, an acoustic surface with large and shallow domes (of heights about twice the film thickness) made from a thin PVDF film should exhibit the best acoustic performance.

For applications that require a flat response (i.e., constant displacement) over a certain frequency range, the dome dimensions should be designed such that the resonance frequency is higher than the frequency range of interest. The analytical dynamic model and the COMSOL simulation are used to study the dependence of the resonance frequency on the dome dimensions. The dynamic model established based on vibration of flat circular film does not consider the impact from the dome height. Therefore, we simulate the influence of dome height on the resonance frequency using COMSOL, and the result is shown in Figure 6-8. A dome with a radius $R = 1$ mm, $h = 12$ $\mu$m (resembles a membrane) and a dome with a radius $R = 350$ $\mu$m, $h = 12$ $\mu$m (resembles a thin plate) are compared, while the Young's modulus and Poisson's ratio are assigned as $E_Y = 2.6$ GPa and $\nu = 0.38$, respectively. The same trend is observed for both domes, i.e., higher resonance frequency with increasing dome height. For shallow domes ($H_0 < h$), the resonance frequency increases slowly with the dome height; as the dome height further increases, the resonance frequency increases almost linearly with the dome height. For flat circular thin films, the theoretical resonance frequencies calculated by (6.43) are $f_r = 60.07$ kHz for $R = 350$ $\mu$m and $f_r = 7.36$ kHz for $R = 1$ mm, respectively, which agree well with the COMSOL results (60.84 kHz and 7.46 kHz) for these flat films. Considering the dependence of the deflection on the dome height in Figure 6-4, shallow domes ($H_0 =\sim 20$ $\mu$m for both $R = 350$ $\mu$m and $R = 1$ mm) are advantageous for sound generation. The corresponding resonance frequencies given by the theoretical model (no dependence on the dome height) are

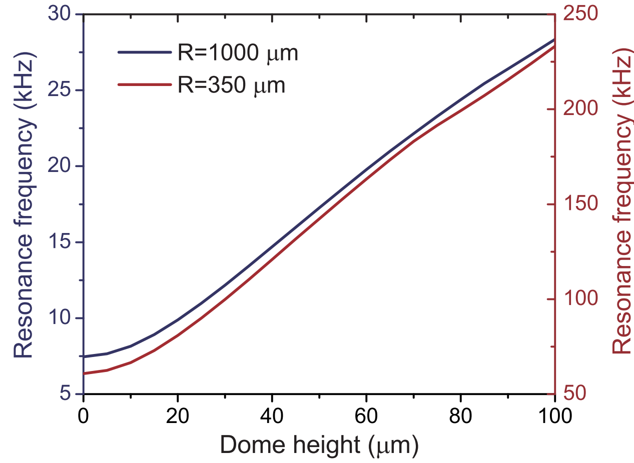


Figure 6-8: Simulated dependence of the resonance frequency of a PVDF dome on its height. Two dome sizes $R = 1$ mm and $R = 350$ $\mu$m are compared.

different from the COMSOL results (80.87 kHz for $R = 350$ $\mu$m and 9.88 kHz for $R = 1$ mm) by around 25% at $H_0 = 20$ $\mu$m.

The dependence of the resonance frequency on the dome radius and the film thickness are presented in Figure 6-9 (a) and (b), respectively. To study the effect from dome radius, we consider two cases by assigning a constant aspect ratio ($H_0/R = 5\%$, $H_0/R = 10\%$) or a constant dome height ($H_0 = 15$ $\mu$m, $H_0 = 35$ $\mu$m), while the film thickness is kept constant as $h = 12$ $\mu$m. The simulation results for both cases are higher than the corresponding theoretical resonance frequencies, due to absence of the dome height in the theoretical model. Particularly for $H_0 = 35$ $\mu$m, the theoretical resonance frequencies are around half of the values from COMSOL simulation. For a constant aspect ratio, the relative error of resonance frequency calculated by the theoretical model gets larger as the dome radius increases. To study the influence of film thickness, two dome heights $H_0 = 15$ $\mu$m and $H_0 = 35$ $\mu$m are simulated, while a constant dome radius $R = 350$ $\mu$m is assigned. The results in Figure 6-9 (b) show that the relative error predicted by the theoretical model is reduced as the film thickness increases. In summary, the theoretical model is able to provide a good estimate of the resonance frequency for a shallow dome with a large film thickness, and large error should be expected for a dome with a large height and a small film

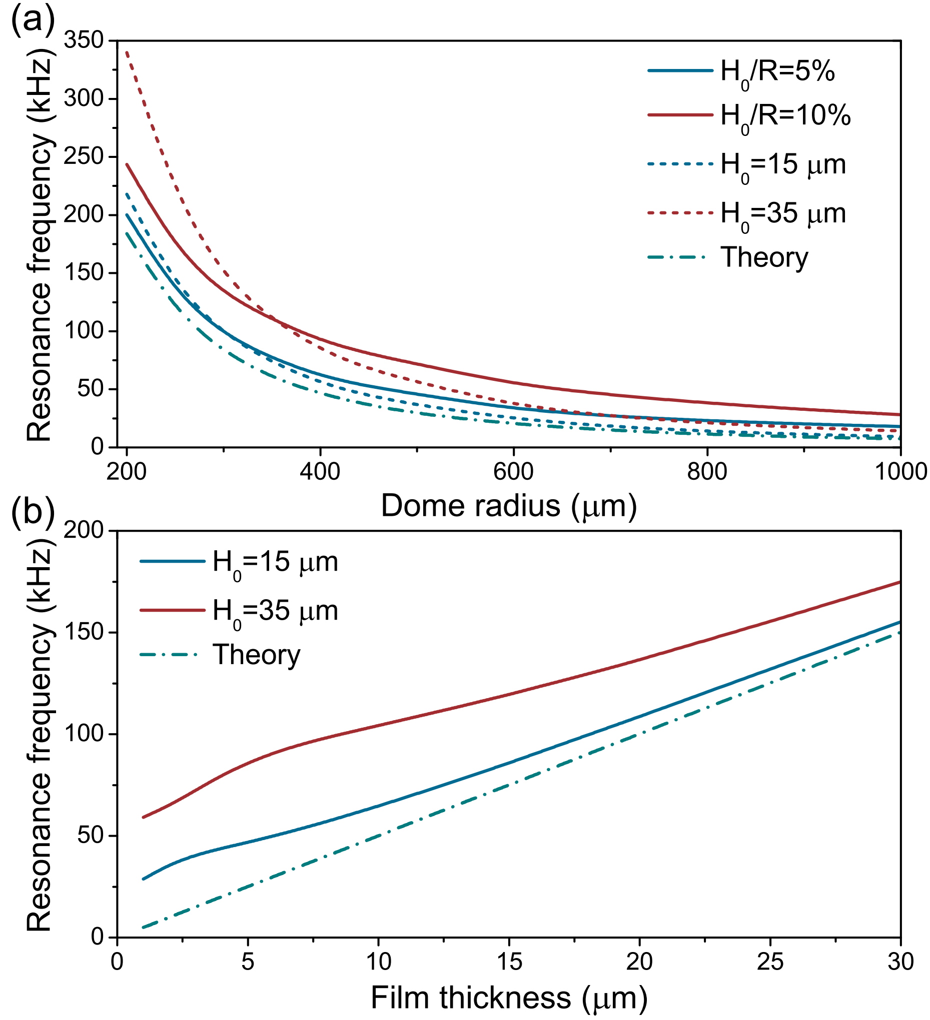


Figure 6-9: Theoretical and simulated dependence of the resonance frequency of a PVDF dome on (a) the dome radius and (b) the film thickness. Two cases are simulated in (a) by keeping either a constant aspect ratio ($H_0/R = 5\%$, $H_0/R = 10\%$) or a constant dome height ($H_0 = 15$ $\mu$m, $H_0 = 35$ $\mu$m) during scaling of a PVDF dome. Two dome heights $H_0 = 15$ $\mu$m and $H_0 = 35$ $\mu$m are compared in (b).

thickness.

## 6.5 Performance of Acoustic Surface in Free Field

In this section, we show a numerical example of calculating the sound generation by an acoustic surface with a PVDF micro-dome transducer array. The acoustic surface is $9 \times 9$ cm$^2$ (square active area), mounted on an infinite rigid baffle. The

domes are evenly distributed on the acoustic surface with a pitch of 1 mm along both $x$-axis and $y$-axis ($z$-axis is normal to the acoustic surface). All the domes have the same dimensions $R = 350$ $\mu$m, $H_0 = 15$ $\mu$m, $h = 12$ $\mu$m. We focus on the performance of the acoustic surface within the audio frequency range and the assigned dome dimensions result in a resonance frequency well above 20 kHz (Figure 6-9). As a result, the dome displacement within the audio frequency range is approximately independent of frequency and equal to the static displacement given by COMSOL simulation. According to the assigned dome dimensions, the dome deformation is close to bending of a thin plate. As a result the average displacement over the entire dome is given by $\overline{w}_d = w_0/3$, where $w_0$ is the deflection at the dome center. All the domes are connected in parallel and driven by the same voltage. The void area in the vicinity of the PVDF domes is assumed as inactive and perfectly clamped. Since the dome size ($R = 350$ $\mu$m) is much smaller than the acoustic wavelength at 20 kHz ($\sim$1.72 cm), we can use (6.29) to calculate the sound generation of each dome by replacing the $A$ and the $\overline{w}$ with the dome area $A_d$ and the average displacement over a single dome $\overline{w}_d$. Then the Rayleigh integral can be discretized and the acoustic pressure at position $\mathbf{r_d}$ generated by the acoustic surface becomes a summation of acoustic pressure generated by all the domes at $\mathbf{r_d}$, which is

$$p(\mathbf{r_d}, f, V) = i2\pi\rho f^2 \overline{w}_d(V) A_d \sum_{n=1}^{N} \frac{e^{ik|\mathbf{r_d} - \mathbf{r'_{dn}}|}}{|\mathbf{r_d} - \mathbf{r'_{dn}}|}, \tag{6.46}$$

where $N$ is the total number of domes on the acoustic surface, $\mathbf{r_d}$ is the vector from the origin to the observation point, and $\mathbf{r'_{dn}}$ is the vector from the origin to the center of dome $n$.

First, the SPLs at different distances from the acoustic surface along $z$-axis (the center of the acoustic surface is designated as the origin) are calculated at 1 kHz, 5 kHz, and 10 kHz, respectively, and the results are shown in Figure 6-10. For comparison purposes, the monopole result of the far-field response is plotted as the red dashed line in each subfigure as a reference. It is observed that the Rayleigh integral result overlaps with the monopole result at a distance large than 20 cm.

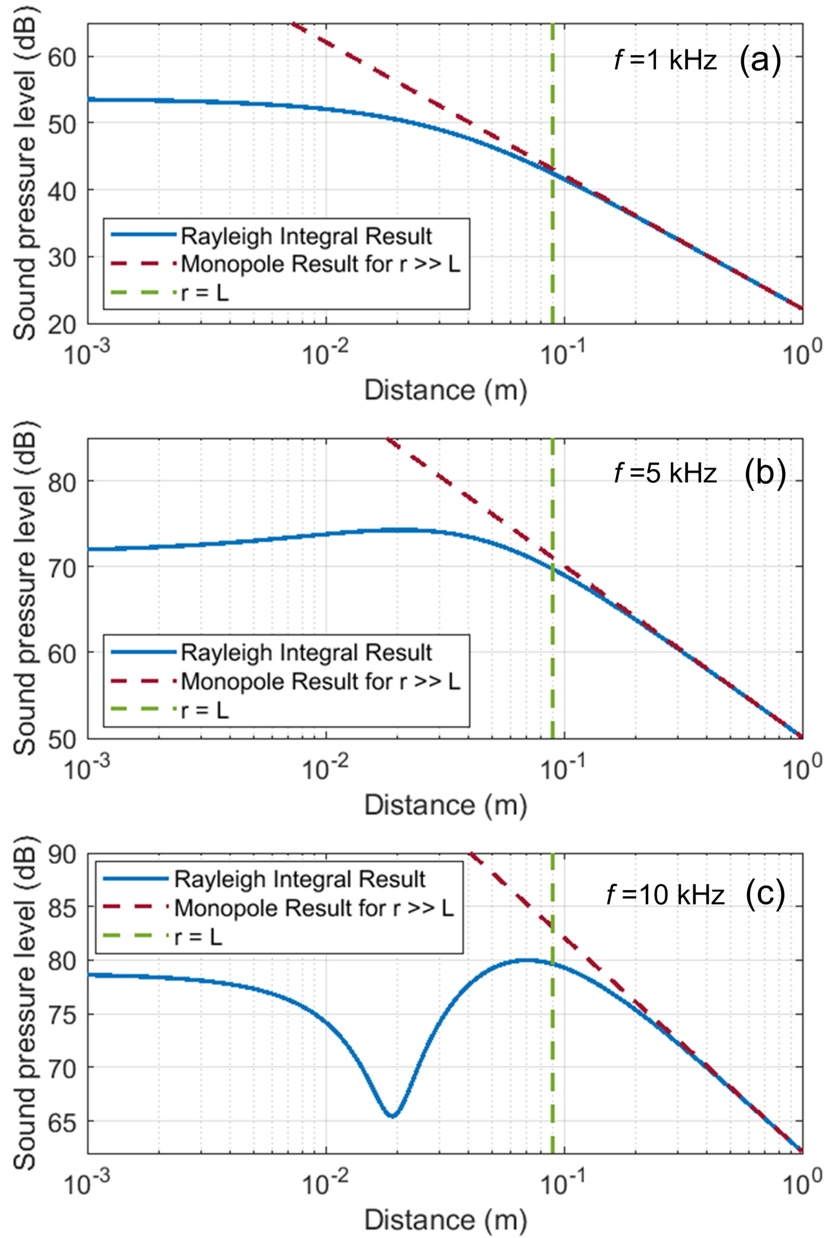


Figure 6-10: On-axis SPL as a function of distance from the acoustic surface, at (a) 1 kHz, (b) 5 kHz and (c) 10 kHz, under a sinusoidal voltage of 10 V in amplitude. The red dashed line presents the monopole result (with perfect reflecting baffle) and the green dashed line marks a distance equal to the side length of the square acoustic surface ($L = 9$ cm).

Besides, the SPL decays at 20 dB/dec as distance increases, and it aligns with the fact that the acoustic pressure decays with $1/r$ in the far field. These indicate that 20 cm is approximately the boundary to separate the near- and far-field responses.

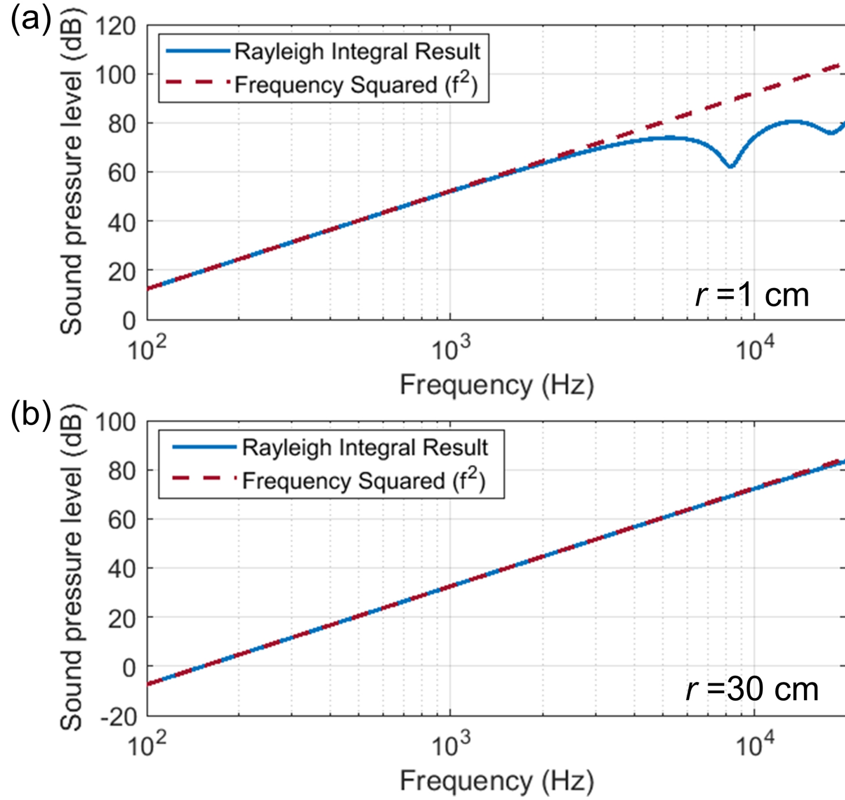


Figure 6-11: On-axis SPL as a function of frequency, at (a) 1 cm (near-field) and (b) 30 cm (far-field) away from the acoustic surface, under a sinusoidal voltage of 10 V in amplitude. The red dashed line presents the frequency dependence ($p \propto f^2$) of a monopole radiator in free field.

Therefore, we choose 30 cm as the distance between the microphone and the sample in order to measure the far-field response (Chapter 8).

The frequency dependence of the SPL generated by the acoustic surface is studied using the Rayleigh integral at 1 cm (near-field) and 30 cm (far-field), respectively, and the results are presented in Figure 6-11. For a monopole radiator in free field, an acoustic pressure proportional to $f^2$ is expected and presented as the red line in each subfigure as a reference. Though the sound generation for each dome should follow this dependency, the interference among thousands of domes in an array could result in deviation, particularly for high frequency. For instance, the acoustic wavelength at 20 kHz is 1.72 cm. For the $9 \times 9$ cm$^2$ acoustic surface, the difference in distance to an observation point at $z = 1$ cm (on-axis) between a dome at the center and a dome at the corner of the acoustic surface is over three wavelengths. As a result, the

interference is important and must be considered for $z = 1$ cm. The fact that not all the domes are vibrating in phase results in an overall sound generation smaller than the monopole result, particularly at a high frequency. However, the difference in distance between the same two domes to an observation point at $z = 30$ cm (on-axis) is less than 0.4 times of the acoustic wavelength at 20 kHz. This explains why the far-field (30 cm) result perfectly aligns with the reference line while the near-field (1 cm) result starts to deviate from a $f^2$ dependence at frequencies above 3 kHz.

The Rayleigh integral can be applied to study the directivity pattern created by the acoustic surface as well, by changing the observation point at different angles to the acoustic surface while maintaining a constant distance of 30 cm to its center. The directivity pattern generated by the acoustic surface is calculated at a series of frequencies (Figure 6-12), and the SPL at each observation point is normalized by the peak SPL at the same frequency (i.e., at $0°$ angle). At 1 kHz, the sound generation is almost uniform in space. At frequencies above 5 kHz, sound generation by the acoustic surface starts to show different directivity patterns. As frequency increases, the sound generation becomes more and more directional. Acoustic beam is formed at frequencies above 15 kHz. Beam forming at lower frequency may be possible by increasing the area of the acoustic surface and applying proper amplitude and phase control of the drive voltages for domes located at different spots on the acoustic surface.

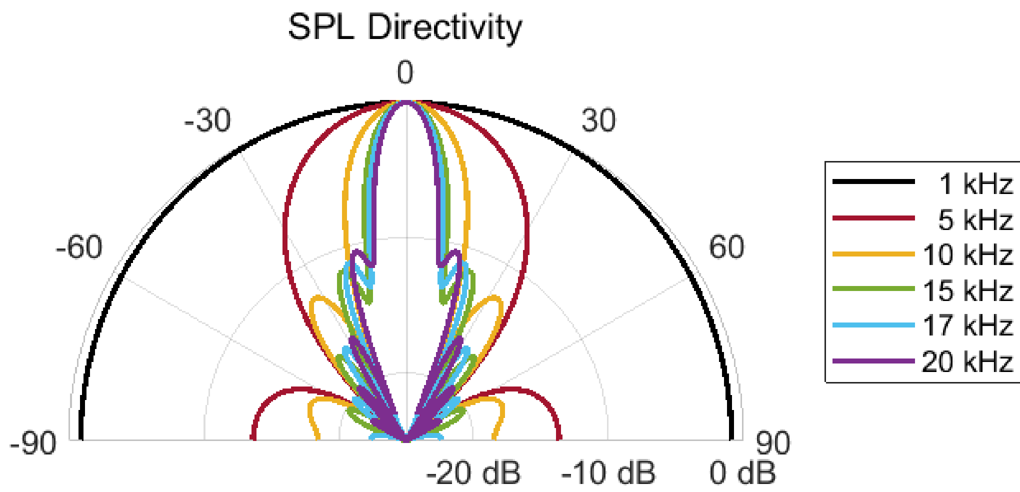


Figure 6-12: SPL directivity patterns at 30 cm from the acoustic surface with respect to frequencies of 1 kHz, 5 kHz, 10 kHz, 15 kHz, 17 kHz, 20 kHz. The SPL values for different observation points at each frequency are normalized by the peak SPL (0° angle) at the same frequency.

# Chapter 7

# Fabrication of Acoustically-Active Surface

## 7.1 Overview of Fabrication Approaches

The performance of an acoustic surface greatly depends on the precise definition of geometry and dimensions of the active micro-domes on the PVDF film. According to our design, a perforated protective film with circular through-holes of the same size as the micro-domes should be fabricated as well. Patterning these polymer films should be of high precision and low cost, and in a scalable fashion to allow mass production of wide-area acoustic surfaces.

Polymer patterning techniques differ from silicon-based microfabrication in many ways, due to their low thermal endurance and broad range of chemical and mechanical properties. In general, patterning microstructures on a polymer can be divided into constructive approaches and destructive approaches. A comprehensive review of typical microfabrication approaches for polymers can be found in [133].

Constructive approaches can be further grouped into photo-based techniques and replication techniques, depending on how the microstructures are shaped. For photo-based methods, light-sensitive liquid organic materials (photoresist or light-senstive resin) are cured by UV (for photolithography), laser beam (for stereolithography) or conventional light sources (e.g., arc lamp for digital light processing). These photo-

based approaches provide fast prototyping and capability of building micrometer-scale features (e.g., photolithography); however, they are generally not suitable for low-cost mass production and the material choice is limited as well. In replication techniques, a master structure (i.e., mold) is required, which is critical to the quality of the molded polymer. In order to achieve good geometrical accuracy, a mold can be made by silicon, electroplated metal or other polymers (e.g., SU8, PDMS) based on microfabrication processing. Stainless steel molds prepared by micro electrode discharge machining can be utilized for fabricating larger structures on polymers. For the hot embossing approach, a hot mold is pressed into a polymer that is heated up to slightly above its glass transition temperature, which thereby transfers the patterns on the mold to the polymer. The high accuracy of this approach allows fabricating features down to a few tens of nanometers and the corresponding technique is named as nanoimprinting. In a similar replication approach, the polymer film can be placed on top of a heated mold and made to conform to the mold profile by pressurized gas. Injection molding and casting are another two popular approaches for polymer fabrication. For injection molding, the polymer material is melted, injected under high pressure into a cavity with mold insert and cooled down to solidify. Casting is widely utilized for shaping elastomer (e.g., PDMS), where elastomer resin is mixed with curing agent, degassed and poured onto the mold to solidify.

Destructive approaches include precision machining, laser ablation and plasma etching. With ultra-small machining tools (e.g., endmills with diameters down to sub-100 $\mu$m), fine features can be created on various polymer materials; however, residuals can be left around the microstructures and the long processing time makes it not suitable for mass production. In laser ablation processing, the high-intensity laser evaporates the polymer at the focal point and microstructures can be patterned with the help of a shadow mask or directly by moving the laser (or the substrate) laterally according to the design. Plasma etching typically relies on a shadow mask and the exposed polymer is removed. This method does not perimt creating deep features with high precision.

These polymer processing approaches have been utilized for fabricating mi-

crostructures on piezoelectric polymers. Hot embossing is particularly popular for creating voids for cellular ferroelectret polymers [90, 134]. Adapted microembossing methods have also been developed to fabricate microstructures on PVDF films. For instance, Si and SU8 molds were utilized to emboss PVDF films into a wavy shape at room temperature [135]. In another work, a PVDF film was pressed onto a mold with SU8 pillars, and an array of dome structures were thus created by thermally inflating the trapped air between the pillar and the PVDF film [136]. Besides the embossing approaches, PVDF-TrFE copolymer can be spincoated on microfabricated molds to obtain dome and bump structures [137], similar to the casting approach. Photo-based methods have been utilized for PVDF patterning as well. Femtosecond laser machining was used to cut the PVDF film and pattern the NiCu electrode layer [138]. A pressure sensor based on patterned PVDF-TrFE was achieved with a combination of photolithography and plasma etching [139]. In addition to these general or adapted polymer processing techniques, piezoelectric polymers can be patterned by selective poling/depoling [140] to achieve pixelated transducers. However, this approach is unable to create microstructures, which can significantly enhance the transducer performance (as discussed in Chapter 6).

## 7.2 Micro-Embossing Process Based on Controlled Vacuum

A micro-embossing process based on controlled vacuum is developed to pattern the micro-dome array on a wide-area PVDF film. The fabrication process is shown in Figure 7-1. To precisely define the dome size, a perforated Si wafer is first prepared by microfabrication. 100-nm-thick aluminum (Al) film is deposited on a 6-inch Si wafer by thermal evaporation. AZ 4620 photoresist is then spin-coated on top of the Al film at 2000 rpm, and soft-baked on hotplate at 110 °C for 3 min, which results in a $\sim$10 $\mu$m thick resist layer. Maskless aligner MLA150 is used to directly write the pattern of through-hole array with 800 mJ/cm$^2$ area dose. After exposure, the

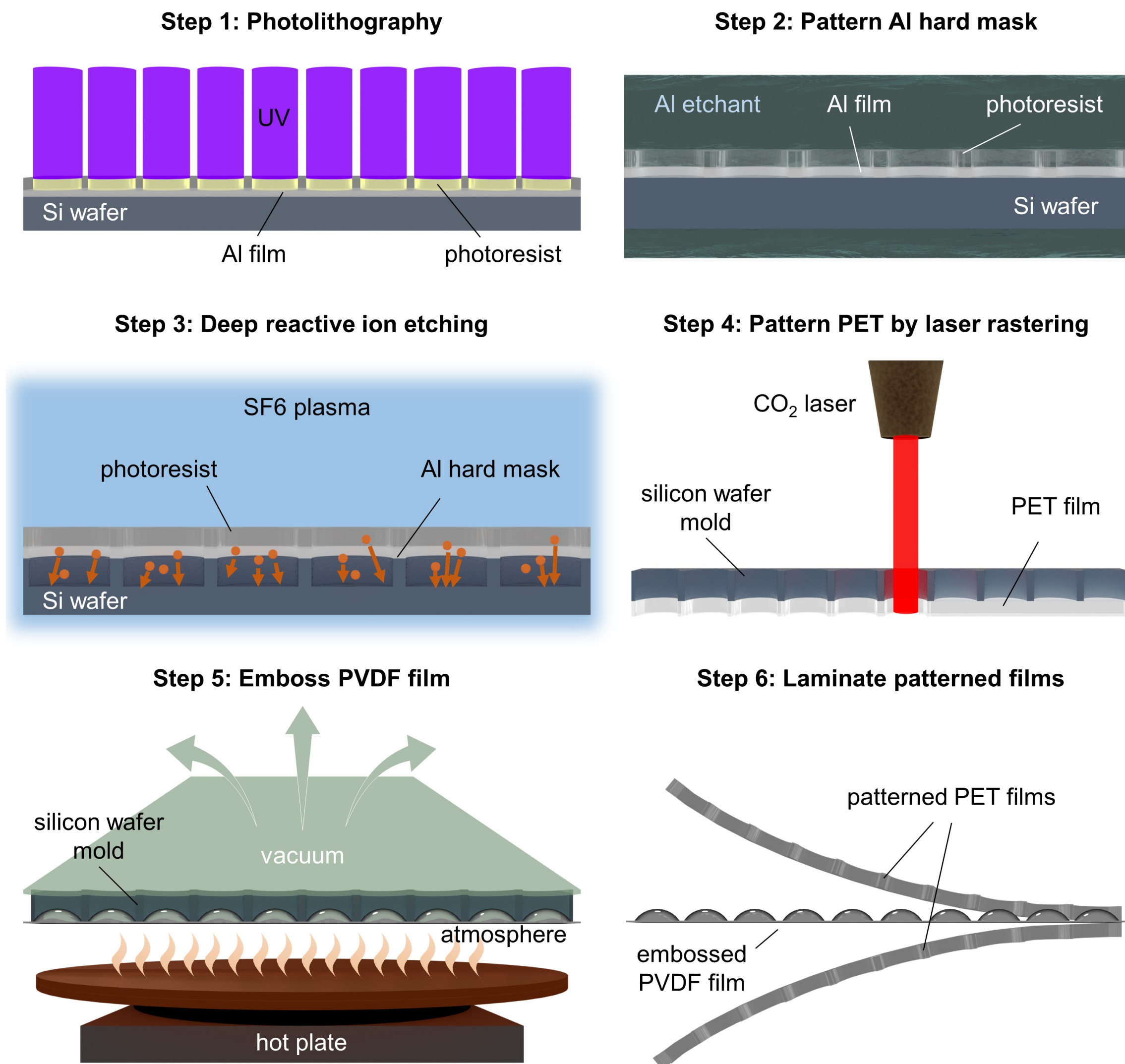


Figure 7-1: Fabrication of an acoustic surface with an array of PVDF domes based on the micro-embossing process.

photoresist is developed in AZ435 developer for 5 min, rinsed with DI water, and dried by nitrogen flow. The sample is further hard-baked in a 120 °C oven for 30 min, and then etched in Al etchant type A for 3 min to pattern the hard mask layer. The Si wafer with both Al hard mask and photoresist soft mask is mounted on a back wafer. Then the exposed Si area is etched through using deep reactive ion etching (Bosch process) to form an array of through-holes. The photoresist layer is then stripped by acetone and the as-fabricated perforated Si mold is shown in Figure 7-2(a). In this

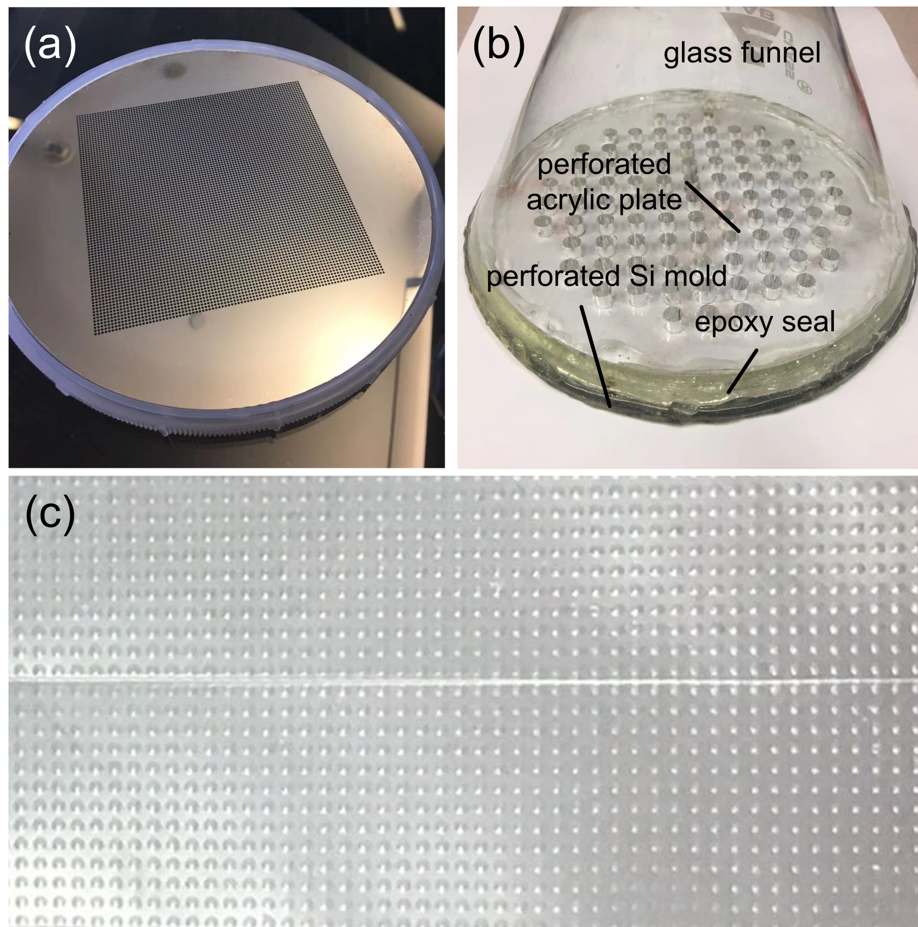


Figure 7-2: Pictures of (a) a perforated Si mold prepared by microfabrication, (b) a setup for embossing domes on a PVDF film, and (c) a PVDF film with micro-domes in an array.

way, the size and shape of the through-holes can be precisely defined, which further define the size and shape of PVDF domes. A significant pressure difference across the perforated Si mold during embossing process could cause the Si wafer to bend and crack. To enhance the strength of the embossing mold, several perforated Si wafers with identical through-hole arrays are prepared, aligned and stacked together to use. Perforated, thick metal plates could be alternatives to the micro-fabricated Si wafer as the mold for the embossing process. A porous, rigid thick plate (glass, acrylic, etc.) can also be employed as structural support to prevent bending of the Si mold. The 6-inch Si mold is adhered to a glass funnel, as shown in Figure 7-2 (b), which is connected to house vacuum through a control valve and a pressure gauge.

To emboss the PVDF micro-dome array, a $10 \times 10$ cm$^2$ PVDF film (PolyK Technologies, Inc., parameters shown in Table 7.1) is adhered to the side of the Si mold that is open to air, while the other side is under vacuum. The area on the PVDF film that aligns with through-holes on the mold deforms into dome profile by the pressure difference. Then a repetitive annealing scheme is employed to relieve the stress and help maintain the dome profile even after removing the vacuum. Specifically, the embossing mold with a PVDF film adhered to it is suspended 1.5 cm above a 250 °C hot plate for 5 min. As a result, the PVDF film is annealed at ∼80 °C in this process, which does not affect the poling of PVDF. Then the embossing mold with the PVDF film is cooled down to room temperature while the vacuum is kept on. Such annealing and cooling treatment is repeated for three times to complete the embossing process. A PVDF film embossed with a micro-dome array using this approach is shown in Figure 7-2 (c). The heights of the embossed domes are dependent on the pressure difference during embossing. A higher vacuum level creates larger deformation and thereby taller domes. We choose a vacuum level around $-25$ kPa so that the embossed domes with a 350 $\mu$m radius have a $\sim 20$ $\mu$m height on average, which is close to the optimal height given by COMSOL simulation (Figure 6-4).

As the theory and simulation suggest in Chapter 6, a reduced thickness of the PVDF film leads to higher sensitivity for sound generation. As a result, a PVDF film down to a few microns in thickness is favorable; however, the structural strengths of the corresponding micro-domes are weak. To protect the domes from collapses caused by mechanical impact (e.g., touching), a perforated plastic film (e.g., polyester) is fabricated and laminated on the embossed PVDF film. The thickness of the plastic film is larger than the dome height (Figure 7-3) and as a result, the domes can avoid collapses caused by mechanical impact. The through-holes on the plastic film, patterned by a $CO_2$ laser cutter in a rastering mode, are aligned with the domes so that these active microstructures can vibrate without being impeded by the protective layer. Another identical perforated plastic film is laminated on the other side of the embossed PVDF film. The through-holes that align with the micro-domes create isolated back cavities. The volume of these back cavities are large enough so that the

Table 7.1: Properties of uniaxially-oriented PVDF films

| Properties | | Typical Value |
|---|---|---|
| thickness | $h$ ($\mu$m) | 12 |
| piezoelectric strain constant | $d_{31}$ ($10^{-12}$ C/N) | $\sim 30$ |
| | $d_{33}$ ($10^{-12}$ C/N) | $\sim -19 \sim 21$ |
| piezoelectric stress constant | $g_{31}$ ($10^{-3}$ V·m/N) | $210 \sim 220$ |
| | $g_{33}$ ($10^{-3}$ V·m/N) | $330 \sim 350$ |
| relative dielectric constant | $\epsilon_r$ | 13.0 (@ 1 kHz, 25 °C) |
| pyroelectric coefficient | $\rho_p$ ($10^{-6}$ C/(m$^2$·K) | $25 \sim 30$ |
| electromechanical coupling factor | $k_{31}$ (%) | $10 \sim 13$ |
| | $k_t$ (%) | $12 \sim 15$ |
| maximum operating voltage | $E$ (V/$\mu$m) | >100 (@ DC voltage, 25 °C) |
| tensile strength | $\sigma_{\mathrm{MD}}$ ($10^9$ N/m$^2$) | $0.4 \sim 0.6$ |
| | $\sigma_{\mathrm{TD}}$ ($10^9$ N/m$^2$) | $0.05 \sim 0.06$ |
| Young's modulus | $Y_{\mathrm{MD}}$ ($10^9$ N/m$^2$) | $2.2 \sim 2.3$ |
| | $Y_{\mathrm{TD}}$ ($10^9$ N/m$^2$) | $\sim 2.0$ |
| elongation at break | $\epsilon_{\mathrm{MD}}$ (%) | $20 \sim 30$ |
| | $\epsilon_{\mathrm{TD}}$ (%) | $5 \sim 7$ |
| speed of sound | $v$ (m/s) | 2300 |
| optical transparency | | >90% |
| melting temperature | (°C) | $170 \sim 175$ |
| surface energy | | >56 dynes |
| thermal shrinkage | | <0.5% MD (@65 °C/3 hour) |

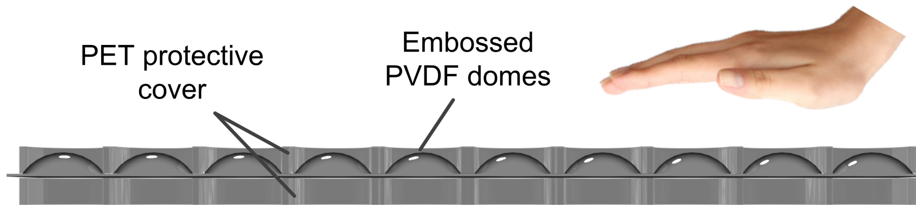


Figure 7-3: Schematic of a flexible, robust acoustic surface with PVDF micro-domes protected by a perforated plastic film.

volume change caused by the dome vibration is negligible. In this way, the pressure in the cavity is always maintained close to atmospheric pressure and does not impede vibration of the domes.

Following the aforementioned approach, a flexible acoustically-active surface can be fabricated comprising two 50-$\mu$m-thick perforated PET films and a PVDF thin film (typical thickness less than 12 $\mu$m) with a micro-dome array and Ag electrodes. Transparent acoustic surfaces can be prepared in the same way, while pure indium tin

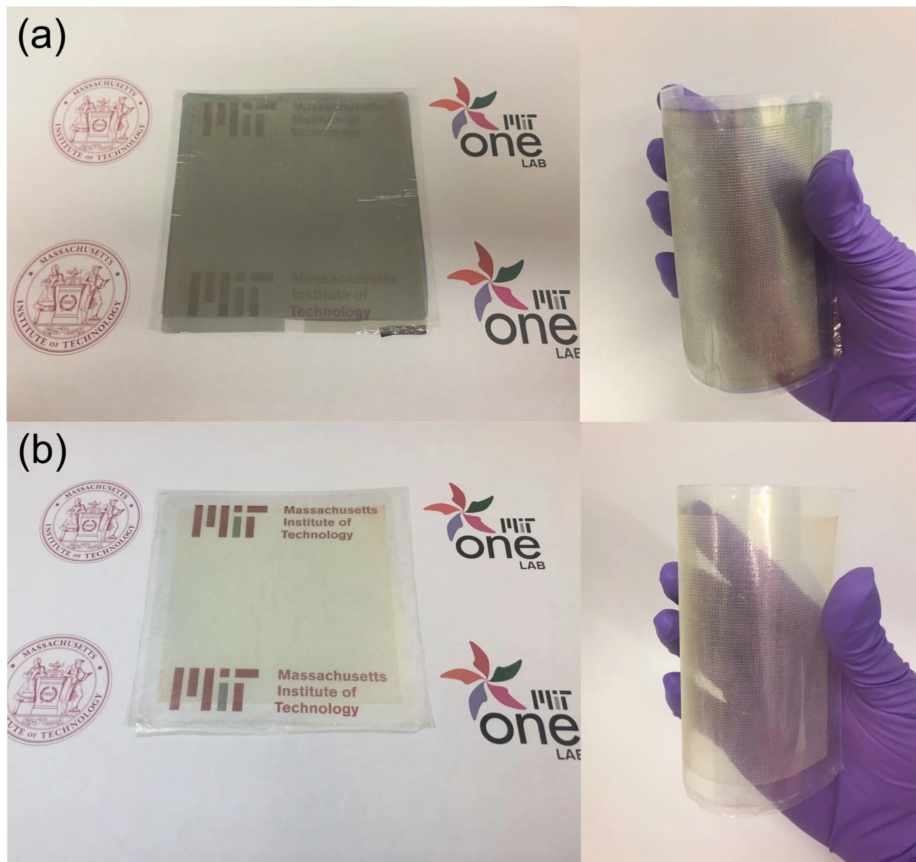


Figure 7-4: Examples of flexible, transparent acoustic surfaces based on (a)Ag/ITO (5 nm/35 nm) electrodes and (b) ITO (50 nm) electrodes.

oxide (ITO) or a combination of Ag and ITO is employed as the electrode material. Pictures of two examples based on different types of electrodes are shown in Figure 7-4.

## 7.3 Self-Aligned Micro-Embossing Process

The micro-embossing process introduced in Section 7.2 is likely to face challenges of alignment between the embossed PVDF film and the perforated plastic films. An example of misalignment between the through-holes on the plastic film and the domes on the PVDF film is shown in Figure 7-5 (a). In this example, the dome vibration can be greatly impeded by the PET film on top, which thereby reduces the sound generation. Such an issue typically occurs as a result of manual alignment while

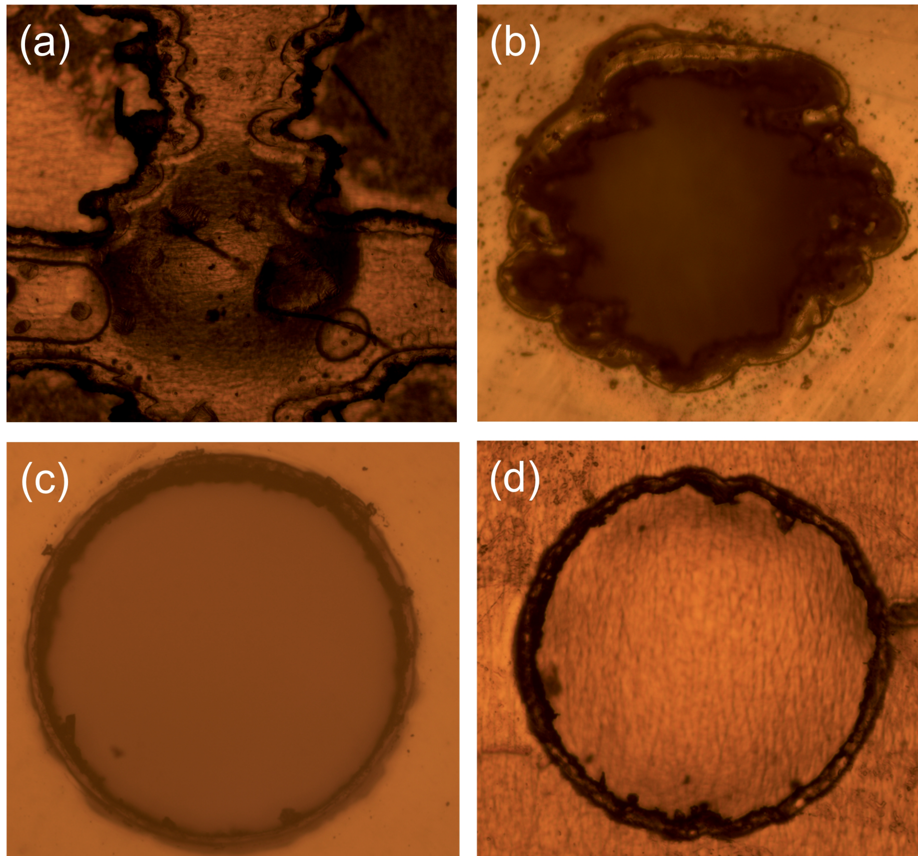


Figure 7-5: Pictures of (a) a PVDF dome misaligned with the through-holes on the top protective film, (b) a through-hole patterned by direct-write $CO_2$ laser rastering, (c) a through-hole patterned by mask-assisted laser rastering, and (d) a dome prepared by self-aligned micro-embossing with a perforated protective film on top.

laminating the films. Besides, a deformed PVDF film after annealing also contributes to the misalignment, which results in a dome pitch different from the pitch of through-holes on the plastic film. When the plastic film is laminated on top of a PVDF film that is not perfectly flat and/or with shifted dome pitch, a good alignment over a wide area is impossible.

To avoid the misalignment issue, a self-aligned micro-embossing process has been developed. This improved approach utilizes the perforated plastic film instead of the Si wafer as the mold to emboss the micro-dome array. The detailed processing steps are presented in Figure 7-6. To achieve a perfect dome profile, the shape of the through-holes on the plastic film is critical. However, the through-holes patterned by direct-write laser rastering are irregular (Figure 7-5 (b)) and nonuniform over a wide

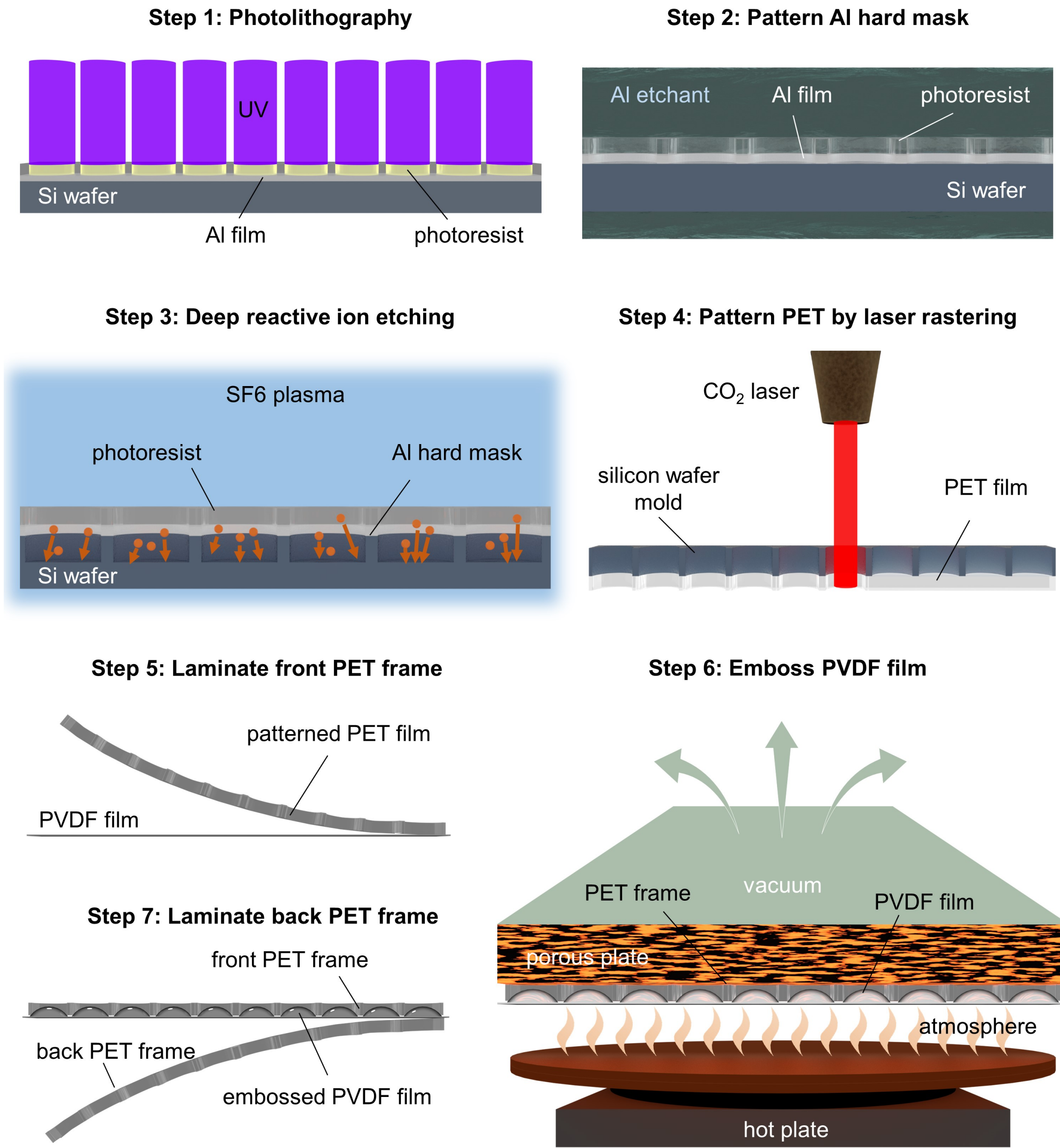


Figure 7-6: Fabrication of an acoustic surface with an array of PVDF micro-domes based on self-aligned micro-embossing process.

area. Therefore, a mask-assisted laser rastering has been developed to achieve perfect circular holes (Figure 7-5 (c)). Specifically, a micro-fabricated Si wafer (prepared in the same way as introduced in Section 7.2) is put on top of the plastic film; the laser cutter does blanket rastering and area of the plastic film that is exposed to the $CO_2$ laser is evaporated. The Si shadow mask is not heated up during the entire rastering

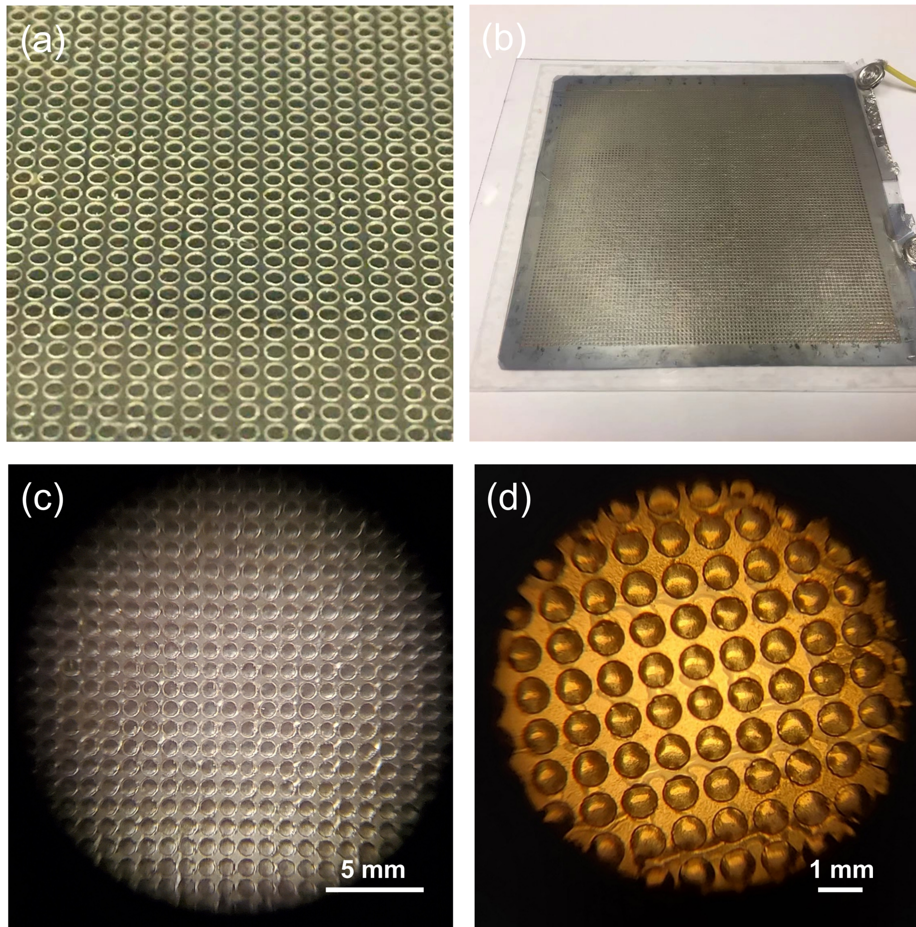


Figure 7-7: (a) Picture of a perforated PET thin film prepared by mask-assisted laser rastering. (b) Picture of an acoustic surface sample adhered to a glass substrate. (c) Microscopic image of PVDF domes in an array. (d) Microscopic image of PVDF domes under a higher magnification.

process, and therefore the plastic film does not deform. Such an approach is not only able to create perfect circular through-holes with dimensions precisely defined by the Si shadow mask, but also scalable to make a wide-area perforated plastic film by laterally moving the plastic film underneath the Si shadow mask. A 50-$\mu$m-thick PET film patterned with an array of through-holes (700 $\mu$m in diameter, 1 mm pitch) is shown in Figure 7-7 (a). For mass production, the perforated plastic film can be fabricated based on other high-throughput polymer processing methods such as hot embossing, injection molding, casting, etc.

The perforated PET film is then laminated on a flat PVDF film with deposited electrodes. The laminate is adhered to a porous thick plate (with pore size smaller

than the size of through-holes on the PET film) that is connected to vacuum. The micro-domes are subsequently embossed under controlled vacuum following the repetitive annealing treatment. Figure 7-5(d) and Figure 7-7 (c), (d) present the microscopic images of an individual micro-dome and of a micro-dome array, formed by the self-aligned embossing process. Then another perforated plastic film is aligned and laminated to the other side of the embossed PVDF film to form isolated back cavities. Such a flexible laminate can be mounted on the surface of an arbitrary object, thereby rendering it acoustically active. To measure the surface velocities of individual domes and the overall acoustic performance, $10 \times 10$ cm$^2$ acoustic surface samples ($9 \times 9$ cm$^2$ active area, 1 mm pitch) are mounted on rigid substrates (e.g., glass substrate) and an example device is shown in Figure 7-7 (b).

It should be pointed out that our developed approach is not limited to fabricating $10 \times 10$ cm$^2$ samples. For instance, a wallpaper size perforated PET film could be prepared by mask-assisted laser rastering and laminated on a wallpaper size PVDF film. The PVDF domes can be embossed simultaneously using a porous thick plate of a similar size that is connected to vacuum, or one region after another by laterally moving the laminated film underneath a small porous thick plate.

# Chapter 8

# Performance of Acoustically-Active Surface

## 8.1 Acoustic Measurement Setup

To evaluate the performance of an acoustic surface, surface velocity is first measured to characterize the vibration of individual PVDF domes. A schematic of the setup to measure surface velocity is shown in Figure 8-1. An Agilent 33220A function generator outputs a sinusoidal AC source voltage signal to a Crest AUDIO 1001A Professional Power Amplifier, which amplifies the source voltage by $10\times$ to drive the sample. The sample is placed on top of an XY linear stage below the microscope of a Polytec CLV 1000 laser vibrometer. The laser vibrometer is able to conduct non-contact measurement of the dome vibration based on the Doppler effect. When the laser beam is directed at the position of interest, the surface vibration causes a Doppler shift, which is translated into a voltage signal to be captured by an oscilloscope. The laser vibrometer model utilized in our experimental setup has 5 mm/s/V and 25 mm/s/V exchange rates to choose from and optional built-in low-pass filters with bandwidths of 5 kHz, 20 kHz, and 50 kHz. The laser beam is adjusted to focus on the sample and directed normal to the surface at a fixed spot. When the sample is moved by the linear stage during measurement, the surface velocities at different positions on the sample can be probed. The displacement amplitude along the direction normal to

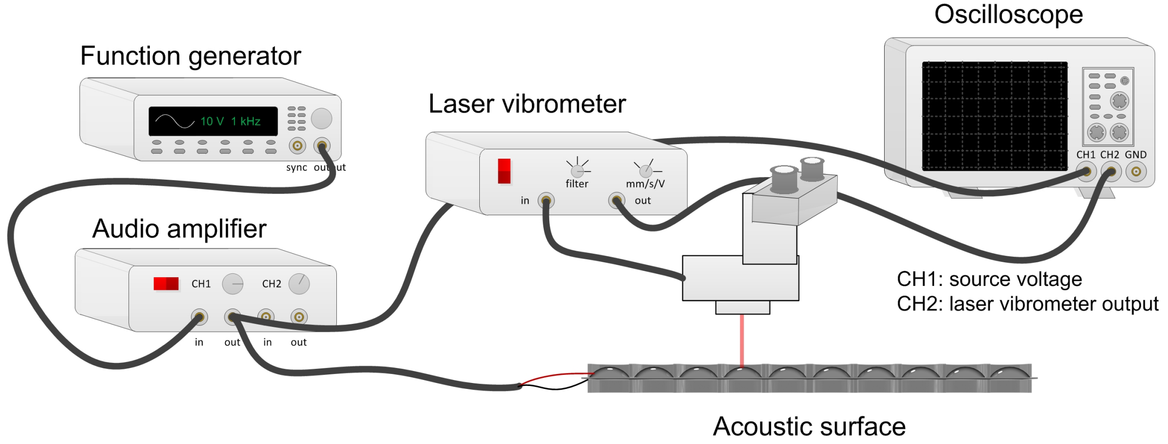


Figure 8-1: Schematic of the setup to measure surface velocities of PVDF domes.

the sample surface can be extracted from the output voltage signal based on selected exchange rate of the laser vibrometer, given by

$$w_0 = \frac{U_{lv,p-p} R_{v-U}}{4\pi f}, \tag{8.1}$$

where: $w_0$ is the peak amplitude of displacement normal to the acoustic surface; $U_{lv,p-p}$ is the peak-peak value of the output voltage from the laser vibrometer; $R_{v-U}$ is the exchange rate of the laser vibrometer; and $f$ is the vibration frequency.

To characterize the sound generation by an acoustic surface, the acoustic pressure and SPL under voltages of different frequencies and amplitudes are measured at a certain distance and a certain angle to the sample. Measurement of the acoustic performance is conducted in an anechoic chamber (Figure 8-2 (b)), and a schematic of the measurement setup is presented in Figure 8-2 (a). A custom LabVIEW measurement interface is developed that controls amplitude and frequency of the sinusoidal AC source voltage signal from an Agilent 33220A function generator. The voltage signal is ampilified by a Crest AUDIO 1001A Professional Power Amplifier by 10× to drive the sample. The function generator and audio amplifier sit outside the chamber and are connected to the in-chamber sample and equipment with through-wall BNC cables. Inside the chamber, the sample is mounted at the center of a $1 \times 1$ m$^2$ acoustic baffle that hangs from the ceiling. The large, rigid acoustic baffle acts as a perfect

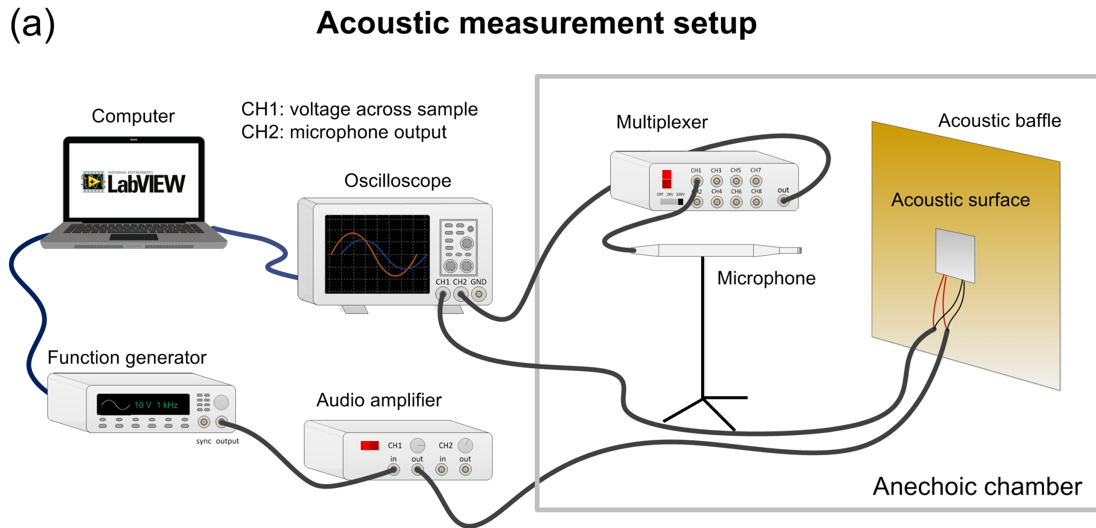

Figure 8-2: (a) Schematic and (b) pictures of the acoustic measurement setup in an anechoic chamber.

reflecting plane and reduces diffraction around the sample.

The sound generation of the sample is measured by a calibrated Brüel & Kjær (B&K) 4136 microphone that points towards the center of the sample. The 1/4-inch-diameter B&K 4136 free-field microphone is condenser-type with high stability, high linearity and low sensitivity to vibration, suitable for random incidence, high-level and high-frequency measurements. The microphone is connected to a 1/2 inch B&K Type 2669 preamplifier via a UA 0035 1/4 inch to 1/2 inch adapter. The preamplifier is then connected to a B&K Microphone Multiplexer 2822 using a 2669B cable. The

microphone is charged by the DC power supply (28 V or 200 V) provided by the multiplexer. The output of the multiplexer is connected to an oscilloscope outside the chamber using a through-wall BNC cable. The LabVIEW interface controls the oscilloscope to acquire the output signal from the multiplexer. Additionally, the voltage that drives the sample is also monitored by a 10× voltage probe and acquired by the oscilloscope.

To obtain an accurate acoustic pressure measurement, the microphone must be calibrated first. The calibration coefficient is obtained by inserting the B&K 4136 microphone into a portable acoustic calibrator (Pistonphone type 4228) with a proper adaptor. The pistonphone produces a known volume displacement in a small cavity, and provides a precisely defined sound pressure level (124 dB SPL at 250 Hz) to the microphone. The given sound pressure level corresponds to a certain reference condition, and correction is needed to take ambient pressure and load volume into account. With the barometer provided with the pistonphone for correction, IEC942(1988) Class 1L standard is satisfied, and the actual SPL that the pistonphone produces is given by

$$SPL_{actual} = SPL_{ref} + \triangle L_p + \triangle L_V, \tag{8.2}$$

where $\triangle L_p$ is directly read from the barometer that comes with the pistonphone, and $\triangle L_V$ is load volume correction, given by

$$\triangle L_V = -20 \log_{10}(\frac{V_{load} + 18.4}{19.733}), \tag{8.3}$$

where $V_{load}$ is the actual effective volume (the sum of the front volume and the microphone equivalent volume, in unit of cm$^3$) dependent on the type of microphone. For the B&K 4136 1/4 inch microphone used in our experiment, the load volume correction is 0. The RMS pressure generated by the pistonphone is therefore given by

$$p_{cal} = p_0 \times 10^{\frac{SPL_{actual}}{20}}, \tag{8.4}$$

where $p_0 = 20\ \mu Pa$ is the reference sound pressure. The calibration coefficient (i.e.,

sensitivity of the microphone) is calculated as

$$K_{mic} = \frac{U_{mic,p-p}}{2\sqrt{2}p_{cal}}, \tag{8.5}$$

where $U_{mic,p-p}$ is the peak-peak output voltage of multiplexer, captured by the oscilloscope. Substituting the calibration data $U_{mic,p-p} = 126$ mV, $SPL_{ref} = 124$ dB, $\triangle L_p = 0.15$ dB, $\triangle L_c = 0$, the calibration coefficient of the microphone is 1.3846 mV/Pa, corresponding to a 200 V DC supply.

To obtain the acoustic pressure generated by the sample, LabVIEW collects the drive voltage applied on the sample and the microphone signal (output from multiplexer) simultaneously. The acquired waveforms are converted into the frequency domain by fast Fourier transform (FFT) in LabVIEW. The frequency component of the drive voltage that has the maximum magnitude indicates the source frequency $f_s$. Then the magnitude of the same frequency component of microphone signal $A_{mic-fs}$ is extracted and converted into RMS acoustic pressure using the calibration coefficient $K_{mic}$ by

$$p_{sample} = \frac{A_{mic-fs}}{\sqrt{2}K_{mic}}, \tag{8.6}$$

which can be further converted into SPL by (6.31). To further improve the signal-to-noise (SNR) ratio, 100 cycles of both the source voltage and the microphone output are collected and transformed by FFT (based on 100 cycles) to extract their amplitudes at the frequency of interest to reduce noise.

The 4136 B&K microphone has a protection grid installed, which causes acoustic pressure attenuation particularly at high frequencies. Therefore, correction is added to the measured acoustic pressure and SPL for frequencies between 4 kHz and 70 kHz according to the free-field correction curve (Figure 8-3, 0° angle) provided by the manufacturer [141]. No correction is added to frequencies below 4 kHz, because the attenuation is small and correction data are absent from manufacturer for that range.

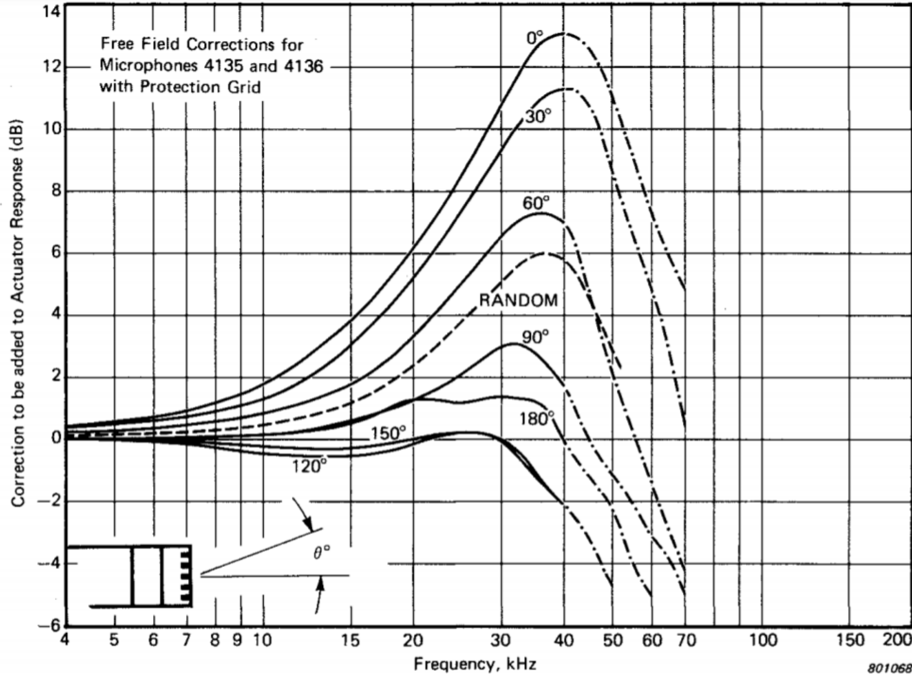


Figure 8-3: Free-field correction curve for the B&K 4136 condenser microphone [141].

## 8.2 Surface Velocities of Individual PVDF Micro-Domes

The distribution of surface velocities of PVDF domes on an acoustic surface is first investigated. The area of the active dome array is $9 \times 9$ cm$^2$ with a 1 mm pitch along both in-plane directions. To conduct a statistical learning, the surface velocities (at the dome center) of $16 \times 16$ domes at different positions of the sample (out of the 8100 domes in total) are measured by laser vibrometer, which corresponds to a sampling rate of 3.16%.

Typically, an acoustic surface sample is adhered to a rigid glass substrate before measurement. In this way, the back cavities of the PVDF domes are sealed, which isolates the domes to reduce crosstalk and avoids interference from the air displacement on the backside of the domes to that on the frontside. Fixing the flexible acoustic surface on a rigid substrate is also expected to reduce vibration of the void area between domes arising from overall bending/wrinkling of the PVDF film. To study the influence of mounting the sample to a rigid substrate, surface velocity distribution of

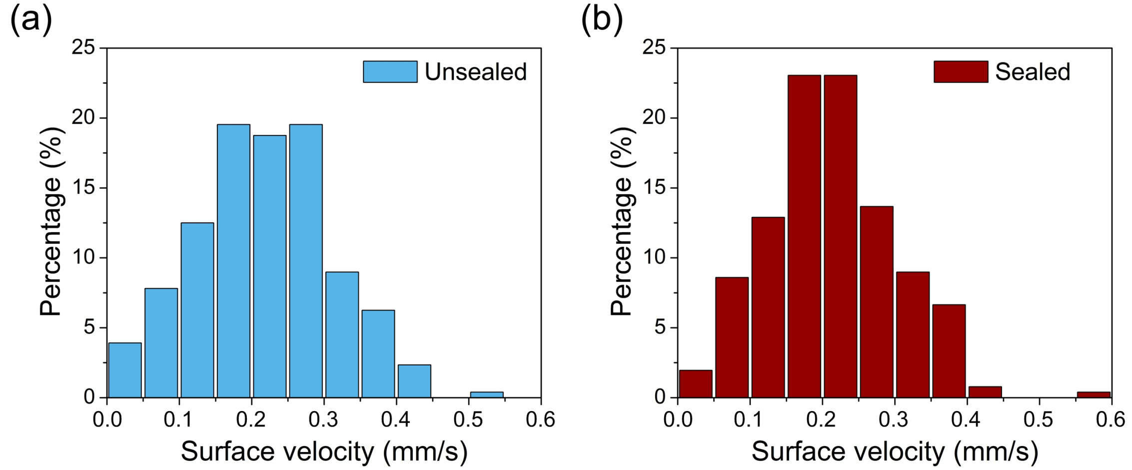


Figure 8-4: (a) Statistics of surface velocities of PVDF domes on a freestanding acoustic surface. (b) Statistics of surface velocities of PVDF domes on an acoustic surface mounted on a glass substrate.

PVDF domes with radius $R = 350$ $\mu$m, film thickness $h = 12$ $\mu$m embossed at -25 kPa vacuum level (resulting in dome heights $H_0 = 14 \sim 22$ $\mu$m) on an acoustic surface sample is first measured under a 10 V (amplitude), 1 kHz sinusoidal drive voltage, and the sample is placed on the stage without bonding. Then the surface velocity distribution of the sample is measured under the same condition after adhering it to a glass substrate using a thin layer of adhesive. The comparison in Figure 8-4 indicates that the surface velocity distributions before and after mounting the sample to a glass substrate both follow Gaussian distributions. The mean and median of surface velocities (0.218 mm/s and 0.209 mm/s, respectively) before mounting the sample are almost identical to those (0.213 mm/s and 0.208 mm/s, respectively) after mounting; however, the distribution is less concentrated before mounting, likely caused by the overall bending of the PVDF film. The deflection amplitude at the dome center is extracted to be 34 nm on average for the sample with back glass substrate. The deflections given by the thin-plate theory and the COMSOL simulation corresponding to the same design variables ($R = 350$ $\mu$m, $h = 12$ $\mu$m, $H_0 =\sim 20$ $\mu$m) for a PVDF dome are 31.8 nm and 50.2 nm, respectively, which agree reasonably well with the experimental deflection. This validates the effectiveness of the theoretical model and simulation in predicting the dome vibration and further the performance of an

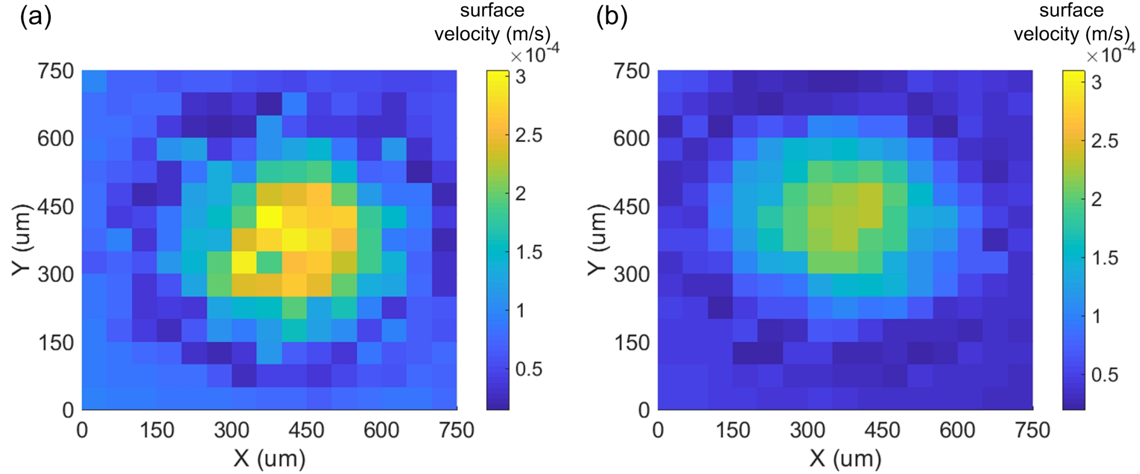


Figure 8-5: (a) Surface velocity mapping of a PVDF dome on a freestanding acoustic surface. (b) Surface velocity mapping of a PVDF dome on an acoustic surface mounted on a glass substrate. The surface velocity is measured under a 1 kHz, 10 V (amplitude) drive voltage in both (a) and (b).

acoustic surface with a PVDF dome array.

The surface velocity mapping for a PVDF dome is also conducted by moving the sample with an incremental step of 50 $\mu$m along both in-plane directions. The surface velocity maps of representative domes before and after mounting the sample to the glass substrate are compared in Figure 8-5. The surface velocity on the inactive area is greatly reduced after mounting, indicating the existence of overall bending of the PVDF film. It should be noticed that the surface velocity on the inactive area after mounting is still non-zero, which contributes to overall sound generation of the sample. The deformation of the dome can be extracted from the surface velocity map. The surface velocities along the cross-section ($X = 400$ $\mu$m) in Figure 8-5 (b) are converted to normalized deflection and added into the plot with theoretical displacement distribution of a deformed membrane (6.18) and that of a deformed thin plate (6.19) in Figure 8-6. Considering that the overall displacement of the PVDF film due to imperfect bonding adds an offset to the dome displacement, the experimental displacement distribution without the offset matches better with the green curve. It indicates that the deformation of a dome with a 350 $\mu$m radius and a 12 $\mu$m thickness follows bending of a thin plate more closely, which agrees with our

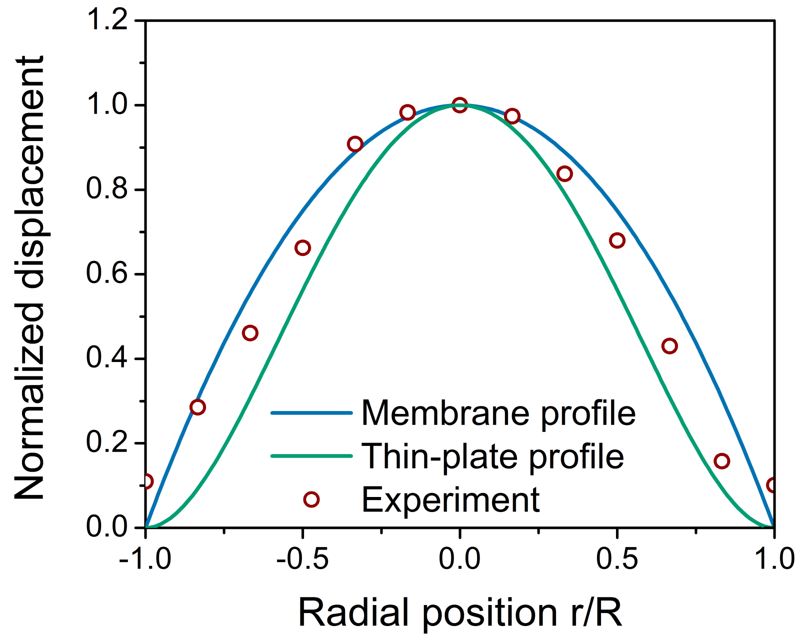


Figure 8-6: Normalized experimental displacements along radial direction of the dome compared with theoretical normalized displacements given by the membrane model and the thin-plate model.

theory and simulation for such design variables.

To study the uniformity in the performance of fabricated samples, another two samples with the same design variables for PVDF domes are fabricated and mounted on glass substrates. The PVDF domes are sampled in the same way and the statistics of their surface velocities are presented in Figure 8-7. The results show similar surface velocity distributions for the three samples (mostly within the range of 0.05 $\sim$ 0.4 mm/s); differences in these distributions may be attributed to variations in the fabrication process, e.g., non-uniform poling over the PVDF film, wrinkled or deformed PVDF film before laminated with flat PET protective film, unevenly coated adhesives, etc. Such variation in performance can be greatly reduced when the fabrication process is automated.

The theoretical modeling and simulation in Chapter 6 suggest that deflections of PVDF domes under unit drive voltage and the resulting sensitivity of the acoustic surface can be tuned by changing the dome dimensions. To demonstrate this tun-

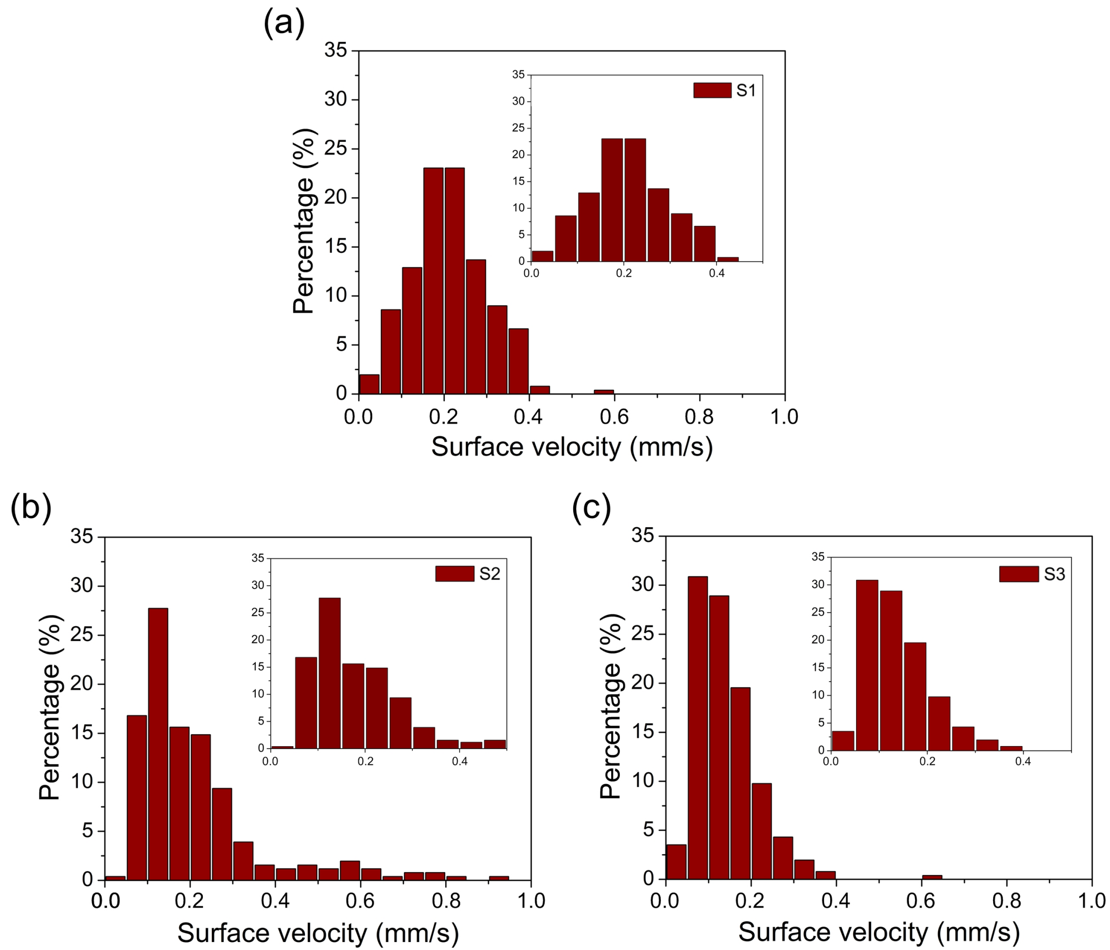


Figure 8-7: Statistics of surface velocities of PVDF domes on three acoustic surface samples ((a) Sample S1, (b) Sample S2, (c) Sample S3) based on the same design variables ($R = 350$ $\mu$m, $h = 12$ $\mu$m, $H_0 =\sim 20$ $\mu$m).

ability, three samples with different dome sizes ($R = 350$ $\mu$m, $R = 275$ $\mu$m, $R = 200$ $\mu$m) are fabricated, while the film thickness (12 $\mu$m) and embossing vacuum level (-25 kPa) are identical to these samples. The statistics of surface velocities of sampled domes for these acoustic surfaces are compared in Figure 8-8. The mean values of surface velocity for the three samples are 0.0213 mm/s ($R = 350$ $\mu$m), 0.0163 mm/s ($R = 275$ $\mu$m) and 0.0036 mm/s ($R = 200$ $\mu$m), and the medians are 0.0208 mm/s, 0.0146 mm/s and 0.0031 mm/s, respectively. The statistics show an increasing average dome displacement under a certain drive voltage as the dome radius increases, which agrees with the theoretical trend in Figure 6-5. The larger dome size further leads to enhanced sound generation. Importantly, the results prove that the sensitiv-

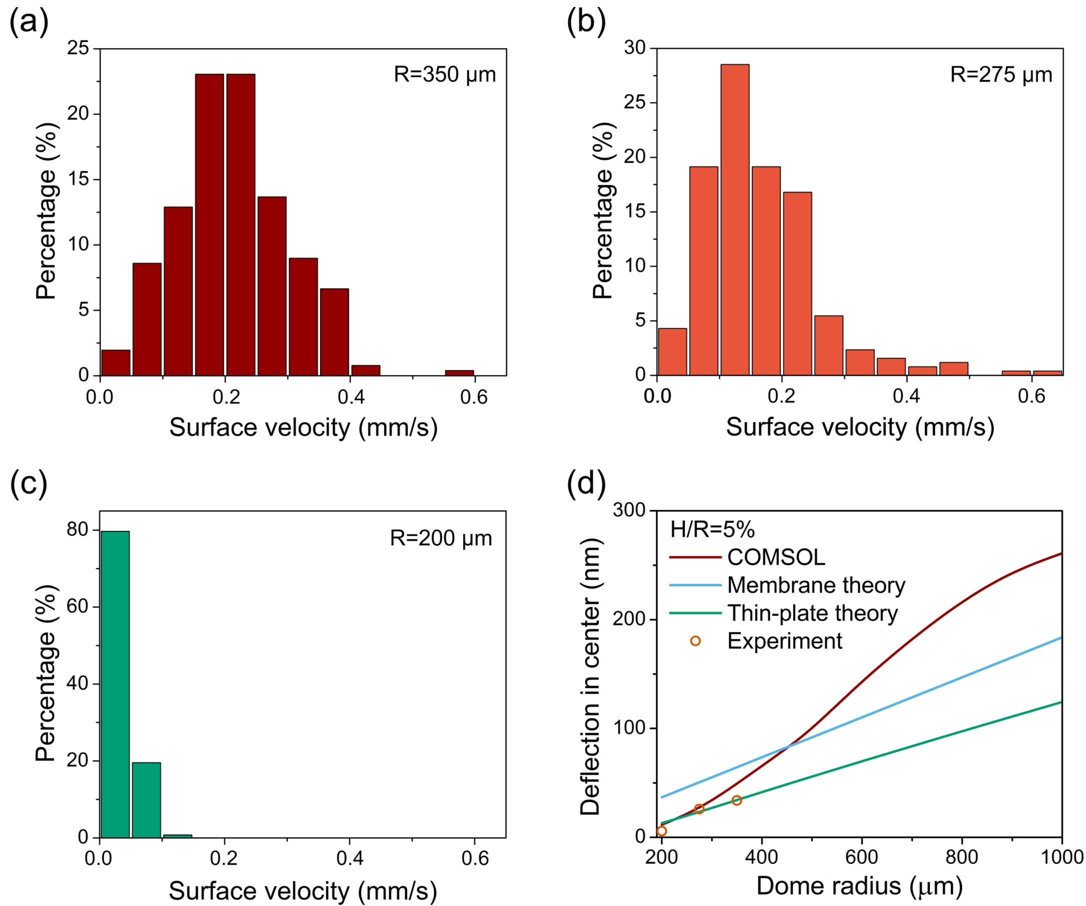


Figure 8-8: Statistics of surface velocities of PVDF domes on three acoustic surface samples based on different dome sizes, including (a) $R = 350$ $\mu$m, (b) $R = 275$ $\mu$m, (c) $R = 200$ $\mu$m. (d) Average experimental deflections of PVDF domes on the three samples compared to those theoretical and simulated deflections. The film thickness and the vacuum level utilized to emboss PVDF domes are identical for these samples.

ity of an acoustic surface can be tuned by designing the dome dimensions.

The relation between the dome displacement and the drive voltage determines the overall linearity of the acoustic surface. The surface velocities at the center of randomly selected PVDF domes ($R = 350$ $\mu$m, $h = 12$ $\mu$m) on a sample are probed and presented in Figure 8-9 (a). The frequency of the sinusoidal AC drive voltage is kept constant at 1 kHz, and the amplitude is varied from 0.05 V to 35 V, where the maximum voltage is constrained by the equipment limit. The results show good linearity between the surface velocity and the drive voltage within the tested range. Linear response between the surface velocity and the drive voltage for PVDF domes

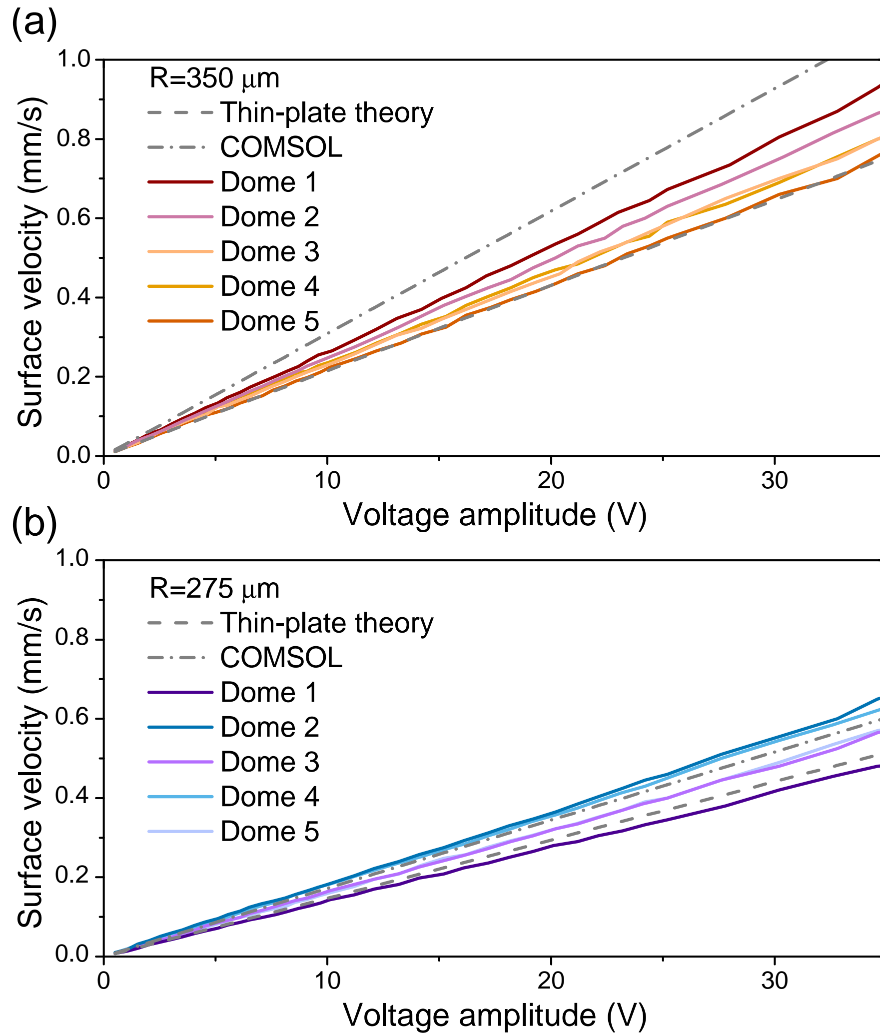


Figure 8-9: Variation of the surface velocity with the drive voltage amplitude for PVDF domes with a radius of (a) $R = 350$ $\mu$m or (b) $R = 275$ $\mu$m. The theoretical and simulated responses between the dome surface velocity and the drive voltage are presented in each subfigure.

of a smaller size ($R = 275$ $\mu$m, $h = 12$ $\mu$m) is shown in Figure 8-9 (b) as another example.

The frequency response of PVDF dome vibration is also studied. A sinusoidal AC drive voltage with a constant amplitude of 5 V is applied, while the frequency is swept from 100 Hz to 120 kHz. The surface velocities of randomly selected domes ($R = 350$ $\mu$m, $h = 12$ $\mu$m) at different frequencies are converted to deflections at the dome center, which are shown in Figure 8-10. Resonance peaks are observed for these domes with resonance frequencies between 72 kHz and 84 kHz. Different

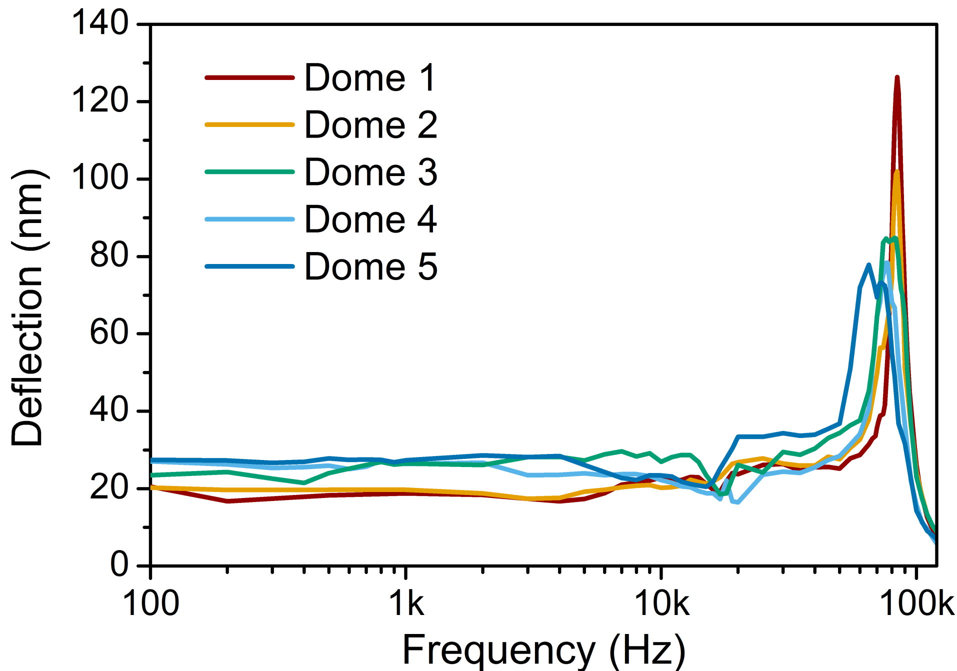


Figure 8-10: Frequency responses of PVDF domes ($R = 350$ $\mu$m, $h = 12$ $\mu$m) driven by a voltage of 5 V in amplitude.

$Q$-factors are also observed, and the domes with higher $Q$-factors (e.g., 6.72 and 4.7 for dome 1 and dome 2, respectively) exhibit smaller deflections at low frequencies but higher peaks at resonance. Besides, these domes exhibit relatively flat frequency responses within the audio frequency range. A dip at $\sim$15 kHz exists in the frequency response for all the tested domes. It is likely attributed to the resonance peak of overall bending/wrinkling of the PVDF film at $\sim$15 kHz, which directly impedes dome vibration.

When a PVDF dome is resonating, the surface velocity signal (output from laser vibrometer) is in phase with the drive voltage, which provides another way to measure the resonance frequency. This is especially useful to measure the resonance frequency for the domes that have low $Q$-factors and resonance peaks difficult to observe. The theoretical modeling and simulation in Chapter 6 indicate that the resonance frequency of a PVDF dome is dependent on the dome size and the film thickness. The resonance frequencies of domes with different radii ($R = 350$ $\mu$m or 275 $\mu$m or 200

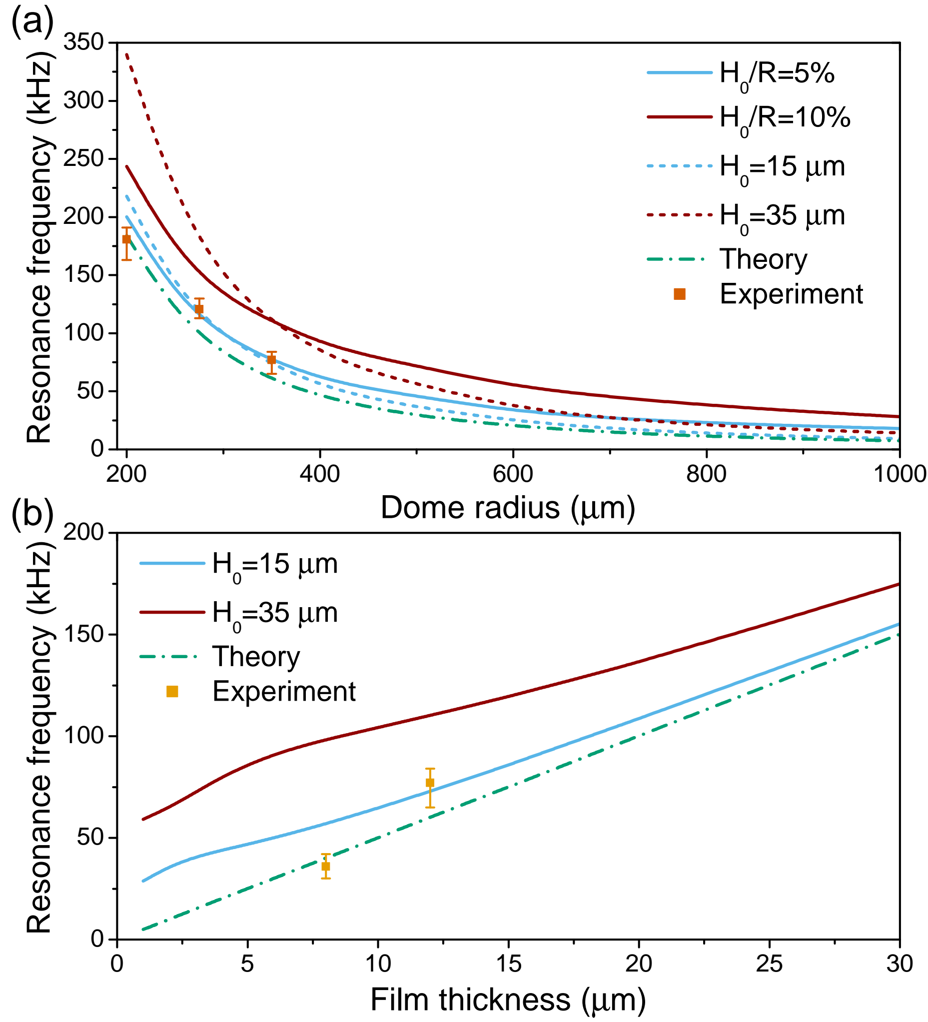


Figure 8-11: Comparison between the experimental resonance frequencies and those predicted by theoretical model and COMSOL simulation, which shows their dependence on (a) the dome radius and (b) the film thickness.

$\mu$m) and the same thickness $h = 12$ $\mu$m are measured and compared with the resonance frequencies predicted by dynamic model and COMSOL simulation (Figure 8-11 (a)). It can be observed that the experimental resonance frequencies of PVDF domes on the fabricated samples (180.8 kHz, 120.7 kHz, 77.0 kHz for $R = 200$ $\mu$m, 275 $\mu$m, 350 $\mu$m, respectively) match well with the theoretical (184.0 kHz, 99.8 kHz, 60.1 kHz) and simulation (200.1 kHz, 115.4 kHz, 76.7 kHz) results, and that the resonance frequency increases as the dome size shrinks. Additionally, resonance frequencies of PVDF domes of the same size ($R = 350$ $\mu$m) but different film thicknesses ($h = 12$

$\mu$m or 8 $\mu$m) are measured. The results in Figure 8-11 (b) show that the resonance frequency decreases with reduced film thickness. The experimental values also align with the thin-plate theory and simulation. These results collectively demonstrate that the resonance frequency of a PVDF dome transducer can be tuned by designing the dome size and the film thickness.

## 8.3 Free-Field Acoustic Performance of Wide-Area Acoustic Surfaces

The performance of a wide-area acoustic surface is evaluated in terms of its sensitivity, frequency response and directivity. These metrics have been measured for samples with PVDF domes of different design variables. Specifically for the prepared samples, the film thickness is either 8 $\mu$m or 12 $\mu$m (based on commercially-available PVDF films), and the PVDF domes are fabricated to be 200 $\mu$m, 275 $\mu$m, or 350 $\mu$m in radius. All samples are embossed under the same vacuum level (~25 kPa). The resulting dome heights are measured using a microscope according to the height difference between the dome center and the dome edge. The variables associated with the dome dimensions for prepared acoustic surface samples are summarized in Table 8.1.

### 8.3.1 Sensitivity

The experiment on sensitivity aims to evaluate the absolute sound level that a sample produces at a certain drive voltage and the linearity of the produced acoustic pressure

Table 8.1: Summary of dome dimensions of fabricated samples

| Sample and design variables | average dome height ($\mu$m) | standard deviation |
|---|---|---|
| S1 ($R = 350$ $\mu$m, $h = 12$ $\mu$m) | 17.7 | 2.03 |
| S2 ($R = 350$ $\mu$m, $h = 12$ $\mu$m) | 17.0 | 1.55 |
| S3 ($R = 350$ $\mu$m, $h = 12$ $\mu$m) | 17.0 | 1.41 |
| S4 ($R = 350$ $\mu$m, $h = 12$ $\mu$m) | 16.0 | 1.61 |
| S5 ($R = 275$ $\mu$m, $h = 12$ $\mu$m) | 10.5 | 2.64 |
| S6 ($R = 200$ $\mu$m, $h = 12$ $\mu$m) | 6.45 | 1.36 |
| S7 ($R = 350$ $\mu$m, $h = 8$ $\mu$m) | 23.6 | 2.92 |

in response to the drive voltage. The measurement of sensitivity is conducted by maintaining a constant frequency and a fixed distance between the sample and the microphone (0° angle, pointing towards the center of the sample), while gradually increasing the amplitude of the drive voltage from 0.05 V to 35 V (i.e., RMS voltage from ~0.035 V to ~25 V). The experimental results of the sensitivities of fabricated samples with different design variables at 30 cm away are shown in Figure 8-12. The sensitivities (acoustic pressure/drive voltage) for each sample at 1 kHz, 5 kHz, and 10 kHz are fitted and summarized in Table 8.2. Considering the low SNR ratio at 1 kHz, the sensitivity curves in Figure 8-12 (a) and (b) are averaged from three consecutive voltage sweeps. Additionally, corrections (Figure 8-3) have been added to 5 kHz and 10 kHz results to compensate the attenuation caused by the protection grid on the B&K 4136 microphone. Good linearity between the produced acoustic pressure and the drive voltage can be observed for all the samples at 5 kHz and 10 kHz; despite the low SNR ratio at 1 kHz, these samples still exhibit responses that follow linear trends. According to the theoretical model established in Chapter 6, the deflection of a PVDF dome is proportional to the drive voltage. As a result, a 20 dB enhancement in the sound pressure level is expected when the voltage is increased by one decade. Linear fits are conducted on the SPL-voltage curves in Figure 8-12 at 1 kHz, 5 kHz, and 10 kHz. The corresponding slopes for different samples are summarized in Table 8.2. All samples show around 20 dB/dec slopes at these frequencies, which suggest no saturation in the voltage range of measurement. The absolute sound levels at 25 V (RMS) are also listed in Table 8.2 for each sample, while SPLs at other voltages can be observed in Figure 8-12.

Figure 8-12 shows nearly identical performance of S1, S2, S3 and S4, which have same dome radius and same film thickness. The sample S7 with the largest domes ($R$ = 350 $\mu$m) and the thinnest film ($h$ = 8 $\mu$m) exhibits the highest sensitivity at all frequencies, while the sample S6 with the smallest domes ($R$ = 200 $\mu$m) and a large film thickness ($h$ = 12 $\mu$m) presents overall the lowest sensitivity. Such a difference in sensitivity verifies the tunability afforded by designing the dimensions of PVDF domes. The trend also aligns with the theory and simulation in Figure 6-5

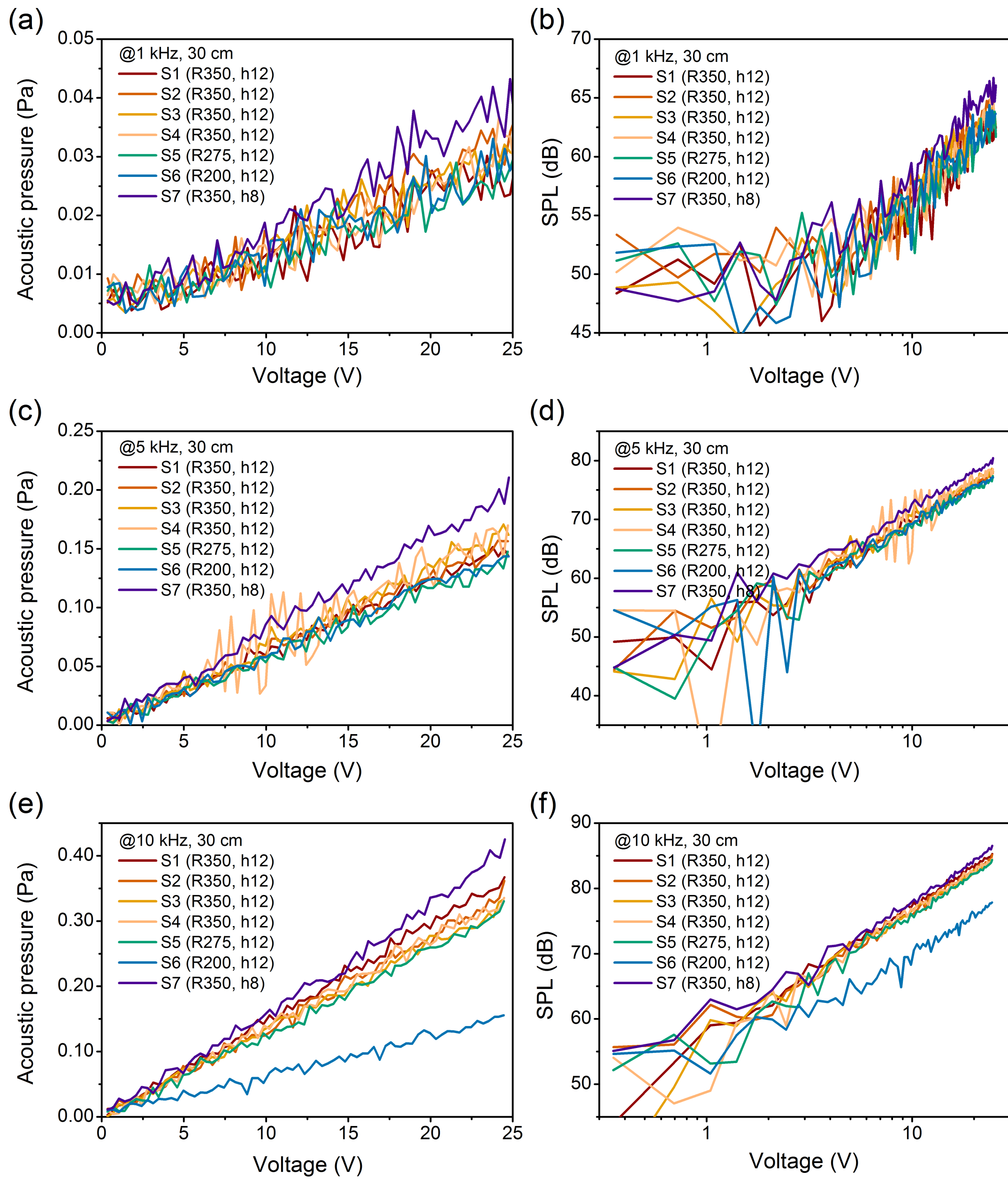


Figure 8-12: Sensitivities of fabricated acoustic surface samples at 30 cm away. Variation of (a) the acoustic pressure and (b) the SPL with the drive voltage (RMS) at 1 kHz. Variation of (c) the acoustic pressure and (d) the SPL with the drive voltage (RMS) at 5 kHz. Variation of (e) the acoustic pressure and (f) the SPL with the drive voltage (RMS) at 10 kHz.

and Figure 6-7. Since the PVDF domes fabricated on S1-S7 (dimensions shown in Table 8.1) should behave similar to thin plates, we further use the thin-plate model

Table 8.2: Summary of the experimental results in terms of sensitivity, SPL-voltage slope and SPL at 25 V (RMS), 30 cm away

| sample | sensitivity (mPa/V) | | | SPL-voltage slope (dB/dec) | | | SPL @ 25 V (RMS) | | |
|---|---|---|---|---|---|---|---|---|---|
| | 1 kHz* | 5 kHz | 10 kHz | 1 kHz* | 5 kHz | 10 kHz | 1 kHz* | 5 kHz | 10 kHz |
| S1 | 1.039 | 6.201 | 14.868 | 16.936 | 19.180 | 20.909 | 63.311 | 77.169 | 85.275 |
| S2 | 1.361 | 6.277 | 13.918 | 19.199 | 18.206 | 18.349 | 65.322 | 77.865 | 85.146 |
| S3 | 1.152 | 6.767 | 13.144 | 17.890 | 20.109 | 21.840 | 63.643 | 78.172 | 84.425 |
| S4 | 1.109 | 6.652 | 13.643 | 15.822 | 20.105 | 20.967 | 62.589 | 78.584 | 84.492 |
| S5 | 0.986 | 5.666 | 12.986 | 16.551 | 19.530 | 19.775 | 61.670 | 77.352 | 84.358 |
| S6 | 1.049 | 5.879 | 7.605 | 16.569 | 19.038 | 20.309 | 63.647 | 77.113 | 77.824 |
| S7 | 1.529 | 7.985 | 16.532 | 18.100 | 19.249 | 18.444 | 66.066 | 80.447 | 86.546 |

*The 1 kHz results in Figure 8-12 are averaged from three consecutive sweeps. The fitting of sensitivity and SPL-voltage slope starts at 4 V, as noise dominates at low voltage for 1 kHz.

to normalize the sensitivities of these samples to the same dome dimensions (i.e., $R = 350$ $\mu$m, $H_0 = 17$ $\mu$m, $h = 12$ $\mu$m). The obtained sensitivities after such normalization should be similar in theory. From Table 8.3, we notice S1-S4 and S7 have consistent normalized sensitivities at each frequency; however, the normalized sensitivities of S5 and S6 are higher. It is mainly attributed to vibration of the void area (i.e., area surrounding the domes) due to bending/wrinkling of the PVDF films, which adds to the overall sound generation. Such a contribution is more evident when the dome deflection is smaller, resulting in the normalized sensitivity of S6 larger than that of S5 (both larger than those of S1-S4 and S7). Vibration of void area could be reduced when PVDF films are less wrinkled when they are laminated with flat protective PET films.

Besides these design variables of PVDF domes, the sound generation is also dependent on the material properties. If an acoustic surface is fabricated based on a void

Table 8.3: Normalized sensitivities of fabricated samples to the same design variables $R = 350$ $\mu$m, $H_0 = 17$ $\mu$m, $h = 12$ $\mu$m (unit: mPa/V)

| Sample and design variables | 1 kHz | 5 kHz | 10 kHz |
|---|---|---|---|
| S1 ($R = 350$ $\mu$m, $H_0 = 17.7$ $\mu$m, $h = 12$ $\mu$m) | 1.061 | 6.330 | 15.178 |
| S2 ($R = 350$ $\mu$m, $H_0 = 17.0$ $\mu$m, $h = 12$ $\mu$m) | 1.361 | 6.277 | 13.918 |
| S3 ($R = 350$ $\mu$m, $H_0 = 17.0$ $\mu$m, $h = 12$ $\mu$m) | 1.152 | 6.767 | 13.144 |
| S4 ($R = 350$ $\mu$m, $H_0 = 16.0$ $\mu$m, $h = 12$ $\mu$m) | 1.078 | 6.464 | 13.257 |
| S5 ($R = 275$ $\mu$m, $H_0 = 10.5$ $\mu$m, $h = 12$ $\mu$m) | 1.391 | 7.995 | 18.325 |
| S6 ($R = 200$ $\mu$m, $H_0 = 6.45$ $\mu$m, $h = 12$ $\mu$m) | 3.055 | 17.123 | 22.151 |
| S7 ($R = 350$ $\mu$m, $H_0 = 23.6$ $\mu$m, $h = 8$ $\mu$m) | 1.141 | 5.959 | 12.338 |

charged polymer film, which usually has an equivalent piezoelectric constant more than 10 times larger than that of a PVDF film, an over 20 dB improvement can be expected compared to a PVDF-based acoustic surface with the same design variables, according to the theoretical model in Chapter 6. Additional factors to enhance the produced sound level include, but are not limited to, increasing drive voltage and active area of the acoustic surface. For instance, when the sample with $9 \times 9$ cm$^2$ active area is scaled up to $1 \times 1$ m$^2$ wallpaper size, a ~40 dB enhancement in SPL can in theory be obtained at 1 kHz, 1 m away.

The distance dependence of the sound generation by an acoustic surface is also studied by conducting sensitivity measurements at different distances (10 cm, 30 cm, 50 cm) from the sample under a constant frequency of 10 kHz. The results in Figure 8-13 show that the sensitivity of sound generation decays with an increasing distance. The theoretical result in Figure 6-10 shows that the SPLs at 10 cm, 30 cm, 50 cm for a $9 \times 9$ cm$^2$ with 350-$\mu$m-radius, 12-$\mu$m-thick, 20-$\mu$m-high PVDF domes are 79.3 dB, 72.3 dB, and 68.2 dB, respectively, under a 10 kHz, 7.07 V (RMS, 10 V in amplitude) voltage. The experimental results of SPL at 10 cm, 30 cm and 50 cm under a 10 kHz, 7.07 V (RMS) voltage are 78.3 dB, 73.2 dB, 71.1 dB, respectively, which agree reasonably well with the theory.

### 8.3.2 Frequency Response

The frequency response evaluates variation of the sound level and the phase shift (compared to the phase of source voltage) with frequency (100 Hz to 100 kHz, evenly sampled in logarithm frequency domain) at a fixed drive voltage (10 V in amplitude) and a constant distance (30 cm) between the sample and the microphone. Considering that the drive voltage applied to the sample decays with increasing frequency due to the load effect, the magnitude of microphone output is corrected by decay factor $\tau$ (i.e., $\tau = A_{s-fs}/10$) of the drive voltage at each frequency, while the magnitude of the source voltage $A_{s-fs}$ at $f_s$ is obtained by taking the FFT of the drive voltage. Additionally, the influence of the protection grid (Figure 8-3) installed on microphone is also corrected up to 70 kHz, which is the highest frequency with available correction

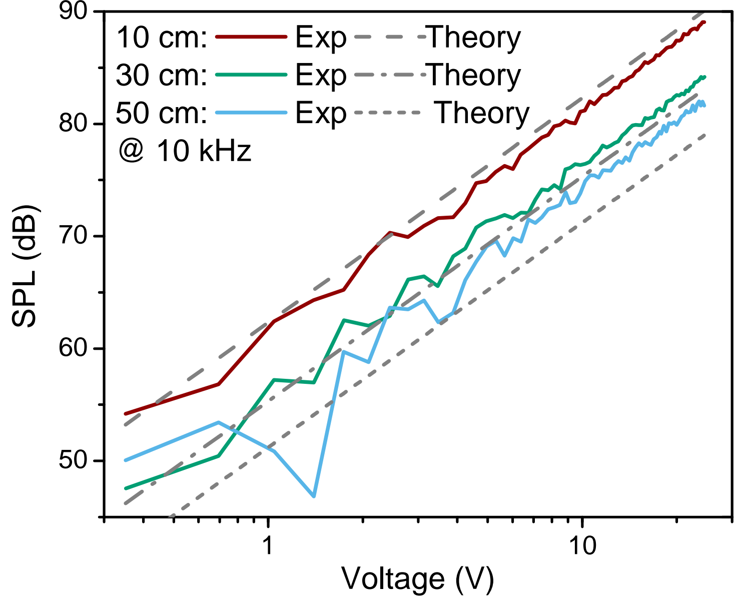


Figure 8-13: Variation of the SPL with the drive voltage (RMS, 10 kHz) at 10 cm, 30 cm, 50 cm away. The theoretical SPL-voltage relations at these distances are also shown in the figure.

data from the microphone manufacturer. The relative phase is obtained from the difference between the phase of the microphone output and that of the source voltage (measured by 10× voltage probe), i.e., $\phi(f) = \phi_{mic}(f) - \phi_s(f)$. Both the magnitude of the microphone output and the relative phase between the microphone signal and the source voltage are averaged from three consecutive frequency sweeps.

The frequency responses (from 100 Hz to 100 kHz) in terms of SPL at 10 V (fixed amplitude of drive voltage) for the fabricated samples are shown in Figure 8-14. For sub-1-kHz frequencies, the sounds produced by these sample are gentle and shadowed by ambient noise. Comparing the results of samples with different dome sizes and film thicknesses, similar trends are observed in the frequency responses as those from sensitivity experiments. The sample S7 with the largest domes ($R = 350$ $\mu$m) and the smallest film thickness ($h = 8$ $\mu$m) overall produces the highest SPL in the audio frequency range. It should be pointed out that the SPLs at frequencies above 70 kHz are not compensated due to the absence of correction data for attenuation caused

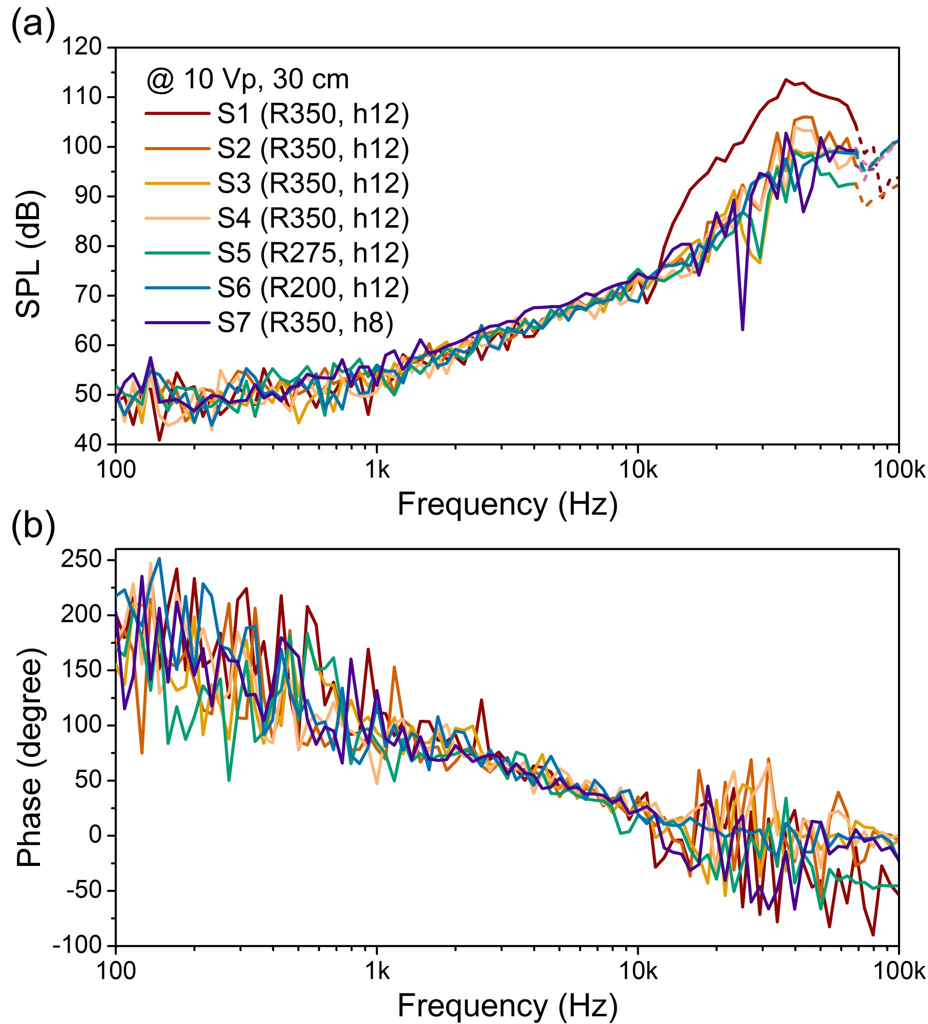


Figure 8-14: Frequency responses of acoustic surface samples: (a) magnitude response; (b) phase response. Compensations for the attenuation from microphone protection grid (4 kHz∼70 kHz) and for the drive voltage decay have been added to the magnitude response. Magnitude response at frequencies above 70 kHz (dashed curves) is uncompensated for microphone attenuation due to absence of correction data from the microphone manufacturer.

by protection grid in that range and thus plotted as dashed curves in Figure 8-14. The peaks in the SPL curves of these samples align with the peak of correction curve (Figure 8-3) and cannot reflect the actual resonance. For Samples S1-S4, S5 and S6, their resonance frequencies are estimated to be 60.08 kHz, 97.31 kHz and 183.98 kHz in theory; however, resonance peaks are not evident in the measured frequency responses. It can be attributed to several factors. First, the resonance frequencies of

Table 8.4: Summary of SPL-frequency slope in different ranges (unit: dB/dec)

| sample | 1 kHz∼20 kHz | 1 kHz∼40 kHz | 20 kHz∼70 kHz | 1 kHz∼70 kHz |
|---|---|---|---|---|
| S1 | 28.088 | 36.918 | 17.763 | 36.960 |
| S2 | 20.609 | 26.545 | 32.027 | 28.465 |
| S3 | 20.440 | 23.511 | 38.513 | 25.788 |
| S4 | 20.543 | 26.131 | 29.198 | 27.765 |
| S5 | 16.879 | 16.477 | 28.148 | 17.576 |
| S6 | 19.865 | 24.923 | 28.127 | 26.525 |
| S7 | 19.767 | 23.084 | 39.097 | 24.353 |

individual domes are not exactly the same, as seen in Figure 8-10, caused by small variations in the dome dimensions. Combining the misaligned resonance peaks over a large number of domes (>8000) may result in a smoothened frequency response. The low $Q$-factors (Figure 8-10) of transducers made with PVDF film may further lead to the disappearance of resonance peaks. In addition, the protection grid on microphone may attenuate the produced sounds at the resonance frequencies and further shadow the peaks.

According to the frequency responses and the correction curve (Figure 8-3), there are four important boundaries in the tested frequency range, namely, 1 kHz (above which SNR is good), 20 kHz (boundary between audible sound and ultrasound), 40 kHz (peak in the correction curve), 70 kHz (highest frequency with corrected SPL). Therefore, we consider four frequency ranges accordingly, i.e., 1 kHz∼20 kHz, 1 kHz∼40 kHz, 20 kHz∼70kHz, and 1 kHz∼70 kHz. The slopes of the frequency responses in Figure 8-14 are fitted within these ranges, which are listed in Table 8.4. According to the theory described in Chapter 6, the acoustic pressure produced by the acoustic surface at a certain distance is quadratic to the frequency of sound, assuming a constant average displacement of the domes. Such a dependence corresponds to a 40 dB enhancement in SPL when the frequency is increased by one decade. However, all the samples present sub-40 dB/dec slopes, particularly in the audio frequency range. It is mainly caused by interference from the overall film vibration. When the adhesive layer between the PVDF film and the PET film underneath is incomplete and/or not strong enough, the void area may vibrate under excitation due to imperfect clamping,

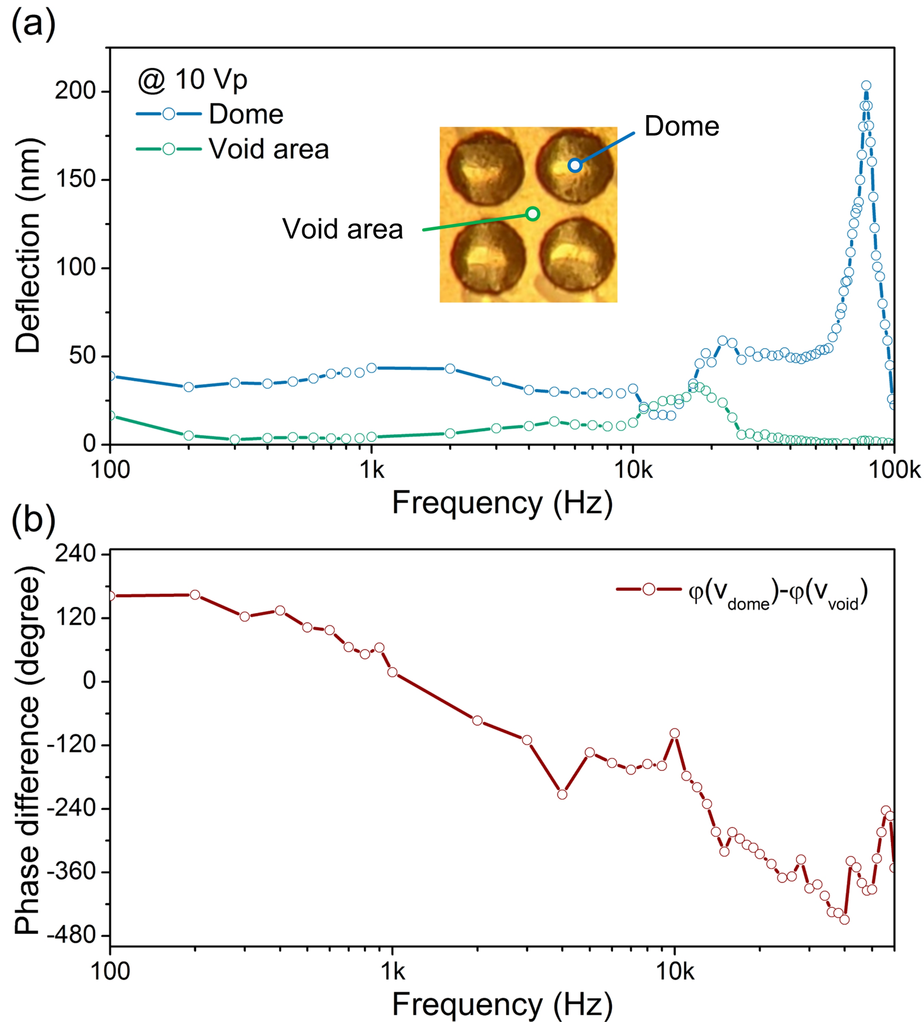


Figure 8-15: Comparison between the surface velocity at the center of a dome and the surface velocity at void area in vicinity of the dome.

especially at low frequencies.

Figure 8-15 (a) shows the comparison of deflection (obtained from surface velocity measurement) at the center of a dome and that at void area close to the dome, when the frequency is swept from 100 Hz to 100 kHz. The deflection curve of the dome at frequencies below 2 kHz is relatively flat, but starts to drop slowly at frequencies above 3 kHz. The phase difference between the dome surface velocity and the void area surface velocity is also extracted using the source voltage as the same reference for phase, shown in Figure 8-15 (b). It is observed that the vibration of the entire film is counteracting the dome vibration, as the phase difference varies from -110° to

-230° for 3 kHz∼13 kHz. As a result, the sound produced by the dome vibration is partly cancelled by the sound arising from the entire film vibration. In addition, the film vibration at the void area is found to exhibit a resonance peak at ∼15 kHz, and it directly impedes vibration of the domes that are close to it, leading to a dip in the dome deflection curve. This further results in reduced sound generation from dome vibration. As a result, the sub-40 dB/dec SPL-frequency slope in the audio frequency range is caused by both the reduced dome vibration and the sound cancellation due to the entire film vibration. At frequencies above 20 kHz, the overall PVDF film vibration decays as the frequency increases and becomes negligible for frequencies higher than 50 kHz. This explains why the slopes fitted in 20 kHz∼70 kHz are closer to 40 dB/dec. With a stronger adhesive and a better coating technique, the void area will be better clamped (no displacement) and a 40 dB/dec SPL-frequency slope can be expected.

### 8.3.3 Directivity

The directivity of sound generation is measured by maintaining a constant distance (30 cm) between the microphone and the sample, while positioning the microphone at different angles (-90° to 90°) relative to the normal direction to the acoustic surface. The drive voltage is kept at 10 V (7.07 V RMS) when the frequency is swept from 1 kHz to 20 kHz. The acquired microphone output signal is converted into normalized SPL. Figure 8-16 shows how the radiation pattern of the produced sound changes with increased frequency in the audible range. At frequencies above 15 kHz, the sound generation shows evident angular dependence, and an acoustic beam forms along the direction normal to the acoustic surface. Compared with the theoretical acoustic radiation patterns (dashed curves) obtained by Rayleigh integral, good agreement between the theory and the experimental results is observed at frequencies above 15 kHz. However, the sample in theory should exhibit directionality at frequencies above 5 kHz, while the SPL shows little dependence on angle at 5 kHz and 10 kHz in Figure 8-16. It is mainly attributed to the interference caused by the entire film vibration. Within that frequency range, the bending/wrinkling of the PVDF

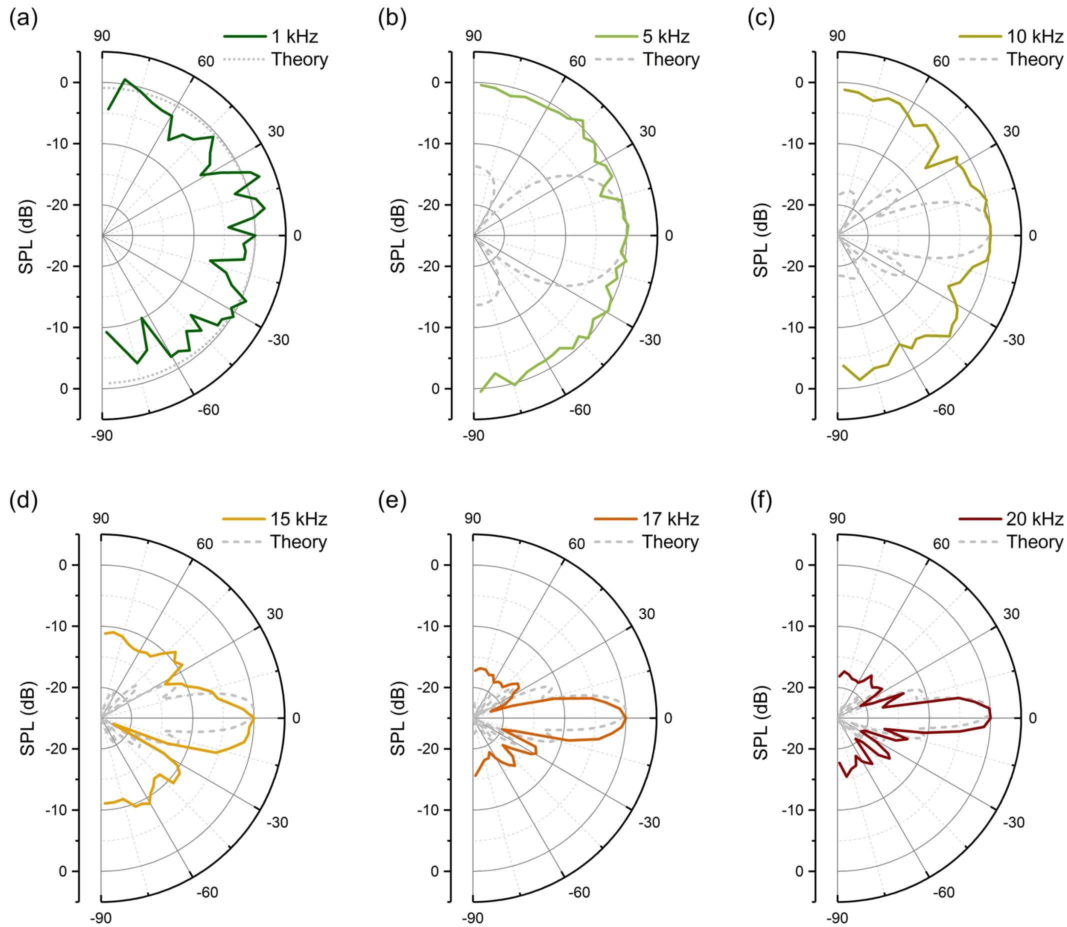


Figure 8-16: Radiation patterns of an acoustic surface at (a) 1 kHz, (b) 5 kHz, (c) 10 kHz, (d) 15 kHz, (e) 17 kHz, (f) 20 kHz. The SPL values at different angles for each frequency are normalized by the value measured at 0° angle for the same frequency. The theoretical directivity patterns are presented as dashed curves for comparison.

film under excitation produces random sound waves that counteract with the sound generated by dome vibration at different angles, and thereby destructively modulates the directivity pattern resulting from dome vibration. As a result, the microphone picks up large acoustic pressure at angles where the sound generation in theory should be minimum if purely based on dome vibration; the acoustic pressure at 0° angle produced by dome vibration is partly cancelled by the counteractive acoustic pressure that comes from the bending/wrinkling of the entire film. These collectively result in uniform acoustic radiations at 5 kHz and 10 kHz. For frequencies above 15 kHz, the overall vibration of the PVDF film starts to shift to be in phase with the dome

vibration, thereby constructively contributing to the acoustic pressure (equivalent to adding positive offsets), which does not change the radiation pattern. When the void area of the embossed PVDF film is better clamped using a stronger adhesive and an improved coating technique, the experimental directivity patterns are expected to match well with the theory at all frequencies.

# Chapter 9

# Towards Multi-Functional Acoustically-Active Surfaces: Summary and Outlook

## 9.1 Summary and Conclusion

An ensemble of high-performance acoustic transducers deployed over a wide area and coordinated to radiate and/or sense acoustic waves as a phased array could enable unprecedented performance and unique functionality unavailable to individual transducers. In particular, when millions of small acoustic transducers are integrated on a flexible thin film, individually addressed and assigned into different roles (speaker, microphone, ultrasonic transceiver), such a thin film can be mounted on surfaces of various objects and thereby render them acoustically active in an inconspicuous way. This yields an emerging concept of multi-functional acoustic surfaces for application in myriad scenarios where sound can work as the medium for sensing and communication, including but not limited to active noise control, smart homes, autonomous navigation, contactless matter manipulation, tactile sensing, etc. Among the candidate technologies, piezoelectric thin films based on active microstructures as individually-addressed acoustic transducers in a phased array show great promise to

deliver the performance and functionalities desired for the acoustic surface.

In this thesis, an acoustic surface is developed based on an array of micro-domes embossed on a wide-area piezoelectric thin film. Each piezoelectric dome is able to either generate sound by displacing air under excitation or sense incident sound from the induced charge accumulation on the electrodes. Specifically for loudspeaker application, actuating these micro-domes simultaneously results in enhanced loudness compared to a planar film, while coordinating the vibration of these micro-domes in a certain way could enable directional sound generation. Theoretical modeling and multiphysics simulation have revealed tunability in the characteristics of both the individual transducers and the overall acoustic surface, afforded by designing the profile and dimensions of these active microstructures.

For proof of concept, we choose commerically-available PVDF thin films as the piezoelectric polymer to make an acoustic surface. Fabrication of the acoustic surface requires molding dome-shaped active microstructures with high precision in a low-cost and scalable fashion. Therefore, we have developed a micro-embossing approach that combines conventional polymer processing and microfabrication techniques, which is able to create precisely-defined micro-domes over a wide area using controlled vacuum. A perforated Si wafer is utilized as the shadow mask to machine a perforated plastic layer by laser rastering. The perforated plastic layer is then laminated onto the PVDF film and works as a mold to emboss micro-domes under vacuum. Such a plastic layer is also able to protect the shallow domes from being collapsed by mechanical impact. Following this approach, acoustic surface samples ($9\times9$ cm$^2$ active area) have been fabricated with PVDF domes of different dimensions.

This thesis primarily studies the sound generation of the acoustic surface. Individual dome vibration is characterized by the surface velocity. The experimental results reveal dependence of the sensitivity and the resonance frequency of the PVDF domes on their dimensions, same as the thin-plate theory and the simulation predict. Specifically, large and shallow domes embossed on a thin PVDF film are preferred for sound generation due to their high sensitivities, while such design variables also result in low resonance frequencies for these domes.

Table 9.1: Comparison with representative wide-area, flexible loudspeakers

| technique | dimensions ($cm^2$) | distance and drive voltage(RMS) | SPL(dB) 10 kHz | sensitivity*@30 cm ($mPa/V/cm^2$) | pixelation and isolation |
|---|---|---|---|---|---|
| this work | $9 \times 9$ | 30 cm, 7.07 V | 75.5 | 0.2075 | easy |
| COC speaker [62] | $12 \times 12$ | 1 m, 70.7 V | $\sim 75$ | 0.0367 | hard |
| COP speaker [61] | $15 \times 15$ | 50 cm, 56.5 V | $\sim 70$ | 0.0083 | hard |
| FEP speaker [90] | $\pi \times (\frac{2.5}{2})^2$ | 2 cm, 7.94 V | $\sim 72$ | 0.1368 | medium |
| EAP speaker [142] | $\pi \times (\frac{10}{2})^2$ | 1 m, 282.8 V | $\sim 72$ | 0.0119 | hard |

*Sensitivity is obtained by converting the reported SPL into acoustic pressure under unit voltage per unit area of speaker at 10 kHz, 30 cm away, assuming all the speakers follow free-field characteristics of sound generation (i.e., acoustic pressure proportional to (drive voltage/distance)). Acronyms: cyclic-olefin polymers (COP), cyclic-olefin copolymers (COC), fluoro-ethylene-propylene (FEP), elastomer electroactive polymer (EAP).

To further demonstrate the tunability on the overall performance of an acoustic surface, comprehensive measurements have been conducted on samples with PVDF domes of different dimensions. The experimental results prove that the acoustic surface with the largest dome size and the smallest film thickness exhibits the highest sensitivity, which aligns with the theory and the results from individual dome characterization. However, no obvious resonance peaks are observed from the frequency responses of these samples, and the SPL-frequency slope in the audio frequency range is below the theoretical 40 dB/dec assuming a constant deflection. The former is likely caused by the low $Q$-factors and the misaligned resonance frequencies of PVDF domes. The latter is primarily due to imperfect interfacial bonding between the films (i.e., poorly clamped void area between domes), which results in sound cancellation and interference from the overall bending/wrinkling of the PVDF film at low frequencies.

There are limited works reported in literature that have the potential to make an acoustic surface technology, and our work is compared with the state-of-the-art in Table 9.1. The comparison confirms that our acoustic surface outperforms other representative techniques in terms of sound generation under the same condition. The superior performance is primarily attributed to the existence of freestanding micro-domes over a wide area. Moreover, the active microstructures in an array allow much easier pixelation with good isolation between adjacent cells for our acoustic surface, compared with existing techniques that rely on vibration of a bulk thin film.

Experiments have also been conducted to characterize the radiation pattern of our acoustic surface. The result shows that the sound generation becomes more directional as the frequency increases. In particular, the directivity pattern of the tested sample demonstrates beam forming at and above 15 kHz. A wide-area acoustic surface with pixelated transducers in an array controlled by a proper adaptive algorithm could enable directional sound generation at even much lower frequencies in the audible range.

Our acoustic surface technology also faces challenges, primarily in device fabrication at this stage. A wrinkeled PVDF film laminated with a flat perforated plastic film leads to inconsistent domes over a wide area after embossing. An adhesive with limited strength and a nonuniform adhesive coating result in imperfect interfacial bonding and allow overall bending/wrinkling of the PVDF film, which causes interference to dome vibration and even cancels the sound generation by the domes within a certain frequency range. Additionally, all of these issues contribute to inconsistent displacements of the PVDF domes at different locations on the acoustic surface, which ruins the directivity pattern and imposes a great challenge for the control algorithm design to achieve the desired functionality. Since these issues are greatly attributed to manual control in processing (such as film lamination, adhesive coating) as well as separated steps of material manufacturing and microstructure fabrication, better consistency among the active microstructures and thus improved performance of the acoustic surface can be expected when the fabrication process is refined and automated.

## 9.2 Outlook

### 9.2.1 Enhancement of Sound Generation

Our acoustic surface technology has demonstrated superior acoustic performance and ease of pixelation compared to existing flexible thin-film loudspeakers. Its sound generation can be further enhanced by engineering the active micro-dome transducers.

Both our theory and simulation suggest embossing larger domes increases the dome displacement and therefore the sensitivity of the acoustic surface. For instance, enlarging the domes from $R = 350$ $\mu$m to $R = 1$ mm (with optimal dome heights) results in an over 8 times increase in dome displacement and an 18 dB improvement in SPL. Though this may also result in lower resonance frequencies of the PVDF domes that fall into the audible range, the relation between the acoustic pressure and the frequency may still approximately follow a quadratic trend, as a result of the low $Q$-factors of PVDF transducers as well as some extent of mialigned resonance peaks of a huge amount of PVDF domes. Moreover, the resonance peaks could be leveraged for enhanced acoustic performance as well. When multiple PVDF domes with resonance frequencies uniformly distributed over the audible range are grouped to work as a single pixel, the overall response of such a group of PVDF domes could still be relatively flat (i.e., constant average deflection) in the audible range based on ensemble average, but the sound generation is enhanced compared to a group without any resonating dome in the audible range.

Embossing domes on a thinner PVDF film is also effective in improving the overall sound generation. For example, reducing the film thickness from 12 $\mu$m to 1 $\mu$m results in an over 20 times increase in dome displacement (26 dB improvement in SPL). However, ultra-thin wide-area PVDF film is in general difficult to fabricate and handle. Breakdown may occur during polarization of an ultra-thin PVDF film. Nonuniformity in the electrical and mechanical properties over a wide area is usually more significant for an ultra-thin film, and thus causes inconsistent performance of PVDF domes. However, the current design and micro-embossing process we develop are fully compatible with ultra-thin films. The protective layer can effectively protect the fragile PVDF domes even with greatly reduced thickness.

Engineering the profile of active microstructures may bring further enhancement in performance as well. The domes based on current design have clamped boundaries and usually smaller displacements compared to cantilevers or suspended beams under the same excitation. Alternatively, fabricating PVDF domes with partially severed edge is likely to increase the displacement without a large modification to the design.

Besides, employing polymers with superior piezoelectric responses also makes a viable approach, but in general is less preferred as it may bring higher inconsistency of material properties over a wide area as well as increased fabrication complexity and cost.

### 9.2.2 Exploring Potentials of the Acoustic Surface

#### Rendering an object acoustically active

An attractive feature of this emerging technology is the capability of rendering an arbitrary surface acoustically active. As a result, virtually anything can be turned into a loudspeaker or a microphone when an acoustic surface adheres to it. We demonstrate this application by mounting a flexible, transparent acoustic surface onto a glass mug (Figure 9-1), which is thereby utilized to play music under a drive voltage below 5 V (RMS). The perforated PET film on top of the embossed PVDF is able to protect the domes and avoid performance degradation, when the mug speaker is touched by hand. Such thin, flexible, robust and even transparent acoustic surfaces can be mounted on walls, ceilings as well as car and aircraft interiors to achieve ubiquitous loudspeakers, surround-sound entertainment, and active noise cancelling.

#### Sound detection

Besides the demonstrated loudspeaker application, PVDF domes on an acoustic surface can be used as distributed microphones to sense sound as well. An incident acoustic wave causes strain in the PVDF domes and thereby induces charge accumulation on the electrodes, which can be amplified by peripheral circuits and correlated to the incident acoustic pressure. Demonstrating the microphonic application of the acoustic surface will be part of our future work.

#### Radiation control and beam forming at a low frequency

Another promising application is active noise control. When active microstructures deployed over a wide area are divided into three categories, i.e., microphone, ultrasonic

Figure 9-1: Pictures of a glass mug speaker enabled by a flexible, robust and transparent acoustic surface.

transceiver, and speaker, an acoustic surface is able to detect ambient noise, localize a person's ears and radiate noise-cancelling sound directed towards the person's ears. This could extend active noise control to free-field application, without need for any wearable device like noise-cancelling earbud/headset with integrated microphone(s). Among required tasks to achieve this functionality, generating sound towards a certain direction (person's ears) could be challenging, particularly in the audio frequency range. Though beam forming has been demonstrated by a $9 \times 9$ cm$^2$ sample at frequencies above 15 kHz, control of sound radiation with directionality at a much lower frequency such as 1 kHz has not been demonstrated and requires increased pixels of the acoustic surface as well as a proper phase control. A Raileigh integral can be applied to simulate tuning of the radiation pattern. Figure 9-2 presents the variation of acoustic radiation pattern at 1 kHz, 1 m away as a result of modulating the amplitude and phase of drive voltages for two or three pixels (each with a $10 \times 10$ cm$^2$ active area). The radiation pattern generated by two pixels with different phases is no longer uniform in space at 1 kHz. When three pixels are driven by voltages with different phases, the sound generation starts to become directional at 1 kHz. Moreover, further control on the amplitude of drive voltage for each pixel can improve

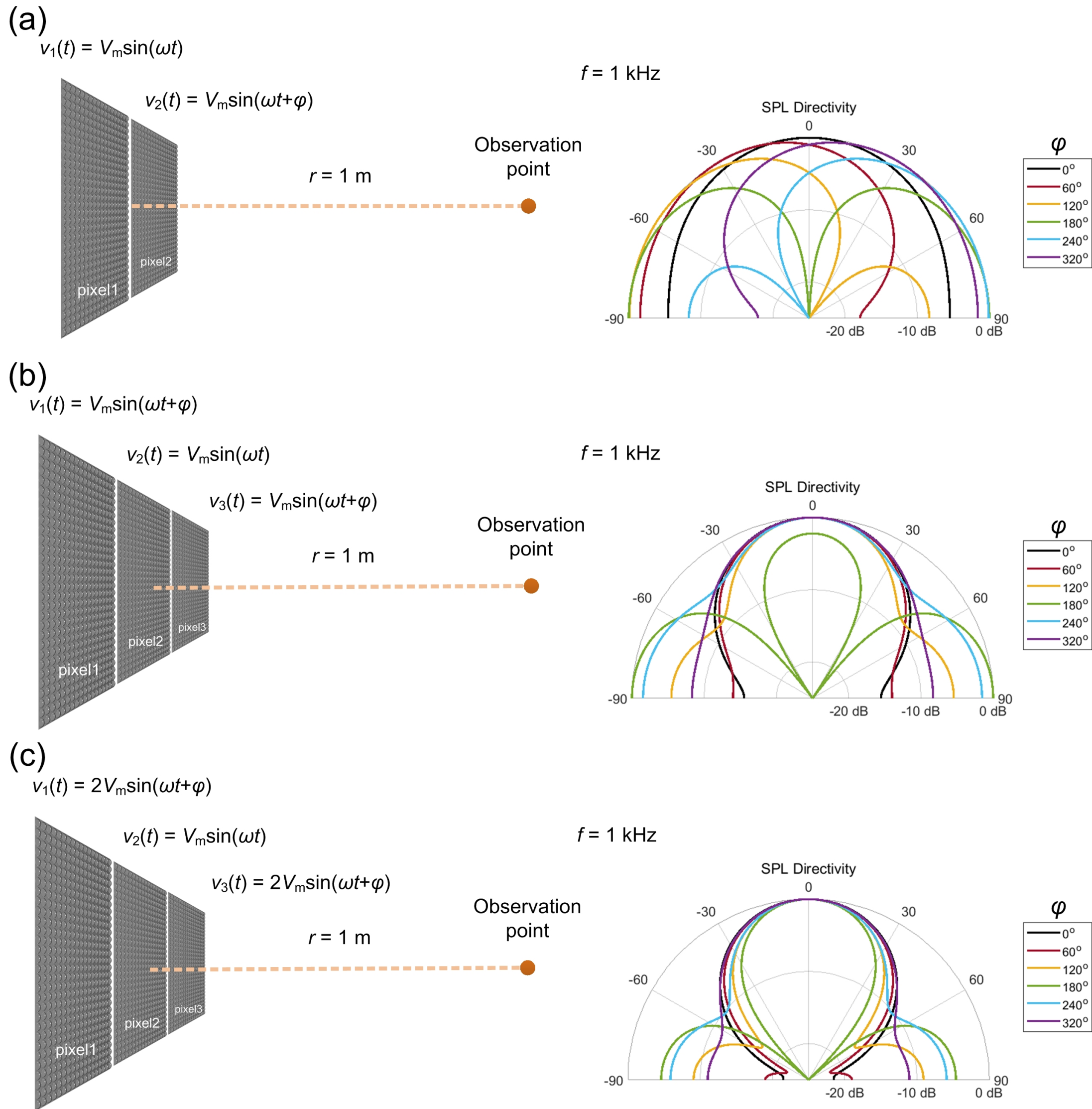


Figure 9-2: Tuning the acoustic radiation pattern at 1 kHz, 1 m away based on (a) two pixels driven by voltages with the same amplitude but different phases, (b) three pixels driven by voltages with the same amplitude but different phases, and (c) three pixels driven by voltages with different amplitudes and phases. Each pixel is $10 \times 10$ cm$^2$ with an array of identical PVDF domes (vibrating in phase, 1 mm pitch). Normalized SPL is presented in the figure.

the directionality. This example assigns all the PVDF domes in the same pixel to vibrate in phase. An improved phase control for PVDF domes could result in a more focused acoustic beam at 1 kHz.

# Chapter 10

# Engineering Electromechanical Devices and Systems: From Nanoscale to Macroscale

Active components usually define the optimal if not the ultimate scale for engineering the performance and functionality of electronic devices and systems. A versatile scheme typically starts from the design of active micro-/nano-structures and then proceeds to assembling them into components of functional devices/units before eventual system integration. Along this path, exploring and exploiting all the degrees of design freedom afforded by individual and/or ensembles of active micro-/nano-structures enables tuning the characteristics of functional units in order to achieve unprecedented device performance and unique system functionality.

The two case studies in this thesis share the aforementioned engineering strategy in common (Figure 10-1). In the first case study, molecules perform as the fundamental design scale. Changing the molecular composition results in a tunable mechanical response of an ensemble of these active nanostructures (self-assembled molecular layer), which functions as a key component with which to build a tunneling nanoswitch. This enables tuning of the $I$-$V$ characteristics and paves a new pathway towards engineering high-performance NEM devices with low actuation voltages. Moving forward to the macroscale, the superior performance achieved by these individual functional units

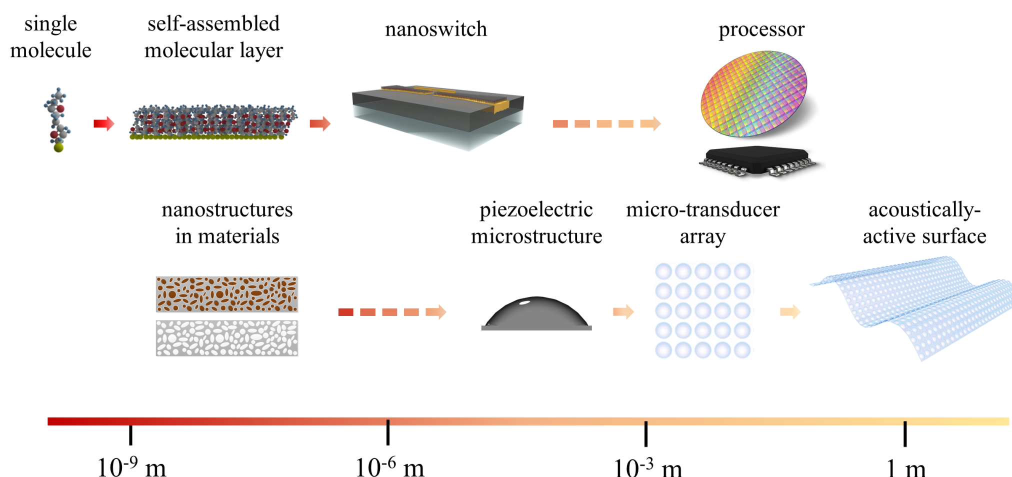


Figure 10-1: Engineering electromechanical devices and systems through active component design at different scales.

(i.e., nanoswitch in this example) lays the foundation to realizing energy-efficient digital integrated circuits with zero standby power consumption that cater to the demand from IOT data processing.

In the second case study, piezoelectric microstructures that are capable of radiating and sensing acoustic waves act as critical active components. Engineering their profile and dimensions brings a broad tunability in the transduction between acoustics and electrics. Assembling a certain number of these microstructures into a functional group (pixel) assigned with a specific task (speaker, microphone, ultrasonic transceiver) and coordinating the resulting pixels with an elaborate control scheme empower wide-area acoustic surfaces with functionality unavailable based on standalone acoustic transducers. There is also plenty of room for improvement at the nanoscale. Engineering nanostructures (e.g., nanopores, nanoparticle dopants) in the piezoelectric material offers more fundamental design freedom to achieve enhanced performance of the acoustic surface.

Comparing these two cases, they intrinsically show the same paradigm based on assembly of active structures into a functional system at the macroscale. The ac-

complishment of unprecendented performance for both cases is primarily attributed to parallel actuation of the fundamental components (molecular nano-springs, piezoelectric micro-transducers). The difference between these two cases lies in the scale of design (nanometer-scale for the tunneling nanoswitch and micrometer-scale for the acoustic surface) and exploration (up to device level for the nanoswitch and system level for the acoustic surface). These two cases collectively demonstrate the strategy for engineering high-performance electromechanical devices and systems based on active components at different scales. This versatile scheme also extends beyond the scope of this thesis, and could be widely adopted for the development of metamaterials, emerging devices and multifunctional systems in the field of electronics, mechanics, optics, magnetics, and thermodynamics.

# Bibliography

[1] A Prasanna De Silva, HQ Nimal Gunaratne, Thorfinnur Gunnlaugsson, Allen JM Huxley, Colin P McCoy, Jude T Rademacher, and Terence E Rice. Signaling recognition events with fluorescent sensors and switches. *Chemical Reviews*, 97(5):1515–1566, 1997.

[2] Digh Hisamoto, Wen-Chin Lee, Jakub Kedzierski, Hideki Takeuchi, Kazuya Asano, Charles Kuo, Erik Anderson, Tsu-Jae King, Jeffrey Bokor, and Chenming Hu. Finfet-a self-aligned double-gate mosfet scalable to 20 nm. *IEEE Transactions on Electron Devices*, 47(12):2320–2325, 2000.

[3] Yasuhiro Shirasaki, Geoffrey J Supran, Moungi G Bawendi, and Vladimir Bulović. Emergence of colloidal quantum-dot light-emitting technologies. *Nature Photonics*, 7(1):13, 2013.

[4] Owen Y Loh and Horacio D Espinosa. Nanoelectromechanical contact switches. *Nature Nanotechnology*, 7(5):283, 2012.

[5] AD Smith, Frank Niklaus, A Paussa, Sam Vaziri, Andreas C Fischer, Mikael Sterner, Fredrik Forsberg, Anna Delin, D Esseni, P Palestri, et al. Electromechanical piezoresistive sensing in suspended graphene membranes. *Nano Letters*, 13(7):3237–3242, 2013.

[6] AM Fennimore, TD Yuzvinsky, Wei-Qiang Han, MS Fuhrer, J Cumings, and A Zettl. Rotational actuators based on carbon nanotubes. *Nature*, 424(6947):408–410, 2003.

[7] J Scott Bunch, Arend M Van Der Zande, Scott S Verbridge, Ian W Frank, David M Tanenbaum, Jeevak M Parpia, Harold G Craighead, and Paul L McEuen. Electromechanical resonators from graphene sheets. *Science*, 315(5811):490–493, 2007.

[8] Jae Eun Jang, Seung Nam Cha, Young Jin Choi, Dae Joon Kang, Tim P Butler, David G Hasko, Jae Eun Jung, Jong Min Kim, and Gehan AJ Amaratunga. Nanoscale memory cell based on a nanoelectromechanical switched capacitor. *Nature Nanotechnology*, 3(1):26, 2008.

[9] Farnaz Niroui, Annie I Wang, Ellen M Sletten, Yi Song, Jing Kong, Eli Yablonovitch, Timothy M Swager, Jeffrey H Lang, and Vladimir Bulovic. Tunneling nanoelectromechanical switches based on compressible molecular thin films. *ACS Nano*, 9(8):7886–7894, 2015.

[10] VV Deshpande, H-Y Chiu, HW Ch Postma, C Miko, L Forro, and M Bockrath. Carbon nanotube linear bearing nanoswitches. *Nano Letters*, 6(6):1092–1095, 2006.

[11] K Jensen, Kwanpyo Kim, and A Zettl. An atomic-resolution nanomechanical mass sensor. *Nature Nanotechnology*, 3(9):533–537, 2008.

[12] Daniel F Hanks, Zhengmao Lu, Jay Sircar, Todd R Salamon, Dion S Antao, Kevin R Bagnall, Banafsheh Barabadi, and Evelyn N Wang. Nanoporous membrane device for ultra high heat flux thermal management. *Microsystems & Nanoengineering*, 4(1):1–10, 2018.

[13] Ryuji Hirayama, Diego Martinez Plasencia, Nobuyuki Masuda, and Sriram Subramanian. A volumetric display for visual, tactile and audio presentation using acoustic trapping. *Nature*, 575(7782):320–323, 2019.

[14] David J Frank, Robert H Dennard, Edward Nowak, Paul M Solomon, Yuan Taur, and Hon-Sum Philip Wong. Device scaling limits of si mosfets and their application dependencies. *Proceedings of the IEEE*, 89(3):259–288, 2001.

[15] The international technology roadmap for semiconductors 2.0 (itrs2.0, 2015): Executive report. http://www.itrs2.net/itrs-reports.html.

[16] Adrian M Ionescu and Heike Riel. Tunnel field-effect transistors as energy-efficient electronic switches. *Nature*, 479(7373):329–337, 2011.

[17] Woo Young Choi, Byung-Gook Park, Jong Duk Lee, and Tsu-Jae King Liu. Tunneling field-effect transistors (tfets) with subthreshold swing (ss) less than 60 mv/dec. *IEEE Electron Device Letters*, 28(8):743–745, 2007.

[18] Sayeef Salahuddin and Supriyo Datta. Use of negative capacitance to provide voltage amplification for low power nanoscale devices. *Nano Letters*, 8(2):405–410, 2008.

[19] Mengwei Si, Chun-Jung Su, Chunsheng Jiang, Nathan J Conrad, Hong Zhou, Kerry D Maize, Gang Qiu, Chien-Ting Wu, Ali Shakouri, Muhammad A Alam, et al. Steep-slope hysteresis-free negative capacitance mos 2 transistors. *Nature Nanotechnology*, 13(1):24–28, 2018.

[20] Kailash Gopalakrishnan, Peter B Griffin, and James D Plummer. I-mos: A novel semiconductor device with a subthreshold slope lower than kt/q. In *Digest. International Electron Devices Meeting,*, pages 289–292. IEEE, 2002.

[21] Jeong Oen Lee, Yong-Ha Song, Min-Wu Kim, Min-Ho Kang, Jae-Sub Oh, Hyun-Ho Yang, and Jun-Bo Yoon. A sub-1-volt nanoelectromechanical switching device. *Nature Nanotechnology*, 8(1):36–40, 2013.

[22] Hamed F Dadgour, Muhammad M Hussain, Casey Smith, and Kaustav Banerjee. Design and analysis of compact ultra energy-efficient logic gates using laterally-actuated double-electrode nems. In *Proceedings of the 47th Design Automation Conference*, pages 893–896, 2010.

[23] Matthew Spencer, Fred Chen, Cheng C Wang, Rhesa Nathanael, Hossein Fariborzi, Abhinav Gupta, Hei Kam, Vincent Pott, Jaeseok Jeon, Tsu-Jae King Liu, et al. Demonstration of integrated micro-electro-mechanical relay circuits for vlsi applications. *IEEE Journal of Solid-State Circuits*, 46(1):308–320, 2010.

[24] Te-Hao Lee, Swarup Bhunia, and Mehran Mehregany. Electromechanical computing at 500 c with silicon carbide. *Science*, 329(5997):1316–1318, 2010.

[25] Xiaoer Hu, Sergio F Almeida, Zhixin Alice Ye, and Tsu-Jae King Liu. Ultra-low-voltage operation of mem relays for cryogenic logic applications. In *2019 IEEE International Electron Devices Meeting (IEDM)*, pages 34–2. IEEE, 2019.

[26] Kyu-Man Hwang, Jun-Young Park, Hagyoul Bae, Seung-Wook Lee, Choong-Ki Kim, Myungsoo Seo, Hwon Im, Do-Hyun Kim, Seong-Yeon Kim, Geon-Beom Lee, et al. Nano-electromechanical switch based on a physical unclonable function for highly robust and stable performance in harsh environments. *ACS Nano*, 11(12):12547–12552, 2017.

[27] L Magnus Jonsson, S Axelsson, Tomas Nord, S Viefers, and Jari M Kinaret. High frequency properties of a cnt-based nanorelay. *Nanotechnology*, 15(11):1497, 2004.

[28] Miao Lu, Xuekun Lu, Min-Woo Jang, Stephen A Campbell, and Tianhong Cui. Characterization of carbon nanotube nanoswitches with gigahertz resonance frequency and low pull-in voltages using electrostatic force microscopy. *Journal of Micromechanics and Microengineering*, 20(10):105016, 2010.

[29] SN Cha, JE Jang, Y Choi, GAJ Amaratunga, D-J Kang, DG Hasko, JE Jung, and JM Kim. Fabrication of a nanoelectromechanical switch using a suspended carbon nanotube. *Applied Physics Letters*, 86(8):083105, 2005.

[30] You Qian, Liang Lou, Minglin Julius Tsai, and Chengkuo Lee. A dual-silicon-nanowires based u-shape nanoelectromechanical switch with low pull-in voltage. *Applied Physics Letters*, 100(11):113102, 2012.

[31] XL Feng, MH Matheny, Christian A Zorman, Mehran Mehregany, and ML Roukes. Low voltage nanoelectromechanical switches based on silicon carbide nanowires. *Nano Letters*, 10(8):2891–2896, 2010.

[32] Sang Wook Lee, Dong Su Lee, Raluca E Morjan, Sung Ho Jhang, Martin Svenningsson, OA Nerushev, Yung Woo Park, and Eleanor EB Campbell. A three-terminal carbon nanorelay. *Nano Letters*, 4(10):2027–2030, 2004.

[33] Anupama B Kaul, Eric W Wong, Larry Epp, and Brian D Hunt. Electromechanical carbon nanotube switches for high-frequency applications. *Nano Letters*, 6(5):942–947, 2006.

[34] Benjamin Osoba, Bivas Saha, Liam Dougherty, Jane Edgington, Chuang Qian, Farnaz Niroui, Jeffrey H Lang, Vladimir Bulovic, Junqiao Wu, and Tsu-Jae King Liu. Sub-50 mv nem relay operation enabled by self-assembled molecular coating. In *2016 IEEE International Electron Devices Meeting (IEDM)*, pages 26–8. IEEE, 2016.

[35] Rhesa Nathanael, Vincent Pott, Hei Kam, Jaeseok Jeon, and Tsu-Jae King Liu. 4-terminal relay technology for complementary logic. In *2009 IEEE International Electron Devices Meeting (IEDM)*, pages 1–4. IEEE, 2009.

[36] Owen Loh, Xiaoding Wei, John Sullivan, Leonidas E Ocola, Ralu Divan, and Horacio D Espinosa. Carbon-carbon contacts for robust nanoelectromechanical switches. *Advanced Materials*, 24(18):2463–2468, 2012.

[37] Peng Li, Zheng You, and Tianhong Cui. Graphene cantilever beams for nano switches. *Applied Physics Letters*, 101(9):093111, 2012.

[38] Changhong Ke and Horacio D Espinosa. In situ electron microscopy electromechanical characterization of a bistable nems device. *Small*, 2(12):1484–1489, 2006.

[39] Jin-Woo Han, Jae-Hyuk Ahn, Min-Wu Kim, Jun-Bo Yoon, and Yang-Kyu Choi. Monolithic integration of nems-cmos with a fin flip-flop actuated channel transistor (finfact). In *2009 IEEE International Electron Devices Meeting (IEDM)*, pages 1–4. IEEE, 2009.

[40] Weon Wi Jang, Jeong Oen Lee, Jun-Bo Yoon, Min-Sang Kim, Ji-Myoung Lee, Sung-Min Kim, Keun-Hwi Cho, Dong-Won Kim, Donggun Park, and Won-Seong Lee. Fabrication and characterization of a nanoelectromechanical switch with 15-nm-thick suspension air gap. *Applied Physics Letters*, 92(10):103110, 2008.

[41] Jin-Woo Han, Jae-Hyuk Ahn, Min-Wu Kim, Jeong Oen Lee, Jun-Bo Yoon, and Yang-Kyu Choi. Nanowire mechanical switch with a built-in diode. *Small*, 6(11):1197–1200, 2010.

[42] Ji-Hun Kim, Zack CY Chen, Soonshin Kwon, and Jie Xiang. Three-terminal nanoelectromechanical field effect transistor with abrupt subthreshold slope. *Nano Letters*, 14(3):1687–1691, 2014.

[43] Hamed Dadgour, Alan M Cassell, and Kaustav Banerjee. Scaling and variability analysis of cnt-based nems devices and circuits with implications for process design. In *2008 IEEE International Electron Devices Meeting*, pages 1–4. IEEE, 2008.

[44] Roozbeh Parsa, W Scott Lee, Mohammad Shavezipur, J Provine, Roya Maboudian, Subhasish Mitra, H-S Philip Wong, and Roger T Howe. Laterally actuated platinum-coated polysilicon nem relays. *Journal of Microelectromechanical Systems*, 22(3):768–778, 2013.

[45] S Axelsson, Eleanor EB Campbell, LM Jonsson, J Kinaret, SangWook Lee, YungWoo Park, and Martin Sveningsson. Theoretical and experimental investigations of three-terminal carbon nanotube relays. *New Journal of Physics*, 7(1):245, 2005.

[46] Owen Loh, Xiaoding Wei, Changhong Ke, John Sullivan, and Horacio D Espinosa. Robust carbon-nanotube-based nano-electromechanical devices: Understanding and eliminating prevalent failure modes using alternative electrode materials. *Small*, 7(1):79–86, 2011.

[47] Ngoc Huynh Van, Manoharan Muruganathan, Jothiramalingam Kulothungan, and Hiroshi Mizuta. Fabrication of a three-terminal graphene nanoelectromechanical switch using two-dimensional materials. *Nanoscale*, 10(26):12349–12355, 2018.

[48] Jungwook Choi, Jae-Ik Lee, Youngkee Eun, Min-Ook Kim, and Jongbaeg Kim. Aligned carbon nanotube arrays for degradation-resistant, intimate contact in micromechanical devices. *Advanced Materials*, 23(19):2231–2236, 2011.

[49] Roya Maboudian and Roger T Howe. Critical review: Adhesion in surface micromechanical structures. *Journal of Vacuum Science & Technology B: Microelectronics and Nanometer Structures Processing, Measurement, and Phenomena*, 15(1):1–20, 1997.

[50] A Kis, K Jensen, S Aloni, W Mickelson, and A Zettl. Interlayer forces and ultralow sliding friction in multiwalled carbon nanotubes. *Physical Review Letters*, 97(2):025501, 2006.

[51] E Dujardin, V Derycke, MF Goffman, R Lefevre, and JP Bourgoin. Self-assembled switches based on electroactuated multiwalled nanotubes. *Applied Physics Letters*, 87(19):193107, 2005.

[52] JE Jang, SN Cha, Y Choi, Gehan AJ Amaratunga, DJ Kang, DG Hasko, JE Jung, and JM Kim. Nanoelectromechanical switches with vertically aligned carbon nanotubes. *Applied Physics Letters*, 87(16):163114, 2005.

[53] D Acquaviva, A Arun, S Esconjauregui, D Bouvet, J Robertson, R Smajda, A Magrez, L Forro, and AM Ionescu. Capacitive nanoelectromechanical

switch based on suspended carbon nanotube array. *Applied Physics Letters*, 97(23):233508, 2010.

[54] Yuhei Hayamizu, Takeo Yamada, Kohei Mizuno, Robert C Davis, Don N Futaba, Motoo Yumura, and Kenji Hata. Integrated three-dimensional microelectromechanical devices from processable carbon nanotube wafers. *Nature Nanotechnology*, 3(5):289–294, 2008.

[55] Jingqi Li, Qing Zhang, Ning Peng, and Qi Zhu. Manipulation of carbon nanotubes using ac dielectrophoresis. *Applied Physics Letters*, 86(15):153116, 2005.

[56] Arunkumar Subramanian, LX Dong, Bradley J Nelson, and Antoine Ferreira. Supermolecular switches based on multiwalled carbon nanotubes. *Applied Physics Letters*, 96(7):073116, 2010.

[57] Zhuo Chen, Lianming Tong, Zhongyun Wu, and Zhongfan Liu. Fabrication of electromechanical switch using interconnected single-walled carbon nanotubes. *Applied Physics Letters*, 92(10):103116, 2008.

[58] Erik M Freer, Oleg Grachev, Xiangfeng Duan, Samuel Martin, and David P Stumbo. High-yield self-limiting single-nanowire assembly with dielectrophoresis. *Nature Nanotechnology*, 5(7):525, 2010.

[59] Wentao Gan, Chaoji Chen, Hyun-Tae Kim, Zhiwei Lin, Jiaqi Dai, Zhihua Dong, Zhan Zhou, Weiwei Ping, Shuaiming He, Shaoliang Xiao, et al. Single-digit-micrometer thickness wood speaker. *Nature Communications*, 10(1):1–8, 2019.

[60] Sang Choon Ko, Yong Chul Kim, Seung S Lee, Seung Ho Choi, and Sang Ryong Kim. Piezoelectric membrane acoustic devices. In *Technical Digest. MEMS 2002 IEEE International Conference. Fifteenth IEEE International Conference on Micro Electro Mechanical Systems (Cat. No. 02CH37266)*, pages 296–299. IEEE, 2002.

[61] Eetta Saarimaki, Mika Paajanen, A Savijarvi, Hannu Minkkinen, Michael Wegener, Olena Voronina, Robert Schulze, Werner Wirges, and Reimund Gerhard-Multhaupt. Novel heat durable electromechanical film: processing for electromechanical and electret applications. *IEEE Transactions on Dielectrics and Electrical Insulation*, 13(5):963–972, 2006.

[62] Wen-Ching Ko, Chien-Kai Tseng, Yih Leu, Wen-Jong Wu, Adam Shih-Yuan Lee, and Chih-Kung Lee. Use of 2-(6-mercaptohexyl) malonic acid to adjust the morphology and electret properties of cyclic olefin copolymer and its application to flexible loudspeakers. *Smart Materials and Structures*, 19(5):055007, 2010.

[63] Apoorva Murarka, Jeffrey H Lang, and Vladimir Bulovic. Printed membrane electrostatic mems microspeakers. In *2016 IEEE 29th International Conference on Micro Electro Mechanical Systems (MEMS)*, pages 1118–1121. IEEE, 2016.

[64] Thorsten S. Albach, Peter Horn, Alexander Sutor, and Reinhard Lerch. Sound generation using a magnetostrictive microactuator. *Journal of Applied Physics*, 109(7):07E510, 2011.

[65] Qin Zhou and A Zettl. Electrostatic graphene loudspeaker. *Applied Physics Letters*, 102(22):223109, 2013.

[66] Rajiv M Reddy, Issa MS Panahi, and Richard Briggs. Hybrid fxrls-fxnlms adaptive algorithm for active noise control in fmri application. *IEEE Transactions on Control Systems Technology*, 19(2):474–480, 2010.

[67] DongYuan Shi, Woon-Seng Gan, Bhan Lam, and Chuang Shi. Two-gradient direction fxlms: An adaptive active noise control algorithm with output constraint. *Mechanical Systems and Signal Processing*, 116:651–667, 2019.

[68] Young Hoon Jung, Seong Kwang Hong, Hee Seung Wang, Jae Hyun Han, Trung Xuan Pham, Hyunsin Park, Junyeong Kim, Sunghun Kang, Chang D Yoo, and Keon Jae Lee. Flexible piezoelectric acoustic sensors and machine learning for speech processing. *Advanced Materials*, 32(35):1904020, 2020.

[69] Jae Hyun Han, Kang Min Bae, Seong Kwang Hong, Hyunsin Park, Jun-Hyuk Kwak, Hee Seung Wang, Daniel Juhyung Joe, Jung Hwan Park, Young Hoon Jung, Shin Hur, et al. Machine learning-based self-powered acoustic sensor for speaker recognition. *Nano Energy*, 53:658–665, 2018.

[70] Daniele Foresti and Dimos Poulikakos. Acoustophoretic contactless elevation, orbital transport and spinning of matter in air. *Physical Review Letters*, 112(2):024301, 2014.

[71] Charles RP Courtney, Christine EM Demore, Hongxiao Wu, Alon Grinenko, Paul D Wilcox, Sandy Cochran, and Bruce W Drinkwater. Independent trapping and manipulation of microparticles using dexterous acoustic tweezers. *Applied Physics Letters*, 104(15):154103, 2014.

[72] Asier Marzo and Bruce W Drinkwater. Holographic acoustic tweezers. *Proceedings of the National Academy of Sciences*, 116(1):84–89, 2019.

[73] Thomas Laurell, Filip Petersson, and Andreas Nilsson. Chip integrated strategies for acoustic separation and manipulation of cells and particles. *Chemical Society Reviews*, 36(3):492–506, 2007.

[74] Jungwoo Lee, Shia-Yen Teh, Abraham Lee, Hyung Ham Kim, Changyang Lee, and K Kirk Shung. Single beam acoustic trapping. *Applied Physics Letters*, 95(7):073701, 2009.

[75] Yuchao Chen, Xiaoyun Ding, Sz-Chin Steven Lin, Shikuan Yang, Po-Hsun Huang, Nitesh Nama, Yanhui Zhao, Ahmad Ahsan Nawaz, Feng Guo, Wei Wang, et al. Tunable nanowire patterning using standing surface acoustic waves. *ACS Nano*, 7(4):3306–3314, 2013.

[76] Filip Petersson, Andreas Nilsson, Cecilia Holm, Henrik Jönsson, and Thomas Laurell. Continuous separation of lipid particles from erythrocytes by means of laminar flow and acoustic standing wave forces. *Lab on a Chip*, 5(1):20–22, 2005.

[77] Adam D Maxwell, Michael Bailey, Bryan W Cunitz, M Terzi, A Nikolaeva, S Tsysar, and Oleg A Sapozhnikov. Vortex beams and radiation torque for kidney stone management. *The Journal of the Acoustical Society of America*, 139(4):2040–2040, 2016.

[78] RJ Naumann and DD Elleman. Containerless processing technology. In *Materials Sciences in Space*, pages 294–313. Springer, 1986.

[79] Dirk Langer and Charles E Thorpe. Sonar based outdoor vehicle navigation and collision avoidance. In *IROS*, pages 1445–1450. Citeseer, 1992.

[80] Alberto Elfes. Sonar-based real-world mapping and navigation. *IEEE Journal on Robotics and Automation*, 3(3):249–265, 1987.

[81] Mohsin I Tiwana, Stephen J Redmond, and Nigel H Lovell. A review of tactile sensing technologies with applications in biomedical engineering. *Sensors and Actuators A: physical*, 179:17–31, 2012.

[82] Danilo De Rossi. Artificial tactile sensing and haptic perception. *Measurement Science and Technology*, 2(11):1003, 1991.

[83] Anthony P Roberts and Edward J Garboczi. Elastic properties of model porous ceramics. *Journal of the American Ceramic Society*, 83(12):3041–3048, 2000.

[84] Cédric Boissiere, David Grosso, Sophie Lepoutre, Lionel Nicole, Aline Brunet Bruneau, and Clément Sanchez. Porosity and mechanical properties of mesoporous thin films assessed by environmental ellipsometric porosimetry. *Langmuir*, 21(26):12362–12371, 2005.

[85] Jeff Dusek, Michael Triantafyllou, Mun Ee Woo, and Jeffrey Lang. Carbon black-pdms composite conformal pressure sensor arrays for near-body flow detection. In *OCEANS 2014-TAIPEI*, pages 1–7. IEEE, 2014.

[86] Apoorva Murarka, Sarah Paydavosi, Trisha Andrew, Annie Wang, Jeffrey Lang, and Vladimir Bulovic. Printed mems membranes on silicon. In *2012 IEEE 25th International Conference on Micro Electro Mechanical Systems (MEMS)*, pages 309–312. IEEE, 2012.

[87] Apoorva Murarka, Corinne Packard, Frank Yaul, Jeffrey Lang, and Vladimir Bulovic. Micro-contact printed mems. In *2011 IEEE 24th International Conference on Micro Electro Mechanical Systems*, pages 292–295. IEEE, 2011.

[88] Justin Young-Hyun Kim. *Parylene-c as a new piezoelectric material.* PhD thesis, California Institute of Technology, 2013.

[89] Bahram Jadidian, Nader Marandian Hagh, Alan A Winder, and Ahmad Safari. 25 mhz ultrasonic transducers with lead-free piezoceramic, 1-3 pzt fiber-epoxy composite, and pvdf polymer active elements. *IEEE Transactions on Ultrasonics, Ferroelectrics, and Frequency Control*, 56(2):368–378, 2009.

[90] RAC Altafim, Heitor Cury Basso, RAP Altafim, L Lima, CV De Aquino, L Gonçalves Neto, and R Gerhard-Multhaupt. Piezoelectrets from thermoformed bubble structures of fluoropolymer-electret films. *IEEE Transactions on Dielectrics and Electrical Insulation*, 13(5):979–985, 2006.

[91] Shiyou Xu, Yao-wen Yeh, Gerald Poirier, Michael C McAlpine, Richard A Register, and Nan Yao. Flexible piezoelectric pmn–pt nanowire-based nanocomposite and device. *Nano Letters*, 13(6):2393–2398, 2013.

[92] Zongjin Li, Dong Zhang, and Keru Wu. Cement-based 0-3 piezoelectric composites. *Journal of the American Ceramic Society*, 85(2):305–313, 2002.

[93] Khaled S Ramadan, Dan Sameoto, and Sthephane Evoy. A review of piezoelectric polymers as functional materials for electromechanical transducers. *Smart Materials and Structures*, 23(3):033001, 2014.

[94] J Hillenbrand and GM Sessler. Quasistatic and dynamic piezoelectric coefficients of polymer foams and polymer film systems. *IEEE Transactions on Dielectrics and Electrical Insulation*, 11(1):72–79, 2004.

[95] John G Simmons. Generalized formula for the electric tunnel effect between similar electrodes separated by a thin insulating film. *Journal of Applied Physics*, 34(6):1793–1803, 1963.

[96] Hermann A Haus and James R Melcher. *Electromagnetic fields and energy*, volume 107. Prentice Hall Englewood Cliffs, NJ, 1989.

[97] G Palasantzas, PJ Van Zwol, and J Th M De Hosson. Transition from casimir to van der waals force between macroscopic bodies. *Applied Physics Letters*, 93(12):121912, 2008.

[98] JI Siepmann and IR McDonald. Monte carlo simulation of the mechanical relaxation of a self-assembled monolayer. *Physical Review Letters*, 70(4):453, 1993.

[99] Qian Huang, Ilsun Yoon, Josh Villanueva, Kanguk Kim, and Donald J Sirbuly. Quantitative mechanical analysis of thin compressible polymer monolayers on oxide surfaces. *Soft Matter*, 10(40):8001–8010, 2014.

[100] Rani Arielly, Ayelet Ofarim, Gilad Noy, and Yoram Selzer. Accurate determination of plasmonic fields in molecular junctions by current rectification at optical frequencies. *Nano Letters*, 11(7):2968–2972, 2011.

[101] Jeremy R Niskala, William C Rice, Robert C Bruce, Timothy J Merkel, Frank Tsui, and Wei You. Tunneling characteristics of au–alkanedithiol–au junctions formed via nanotransfer printing (ntp). *Journal of the American Chemical Society*, 134(29):12072–12082, 2012.

[102] Hylke B Akkerman, Ronald CG Naber, Bert Jongbloed, Paul A van Hal, Paul WM Blom, Dago M de Leeuw, and Bert de Boer. Electron tunneling through alkanedithiol self-assembled monolayers in large-area molecular junctions. *Proceedings of the National Academy of Sciences*, 104(27):11161–11166, 2007.

[103] Sarbajit Banerjee, Brian E White, Limin Huang, Blake J Rego, Stephen O'Brien, and Irving P Herman. Precise positioning of single-walled carbon nanotubes by ac dielectrophoresis. *Journal of Vacuum Science & Technology B: Microelectronics and Nanometer Structures Processing, Measurement, and Phenomena*, 24(6):3173–3178, 2006.

[104] Timo Schwamb, Tae-Youl Choi, Niklas Schirmer, Nicole R Bieri, Brian Burg, Joy Tharian, Urs Sennhauser, and Dimos Poulikakos. A dielectrophoretic method for high yield deposition of suspended, individual carbon nanotubes with four-point electrode contact. *Nano Letters*, 7(12):3633–3638, 2007.

[105] Qing Cao, Shu-jen Han, and George S Tulevski. Fringing-field dielectrophoretic assembly of ultrahigh-density semiconducting nanotube arrays with a self-limited pitch. *Nature Communications*, 5(1):1–7, 2014.

[106] Farnaz Niroui, Mayuran Saravanapavanantham, Jinchi Han, Jatin J Patil, Timothy M Swager, Jeffrey H Lang, and Vladimir Bulovic. Hybrid approach to fabricate uniform and active molecular junctions. *Nano Letters*, 21(4):1606–1612, 2021.

[107] Gheorghe Stan, Frank W DelRio, Robert I MacCuspie, and Robert F Cook. Nanomechanical properties of polyethylene glycol brushes on gold substrates. *The Journal of Physical Chemistry B*, 116(10):3138–3147, 2012.

[108] Hylke B Akkerman, Paul WM Blom, Dago M De Leeuw, and Bert De Boer. Towards molecular electronics with large-area molecular junctions. *Nature*, 441(7089):69–72, 2006.

[109] Gabriel Puebla-Hellmann, Koushik Venkatesan, Marcel Mayor, and Emanuel Lörtscher. Metallic nanoparticle contacts for high-yield, ambient-stable molecular-monolayer devices. *Nature*, 559(7713):232–235, 2018.

[110] Yu-Tai Tao, Chien-Ching Wu, Ji-Yang Eu, Wen-Ling Lin, Kwang-Chen Wu, and Chun-hsien Chen. Structure evolution of aromatic-derivatized thiol monolayers on evaporated gold. *Langmuir*, 13(15):4018–4023, 1997.

[111] Shun-Chi Chang, Ito Chao, and Yu-Tai Tao. Structure of self-assembled monolayers of aromatic-derivatized thiols on evaporated gold and silver surfaces: Implication on packing mechanism. *Journal of the American Chemical Society*, 116(15):6792–6805, 1994.

[112] Nupur Garg, Edwin Carrasquillo-Molina, and T Randall Lee. Self-assembled monolayers composed of aromatic thiols on gold: Structural characterization and thermal stability in solution. *Langmuir*, 18(7):2717–2726, 2002.

[113] Supachai Rittikulsittichai, Chul Soon Park, Andrew C Jamison, Daniela Rodriguez, Oussama Zenasni, and T Randall Lee. Bidentate aromatic thiols on gold: new insight regarding the influence of branching on the structure, packing, wetting, and stability of self-assembled monolayers on gold surfaces. *Langmuir*, 33(18):4396–4406, 2017.

[114] Joseph F Ford, Thomas J Vickers, Charles K Mann, and Joseph B Schlenoff. Polymerization of a thiol-bound styrene monolayer. *Langmuir*, 12(8):1944–1946, 1996.

[115] Taisun Kim, Kwok C Chan, and Richard M Crooks. Polymeric self-assembled monolayers. 4. chemical, electrochemical, and thermal stability of $\omega$-functionalized, self-assembled diacetylenic and polydiacetylenic monolayers. *Journal of the American Chemical Society*, 119(1):189–193, 1997.

[116] Laongnuan Srisombat, Andrew C Jamison, and T Randall Lee. Stability: A key issue for self-assembled monolayers on gold as thin-film coatings and nanoparticle protectants. *Colloids and Surfaces A: Physicochemical and Engineering Aspects*, 390(1-3):1–19, 2011.

[117] Shishan Zhang, Andrew C Jamison, Daniel K Schwartz, and T Randall Lee. Self-assembled monolayers derived from a double-chained monothiol having chemically dissimilar chains. *Langmuir*, 24(18):10204–10208, 2008.

[118] Frank W DelRio, Kristen L Steffens, Cherno Jaye, Daniel A Fischer, and Robert F Cook. Elastic, adhesive, and charge transport properties of a metal-molecule- metal junction: the role of molecular orientation, order, and coverage. *Langmuir*, 26(3):1688–1699, 2010.

[119] Frank W DelRio, Cherno Jaye, Daniel A Fischer, and Robert F Cook. Elastic and adhesive properties of alkanethiol self-assembled monolayers on gold. *Applied Physics Letters*, 94(13):131909, 2009.

[120] AR Burns, JE Houston, RW Carpick, and TA Michalske. Molecular level friction as revealed with a novel scanning probe. *Langmuir*, 15(8):2922–2930, 1999.

[121] Frank W DelRio, David M Rampulla, Cherno Jaye, Gheorghe Stan, Richard S Gates, Daniel A Fischer, and Robert F Cook. Structure–property relationships for methyl-terminated alkyl self-assembled monolayers. *Chemical Physics Letters*, 512(4-6):243–246, 2011.

[122] Huiwen Liu and Bharat Bhushan. Investigation of nanotribological properties of self-assembled monolayers with alkyl and biphenyl spacer chains. *Ultramicroscopy*, 91(1-4):185–202, 2002.

[123] Seunghwan Lee, Young-Seok Shon, Ramon Colorado, Rebecca L Guenard, T Randall Lee, and Scott S Perry. The influence of packing densities and surface order on the frictional properties of alkanethiol self-assembled monolayers (sams) on gold: a comparison of sams derived from normal and spiroalkanedithiols. *Langmuir*, 16(5):2220–2224, 2000.

[124] Victor Chechik, Holger Schönherr, G Julius Vancso, and Charles JM Stirling. Self-assembled monolayers of branched thiols and disulfides on gold: Surface coverage, order and chain orientation. *Langmuir*, 14(11):3003–3010, 1998.

[125] Supachai Rittikulsittichai, Andrew C Jamison, and T Randall Lee. Self-assembled monolayers derived from alkoxyphenylethanethiols having one, two, and three pendant chains. *Langmuir*, 27(16):9920–9927, 2011.

[126] Abdulilah M Mayet, Aftab M Hussain, and Muhammad M Hussain. Three-terminal nanoelectromechanical switch based on tungsten nitride—an amorphous metallic material. *Nanotechnology*, 27(3):035202, 2015.

[127] JE Jang, SN Cha, Y Choi, TP Butler, DJ Kang, DG Hasko, JE Jung, YW Jin, JM Kim, and GAJ Amaratunga. Nanoelectromechanical switch with low voltage drive. *Applied Physics Letters*, 93(11):113105, 2008.

[128] Stephen P Timoshenko and Sergius Woinowsky-Krieger. *Theory of plates and shells*. McGraw-hill, 1959.

[129] Theodor Krauthammer. *Thin plates and shells: theory, analysis and applications*. Dekker, 2001.

[130] RA Abram. The theory of a piezoelectric plastic film transducer for earphones. *Journal of Physics D: Applied Physics*, 13(2):201, 1980.

[131] Geoffrey M Garner and Anthony J Holden. Tone ringer using polyvinylidene fluoride (pvdf) piezoelectric film. *The Journal of the Acoustical Society of America*, 83(5):1940–1945, 1988.

[132] Hideo Suzuki, Naoki Yamaguchi, and Hideaki Izumi. Theoretical and experimental studies on the resonance frequencies of a stretched circular plate: Application to japanese drum diaphragms. *Acoustical science and technology*, 30(5):348–354, 2009.

[133] Holger Becker and Claudia Gärtner. Polymer microfabrication technologies for microfluidic systems. *Analytical and Bioanalytical Chemistry*, 390(1):89–111, 2008.

[134] X Zhang, J Hillenbrand, GM Sessler, S Haberzettl, and K Lou. Fluoroethylene-propylene ferroelectrets with patterned microstructure and high, thermally stable piezoelectricity. *Applied Physics A*, 107(3):621–629, 2012.

[135] Guo-Hua Feng and Ming-Yen Tsai. Acoustic emission sensor with structure-enhanced sensing mechanism based on micro-embossed piezoelectric polymer. *Sensors and Actuators A: Physical*, 162(1):100–106, 2010.

[136] Myoung-Soo Kim, Hye-Rin Ahn, Seok Lee, Chulki Kim, and Yong-Jun Kim. A dome-shaped piezoelectric tactile sensor arrays fabricated by an air inflation technique. *Sensors and Actuators A: Physical*, 212:151–158, 2014.

[137] Chunyan Li, Pei-Ming Wu, Soohyun Lee, Andrew Gorton, Mark J Schulz, and Chong H Ahn. Flexible dome and bump shape piezoelectric tactile sensors using pvdf-trfe copolymer. *Journal of Microelectromechanical Systems*, 17(2):334–341, 2008.

[138] Seongkuk Lee, Evgueni V Bordatchev, and Marco JF Zeman. Femtosecond laser micromachining of polyvinylidene fluoride (pvdf) based piezo films. *Journal of Micromechanics and Microengineering*, 18(4):045011, 2008.

[139] Tushar Sharma, Sang-Soo Je, Brijesh Gill, and John XJ Zhang. Patterning piezoelectric thin film pvdf–trfe based pressure sensor for catheter application. *Sensors and Actuators A: Physical*, 177:87–92, 2012.

[140] Xunlin Qiu. Patterned piezo-, pyro-, and ferroelectricity of poled polymer electrets. *Journal of Applied physics*, 108(1):8, 2010.

[141] Condenser microphones and microphone preamplifiers for acoustic measurements. *Data Handbook*, page 52, 1982.

[142] Richard Heydt, Roy Kornbluh, Joseph Eckerle, and Ron Pelrine. Sound radiation properties of dielectric elastomer electroactive polymer loudspeakers. In *Smart Structures and Materials 2006: Electroactive Polymer Actuators and Devices (EAPAD)*, volume 6168, page 61681M. International Society for Optics and Photonics, 2006.